Lysozyme Encapsulated Gold Nanocluster for Studying Protein Denaturation

A Thesis submitted to the University of Strathclyde for the degree of Doctor of Philosophy

By

Nora A. Alkudaisi

Photophysics Research Group
Department of Physics
University of Strathclyde
Glasgow

2020

‘This Thesis is the result of the author’s original research. It has been composed by the author and has not been previously submitted for examination which has led to the award of a degree.’

Signed:
Date:

Acknowledgements

I would like to express my sincere gratitude to my advisor, Dr Yu Chen, for her support during my PhD studies and her patience over the years.

I would like to offer my special thanks to my advisor, Prof David Birch, for his enthusiasm, for motivating and encouraging me. My sincere thanks also go to Dr Olaf Rolinski, Dr Ben Russell, and Dr Barbara Jachimska for their time and constructive suggestions during my research. I would also like to thank Dr Philip Yip and Dr Jens Sutter for their help with the fluorescence measurements.

I would like to express my gratitude to Saudi Arabia Cultural Bureau in the UK (UKSACB) for providing me with a PhD studentship and Imam Abdulrahman Bin Faisal University in Saudi Arabia for giving me the opportunity to develop myself.

I would like to express my very great appreciation to various people for their assistance in handling the instruments: Chloe Chung, Hazel Stewart, Alastair Davy, Abeer Alghamdi, and Zendesha Mbalaha.

I would like to thank my best friend, Intisar Albandar, for continuously supporting me. Last but not least; I would like to thank my family: my brother Khalid, who came with me to study in the UK and kept me company, and other members of my family in Saudi Arabia for patiently waiting for me to finish my PhD.

Abstract

Protein denaturation is a change in a protein's structure from its native folded state to a non-native misfolded state. Protein denaturation is the cause of many diseases. Current methods used for protein denaturation studies have provided useful information regarding protein structures, but have limitations, such as their inability to detect early aggregation of protein; hence, a new method for detecting early aggregation is needed. Lysozyme-encapsulated gold nanoclusters (Lyz-AuNCs) have interesting fluorescence properties that can be used in a variety of fluorescence measurement techniques and maybe a promising tool for studying protein denaturation. So far, studies of the fluorescence characteristics of Lyz-AuNCs under protein denaturation conditions, and their correlation to protein unfolding, have been limited. The goal of this research was, therefore, to discover the influence of environmental factors and protein denaturation on the fluorescence properties of Lyz-AuNCs and further explore the potential of Lyz-AuNCs to inhibit human beta-amyloid (1-40) $A\beta_{40}$ aggregation.

In our study, changes in pH were observed to alter the fluorescence properties of Lyz-AuNCs. At an excitation wavelength 470 nm, the fluorescence intensity of AuNCs increased and redshifted when the pH is increased from pH 7 to 12. This increase correlated to a decrease in its fluorescence lifetime, suggesting a possible mechanism of the enhanced radiative process. Moreover, hen egg-white lysozyme (HEWL) was added to Lyz-AuNCs solutions to study the effect of HEWL concentrations on their fluorescence properties. Especially, the fluorescence lifetime was found to be sensitive to the concentration of HEWL at pH 3, possibly due to the aggregation that changed the local environment. Furthermore, unfolding of Lyz-AuNCs was induced by urea, sodium dodecyl sulphate and elevated temperature. It was found that the fluorescence intensity of Lyz-AuNCs decreased due to increased collisional quenching. Finally, the interaction between $A\beta_{40}$ and Lyz-AuNCs was studied. The observed decrease in fluorescence intensity was believed to be due to static quenching. Significantly, Lyz-AuNCs was found to inhibit

$A\beta_{40}$ fibre formation. This result suggested Lyz-AuNCs as a promising candidate for Alzheimer's disease (AD) treatment as well as a probe to study $A\beta_{40}$ accumulation in AD pathology.

Publications

Nora Alkudaisi, Ben A. Russell, Barbara Jachimska, David J. S. Birch and Yu Chen ''Detecting lysozyme unfolding via the fluorescence of lysozyme encapsulated gold nanoclusters'' *Journal of Materials Chemistry B* 7.7 (2019): 1167-1175.

Nora Alkudaisi, Ben A. Russell, David J. S. Birch and Yu Chen ''Lysozyme encapsulated gold nanoclusters for probing the early stage of lysozyme aggregation under acidic conditions'' *Journal of Photochemistry and Photobiology B: Biology* (2019): 111540.

Conference Proceedings

N.A. Alkudaisi, D. J. S. Birch Y. Chen, "Lysozyme encapsulated gold nanoclusters for studying protein aggregation", Poster Presentation, 2017, 12th FluoroFest International Workshop, Glasgow.

N.A. Alkudaisi, D. J. S. Birch and Y. Chen, "The effect of protein unfolding on fluorescence Properties of Ly-AuNCs", Poster Presentation and Oral Presentation, 2018, International Conference on Nanotechnology, Edinburgh

Abbreviations

11-MUA–AuNCs	11-Mercaptoundecanoic acid- gold nanocluster
$A\beta_{40}$	Human Beta amyloid
AD	Alzheimer's disease
ADC	analogue-to-digital converter
AFM	atomic force microscopy
ANS	1-anilinonaphthalene-8- sulfonate
ATP	adenosine-5'-triphosphate
DHLA-AuNCs	dihydrolipoic acid encapsulated gold nanocluster
CEW-AuNCs	chicken egg white encapsulated gold nanocluster
AuNPs	Gold nanoparticles
$Au_{YY}NCs$	Gold nanocluster, YY is the number of the gold atom
BBB	blood-brain barrier
BSA	Bovine serum albumin
BSEs	backscattering electrons
CD	circular dichroism
CFD	constant function discriminator
CFTR	Cystic fibrosis transmembrane conductance regulator
CR	Congo Red
CTAB	Cetyl trimethylammonium bromide
DNA	deoxyribonucleic acid
DPA	D-penicillamine
F	Franck-Condon
FRET	Fluorescence Resonance energy transferee
FTIR	Fourier Transform Infrared
GSH	Glutathione
HAS	human serum albumin
HD	Huntington's disease
$HepG_2$	human hepatoma cells or human hepatocarcinoma
HEWL	Hen egg white lysozyme
HOMO	highest occupied molecular orbital
K562	leukemia
L-NIBC	N-isobutyryl-L-cysteine
LOD	limit of detection
LUMO	lowest unoccupied molecular orbital
Lyz-AuNCs	Lysozyme encapsulated gold nanocluster
MMA	poly(methyl methacrylate)
NAC	N-acetyl-L-cysteine
NAG	N-acetylglucosamine sugar
NAM	N-acetylmuramic acid sugar
nBMA	poly(n-butyl methacrylate)
NIR	Near infrared region
NLLS	Nonlinear Least Squares
P53	cellular tumour antigen

PAA	Poly(acrylic acid)
PAH	poly(allylamine)hydrochloride
PAMAM	Poly(amidoamine)
PD	Parkinson's disease
pI	isoelectric point
PNIPAM MGs	poly(N-isopropylacrylamide) microgel
PPI	poly(propylene imine)
PTMP-PMAA	multidentate thioether-terminated poly(methacrylic acid)
PVP	poly(N-vinylpyrrolidone)
QCSE	Quantum Confined Stark Effect
QY	quantum yields
R	relaxed states
SDS	sodium dodecyl sulphate
SEM	scanning electron microscope
TAC	time-to-amplitude converter
tBMA	poly(tert-butyl methacrylate)
TCSPC	Time-Correlated Single Photon Counting
TEM	transmission electron microscope
ThT	Thioflavin T
TRES	Time-Resolved Emission Spectra
UA	Uranyl Acetate
UV-Vis	Ultraviolet-Visible
XPS	X-ray photoelectron

Table of Contents

Chapter 1: Introduction

1.1 Fluorophores Used in Studying Protein's Structure

Fluorescence spectroscopy is a sensitive and powerful tool in bio-applications such as imaging and sensing biomolecules. Additionally, monitoring the protein's structure using fluorophores has become an important procedure in the pharmaceutical market and clinical diagnosis. The production of protein requires assuring protein's structure is intact during synthesising and storage. Moreover, the protein's structure is subject to change in different conditions leading to many diseases. The change in protein is known as protein denaturation (1).

1.2 Protein Denaturation

The conformation of proteins is essential for their effective functioning. The secondary, tertiary, and quaternary protein structures rely on diverse types of interactions; for instance, electrostatic interactions, hydrophobic interactions, and hydrogen bond formation, which are controlled by distinctive amino acids residues. The conformation of proteins changes to ensure optimal functioning and a destressed state. In this state, the protein is noted as folded protein. In some cases, proteins can misfold as a result of deoxyribonucleic acid (DNA) mutations or transcription or translation errors. Additionally, changes in the local environment, such as in the ionic strength, pH, and temperature, can unfold proteins, leading to the hydrophobic regions of the protein being exposed, forming bonds with other proteins, and hence forming an aggregate (2). Misfolded proteins can occur inside the body, where chaperone proteins can reverse the misfolding and facilitate efficient folding by binding to hydrophobic residues or unpaired cysteines (Cys) (2,3).

The folding and unfolding processes control cellular activity. If the protein fails to fold into a native state in the cell, many diseases occur due to the failure of the cell to function normally. These diseases are due to misfolded protein caused by a mutation (a change in the DNA sequence of nucleotides) leading to a change in the

sequence of amino acids in the protein. The sequence of amino acids in a protein determines the interaction between amino acids within the protein to form three-dimensional protein structures and, hence, affects its function; for example, a mutation in the cystic fibrosis transmembrane conductance regulator (CFTR) protein leads to cystic fibrosis. Another example is a mutation of the α-keto acid dehydrogenase complex protein leading to maple syrup urine disease (4). Protein aggregation and the formation of fibrils, such as in the mutation of human lysozyme, leads to hereditary systemic amyloidosis (5). Cancer also may arise due to misfolding of the cellular tumour antigen (P53), since p53 plays a vital role in preventing cancer (6). Many researchers believe that amyloid fibrils are related to neurodegenerative disease (7–9). Each amyloid disease arises from aggregation of a specific protein (e.g. amyloid-beta (AB) aggregation leading to Alzheimer's disease (AD) (7), α-synuclein aggregation to Parkinson's disease (PD)(8), and huntingtin to Huntington's disease (HD))(9).

In some cases, protein can misfold into two distinct routes: amorphous aggregates and amyloid fibrils. Amorphous aggregations occur when the proteins form a highly disordered structure, known as an off-folding pathway. Amyloid fibrils occur when the native protein structure changes from its native state to form a highly ordered fibrous structure and insoluble protein with cross βeta sheets, which is deposited in organs and tissues (10) and is known as an on-folding pathway; for example, Concanavalin A, a member of the legume lectin family, can form amorphous aggregates via an off-folding pathway at pH 5 and amyloid fibrils via an on-folding pathway at pH 9 (11).

Protein aggregation is a multistage process. As revealed by Waugh et al. (12), this includes nucleation, growth of fibrils, and assembly of fibrils. Firstly, the native protein (a single molecule known as a monomer) can be destabilised by several conditions, such as elevated temperature or mutation. When the monomer is destabilised, the structure of the protein partially or completely unfolds, depending on the condition. These unfolded monomers then interact with each other, forming

an oligomer in the nucleation phase. After that, the secondary aggregation structure changes to form cross-β-sheets in the elongation phase. In the next stage, these oligomers bind with each other to form amorphous aggregates or micelles, which can further aggregate to form fibrillary species with rich cross-β-sheets (13–15). Mauro et al. studied human insulin and found that, firstly, insulin molecules aggregated, changing their state from monomeric and dimeric to oligomer and protofibril. Secondly, these oligomers aggregated to form elongated fibrils via heterogeneous nucleation, finally forming clusters of fibrils (16).

A variety of techniques have been employed to study the structure of amyloid fibrils. Atomic force microscopy (AFM) and Cryo-electron microscopy provide morphological information, while X-ray diffraction permits the three-dimensional structure of proteins to be examined. Circular dichroism (CD) provides information about the secondary structure of proteins. For example, cryo-electron microscopy imaging and AFM shows that amyloid fibrils consist of two to six protofilaments twisted around each other to form long unbranching thread-like forms (15, 16). As shown by X-ray diffraction, amyloid fibrils are abundant with cross-β sheets. There are two diffractions: 4.8 Å, relating to the inter-β strand spacing, and 10 Å, relating to the antiparallel β-sheets spacing, as shown in Figure 1.1 (19).

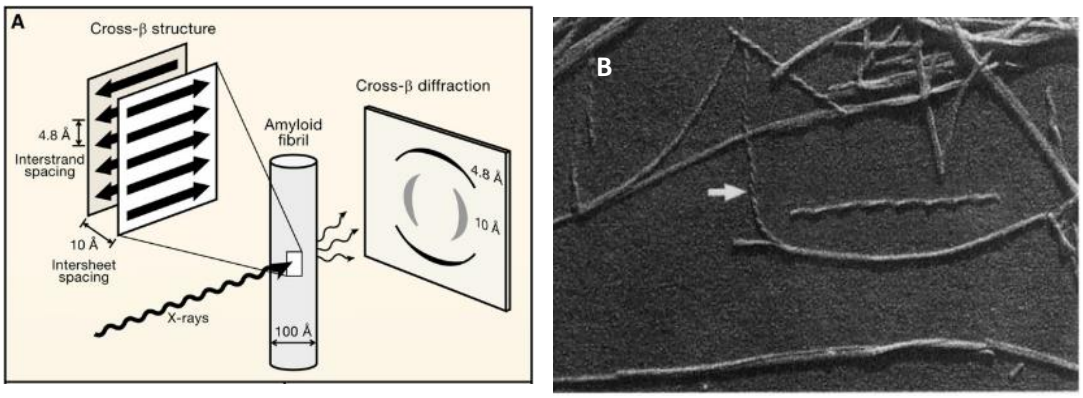

Figure 1.1. (A) A schematic showing characterisation of the diffraction pattern of cross-β sheets obtained after amyloid fibre being exposed to X-rays image. The distance between arrowheads shows the spacing of inter-strand (4.8 Å) and the distance between the vertical arrows show the spacing of the inter-sheet spacing reflection (10 Å)(20). (B) The structure of amyloid fibrils using an AFM (17).

In addition, circular dichroism (CD) can disclose changes in the secondary structure of a protein. When a protein forms into amyloid fibrils, the CD shows a peak at 219 nm, which is an indication of increased cross-β-sheets (21).

One of the most powerful tools for detecting changes in protein structure is fluorescence. There are two types of fluorophores: intrinsic and extrinsic. Intrinsic fluorophores include phenylalanine (Phe), tryptophan (Trp), and tyrosine (Tyr). The fluorescence of Trp is more responsive to the polarity of the surrounding area than Tyr. Some proteins have more than one Trp in different locations; for example, hen egg-white lysozyme (HEWL) has six Trps, four of them (Trp62, Trp63, Trp108 and Trp123) surrounded by a solvent. Two Trps (Trp28 and Trp123) are contained inside HEWL (22). The fluorescence intensity of Trp, depending on the location and when protein unfolds, may increase, due to a decrease of the quenching process of neighbouring molecules. In addition, unfolding could make it more exposed to solvent and increases collisional quenching. For example, the fluorescence intensity of Trp surrounded by solvent decreases in the presence of iodide. In contrast, the fluorescence intensity of buried Trps is not affected by iodide. However, these Trps may interact with each other through energy transfer (23), leading to a change in the fluorescence intensity of Trp, which makes it challenging to study the protein unfolding based merely on the fluorescence intensity of Trp.

Therefore, extrinsic dyes are used to study changes in protein structure. 8-anilino-1-naphthalenesulfonate (ANS) is one of these dyes that is sensitive to the polarity environment (1). Other dyes that can be used to detect amyloid fibrils include Congo Red (CR) (24) and Thioflavin T (ThT) (25). However, ThT is highly specific to the amyloid fibrils and cannot detect protein unfolding or oligomer growth (26). Moreover, both the CR and ThT dyes are polar, with charged molecules, and these properties make both CR and ThT unable to pass the blood-brain barrier (BBB). In other words, ThT and CR cannot be used for fluorescence imaging in vivo for diagnosing AD, nor for detecting the therapeutic effect of drug trials (27).

Other imaging methods, such as computerised tomography (CT) and magnetic resonance imaging (MRI) have limitations, with CT producing low-resolution hippocampal formation images. Usually, in patients with AD, the hippocampal formation area is damaged. MRI takes a long time to generate an image, during which time, the patient must not move; otherwise, artefact in the image will be generated. In addition, the cost of an MRI is very high. Early diagnosis cannot be achieved by these methods, and they are, therefore, unable to prevent the progress of AD. A new technique needs to be developed, and one promising method is to use nanotechnology; in particular, gold nanoparticles (AuNPs).

1.3 Gold Nanoparticles (AuNPs)

Gold nanoparticles (AuNPs) are gold particles with a size range of 1 nm to 100 nm (28). Often AuNPs are split into two groups: gold nanoclusters (AuNCs) with a size less than 2 nm, and AuNPs with a size of 2 nm to 100 nm. This happens because AuNCs have different properties from AuNPs (29). AuNPs have surface plasma resonance (SPR), while AuNCs do not. When the size of particles decreases, the size of AuNCs is equivalent to the Fermi wavelength of electrons, and the continuous energy band breaks down into separate energy levels. As a result, the optical and electronic properties of AuNCs differ from those of AuNPs (30).

Functionalized AuNCs have received a great deal of attention in the last decades. The research in functionalized AuNCs covers a wide range of topics from the diversity of the method of synthesis to various applications. Functionalized AuNCs have unique fluorescent properties and have been used to detect chemical and biological molecules (31); for example, the detection of chemical molecules such as Hg^{2+}, Cu^{2+}, Cd^{2+}, (CN^{-}), Pb^{2+}, and (S^{2-}). Increasing the concentration of Hg^{2+} causes a reduction in the fluorescence intensity of AuNCs, possibly because of high-affinity metallophilic between Hg^{2+} and Au^{+} and affects the electronic structure of AuNCs causing the fluorescence intensity of functionalized AuNCs decreases. Different stabilised AuNCs have different limits of detection (LOD) of Hg^{2+}; for example, the LOD of Hg^{2+} is 1.9 nM using Poly(N-isopropylacrylamide) microgel-protected AuNCs

(PNIPAM MGs-AuNCs), while the LODs of Hg^{2+} are 50 ± 10 nM and 10 nM using Trypsin-AuNCs and Lyz-AuNCs respectively (30,32–34). The detection of Hg^{2+} depends on the pH and ionic strength; therefore, higher stable AuNCs in complicated samples are needed. PNIPAM MGs-AuNCs show only a 9 % increase in fluorescence intensity with the concentration of NaCl at about 500 mM, due to electrostatic repulsion, whereas 11-mercaptoundecanoic acid AuNCs (11-MUA−AuNCs) show a 55 % decrease in fluorescence intensity due to aggregations of 11-MUA−AuNCs. GSH−AuNCs is used to determine Cr^{3+} and Cr^{6+} since Cr^{3+} is important for human and animal nutrient while Cr^{6+} ions can cause cancer. The emission intensity of GSH−AuNCs reduces when Cr^{3+} and Cr^{6+} exist due to the complex formation and redox reactions, respectively (34).

AuNCs have also been used to detect biomolecules, such as glucose, using glucose oxidase-functionalised AuNCs. The fluorescence intensity of AuNCs decreases in the presence of glucose, because an enzymatic product of H_2O_2 interacts with AuNCs, leading to oxidation in the cores of the AuNCs and aggregates. Adenosine-5'-triphosphate (ATP) is detected using GSH−AuNCs (34) and chicken egg white encapsulated AuNCs CEW-AuNCs-Cu^{2+} conjugates, and the CEW-AuNCs consists of AuNCs prepared by utilising chicken egg white proteins (35). N-acetyl-L-cysteine (NAC) can be used to prepare AuNCs (NAC-AuNC). NAC-AuNC is used to detect urea and urease (36). Urea in blood samples has been detected using urease-AuNCs (37); folic acid has been detected using BSA-Au_{25}NCs. Increasing the concentrations of these molecules causes changes in the fluorescence intensity of AuNCs (34).

AuNCs have also been used for biolabelling and imaging. Protein-encapsulated AuNCs are superior for cell imaging and therapy, due to their excellent photostability, long fluorescence lifetime, non-toxicity, large Stoke shift, biocompatibility, functionality, and facile conjugation. Insulin-AuNCs can locate overexpressed cells (C_2C_{12} cells) (34). Lin et al. prepared dihydrolipoic acid encapsulated gold nanocluster DHLA-AuNCs particles and used them to label

endogenous biotin in human hepatoma cells ($HepG_2$). They also studied the cell uptake of DHLA-AuNCs since DHLA-AuNCs is non-toxic to living endothelial cells (38). Su et al. used GSH-AuNCs to image thiols in HeLa cell using confocal microscopy (39).

1.4 Synthesis of AuNCs

There are two approaches for preparing AuNCs; a first approach is a top-down approach which involves reducing the size of AuNPs by using thiol components. The second approach is bottom-up approach which involves reducing Au^{+3} to Au atom to build up AuNCs through chemical reduction, electroreduction, photoreduction or bioreduction. As shown in Figure 1.2.

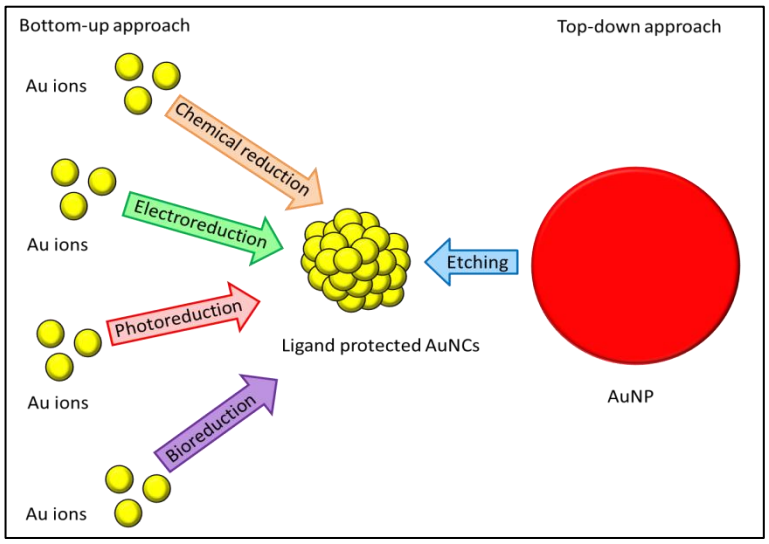

Figure 1.2. A schematic showing synthetic strategies of fluorescent AuNCs.

1.4.1 Etching

AuNPs with a size of 6 nm are prepared in toluene and stabilised using didodecyldimethylammonium bromide (DDAB). Next, a gold precursor solution is prepared, and the aDDAB-toluene solution is added dropwise to the DDAB-AuNPs until the colour of the solution changes from wine red to clear, indicating a reduction of the size of the AuNPs and the formation AuNCs in DDAB (DDAB-AuNCs). Lipoic acid is mixed with tetrabutylammonium borohydride (TBAB) at a ratio of 4:1 to produce dihydrolipoic acid (DHLA); this mixture is then added to

DDAB-AuNCs in order to change the solvent from toluene to water. The solution colour changes from clear to light brown. After the solution is centrifuged to separate the supernatant and toluene from the gold particles, the particles are dispersed in methanol. Further centrifugation is then performed to remove excess DHLA (38). The disadvantages of this process are that it involves several steps and is time-consuming (40).

1.4.2 Chemical Reduction

The AuNCs are synthesised via reducing the gold precursors, such as chloro(triphenylphosphine) gold (I) salt and Chloroauric acid ($HAuCl_4$), to Au atom using reducing agents including citrate, sodium borohydride ($NaBH_4$), hydrazine hydrate and ascorbic acid. Stabilize agents including DNA oligonucleotides, small thiol molecules, polymers, Dendrimers, peptides and proteins are used to prevent the aggregation of gold atoms and form AuNPs.

The AuNCs can be stabilized by DNA oligonucleotides or single nucleotide. For example, Thomas et al. prepared AuNCs coated with poly-adenine DNA oligonucleotides shows blue fluorescence emission (41). The fluorescence properties of DNA-AuNCs depend on the kinds of DNA sequences, e.g. hairpin DNAs, single-stranded DNAs (ssDNA) and fully matched DNAs (42). The loop sequences affect the fluorescence properties of hairpin DNA-AuNCs. Cytosine loop prepares AuNCs highly effective. Multi-coloured fluorescent AuNCs was prepared using single cytidine units. The emissions colours of AuNCs depends on reaction times and pH environments (43).

Thiol compounds are used as a stabilize agent due to the strong interaction between Au and S and form a covalent bond. Thiol compounds including GSH (44), dodecanethiol (45), lipoic acid (46), captopril (47), D-penicillamine (DPA) (48), thiolate α- cyclodextrin (49), phenylethylthiolate (50), dihydrolipoic acid (51) and mercaptopropionic acid (52) are used to synthesis AuNCs in the presence of $NaBH_4$. The fluorescence of the coated AuNCs above have low quantum yields (QYs) nearly

0.1% (53). High fluorescence QY of thiol AuNCs are prepared by Luo et al. They found that increasing the GSH to Au ratio (1.5:1) the fluorescence QY increase about ~15% (54). In addition, changing the GSH to Au ratio can produce stabilized AuNCs with 600 nm or 800 nm emissions wavelength (55).

Dendrimers such as Poly (amidoamine) (PAMAM) and poly (propylene imine) (PPI) used to synthesis AuNCs in the presence of $NaBH_4$. When the PAMAM-AuNCs is excited at a 384 nm wavelength, the emission wavelength is 450 nm with QY is about 41% (56). As the molar ratio of PAMAM/Au increased from 1:1 to 1:15, the sizes of fluorescent AuNCs increased with verity sizes such as Au_5, Au_8, Au_{13}, Au_{23}, and $Au_{31.}$ The fluorescence shift from UV to NIR with QYs shift from 70% to 10% (57). As shown in Figure 1.3.

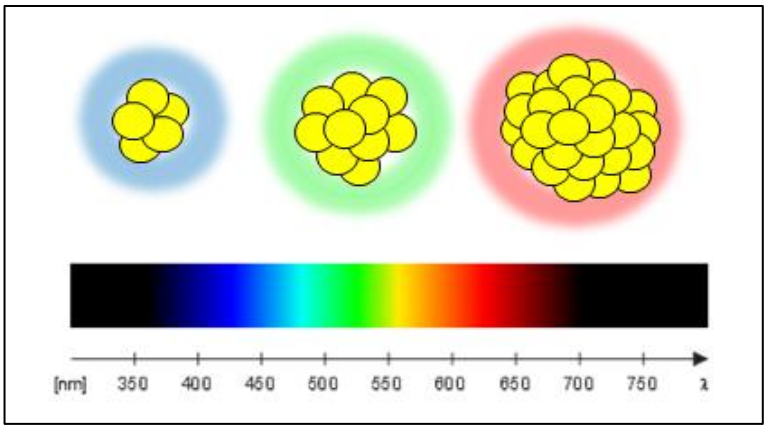

Figure 1.3. A schematic showing the effect of the size AuNCs on the fluorescence properties on AuNCs.

When the size of the AuNCs becomes comparable to the Fermi wavelength of electrons, the strong quantum confinement of free electrons leads to separate the electronic states showing optical properties different from AuNPs. The fluorescence of AuNCs is affected by their sizes as predicted from free-electron theory. The energy level spacing E_δ depends on the number of the Au atom (N) and, this affects the fluorescence properties of AuNCs.

$$E_\delta = \frac{E_f}{N^{1/3}} \qquad (1-1)$$

With increasing the number of Au atom, the fluorescence emission shifts to longer wavelength, as demonstrated in equation (1-1). The fluorescence emission is UV (Au_5), green (Au_{13}), red (Au_{23}). When the N reach higher than 30, the AuNCs does not emit in the visible region (34,57).

Polymers poly(acrylic acid) (PAA) (58) and multidentate thioether-terminated poly(methacrylic acid) (PTMP-PMAA)(59) were used to prepare AuNCs. The fluorescence properties and the size of AuNCs are affected by the molar ratio of polymers /Au (60).

Various of protein have been reported to synthesise AuNCs such as BSA (61), pepsin (62), HEWL (40), DNase I (63), horseradish peroxidase (64), egg white (65) and insulin (66). The property of the fluorescence of AuNCs depends on several conditions (see 1.5 Factors Influencing Fluorescence Properties). The function of protein retains after synthesis AuNCs (66).

When using protein to synthesise AuNCs, the protein serves as a stabilising agent due it containing Cys residues, which enable the thiol group to interact with the gold strongly, leading stable AuNCs. Furthermore, the Tyr in protein serves as a reducing agent; thus, using protein for synthesis of AuNCs eliminates the need for an additional reducing agent (67). Using protein to synthesise AuNCs helps to reduce the number of the chemicals used and, hence, simplifies the process. In addition, some stabilising agents, such as cetyltrimethylammonium bromide (CTAB), are toxic to cell (68) or using $NaBH_4$ as a reducing agent is hazardous to health (34).

This thesis utilised HEWL to synthesise AuNCs and studied how changing the environment affected the fluorescence properties of AuNCs. HEWL was chosen for several reasons. Firstly, the egg white of hens is rich in lysozyme (about 3.5%) and readily available (69). Secondly, HEWL is similar to human lysozyme (about 60% in sequence identity) and has been extensively studied. Finally, HEWL has been used to examine amyloid aggregation as a protein model because HEWL can self-assemble (70,71).

According to Wei et al., lysozyme AuNCs (Lyz-AuNCs) can be synthesised in basic conditions. In his method, lysozyme aqueous solution (10 mg/ml) is added to an equal amount of $HAuCl_4$ solution (4 mM). The reaction solution is vigorously stirred for 5 min, then NaOH (1 M) is added to adjust the pH to 12. The reaction solution is then stored at 37℃ for 8 h (32). After 8 h, the colour of sample changes from yellow to brown, indicating the formation of AuNCs.

1.4.3 Electroreduction

Electroreduction have been used to synthesise AuNCs in the presence of homopolymer, poly (N-vinylpyrrolidone) (PVP). The AuNCs synthesise by this method compose about two and three atoms with stable photoluminescent properties. Employing these ultrasmall AuNCs in biomedicine or catalysis would have to gain a great deal of attention (72).

1.4.4 Photoreduction

Photoreduction does not need to add hazardous chemical such as $NaBH_4$. It is also eco-friendly methods. AuNCs was prepared using Photo-reduction by Zhang et al. (73). Variety of Tridentate thioether terminated polymers such as poly (tert-butyl methacrylate) (tBMA), poly (methyl methacrylate) (MMA) and poly (n-butyl methacrylate) (nBMA) were used to prepare AuNCs via photo-reduction. The QYs of these polymer-AuNCs of 20.1%, 3.8% and 14.3%, respectively. Size and QYs of AuNCs depend on the type of polymer and molar ratio of polymer/Au ions (74).

1.4.5 Bioreduction

Bioreduction of the AuNCs is synthesised of AuNCs in living organisms. The AuNCs can be synthesised in various cancer cell lines including human hepatocarcinoma (HepG2) and leukemia (K562). The Au ions reduce in cell's cytoplasms making the AuNCs is good for cell imaging. In particular, cancer cell since health cell cannot synthesis AuNCs (75).

1.5 Factors Influencing Fluorescence Properties

Several factors can affect the fluorescence properties of AuNCs, depending on the conditions during the synthesis; for example, the temperature during the chemical reaction, the pH, the ratio of protein to Au, and the type of protein. The first factor is pH during the chemical reaction. pH plays an important role in the synthesis of protein-encapsulated AuNCs and determines their fluorescence intensity. It was found that, during the synthesis of BSA-Au_{25}NCs, adding NaOH was necessary for adjusting the pH to 12 in order to activate the ability of Tyr to reduce Au^{3+} or Au^{+} ions via their phenolic groups (otherwise the reaction would produce large non-fluorescent AuNPs) (34,61).

Two types of AuNCs can be synthesised with Lysozyme, depending on the pH. Tzu-Heng Chen and Wei-Lung Tseng synthesised Lyz-Au_8NCs in acidic conditions at pH 3 by adding $HAuCl_4$ to Lysozyme VI. NaOH was added to adjust the pH to 3 at a temperature of 37℃ for 12 h (40,76), and the small-sized AuNCs produced a blue fluorescence emission. Wei et al. synthesised Lyz-AuNCs at pH 12 (32) providing relatively large sized AuNC generated a red fluorescence emission, showing that changing the pH affected the size of the AuNCs and, hence, the colour of the fluorescence emissions.

The second factor is temperature; the reaction temperature can influence the speed of reaction and the quantum yield (QY) of AuNCs. Xie et al. found that, when using BSA to synthesise AuNCs at 25℃, AuNCs did not form after 12 h. At 37℃, the AuNCs formed with a QY of ~6% after 12 h. They also found that, at 100℃, AuNCs were formed, with a low QY (~0.5%), within a few minutes (61).

The third factor is the molecular ratio of protein to Au (34). Xie et al. found that, with a concentration of gold at 5mM and a concentration of BSA protein at 37 μM, the reaction produced large non-fluorescent AuNPs. When the concentration of BSA was increased to 50 mM, the reaction produced AuNCs with fluorescence emission at a wavelength of 690 nm (61). In the case of lysozyme type VI (Lyz VI), when the

gold solution was fixed at 10mM and the concentration of Lyz VI protein varied from 20–40 mg/ml, the Lyz VI-AuNCs showed absorption bands at a wavelength of 400 nm and the colour of the sample turned brown, indicating the formation of AuNCs. At a concentration of 10 mg/ml, the sample showed two absorption bands: one at 400 nm originated from the AuNCs and the second, at 547 nm, originated from the AuNPs (77). It is clear that the concentration of protein affects the formation of AuNCs. Reducing the concentration of protein leads to a reduced number of Cys (78) which affects the stabilisation of the AuNCs; hence, AuNPs are formed.

The peak wavelength of the AuNCs' fluorescence redshifted from 628 nm to 636 nm when the concentration of Lyz VI decreased from 40 mg/ml to 20 mg/ml; this redshift was possibly due to the increase in the size of the AuNCs caused by lowering the concentration of Lyz VI. The increase in the size of AuNCs led to a reduction in the energy gap between the $5d^{10}$ band and the 6sp band, leading to a redshift of the fluorescence peak (77). The concentration of Lyz VI not only had an impact on the fluorescence peak but also on the fluorescence intensity (i.e., the QY). The QY increased as the size of the AuNCs decreased. This increase probably occurred because, with small-sized AuNCs, the surface-to-volume ratio increased, leading to larger numbers of the core atoms of AuNCs bonding with core-capping ligands. These surface ligands affected the fluorescence properties of the AuNCs. In addition, the fluorescence of AuNCs is weak at a concentration of 10 mg/mL, due to the presence of AuNPs statically quenching the fluorescent AuNCs (77).

GSH-AuNCs show low QYs because of weak GSH reduction. In order to increase the QYs of GSH-AuNCs, adding GSH to GSH-AuNCs at a ratio of 1.5:1 leads to an increase in QYs of about 15% that can affect the aggregation of the Au(I)-thiol complex on the surfaces of the AuNCs' cores. Increasing the PAMAM: Au molar ratio to 1:15 leads to an increase in the size of AuNCs, with different colours and QYs, from UV with a QY of 70% to NIR with a QY of 10% (57).

The fourth factor affecting the fluorescence properties of AuNCs is a type of protein. Xu et al. studied the fluorescence properties of AuNCs using four types of proteins: BSA, trypsin, HEWL, and pepsin. When the ratio of these proteins to gold was fixed at 0.04, the peak emission wavelength of BSA-Au_{25}NCs was 705 nm; of trypsin-AuNCs, 643nm; of Lyz-AuNCs, 640nm; and of pepsin-AuNCs, 620 nm. Pepsin-AuNCs showed low fluorescence intensity, because it also formed large AuNPs (67). The explanation was that pepsin has as few as four amine-containing, which are not sufficient to form a complex AuCl_4^-.

Moreover, a large amount of Tyr and Trp leads to reduced gold ions and the formation of large AuNPs. Xu et al. suggested that the blue shift in the fluorescence emission of both Lyz-AuNCs and trypsin-AuNCs in comparison to BSA-Au_{25}NCs is caused by the small protein and low Cys contents that cannot be unable to stabilise AuNCs. They also suggested that the blue shift is due to the interaction of AuNCs with surrounded environments (i.e. hydrophobicity or functional groups)(67). Changing the type of the protein affects the number of amino acid, in particular Trp, Tyr, and Cys. Trp and Tyr reduce Au^{+3}, while the Cys stabilises the AuNCs' structure via the sulphur–gold bond, therefore, affecting the AuNCs formation and their fluorescence properties.

Zhikun Wu and Rongchao Jin found that different ligands produced AuNCs with different QYs. They studied AuNC stabilized using four different thiolate ligands $[Au_{25}(SC_2H_4Ph)_{18}]^-$, $[Au_{25}(SC_6H_{13})_{18}]^-$ and $[Au_{25}(SC_{12}H_{25})_{18}]^-$.The QYs were ordered as follows: $PhCH_2CH_2$ > $C_{12}H_{25}$ > C_6H_{13}. The $PhC_2H_4^-$ group has strong electron-donating capability compared with long-chain alkyl groups. With increasing chain alkyl groups, the number of electrons transferred to the sulphur, and then to Au via S–Au bonds, increased, causing an increase in the fluorescence intensity of AuNCs. This proved that the fluorescence intensity of AuNCs is not only affected by the metal core quantisation effect, but also by surface ligands (79).

Another factor that can affect the QYs of AuNCs is the charge of their cores. Zhikun Wu and Rongchao Jin found that, when the AuNCs oxidised to higher

charged states, the fluorescence intensity increased in $[Au_{25}(SC_2H_4Ph)_{18}]^0$; however, increasing the electropositivity (or oxidation state) in glutathione-capped $[Au_{25}(SG)_{18}]^-$ NCs led to reduced fluorescence intensity. The electron-withdrawing groups (e.g., the carboxyl and amide groups) were responsible for the decrease in fluorescence intensity (79).

1.6 Effect of AuNCs and AuNPs on Peptide and Protein Structure

Studying the effect of AuNPs and AuNCs on protein structure is important for discovering their potentially beneficial applications and their potential risks to human health. In this section, three topics will be discussed. Firstly, the effect of gold ions on the HEWL structure will be discussed. Secondly, the effect of AuNPs on the formation of amyloid fibrils in different proteins will be discussed. Thirdly, recent research on AuNCs that has investigated protein aggregation in relation to AD treatment and diagnosis will be reviewed.

Synthesising AuNCs using HEWL affects the structure of HEWL. Ghosh et al. studied the effect of the synthesis of AuNCs on the HEWL structure, at an early stage of the synthesis of AuNCs, at pH 5.5. They found that synthesising AuNCs using HEWL could change the conformation of HEWL when the gold ions increased from one to eight. The secondary structure of the protein was modified as a result of the breakage of disulfide bonds and binding Cys with gold ions. In addition, hydrogen bonds decreased due to the presence of gold ions (80). Baksi et al. found that synthesising AuNCs breaks the disulfide bonds; as a result, the helical content of HEWL decreased (81). Mudedla et al. found that AuNCs could change the structure of HEWL and its internal motions. They found that the change in the structure of HEWL was due to the noncovalent interactions of protein molecules with AuNCs. Precisely, in their third model, the small 3_{10} helix contained three amino acids (Methionine (Met)105, Alanine (Ala)106, and Asparagine (Asn)107) and the α helices, from Ala110 to Cys115 and from Ala32 to glutamic acid (Glu)35, turned, depending on the interaction of protein molecules with AuNCs (82).

Many studies were conducted on AuNPs' influence in inducing or inhibiting fibrils. Barros et al. studied the interaction between AuNPs and HEWL. Increasing the concentration of AuNPs can increase the lag phase of the formation of HEWL amyloid, leading to a delay in the formation of amyloid fibrils. When AuNPs are added to preformed fibrils of HEWL, the beta-sheet structure decreases (83). The effects of AuNPs on the aggregation of $A\beta_{40}$ and other polypeptides are determined by the physical characteristics of the AuNPs; for example, their sizes, shapes, concentrations, and surface properties. Some researchers found that AuNPs can facilitate $A\beta_{40}$ and polypeptide fibril aggregation; for example, Gladytz, et al. found that AuNPs with a size of 20 nm accelerated the aggregation of human islet amyloid peptide sequences (NNFGAIL) (84), while others found that AuNPs inhibit amyloid formation, as shown in the examples below.

The size of AuNPs can affect $A\beta_{40}$ fibrils. Gao et al. found that the size of AuNPs could accelerate or inhibit fibril aggregation. They found that AuNPs coated with L-glutathione (GSH) (Au-GSH-NPs), with sizes of 36.0 ± 3.0 nm and 18.1 ± 3.0 nm, led to rapid $A\beta_{40}$ fibrillation, whereas the Au-GSH-NPs with a size of 6.0 ± 2.0 nm and GSH-AuNCs with a size of 1.9 ± 0.7 nm could significantly restrain the assembly of fibrils, with concentrations of AuNCs as high as 10 ppm achieving complete inhibition. Transmission electron microscope (TEM) measurements showed that AuNPs with sizes larger than 18 nm formed a larger number of fibrils bound to AuNPs. AuNPs with sizes less than 6 nm bound to $A\beta_{40}$ and prevented the aggregation of the $A\beta_{40,}$ because of their size. AuNPs with sizes less than 6 nm could organise GSH motifs on the surface of AuNPs in a way that prevented the formation of amyloid fibril aggregation. This ability became stronger when the size of AuNPs was less than 2nm. Furthermore, the formation of amyloid fibril aggregation was prevented by the perturbation of the nucleation process by AuNCs; therefore, AuNCs prevented amyloid fibril formation (85). In addition, Moore et al. found that the size of polyacrylic acid-coated gold nanoparticles (PAA-coated AuNPs), at both 8 and 18 nm, could inhibit $A\beta_{40}$ aggregation, although PAA-coated AuNPs with a size of 40 nm could not do so (86).

The charge on the surface of AuNPs can affect $A\beta_{40}$ aggregation. Liao et al. found that bare AuNPs and carboxyl-conjugated AuNPs could inhibit the formation of amyloid fibrils, while amine-conjugated AuNPs could not influence amyloid aggregation. Furthermore, bare AuNPs were more likely to bind to mature fibrils; as a result, the morphology of the fibrils changed into oligomers. Bare AuNPs with concentrations of 0.042 to 2.72 nM and size around 30 nm in diameter affected the growth of $A\beta_{40}$ (50 uM), leading to the formation of oligomers in the range of 10 to 15 nm. They also altered the $A\beta_{40}$ fibrils' morphological structure into small oligomer structures, ranging in size from $\sim$ 5 to 8 nm. Negatively charged AuNPs can affect the $A\beta_{40}$ growth, but positively charged AuNPs cannot.

The rate of $A\beta_{40}$ growth in the nucleation phase depends on hydrophobic interactions, and only hydrophobic nanoparticles can disturb this interaction. In the elongation phase, hydrogen formation and electrostatic interactions disturb $A\beta_{40}$ growth, leading to the conclusion that electronegative AuNPs can prevent $A\beta_{40}$ aggregation. TEM measurements have shown that amine-conjugated AuNPs do not affect the growth of $A\beta_{40,}$ but small sizes $A\beta_{40}$ fibrils and oligomers form in the presence of carboxyl-conjugated AuNPs (87). Another study found that the surface charges of AuNPs affected the growth of amyloids of $A\beta_{40}$ (40 μM) at pH 7, with CTAB and poly (allylamine) hydrochloride (PAH) having a positive charge and citrate and PAA, a negative charge. 200 pM citrate, PAH-coated AuNPs, and CTAB-coated NPs with a size of 18 nm reduced the amount amyloid fibril of $A\beta_{40,}$ while 200 pM of PAA-coated NPs inhibited amyloid fibril of $A\beta_{40}$ (86).

Recent publications regarding AuNCs have studied protein aggregation in relation to AD treatment and diagnosis. Gao et al. found that AuNCs could be used to treat Parkinson's disease (PD). They also found that N-isobutyryl-L-cysteine (L-NIBC)-protected AuNCs could inhibit α-synuclein (α-syn) amyloid fibrils in vitro (88). Han et al. found that AuNCs could be used as receptors for detecting the sera of AD (89).

Despite the various studies on AuNCs, understanding of the fluorescent properties of Lyz-AuNCs is far from complete. This gap in the knowledge may limit the applications of AuNCs; for example, the possibility of using Lyz-AuNCs for protein denaturing has not yet been studied; nor has the interaction between Lyz-AuNCs and $A\beta_{40}$. Understanding this interaction could provide further information about how the presence of AuNCs affects the functioning of HEWL due to changes in its structure.

1.7 Thesis Summary

This research aimed to investigate the fluorescence properties of Lyz-AuNCs in conditions that lead to protein denaturation. It also aimed to study the interaction between Lyz-AuNCs and $A\beta_{40}$. These aims were achieved using ultraviolet-visible (UV-Vis) spectroscopy, steady-state and time-resolved fluorescence spectroscopy to disclose changes in the optical properties of Lyz-AuNCs in the denatured condition of lysozyme and the presence of $A\beta_{40}$.

The purpose of studying the fluorescence properties of Lyz-AuNCs in protein denatured conditions was to understand their behaviours under such conditions and thus increase knowledge of the fluorescence properties of AuNCs. A possible benefit of this knowledge is to increase their applications, such as their use as a tool for monitoring changes in protein structure and functioning. The purpose of studying the interaction between the Lyz-AuNCs and $A\beta_{40}$ was to ascertain how the presence of AuNCs may affect HEWL's function as an inhibitor of amyloid fibrils and how fluorescence changes in the presence of $A\beta_{40}$.

Chapter 2 provides details of the fundamentals of photoluminescence and an introduction to protein structures in relation to the relevant research and discussions.

Chapter 3 explains the instruments and their components, usage, and principles. The instruments in question are UV-Vis spectroscopy, spectrofluorimetry,

photoluminescence lifetime measurement, anisotropy measurement, and scanning electron microscopy (SEM).

Chapter 4 discusses the impact of pH and increased concentrations of HEWL on the fluorescence properties of Lyz-AuNCs. The results showed that the fluorescence intensity of AuNCs increased and showed redshift with increasing pH or concentrations of HEWL at pH 3. In both cases, the long fluorescence lifetime component of AuNCs emission decreased. In addition, Time-Resolved Emission Spectra (TRES) showed that both AuNC fluorescence components increase in intensity and redshift with increasing pH while only the long lifetime component of AuNC was observed to change when adding HEWL to solution; indicating that the underlying mechanisms for the changes observed are fundamentally different for each case. It is possible that the sensitivity of Lyz-AuNCs to HEWL concentration could be utilized to study early-stage aggregation.

Chapter 5 discusses the effect of urea, SDS, and long-term heating at a temperature of $65℃$ on the fluorescence properties of Lyz-AuNCs. Adding urea and SDS to Lyz-AuNCs led to a decrease in the fluorescence intensity of AuNCs at an excitation wavelength of 470 nm. This decrease in the fluorescence intensity was due to protein unfolding. In addition, there was a redshift of the peak emission wavelength of AuNCs in the presence of urea, due to an interaction between Cys and urea. There was no change in the peak emission wavelength of AuNCs in the presence of SDS. The effect of temperature led to a decrease in the fluorescence intensity of AuNCs, with a redshift due to a change in the structure.

Chapter 6 discusses the interactions of both HEWL and Lyz-AuNCs with $A\beta_{40}$. A large aggregation formed in the presence of both HEWL and $A\beta_{40}$ as the result of an attraction force between HEWL and $A\beta_{40}$. The fluorescence intensity of Trp decreased, with a blue shift indicating a hydrophobic interaction between HEWL and $A\beta_{40}$. By contrast, the interactions between Lyz-AuNCs and $A\beta_{40}$ did not cause a large aggregation, but produced an increase in the absorbance at 350 nm, indicating binding occurred between Lyz-AuNCs and $A\beta_{40}$. SEM measurements showed that

there were no fibrils or large aggregations in the presence of Lyz-AuNCs, although there were large aggregations in the presence of HEWL. This result suggested the potential of using Lyz-AuNCs as an inhibitor of amyloid fibrils.

Chapter 2: Theory

2.1 Principle of Photoluminescence

2.1.1 Introduction to Photoluminescence

Luminescence is the light that is emitted from substances after irradiation. There are two types of luminescence. The first type is fluorescence, where the electronic transition occurs between the electronic singlet states in which the electrons in the ground electronic state have an opposite spin to the electrons in the excited electronic state. The second type is phosphorescence, where the electronic transition occurs between the singlet and triplet states where the electrons in the ground electronic state have the same spin orientation as the electrons in the excited electronic state (Figure 2.1 (A)). The Jablonski diagram provides a good description of the electronic transition, as shown in Figure 2.1 (B).

All electrons exist in the electronic ground state at room temperature since the thermal energy is less than the energy between the first electronic excited state S_1 and the electronic ground state S_0. Therefore, there is not enough energy to excite electrons to a higher electronic energy level, so a light source is used to excite the electrons.

A substance consists of atoms that have electronic energy levels. Each electronic state has sub-levels called vibrational energy levels. After light absorbance, the electrons in the S_0 are elevated to higher vibrational energy levels in the higher electronic singlet excited states S_1 or S_2. The light absorbance process occurs in 10^{-15}s (Figure 2.1(B)). In this short amount of time, there is no change in the location of the nuclei according to the Franck-Condon principle. The electrons can then move from a higher vibrational energy level to a low vibrational energy level in the excited electronic states within $(10^{-10} - 10^{-12})\ s$. As a result of this movement, electrons lose energy to the heat. The transition between the vibrational energy level in the excited electronic state is known as a vibrational

relaxation. The electron also relaxes from the lower vibrational levels of the second excited electronic energy level to the higher vibrational levels of the first excited electronic energy level through a process known as an internal conversion within $(10^{-11} - 10^{-14})\ s$. The electrons in the low vibrational energy states in the singlet excited state S_1 return to the electronic ground state S_0 with the light-emitting process known as fluorescence. This process occurs at about 10^{-8}s in the thermal equilibrium (90).

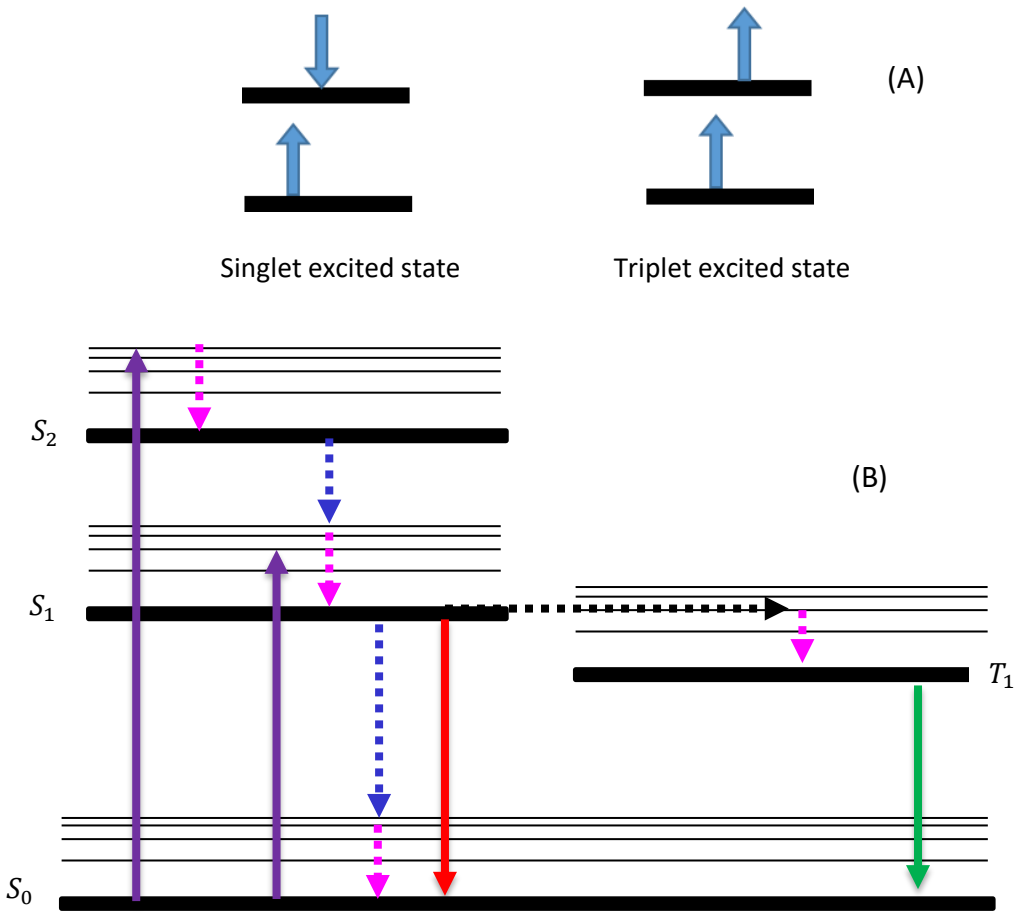

Figure 2.1. (A) The difference in the electron spins at the singlet energy level and triplet energy level. (B) The Jablonski diagram demonstrates the process of non-radiative decay rate (dotted line arrow) and radiative decay rate (solid line arrow). For example, absorption (purple arrow), vibrational relaxation (pink arrow), internal conversion (blue arrow) fluorescence (red arrow) and phosphorescence (green arrow), intersystem crossing (black arrow).

When an electron is in the first excited electronic state, its spin could be orientated by intersystem crossing. If this occurs, the electron in the first excited electronic single state S_1 will move to the first excited electronic triplet state T_1. When the electron in the electronic triplet state returns to the ground states, it emits phosphorescence at a longer wavelength. Generally, this transition is forbidden; therefore, the constant rate of this process is very low and occurs at about $10^{-3}s$ in comparison to the fluorescence process (91).

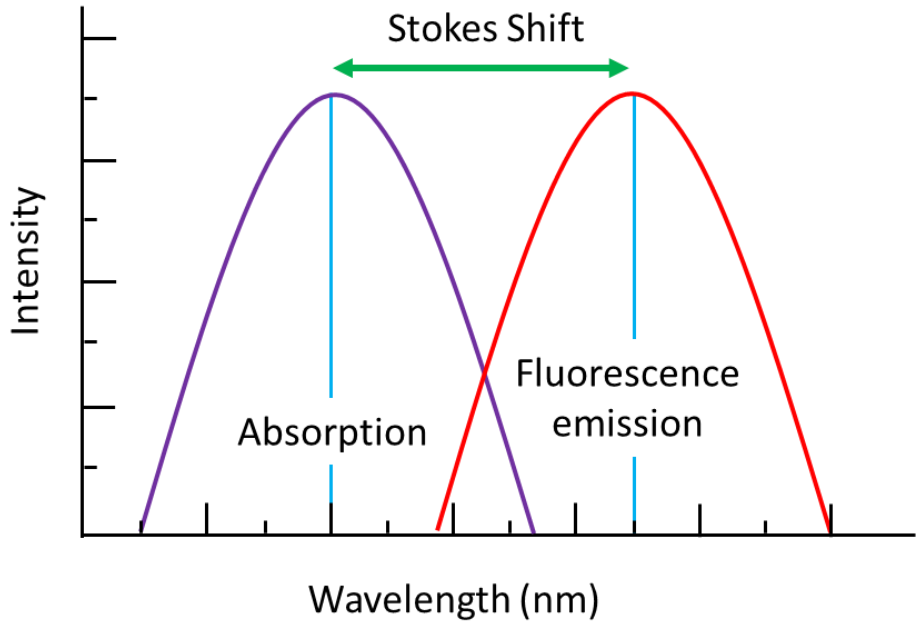

Figure 2.2. The general spectrum of absorbance and fluorescence emission. The separation between the peak of the absorption wavelength and the peak of fluorescence emission wavelength is the Stokes shift.

The Stokes shift is a phenomenon in which the photoluminescence energy is lower than the energy of the absorbance light as a result of the non-radiative process that occurs in the excited state (Figure 2.2). It was first discovered by Sir GG Stokes in 1852 (91). Moreover, the redshift can increase due to the interaction between fluorophores and the solvent molecules.

For example, if the fluorophore with a larger dipole moment in the excited state in comparison to the ground state is excited to higher excited states, the solvent dipoles will interact with the new position of the dipole moment of the fluorophore in the excited states by changing their orientation. This process leads to a decrease

in the energy of the excited state. This shifts the fluorescence emission peak to a longer wavelength (92). Since the process, known as dielectric relaxation (solvent relaxation), is complete before the fluorescence emission process occurs, the fluorescence emission for some fluorophores is highly sensitive to the polarity of the solvent (Figure 2.3).

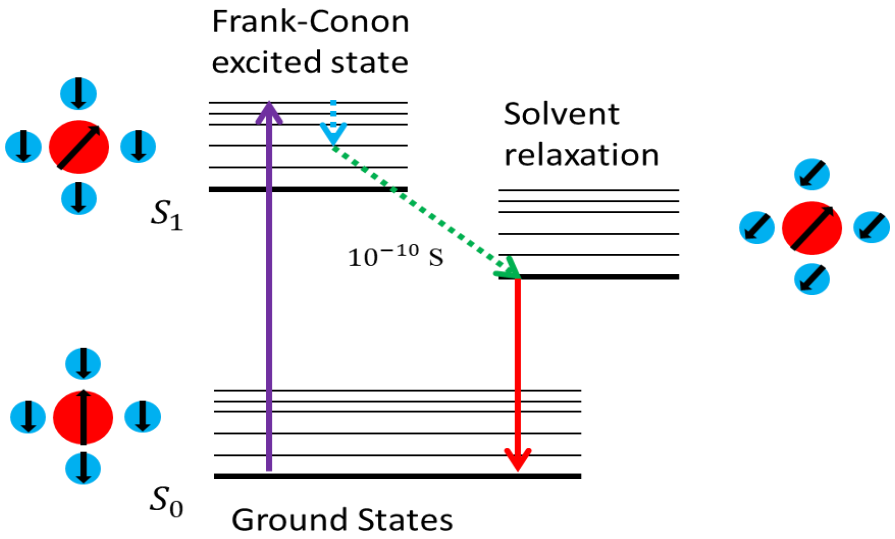

Figure 2.3. The influence of the dipole moment of the solvent on the dipole moment of a fluorophore and its fluorescence emission. Fluorophore (red circle), solvent molecules (blue circle), dipole moment (black arrow), absorption (purple arrow), vibrational relaxation (light blue arrow) solvent relaxation (green arrow) and fluorescence (red arrow).

2.1.2 Quantum Yields and Lifetime

When electrons are excited to higher electronic states, there are two possible ways that electrons could return to the ground state: the radiative process in which photons are emitted and the non-radiative process in which the electrons do not emit photons (Figure 2.1 (B)). The ratio of the number of emitted photons to the number of absorbed photons is the fluorescence quantum yield (QY). QY is obtained from the following equation:

$$QY = \frac{K_r}{K_r + K_{nr}} \qquad (2\text{-}1)$$

Where K_r is the radiative rate and K_{nr} is the non-radiative rate. QY is 1 when the non-radiative rate is 0 (91). The lifetime (τ) is the average time that the electron

stays in the excited states before returning to the ground state. The relation between lifetime and QY is giving by:

$$\tau = \frac{QY}{K_r} = \frac{1}{K_r + K_{nr}} \qquad (2\text{-}2)$$

Photoluminescence is a random process. If a fluorophore has single exponential decay, 63% of the photons emit before time $t \leq \tau$ and 37% of the photons emit at $t > \tau$. The intrinsic or natural lifetime is the lifetime of fluorophore without the non-radiative rate.

$$\tau_n = \frac{1}{K_r} \qquad (2\text{-}3)$$

The lifetime and QY of a fluorophore can vary depending on the value of K_r or K_{nr}. For instance, when K_{nr} is very high due to the internal conversion process or slow rate emission, the molecules become non-fluorescent. The lifetime of a fluorophore is shorter when the radiative rate is higher, hence the QY is higher. The QY of aromatic substances containing the $-NO_2$ group is very low due to the large K_{nr} value. The QY of a phosphorescence substance is low in fluid solutions at ambient temperature since the triplet-to-singlet transition is forbidden by symmetry (91). The lifetime measurement will be discussed in Chapter 3 (see 3.3.Time-resolved photoluminescence measurement).

2.1.3 Fluorescence Quenching

The decrease in photoluminescence intensity is called quenching. Many processes can cause photoluminescence quenching, including forming complexes in the ground state, collisional quenching and energy transfer. Moreover, the optical properties of the fluorescent molecules can cause fluorescence quenching; for example, a decrease in fluorescence intensity due to turbidity or high optical densities.

Photoluminescence quenching can be used to determine the location of the fluorophore in a macromolecule. For example, if the fluorophore is on the surface of a macromolecule, the fluorescence intensity will be lower than the intensity of a buried fluorophore. There are two types of photoluminescence quenching. Dynamic quenching refers to the collisional interaction between the quencher molecules and the fluorophore molecules. Static quenching is the reduction in fluorescence intensity resulting from the fluorophore molecules binding to the quencher molecules.

In dynamic quenching, the quencher molecules interact with the excited fluorophore molecules without any changes in the molecular structure; depending on the interaction, the fluorophore molecules return to the ground state via the non-radiation process, as shown in Figure 2.4 (A). In static quenching, the quencher molecules interact with the fluorophore molecules and form a non-fluorescent complex. The complex can be elevated to the excited states and then returned to the ground state without emitting photons, as shown in Figure 2.4 (B) (93).

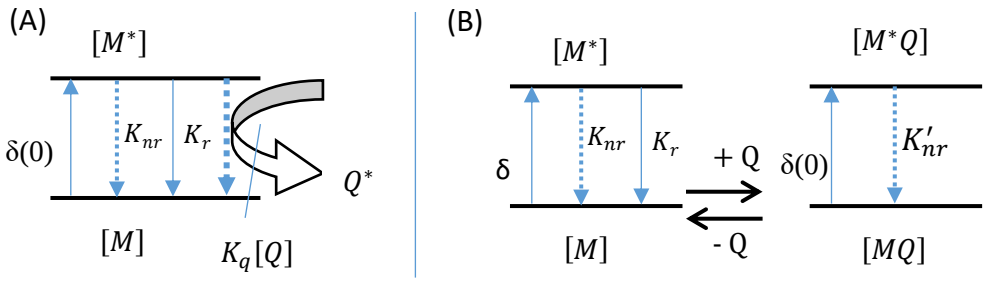

Figure 2.4. The mechanism of quenching. (A) Static quenching and (B) dynamic quenching.

As seen below, the Stern-Volmer equation describes the quenching of fluorescence:

$$\frac{F_0}{F} = 1 + k_q \tau_0 [Q] = 1 + K_D [Q] \qquad (2\text{-}4)$$

$$K_q = \frac{K_D}{\tau_o} \qquad (2\text{-}5)$$

Where F_0 and F are the fluorescence intensity without and with the quencher, respectively; k_q is the bimolecular quenching constant; τ_0 is the lifetime of the fluorophore without the quencher; $[Q]$ is the concentration of the quencher and K_D *or* K_{SV} is the Stern-Volmer quenching constant when the quenching is dynamic or static, respectively. The constant K_D *or* K_{SV} varies depending on the location of the fluorophore and the accessibility to the quencher. It is a high value when the fluorophore is on the surface of the molecule or free in a solvent. It is a low value when the fluorophore is buried in a macromolecule (91).

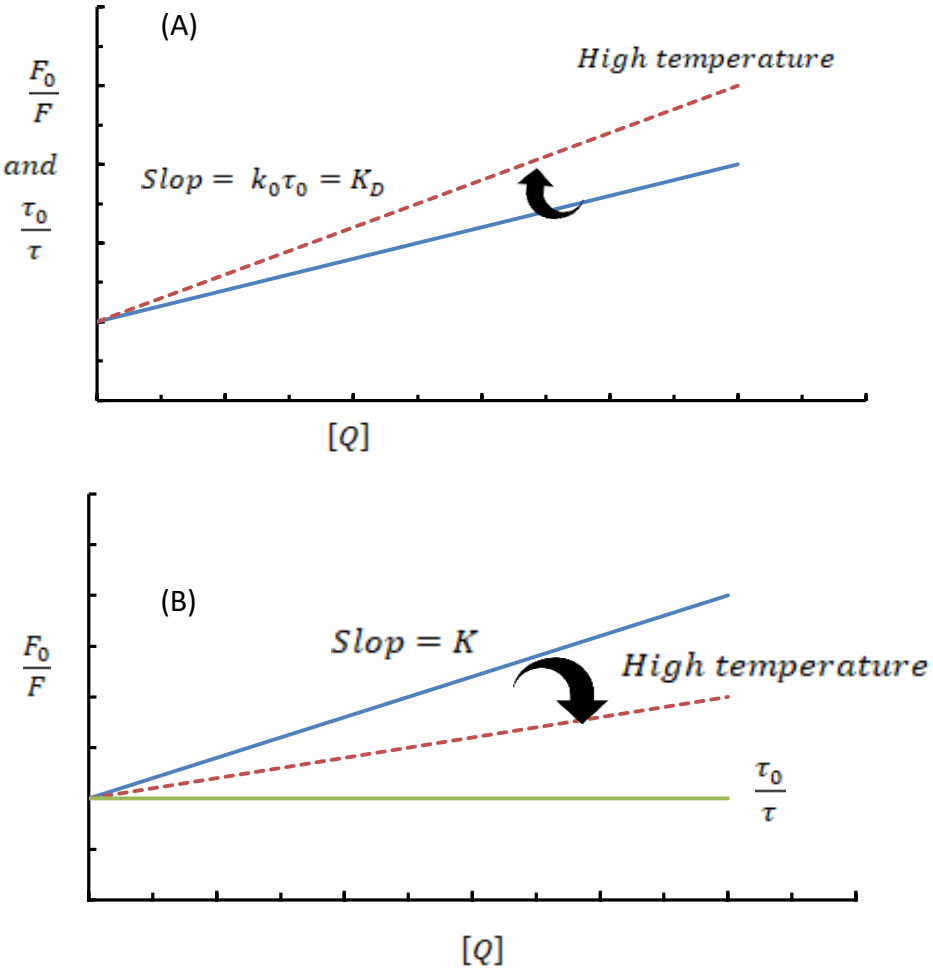

Figure 2.5. Dependence of the fluorescence intensity and lifetime of the fluorophore on the concentration of the quencher; (A) dynamic quenching and (B) static quenching.

Two methods can be used to determine the type of quenching: time-resolved fluorescence measurement and temperature-dependent measurement. The time-resolved fluorescence measurement is preferred since it is straight forward (91) if the dynamic quenching occurs, the lifetime of the fluorophore molecules decrease since the quencher molecules interact with fluorophore molecules in the excited states leading to rapidly decay while if the static quenching occurs, the lifetime of fluorophore molecules does not change since the non-fluorescent complexes are formed and these complexes are returned to the ground state without emitting photons.

An increase in the temperature helps to determine the type of quenching. If the quenching is dynamic, then the linear Stern-Volmer will tilt to the y-axis. The increase in the ratio of F_0/F is due to an increase in the diffusion of the molecules at a higher temperature (Figure 2.5(A)). However, if the quenching is static, the linear Stern-Volmer will tilt to the x-axis as the temperature increases. The reduction in the ratio of F_0/F is due to the breakdown of the weak bonds of complex molecules (Figure 2.5(B))(91).

Generally speaking, a linear Stern-Volmer plot is used to determine whether it is possible for the quenchers to access to all fluorophores. For example, proteins could have more than one fluorophore, and not all of them are quenched. Hence, the Stern-Volmer plots will deviate from linearity toward the x-axis (91). It also can be used to determine the type of quencher. If the K_q higher than $2 \times 10^{10} L\, mol^{-1}\, s^{-1}$, as in the case of Lyz-AuNCs, then, the quenching is static (91).

2.1.4 Förster Resonance Energy Transfer (FRET)

FRET has been used to sense the interaction between biomolecules by measuring the energy transfer between two fluorophores. It can be used to detect the conformation change in proteins (91). The most interesting protein encapsulated AuNCs shows the FRET from proteins to AuNCs where the donor is Trp and the

acceptor is AuNCs. Xavier et al. observed that the fluorescence intensity and lifetime of Trp decrease after AuNCs synthesis (94). Raut et al. studied the FRET in bovine serum albumin (BSA) and human serum albumin (HAS) protected AuNCs in order to measure the distance between AuNCs and Trp (95). Russell et al. also used FRET to locate the nucleation site of AuNCs (96).

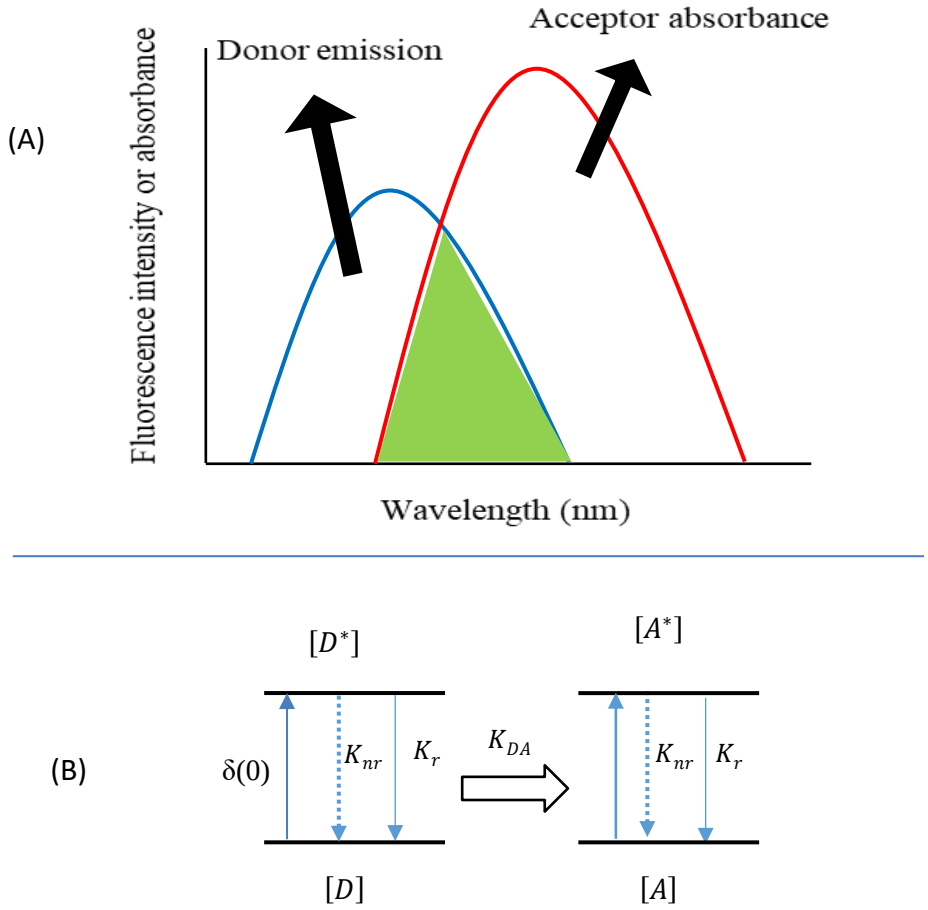

Figure 2.6. (A) Spectral overlap for FRET. The blue line is the emission from the donor; the red line is the absorbance spectra of the acceptor. (B) FRET process demonstration.

Theodor Förster explained FRET and its criteria. FRET occurs in the excited state when there is an overlap between the donor emission spectrum and the acceptor absorption spectrum (Figure 2.6). The interaction between the donor and the acceptor is a dipole-dipole interaction. The amount of energy that transfers from the donor to the acceptor depends on the distance between them. It also depends on the extent of the spectral overlap, as shown in Figure 2.6 (A) (97).

The rate of energy transfer $K_T(r)$ and the energy transfer efficiency, E, of the energy transfer are given by the following equation:

$$K_T(r) = \frac{1}{\tau_D}\left(\frac{R_0}{r}\right)^6 \qquad (2\text{-}6)$$

$$E = \frac{R_0^6}{R_0^6 + r^6} \qquad (2\text{-}7)$$

Where r is the distance between the donor and acceptor and τ_D is the lifetime of the donor in the absence of the acceptor. FRET is a very sensitive tool that is used to measure the distance between the donor and the acceptor because the rate of energy transfer is proportional to the inverse sixth power of the distance. When the distance between the donor and acceptor is equal to the Förster distance $(R_0 = r)$ and is substituted in equations (2-6) and (2-7), the rate of energy transfer is equal to the decay rate of the donor, and the energy transfer efficiency is 50%. Therefore, R_0 is the Förster distance, defined as the distance at which the energy transfer efficiency is 50% as shown in Figure 2.7(A), and it is determined by the following equation (91):

$$R_0^6 = \frac{9000\, ln(10) k^2 \Phi_f}{128\pi^5 N_A n^4} \int_0^\infty I_D(\lambda)\varepsilon_A(\lambda)\lambda^4 d\lambda \qquad (2\text{-}8)$$

Where Φ_f is the QY of the donor fluorescence (in the absence of the acceptor); N_A is the Avogadro's number; n is the refractive index of the intervening medium; λ is the wavelength; $I_D(\lambda)$ is the donor emission spectrum and $\varepsilon_A(\lambda)$ is the acceptor absorption spectrum. The degree of spectral overlap between the donor emission spectrum and the acceptor absorption spectrum is represented by the integral in equation (2-8). R_0 is higher when the spectral overlap is higher. Furthermore, R_0 is affected by k^2, which is the orientation factor. k^2 is given by the following equation (93):

$$k^2 = [cos\,\theta_T - 3\,cos\,\theta_D\,cos\,\theta_A]^2 \qquad (2\text{-}9)$$

The angles are illustrated in Figure 2.7(B). The orientation factor k^2 value ranges from 0 to 4. When the orientation of donor and acceptor is random, the average of k^2 over time is 0.67. In some cases, this presumption is not correct, which has a higher negative effect on obtaining information from FRET.

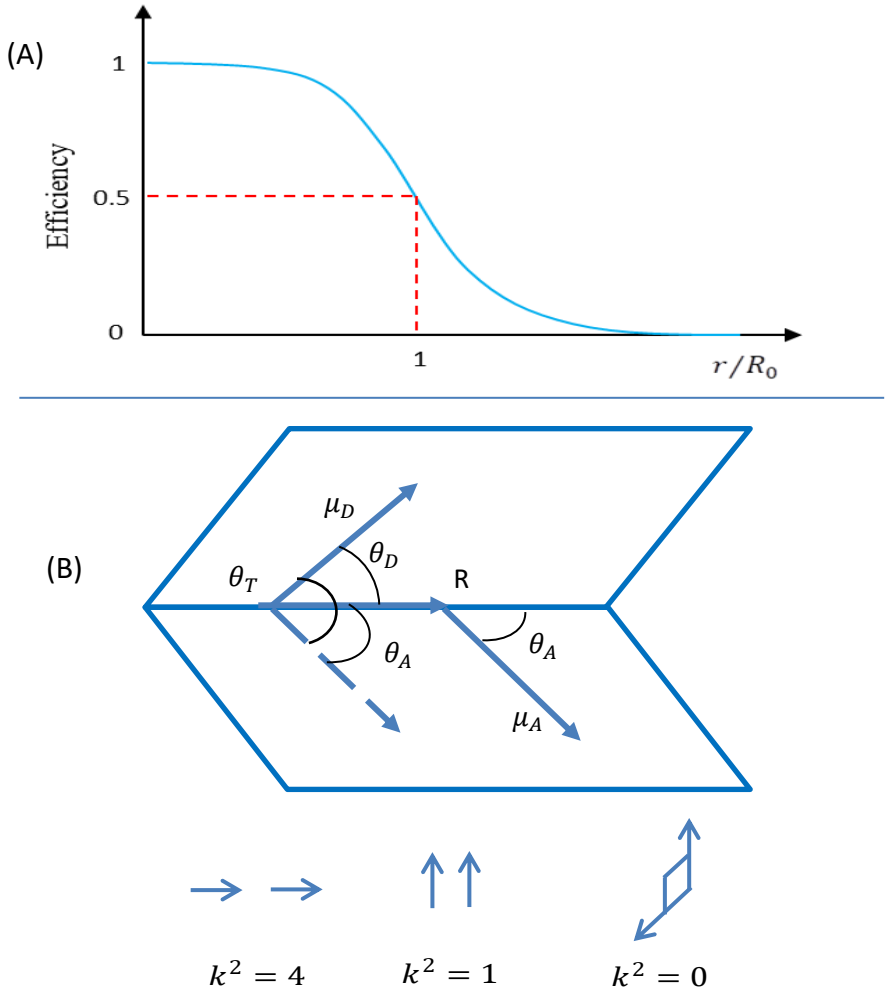

Figure 2.7. (A) The correlation between energy transfer efficiency and the distance r between the donor and the acceptor. (B) The orientation factor in FRET. The transition dipole moments of both the donor and acceptor molecules are μ_D and μ_A , respectively. The separation vector is R.

The Förster distance can be simplified by substituting the value of the constant to become the following:

$$R_0 = 0.211(k^2 n^{-4} \Phi_f \, Y(\lambda))^{1/6} \quad in \text{ Å} \qquad (2\text{-}10)$$

Where

$$Y(\lambda) = \int_0^{\infty} I_D(\lambda)\varepsilon_A(\lambda)\lambda^4 d\lambda \quad in\ M^{-1}cm^{-1}nm^4 \qquad (2\text{-}11)$$

The energy transfer efficiency, E, can be determined in the lab by measuring the fluorescence intensity of the donor with the acceptor I_{DA} and without the acceptor I_D and then substituting them into the following equation:

$$E = 1 - \frac{I_{DA}}{I_D} \qquad (2\text{-}12)$$

In a similar manner, it is possible to measure the lifetime of the donor with the acceptor τ_{DA} and without the acceptor τ_D.

$$E = 1 - \frac{\tau_{DA}}{\tau_D} \qquad (2\text{-}13)$$

FRET is also known as the third type of quenching fluorescence due to a reduction in the fluorescence intensity. However, it is possible to differentiate different mechanisms. Fluorescence quenching occurs when there is contact between the fluorophore and the quencher; FRET occurs in a through-space interaction. While both cause a decrease in the fluorescence intensity, the quenching process dissipates the energy as heat while the FRET transfers the energy from the donor to the acceptor (91).

2.1.5 Anisotropy

Anisotropy is a useful technique in biochemical and medical applications. It has been used to measure the size of a protein in order to track the size of the protein aggregation. Ravi et al. have used anisotropy measurement to obtain information on the size of HEWL aggregations at pH 12 (98). Li et al. studied the size of BSA-Au_{25}NCs and found that by monitoring the fluorescence anisotropy of AuNCs, the BSA size increased as the pH decreased from 7 to 3.1 (99). Soleilhac et al. studied the size of BSA-Au_{25}NCs and Lyz-AuNCs and found that the size of BSA and HEWL increases after synthesis of AuNCs (100). The interest of these studies is the how size of the protein increases due to changes in the protein structure, aggregations or after the synthesis of AuNCs.

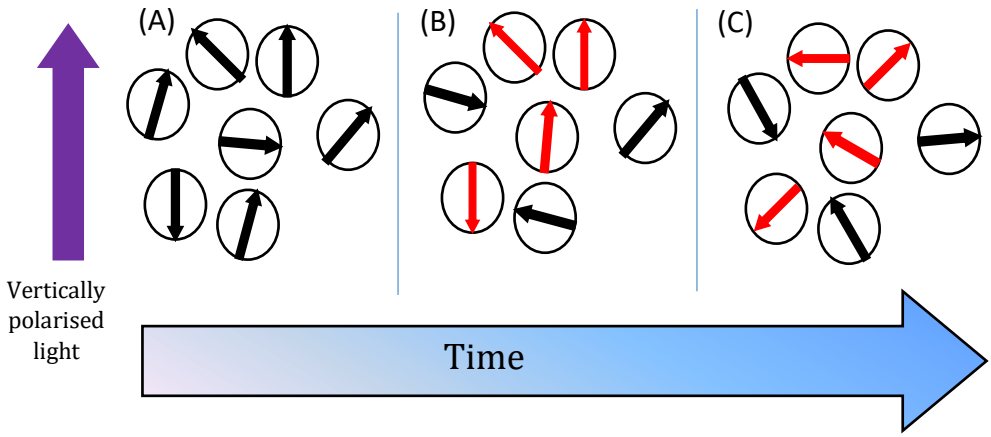

Figure 2.8. Representation of the photon selection process that occurs when fluorophores are excited by polarised light (the purple arrow is vertically polarised light). (A) Fluorophores in the ground state are randomly orientated. (B) Only fluorophores with a transition moment overlap the electric vector light excite (red). The probability of fluorophores to absorb the light is proportional to $\cos^2\omega$, where ω is the angle between the emission moments and the absorption dipole. (C) Brownian rotation causes depolarised fluorescence emission.

As shown in Figure 2.8, fluorophores in the ground state are randomly oriented in a homogeneous solution. Their transition moment orientates with the rotation of the molecular axis. When they are irradiated by polarised light, the fluorophores with absorption transition moments that overlap with the electric vector of the polarised light are more likely to elevate to the higher energy level, as shown in equation (2-14) (91):

$$r = \frac{3\langle cos^2\,\omega\rangle - 1}{2} \qquad (2\text{-}14)$$

Then, the fluorophore returns to the ground state and emits polarised light with transition moments fixed at the molecular axis. However, loss of emission polarisation may occur as a result of rotational diffusion.

The anisotropy (r) is given by the Perrin equation for spherical rotation:

$$r = \frac{r_0}{1+(\tau/\theta)} = \frac{r_0}{1+(6\tau D_r)} \qquad (2\text{-}15)$$

Where r_0 is the anisotropy without the rotational diffusion and θ is the rotational correlation time. Presume that $r_0 = 0.4$, then $r = 0.2$. The anisotropy could be lower when the lifetime is long, as can be seen from equation (2-15). A

relation between the rotational correlation time θ and the rotational diffusion coefficient D_r is given as:

$$\theta = \frac{1}{6D_r} \qquad (2\text{-}16)$$

Rotational correlation time θ depends on the size of the protein, as can be seen in the flowing equation:

$$\theta = \frac{\eta V}{RT} \qquad (2\text{-}17)$$

Where η is the viscosity, V is the volume of the molecule, R is the gas constant, and T is the temperature in$°K$. From equation (2-15) and equation (2-17), it is clear that the anisotropy measurement can be used in biological applications to provide information about the size and shape of macromolecules, such as protein-protein aggregation and the fluidity of membranes. When the size of the protein increases due to aggregation, it rotates slowly and shows an increase in the rotational correlation time (θ) and an increase in anisotropy (91). The measurement of anisotropy will be described in the measurement techniques in chapter 3 (see 3.3: Time-resolved photoluminescence measurement).

2.1.6 Time Resolved Emission Spectra (TRES) and Decay-Associated Spectra

The process that occurs in the excited states during the lifetime of an excited molecule could affect the emission spectra. To study these processes, a time-resolved emission spectra (TRES) measurement is used. Two models are used to explain the change in time-dependent spectra. In general, the first model is a continuous spectral model (Figure 2.9 (A)); it is suitable to determine the solvent effects. In this model, the fluorescent molecules are excited to an unrelaxed state known as the Franck-Condon (F) state after pulsed excitation. The solvent dipole moment reorients around the excited-state dipole moment of the fluorescent molecules. If the lifetime of the fluorescent molecules τ is longer than the solvent relaxation time τ_r, the fluorescent molecules return to the ground state from the

relaxed (*R*) state. If the lifetime of the fluorescent molecules τ is shorter than the solvent relaxation time τ_r, then the fluorescent molecules return from the F state. If the lifetime τ is close to the τ_r, then the average emission will be from the *R* state in the process. The shape of the fluorescence emission does not change in this model. In some cases, the width of the emission spectra changes (91).

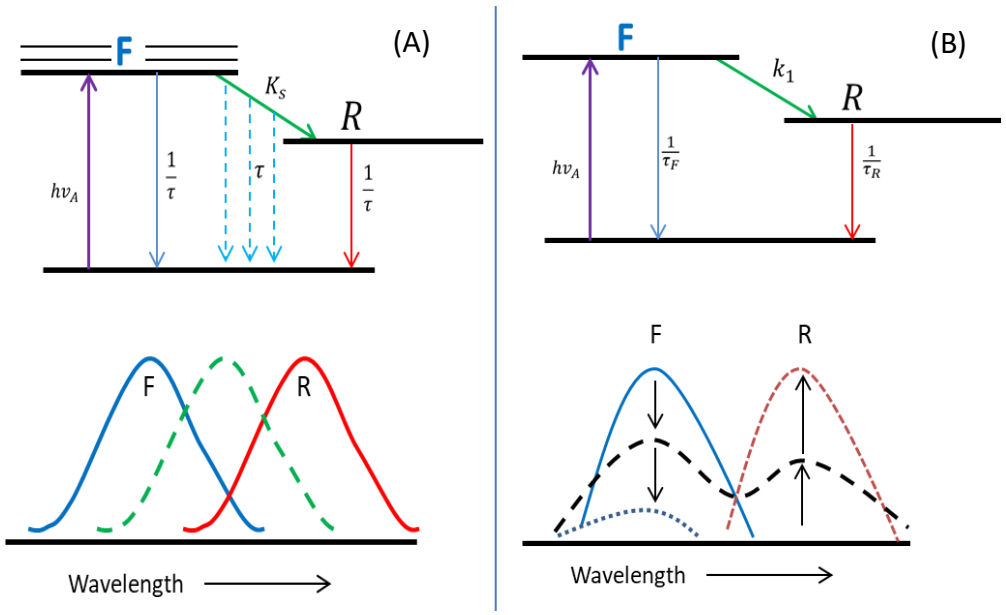

Figure 2.9. Types of models illustrate the change in the fluorescence intensity spectra (A) continuous spectra and (B) two-state model or excited-state reaction (ESR).

The second model is a two-state model or excited-state reaction (ESR). In this model, there are two excited states and two different emissions that emit from different fluorescent molecules, which have different chemical structures (Figure 2.9(B)). The first emission result is from the F state with lifetime τ_F and the second emission result is from the *R* state with lifetime τ_R. These lifetimes are related to the rate of constant K_1. If the decay rate of the F state τ_F^{-1} is higher than the rate constant K_1, then the excited fluorescent molecules return from the F state. If the decay rate of the F state τ_F^{-1} is lower than the rate constant K_1, then the excited fluorescent molecules return from the *R* state. If the rate constant K_1 and decay rate of the F state τ_F^{-1} are similar, each excited state emits photons. In this model, the emission spectra show a clear distinctive excited state either in the F state or the *R* state. In some cases, the emission could occur from both excited states,

leading to wider emission spectra than is seen with single fluorescence emission spectra (91).

The process that occurs in the excited states leads to complicated decays, as illustrated in Figure 2.10. As seen, the continuous black line represents the overall intensity decay. If the decay measurement is detected at the short-wavelength part of the overall emission, it would only provide the emission from the F state. Consequently, this decay is faster than the overall intensity decay since the emission occurs from both the F state and the *R* state. If the decay measurement is detected at the long-wavelength part of the overall intensity decay, the excited molecules have consumed time to move from the F state to *R* state; therefore, the decay is slower in comparison to the overall intensity decay. This technique is useful since it provides information on the R state and it is assumed that all molecules are excited to the F state. When these molecules are moved to the *R* state, there will be an increase in the time in the intensity decay (91).

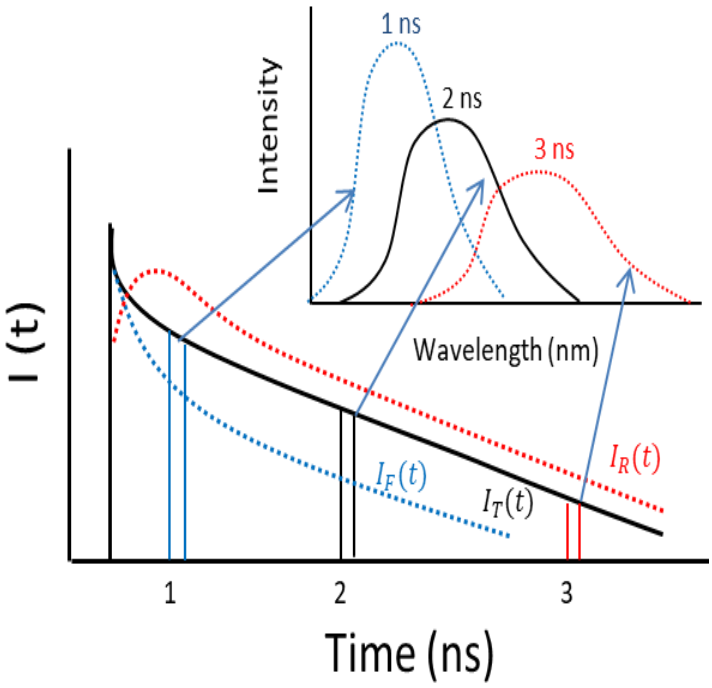

Figure 2.10. Illustration of the change in intensity decays based on interactions in the excited state.

The TRES measurement is acquired from time-correlated single-photon counting (TCSPC) by detecting the fluorescence intensity decay at a selected range of emission wavelengths $I\ (\lambda, t)$. The fluorescence intensity decay relies on emission wavelengths. In comparison to the fluorescence intensity decay at shorter emission wavelengths, at longer emission wavelengths, the fluorescence intensity decay occurs slowly since all the molecules relax before the emission occurs (91). The data analyses of the TRES of the intensity decays are obtained using a multi-exponential model.

$$I(\lambda, t) = \sum_{i=1}^{n} \alpha_i(\lambda) exp[-t/\tau_i(\lambda)] \qquad (2\text{-}18)$$

Where $I(\lambda, t)$ are the intensity decays at each wavelength; $\alpha_i(\lambda)$ is the pre-exponential factor that also can be used to calculate the decay-associated spectra (DAS) in the case of the two-state excitation model and $\tau_i(\lambda)$ is the decay time with $\sum_{i=1}^{n} \alpha_i(\lambda) = 1$. For the continuous model, the decay time (lifetime) depends on the wavelength; for the two-state model, the decay time does not depend on the wavelength.

Although it is assumed that, in the continuous model, the lifetime depends on the wavelength and in the two-state model, the lifetime does not depend on wavelength, the data analysis of TRES can be obtained by fitting with the wavelength-dependent $\tau_i(\lambda)$ lifetime or the wavelength-independent τ_i lifetime due to the resolution limitation and the parameter correlation (91).

Another concept that can be calculated from the TRES measurement is DAS $I_i(\lambda)$, which is given in the following equation:

$$I_i(\lambda) = \frac{\alpha_i(\lambda)\tau_i\, I(\lambda)}{\sum_j \alpha_j(\lambda)\tau_j} \qquad (2\text{-}19)$$

Where $I(\lambda)$ is the steady-state emission spectrum of the total fluorescence intensity. The DAS provides information on individual species that can be observed in the overall fluorescence spectra (101).

2.2 Introduction to Protein Structure

2.2.1 Amino Acids

Proteins are bioorganic molecules that contain one or more polypeptide chains with the reiterating structure - (NH-CHR-C=O). Peptides made of α-amino acids bind together via peptide bonds (102). An amino acid is a molecule that contains a carboxyl functional group (-COOH) and an amino group ($-NH_2$). It is also known as an α- amino acid since the carbon atom creates a bond between these four groups, as shown in Figure 2.11.

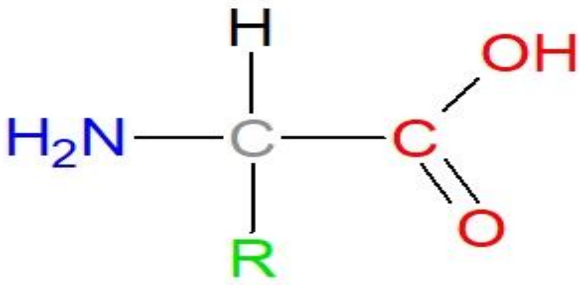

Figure 2.11. Amino acid structure. Blue is the amino group, grey is the α- carbon atom, red is the carboxyl group and green is the R group.

The R group (side chain) is unique for different amino acids. The R group could, sulfur-containing groups, a nonpolar and a polar side chain (102).

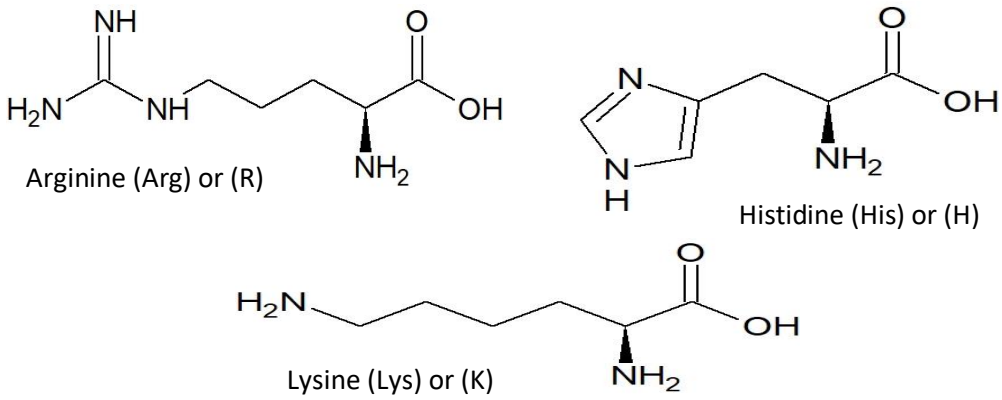

Figure 2.12. The structure of amino acids with basic side chains.

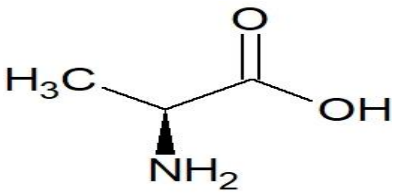

Alanine (Ala) or (A)

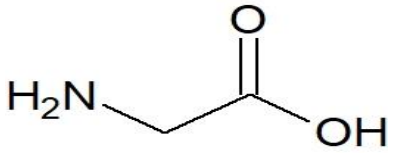

Glycine (Gly) or (G)

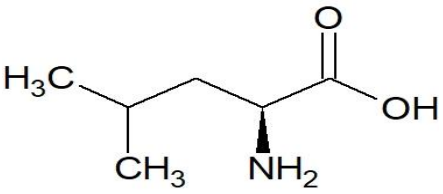

Leucine (Leu) or (L)

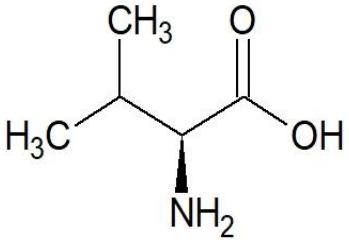

Valine (Val) or (V)

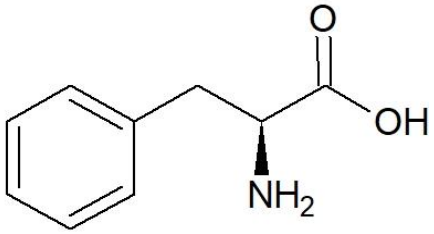

Phenylalanine (Phe) or (F)

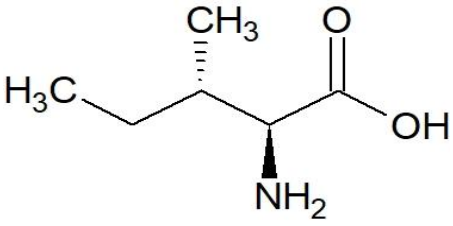

Isoleucine (Ile) or (I)

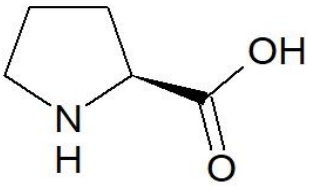

Proline (Pro) or (P)

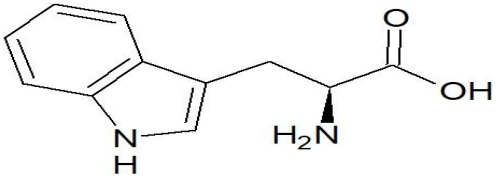

Tryptophan (Trp) or (W)

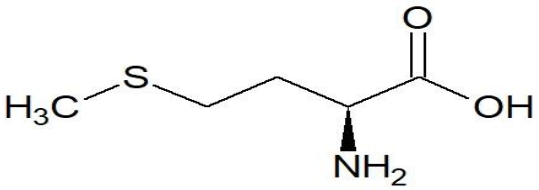

Methionine (Met) or (M)

Figure 2.13. The structure of amino acids with a nonpolar side chain.

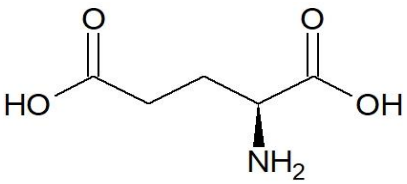

Glutamic acid (Glu) or (E)

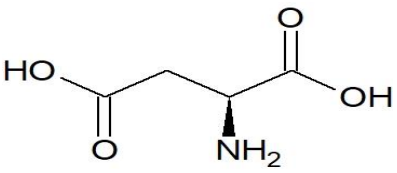

Aspartic acid (Asp) or (D)

Figure 2.14. The structure of amino acids with an acidic side chain.

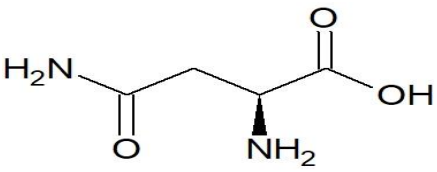

Asparagine (Asn) or (N)

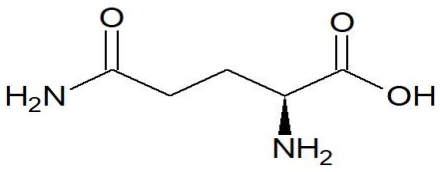

Glutamine (Gln) or (Q)

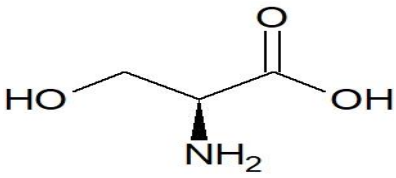

Serine (Ser) or (S)

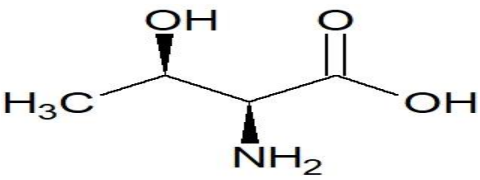

Threonine (Thr) or (T)

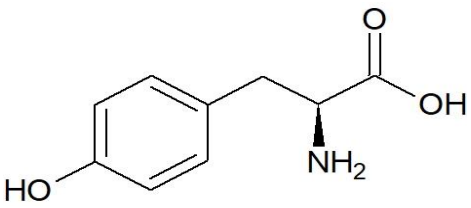

Tyrosine (Tyr) or (Y)

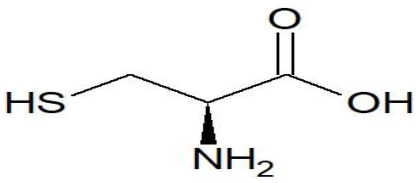

Cysteine (Cys) or (C)

Figure 2.15. The structure of amino acids with a polar side chain

2.2.2 Protein Structure

Proteins have a primary structure, a secondary structure, a tertiary structure and a quaternary structure.

2.2.3 Primary Structure

The primary structure of proteins is described as the arrangement and unique order of the amino acid sequence, as shown in Figure 2.16. The primary structure determines the properties of the protein, such as catalytic activity and hydrogen bonding or folding (103).

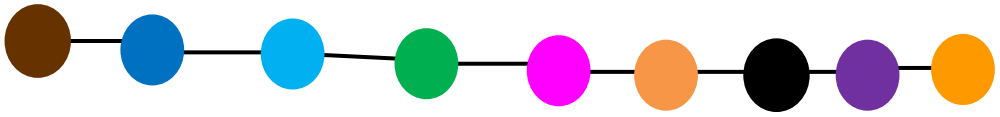

Figure 2.16. The primary structure of a protein. The circles represent different types of amino acids, and the black line is the peptide bond (104).

2.2.4 Secondary Structure

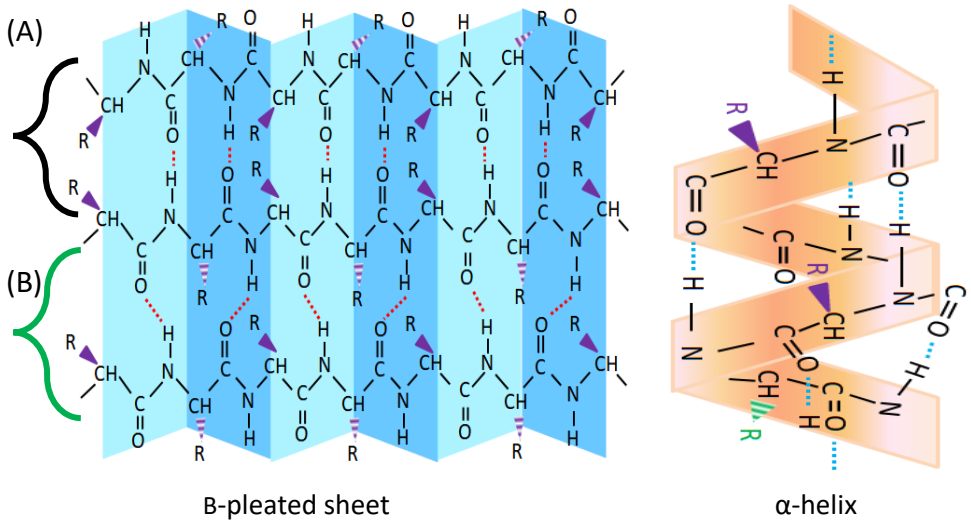

Figure 2.17. Two types of patterns the α-helix and the β-pleated sheet. The antiparallel β-pleated sheet (A) and the parallel β-pleated sheet (B).

The protein structure can be organised by forming hydrogen bonds between the carbonyl C=O oxygen atoms and the amide N-H_2 hydrogens. As a result of this hydrogen bond, proteins form two types of orderly patterns: the α-helix and the β-

pleated sheet. The presence of these patterns in the structure of a protein is called the secondary structure (103,105).

The α-helix structure occurs when a peptide chain twists and forms a helical coil. The α-helix contains amino acid residues binding with a hydrogen bond between the carbonyl C=O oxygen atoms of amino acid residues n and the amide N-H_2 hydrogens of amino acid residues n+4, as shown on the right-side of Figure 2.17. The β-pleated sheet occurs when the segments of a polypeptide chain, known as β-strands, lie alongside each other and form hydrogen bonds with the carbonyl C=O oxygen atoms on one line and the amide N-H_2 hydrogens on the next line. The β-strands can interact with another β-strands in two ways. The first way is the antiparallel β-pleated sheet when the first line of the β-strands is in the opposite direction of the second line of β-strands, as shown on the left-side of Figure 2.17(A). The second way is the parallel β-pleated sheet, when the first line of β-strands is in the same direction as the second line of β-strands, as shown on the left-side of Figure 2.17(B). A two-dimensional sheet is formed by these arrangements.

2.2.5 Tertiary Structure and Quaternary Structures

The tertiary structure of a protein describes the folding of the protein to form a three-dimensional (3D) conformation. This includes the primary and secondary structure. Some parts of the protein may have an α-helix, while other parts have a β-pleated sheet (105). Some proteins, such as HEWL, may have a single polypeptide chain, while other proteins with two or more polypeptide chains, such as haemoglobin, have quaternary structures. Thus, the quaternary structure of a protein is the combination of two different proteins (106).

2.2.6 Lysozyme Background

Lysozyme, also known as N-acetylmuramidase and muramidase, was discovered by Alexander Fleming in 1922 (107). He noticed that lysozyme had an antibacterial property when he placed a drop of nasal mucus obtained from a patient with coryza into an agar plate that contained *Miicrococcus lysodeikticus* (now referred to as *Micrococcus luteus*). The result showed that the lysozyme inhibited the growth of *Micrococcus lysodeikticus*. Fleming found that the lysozyme can exist in saliva, hair, tears, fingernails and skin. Lysozyme can also be found in the egg whites of a hen's egg (HEWL)(108). Lysozyme from various sources serves as a catalyst enzyme due to the hydrolysis reaction of the beta (1-4) glycosidic bond between N-acetylglucosamine sugar (NAG) and N-acetylmuramic acid sugar (NAM) in bacterial cell walls, as shown in Figure 2.18 (109). Since its discovery, lysozyme has been used as an antibacterial agent.

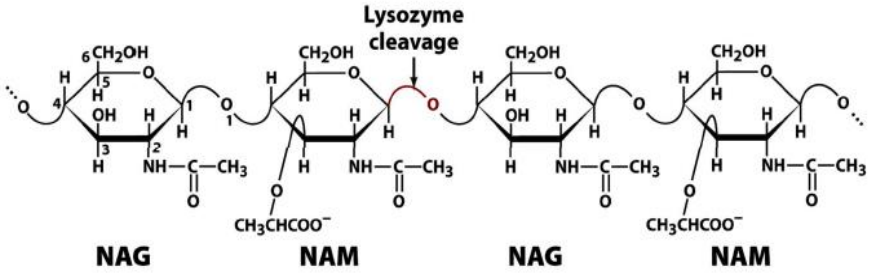

Figure 2.18. Illustration of the lysozyme hydrolysis mechanism.

HEWL is approved as a safe antibacterial agent by the US Food and Drug Administration (FDA). Therefore, it has been used in the food industry to preserve meat, vegetables, cheese, wine and beer by inhibiting the growth of bacteria in these products (110). Lysozyme can kill Gram-positive bacteria, but it cannot kill Gram-negative bacteria because the structure of Gram-negative bacteria makes them immune to lysozyme. Nevertheless, several studies have modified lysozyme to be effective agents against Gram-negative bacteria, e.g. using denatured treatment (111) and ultrafiltration treatment (112). In addition to its antibacterial applications, lysozyme has been used in drug delivery. Lysozyme is used as a drug carrier for

kidney diseases; its small molecular weight (14 kDa) enables it to enter the kidneys (113).

The structure and physical properties of HEWL have been studied. The amino acid sequence of HEWL was reported by Canfield and Robert in 1963 (114). The 3D structure of HEWL was reported by Blake et al. in 1965 (115). Figure 2.19 shows the 3D structure of lysozyme obtained from the protein data bank (PDB). HEWL contains 129 amino acid residues in a mono-polypeptide chain (14.3 kDa) with four disulphide bonds and an isoelectric point (pI) 11.35. HEWL is widely used because it is commercially available and effortlessly crystallised, has antibacterial properties as discussed above and the ability to self-assembly (116).

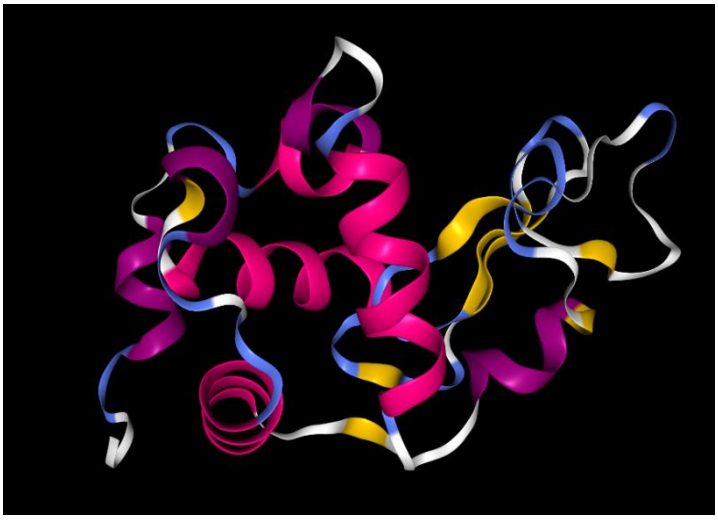

Figure 2.19. Structure of HEWL from PDB files 1HEW.

In nanotechnology, HEWL has been used in the synthesis of AuNCs, as discussed in 1.4 Synthesis of AuNCs in Chapter 1. The interest in the synthesis of AuNCs using proteins has increased since the size of the proteins is at the nanoscale, and various proteins have different specific bio-functions (117). Moreover, HEWL has been used as a model system in many research studies to investigate protein unfolding and aggregation (71) due to its ability to self-assembly (70).

Chapter 3: Experimental Techniques

3.1 Ultraviolet-Visible Absorbance Spectroscopy

Ultraviolet-visible absorbance spectroscopy (UV-Vis spectroscopy) is an important technique used in biological laboratories and many research areas. One of its uses is measuring the concentration of biomolecules, such as protein and DNA (118). Helmfors et al. used UV-Vis spectroscopy to measure the concentration of HEWL in cerebrospinal fluid obtained from patients with AD (119). Another use of UV-Vis spectroscopy is measuring the turbidimetry of a sample to determine the aggregation of proteins. For instance, Khan et al. measured the turbidity of HEWL with SDS at a pH two points below pI, which indicated the aggregation of HEWL with SDS at this pH (120). Additionally, since the discovery of AuNCs and AuNPs, UV-Vis spectroscopy has been used to differentiate them (77).

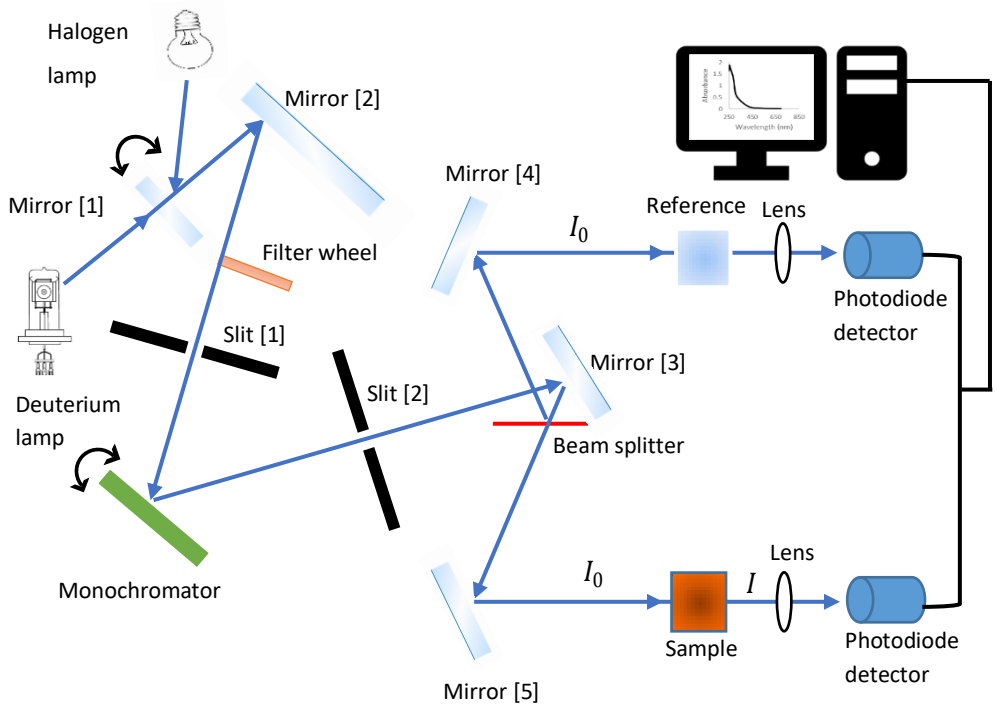

Figure 3.1. Schematic diagram of the UV-Vis instrument.

Figure 3.1 shows the components of a typical UV-Vis spectrometer. The instrument consists of two light sources; one is a deuterium lamp (or hydrogen lamp) with a wavelength in the UV range, and the second is the halogen, which has a wide range of wavelengths in the visible light. Two plane mirrors are needed to reflect the light. Mirror [1] is used to select the range of the light wavelength. For example, to obtain light in the visible range, mirror [1] will block the light from the deuterium lamp and reflect the light of the halogen to mirror [2] simultaneously. The light source switches automatically during the measurement, and the rotational position of the filter wheel is synchronized with a monochromator. The emission of light passes the optical filter then passes the entrance slit [1] of the monochromator.

The monochromator used in the present work contains a holographic concave grating with 1053 lines/mm in the centre. Light is diffracted by the grating, generating a spectrum. The monochromator specifically chooses a portion of the spectrum and then sends this portion to exit slit [2] with a bandpass 1 cm to mirror [3]. The mirror then reflects light to the beam splitter, which splits the light into two equal beams. One beam (I_0) is reflected by mirror [4] and then passes through the reference (e.g., water, buffer), continuing through a convex lens and then to the photodiode detector. The second beam is reflected by mirror [5] and then passes through a sample of interest. Some of the light is absorbed, and the remaining light is transmitted (I_t). Continuing its path through a convex lens to the photodiode detector. Finally, the data are analysed by computer software that connects to the instrument (118).

The ratio of the light intensity entering the sample (I_0) to the light exiting the sample (I_t) at a particular wavelength is defined as the transmittance (T), which is given as follows:

$$T = \frac{I_0}{I_t} \times 100\ \% \qquad (3\text{-}1)$$

The absorbance (A) is the negative logarithm of the transmittance, as follows:

$$A = -\log T \qquad (3\text{-}2)$$

The absorbance (A) increases linearly as the concentration of the sample increases in an ideal solution. This is known as the Beer-Lambert law, as follows:

$$A = \varepsilon\, c\, d \qquad (3\text{-}3)$$

Where ε is the decadic molar extinction coefficient in M^{-1} cm^{-1}, c is the concentration of the sample in M, and d is the light path through the sample in cm (118).

3.2 Spectrofluorimetry

Spectrofluorimetry is a technique used to measure the fluorescence intensity of a sample of interest. It has been employed to monitor protein conformation changes by detecting the change in the fluorescence wavelength of Trp (121). Additionally, it has been used to detect the presence of beta-amyloid fibrils by monitoring the rise in the fluorescence intensity of ThT (122).

Changes in the fluorescence intensity of AuNCs has been used to sense different biomolecules (123) and toxic metals (77). As shown in Figure 3.2, the components of spectrofluorimetry include a light source, particularly a Xenon Arc lamp, which has a high intensity at wavelengths ranging from 250–800 nm. This lamp is better than a halogen lamp, which has a low intensity at wavelengths below 400 nm; therefore, the halogen lamp is not suitable for fluorescence study.

In spectrofluorimetry, the light passes through the excitation monochromator. Monochromators are used to separate the white light into various colours with diffraction gratings or prisms. Diffraction gratings are the most common; the concave gratings are used because the gratings reduce stray light. These monochromators are programmed to the scrutinizing wavelength mechanically.

Next, the light passes through the sample to excite the fluorescent molecules in the sample. The fluorescence emission is detected using the L-format configuration to avoid detecting excitation light. The fluorescence emission from the sample passes through an emission monochromator, followed by a photomultiplier tube detector that converts the photon to an electronic signal (current). This current increases with an increase in light intensity.

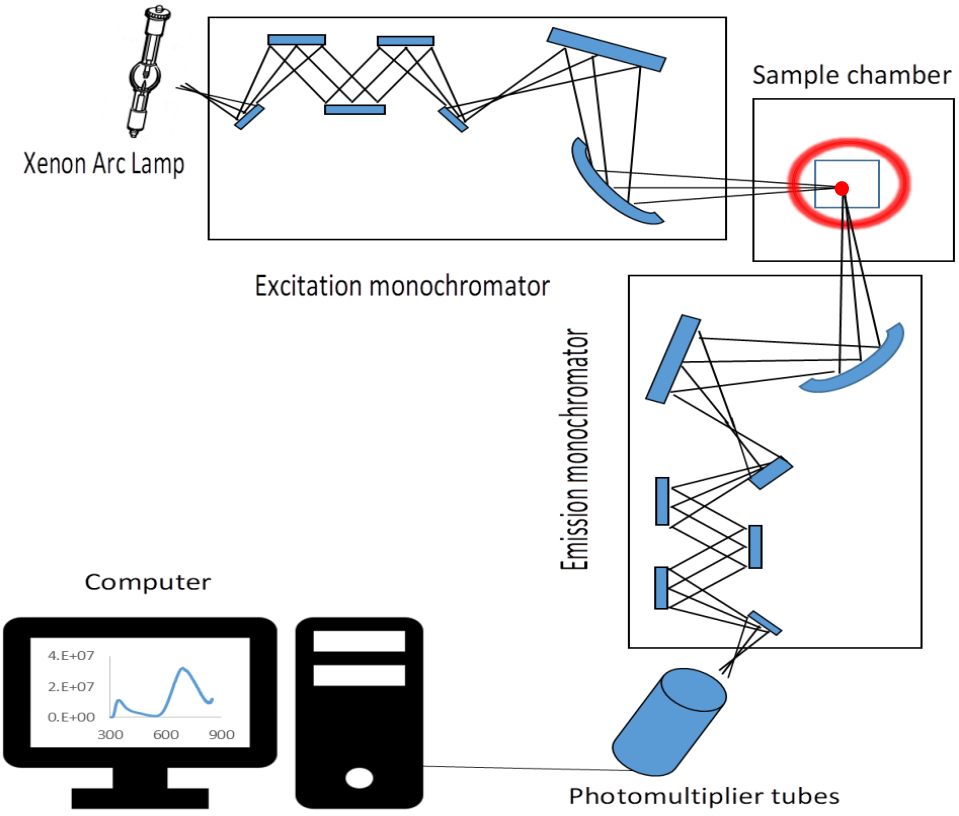

Figure 3.2. Schematic diagram of the spectrofluorimetry instrument.

The steady-state anisotropy can be measured by adding polarisers. Two polarisers are used; one is an excitation polariser that is placed next to the source, while the second emission polariser is placed next to the detector. The polarisers can be used for measuring steady-state or time-resolved anisotropy, and they are also removable. Finally, the data are analysed using origin software in a computer (91).

3.3 Time-Resolved Photoluminescence Measurement

Time-resolved photoluminescence measurement has been used in bioapplications like cellular imaging, and this measurement provides more information than steady-state spectroscopy (spectrofluorimetry). For example, the lifetime measurement can determine the type of fluorescence quenching, as described in chapter 2 (see 2.1.3 Fluorescence quenching). Two types of time-resolved fluorescence measurement have been developed: the time-domain and frequency-domain methods. In the time-domain method, the sample is excited with a pulsed light source. The time-dependent intensity I(t) is detected and presented in a histogram. The ln (I[t]) is plotted on the y-axis, and time is plotted on the x-axis; then, lifetime is calculated from the slope. In the frequency-domain or phase-modulation method, the sample is excited with an intensity-modulated light, which results in fluorescence with a modulation frequency and a delay due to the lifetime. The lifetime is then calculated from the phase shift (91).

3.3.1 Time-Correlated Single Photon Counting (TCSPC)

For this thesis, lifetime measurement was performed using time-correlated single photon counting (TCSPC). In TCSPC, The light source is used to excite a sample as shown in Figure 3.3. Simultaneously, another light signal passes to a detector to generate an electronic signal (this known as a reference signal). This signal then goes through a constant function discriminator (CFD) to measure the arrival time of the excitation pulse precisely. Any undesired value arising from amplitude is removed, thus providing sub-nanosecond resolution. Then, the signal passes across a time-to-amplitude converter (TAC) and generates a signal to start a voltage ramp. Second, the light passes across the fluorescent sample, thereby emitting photons. These photons are detected by the second detector, causing a signal to be generated. This signal passes across the second CFD to measure the arrival time of the photons precisely and generates a signal to stop the voltage ramp in the TAC. The value of voltage is linearly proportional with the time difference between the start and stop signals. Then, the signal passes through an analogue-to-digital

converter (ADC). In ADC, the TAC output pulse is converted from analogue pulse into digital timing value.

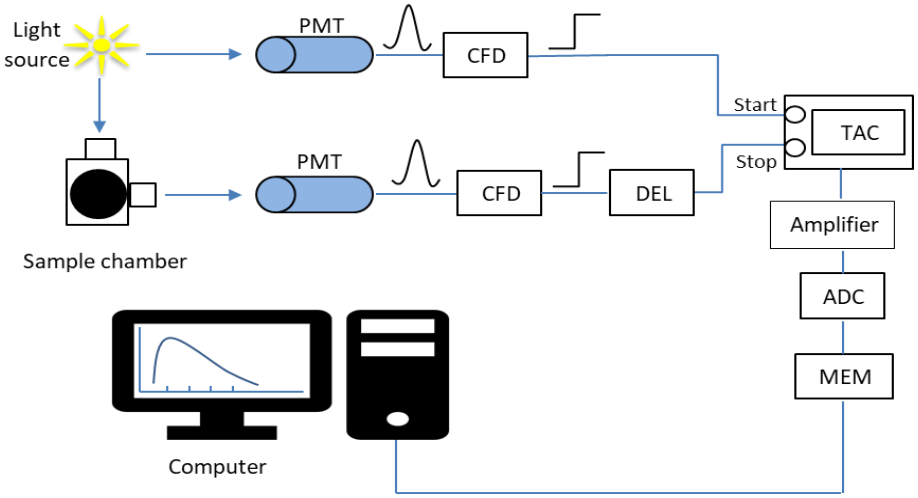

Figure 3.3. Schematic diagram of an instrument for measuring lifetime using TCSPC. The components are a light source (shining sun), sample chamber, photomultiplier tube detector (PMT), constant function discriminator (CFD), electrical delays (DEL), time-to-amplitude converter (TAC), amplifier, analogue to digital converter (ADC) and digital memory (MEM).

In other words, the output signal of the TAC is collected in different time bins, commonly known as channels. The width of the channel is the ratio of the full-time range (the TAC range, nanoseconds) to the time resolution of the ADC in nanoseconds/channel (124). The output of ADC is used to generate a histogram and stored in digital memory (MEM). Generally, the time between the exciting pulse and the emission is measured and plotted in a histogram that shows the intervals of time on the x-axis and the number of photons correlated to the x-axis on the y-axis. This histogram is produced by repeating this process until 10,000 photon counts are accumulated; this provides good statistical data precision (91). Then the fluorescence decay is analysed using computer software as discussed in (3.3.2 Analysis of TCSPC Data). To measure the lifetime at a specific fluorescence emission wavelength, a monochromator is used. Polarizers are also used to remove the effect of anisotropy on lifetime by setting the emission polarizer at the angle of 54.7^{o} (92,125).

TCSPC is adjusted to detect one photon per 100 excitation pulses. At high photon counts, the histogram is biased to shorter decay times as only the first photons are

measured and both the detector and electronics experience an event known as “dead time”, during which any delayed photons will not be detected. The dead time occurs around a nanosecond after the first photon is detected. When the photon counts exceed one photon per 100 excitation pulses, it is called a pile-up effect (126). To avoid the pile-up effect, the average detector count rate was set below 2% for all experiments in this thesis.

A TCSPC system can be operated in either forward mode or reverse mode. In forward mode, the TAC is started by the light source signal and stopped by the emission signal. This mode is used when the rate of a light source is not sufficiently high, and there is no need for using shifting delay since the fluorescence photons have appeared at longer time intervals. Due to the development of light sources and their higher rates, though, most TCSPC systems are operated in reverse mode. In reverse mode, the signal of the emission triggers the start of the TAC, and the light source signal stops the TAC (124). Using a light source with a higher pulse rate is not preferred in the forward mode for two reasons. First, the TAC cycles will start, but the stop signal will not be received. Therefore, the TAC will reset at overflow. Second, it takes a finite time to reset the voltage ramp, and if the TAC were to be started by each laser trigger, many counts would be lost while the TAC was being reset. Therefore, the reverse mode is used with light sources with higher rates (124).

3.3.2 Analysis of TCSPC Data

The data obtained from single-photon counting are shown in Figure 3.4. The instrument response function is represented as $L(t)$; this is known as the prompt. The measured data is $N(t)$, and the calculated decay is $N_T(t)$. The photon counts are grouped into channels. The channels have a specified time (t) and width (Δt); therefore, the curves are a function of discrete times (t). The instrument response function (IRF) is the reaction of the instrument to light from the scattered and non-fluorescent sample. The width of the IRF is determined using the timing electronics and the detector. The measured data $N(t)$ are collected using the sample of

interest. Calculated decay $N_T(t)$ is the fitted function in which those measured data are convoluted with the IRF (91).

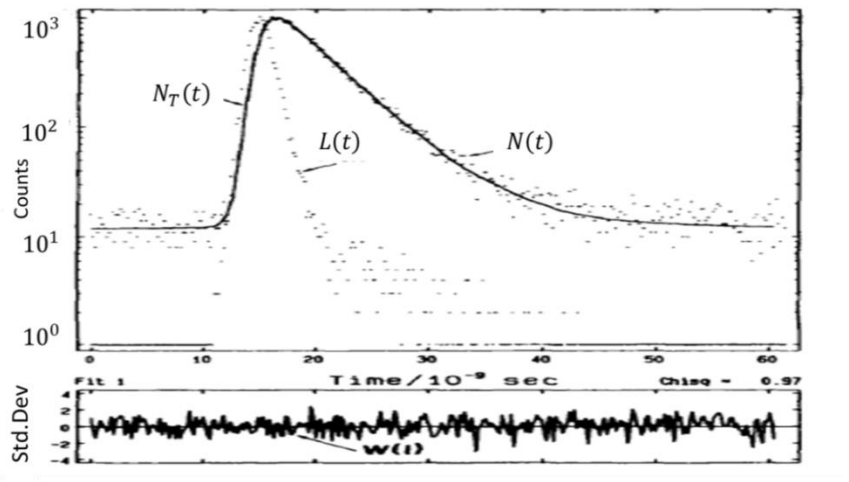

Figure 3.4. Data analysis of the time-domain of measuring time-resolved fluorescence from ref (125).

The light intensity of an exciting light source is not a δ-function. As a result, one assumes that $I(t - t_k)$, an excitation pulse is a group or set of δ-functions with various amplitudes. All individual δ-functions create a signal from the sample, and the signal's intensity increases with an increase in the δ-function pulse as described as follows:

$$I_k(t) = L(t_k)I(t - t_k)\Delta t \qquad (t > t_k) \quad (3\text{-}4)$$

Each δ-function creates a signal from a sample at time t_k. The amplitude of the signal created at t_k increases with increasing intensity of the light source $L(t_k)$. If the light source emits a pulse at time t_k, the sample is excited to a higher energy state and spends some time before returning to the ground state and emitting a photon. For this reason, $(t - t_k)$ is the period during which the fluorophore is excited, and no fluorescence exists from the prior sample excitation. The fitting function $N(t_k)$ is the sum of fluorescence signals from the sample following the excitation from each δ-function pulse at time t_k (6), as follows:

$$N(t_k) = \sum_{t=0}^{t=t_k} L(t_k)\, I(t - t_k)\Delta t \qquad (3\text{-}5)$$

When Δt is extremely small, the alternative equation is written as an integral, as follows:

$$N(t) = \int_0^t L(t_k) I(t - t_k) dt_k \qquad (3\text{-}6)$$

$N(t)$ is the total of the signal intensities generated by a pulsed light until time t. The $t_k = t - \mu$ was substituted in equation (3-6), where μ is the time delay from the starting point when a fluorescence signal is produced by the δ-function signal.

$$N(t) = \int_0^t L(t - \mu) I(\mu) d\mu \qquad (3\text{-}7)$$

The purpose of lifetime analysis is to fit the experimental data with impulse response function I(μ). The best-fitting function is determined using nonlinear least squares (NLLS) to examine the consistency of the model with the experimental data. In lifetime measurement using TCSPC, the experimental data are $N(t)$, and the theoretical data $N_T(t)$ are tested by reducing the goodness-of-fit parameter χ^2, which is described as follows (91,93):

$$\chi^2 = \sum_{t=1}^{n} \left[\frac{N(t) - N_T(t)}{\sqrt{N(t)}} \right]^2 \qquad (3\text{-}8)$$

Where $N(t) - N_T(t)$ is the actual deviation (residual) at each giving point, $\sqrt{N(t)}$ is the expected standard deviation, and n is the number of channels. For a good fit, χ^2 should range from 0.97–1.28. Another possible method to test for a good fit is the weighted residuals W_t, a follows:

$$W_t = \frac{N(t) - N_T(t)}{\sqrt{N(t)}} \qquad (3\text{-}9)$$

The weighted residuals show randomly distributed points around zero if the fit is good (91).

The number of fluorophores in excited electronic states after illumination is denoted as n_0 at time t = 0. The following equation gives the decay rate of the fluorophores population:

$$\frac{dn(t)}{dt} = -(K_r + K_{nr})n(t) \qquad (3\text{-}10)$$

Where n(t) is the number of fluorophores in excited states at time t, K_r is the radiative rate, and K_{nr} is the non-radiative rate. The integration of the equation results in an exponential decay, as follows:

$$\frac{dn(t)}{n(t)} = \frac{1}{\tau}\, dt \qquad (3\text{-}11)$$

Where $\tau = \frac{1}{K_r + K_{nr}}$ is the lifetime.

$$n(t) = n_0 exp\left(-\frac{t}{\tau}\right) \qquad (3\text{-}12)$$

The number of fluorophores in excited states at time t cannot be measured in the lab; instead, the fluorescence intensity I(t) is measured as follows:

$$I(t) = I_0 exp\left(-\frac{t}{\tau}\right) \qquad (3\text{-}13)$$

Where I_0 is the intensity at time t = 0.

For fluorophores have more than one lifetimes, multiple exponential fit is used, as determined by the following equation:

$$I\,(t) = \sum_i \alpha_i\, exp\left(\frac{-t}{\tau_i}\right) \qquad (3\text{-}14)$$

Where α_i is a pre-exponential factor or amplitudes that show the fractional amount of species with $\sum \alpha_i = 1$ (91).

3.4 Anisotropy Measurement

Anisotropy measurement was developed from the concept of photoselective excitation, which states that only fluorescent molecules with a transition moment analogous to electric vectors of exciting photons will be excited. Therefore, two polarisers are added to the spectrofluorimetry (to measure steady-state fluorescence anisotropy) or time-resolved emission spectroscopy instrument (to measure time-resolved anisotropy). There are two types of anisotropy

measurements. One is the L-format method, in which only one path of light extends from the source to the sample and from the sample to the detector, as shown in Figure 3.5 (A) (91).

The second is the T-format method, in which polarized light excites the sample, and emission is detected in two paths (Figure 3.5 (B)) (91). One of these paths is used to detect vertically polarised fluorescence emission, while the second is used to detect horizontally polarised fluorescence emission. The most common method is the L-format, as maintaining the balance between the two sets of detectors used in the T-format method is difficult (127). Thus, only the L-format was used and is described further in this thesis.

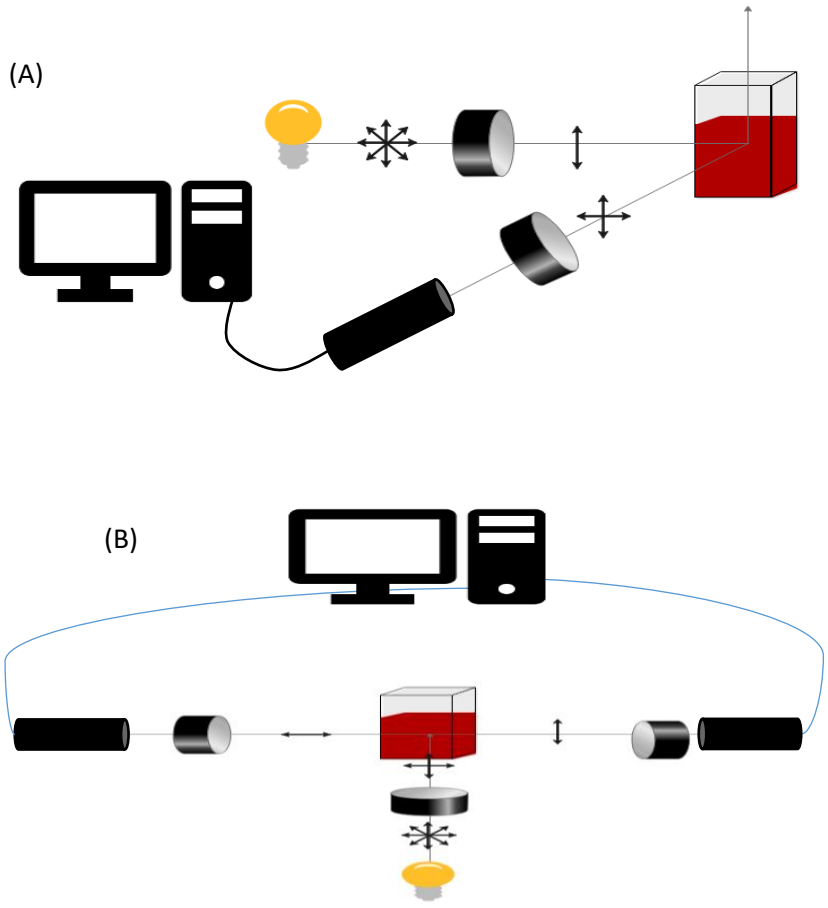

Figure 3.5. Schematic of the measurement of fluorescence anisotropies (A) using the L-format and (B) using the T-format.

For anisotropy measurement, the sample of interest is first irradiated using vertically polarised light. Then, the vertically and horizontally polarized emission of

the sample is detected by adjusting the emission polariser in the vertical and horizontal positions (usually, this polariser is automatically changed after 30 or 60 seconds). This emission is donated as I_{VV} and I_{VH}, respectively. Then, both I_{VV} and I_{VH} are substituted in the following equation to obtain fluorescence anisotropy (r):

$$r = \frac{I_{VV} - I_{VH}}{I_{VV} + 2I_{VH}} \qquad (3\text{-}15)$$

Polarisation (P) is calculated using the following equation:

$$\mathrm{p} = \frac{I_{VV} - I_{VH}}{I_{VV} + I_{VH}} \qquad (3\text{-}16)$$

Where I is the fluorescence intensity, and VV and VH are descriptions of the polarizer's orientation. The first letter represents the orientation of the excitation polariser, while the second letter represents the orientation of the emission polariser. V indicates the vertical position, and H indicates the horizontal position. Fluorescence anisotropy (r) can be related to polarisation (P), and vice versa, as follows:

$$\mathrm{P} = \frac{3\mathrm{r}}{2+\mathrm{r}} \qquad (3\text{-}17)$$

$$\mathrm{r} = \frac{2\mathrm{p}}{3-\mathrm{p}} \qquad (3\text{-}18)$$

Polarisation (P) is not as common as fluorescence anisotropy (r) since the anisotropy difference intensity ($I_{VV} - I_{VH}$) is divided by the total fluorescence intensity of sample ($I_T = I_{VV} + 2I_{VH}$) (127).

Next, the anisotropy measurement is repeated, and the average anisotropy $\bar{r}$ is calculated as follows:

$$\bar{r} = \sum_i f_i r_i \qquad (3\text{-}19)$$

Where f_i are fractional intensities, and r_i are the anisotropies of the molecules. Equation (3-19) is used for steady-state measurements of fluorescence anisotropy. The time-resolved measurement is utilized to obtain the rotational diffusion and association reactions, as follows:

$$r(t) = r_0\, exp\left(\frac{-t}{\theta}\right) \qquad (3\text{-}20)$$

Where $r(t)$ is the anisotropy decay at time t, θ is the rotational correlation time, and r_0 is the anisotropy at t = 0. For a large protein or a fluorophore binding to a large molecule, the rotational correlation time is high. In some cases, the sample possibly contains a mixture of a single protein, which is known as a monomeric sample, and associated proteins that are identified as tetrameric proteins. The anisotropy decay of a mixture of two proteins of different sizes is two exponentials.

$$r(t) = r_0 f_M\, exp\left(\frac{-t}{\theta_M}\right) + r_0 f_T\, exp\left(\frac{-t}{\theta_T}\right) \qquad (3\text{-}21)$$

Where the f_M is the fraction amount of monomeric proteins corresponding to rotational correlation time θ_M, and f_T is the fraction amount of tetrameric proteins corresponding to rotational correlation time θ_T, $f_M + f_T = 1$ (91). In more complex cases, the anisotropy decay is expressed as follows:

$$r(t) = \sum_j r_{oj}\, exp\left(\frac{-t}{\theta_j}\right) \qquad (3\text{-}22)$$

Where r_{oj} is the decay of the fractional anisotropies that corresponds to correlation time θ_j.

In the L-format method, the polarized fluorescence emission passes through a monochromator. A monochromator can cause artefact because vertically polarised light may transmit through the monochromator with an efficiency different from that of horizontally polarised light. Therefore, the measurement must be corrected using the G factor. The G factor is the ratio of responsiveness detection of vertically polarised emission S_V to responsiveness detection of horizontally polarised emission S_H (91,125,127).

$$G = \frac{S_V}{S_H} \qquad (3\text{-}23)$$

To measure the G factor, a horizontally polarized light source is used to detect the horizontally and vertically polarized emissions I_{HH} and I_{HV}, respectively. The

change in these values arises from the detection system (91,125,127). The G factor is calculated as follows:

$$G = \frac{I_{HV}}{I_{HH}} = \frac{S_V}{S_H} \qquad (3\text{-}24)$$

Then, the anisotropy is corrected with the G factor using the following equation:

$$r = \frac{I_{VV} - GI_{VH}}{I_{VV} + 2GI_{VH}} \qquad (2\text{-}25)$$

3.5 Scanning Electron Microscopy

Scanning electron microscopy (SEM) is employed to examine the morphology and topography of the sample. For example, SEM is used to study protein aggregation and amyloid formation (84). Additionally, SEM has been utilised to investigate the morphology and size of AuNPs (117).

In this microscope, an electron beam is used to probe the sample. The spatial resolution limitation of SEM refers to the instrument's ability to measure the minimum distances of separation and differentiate two objects.

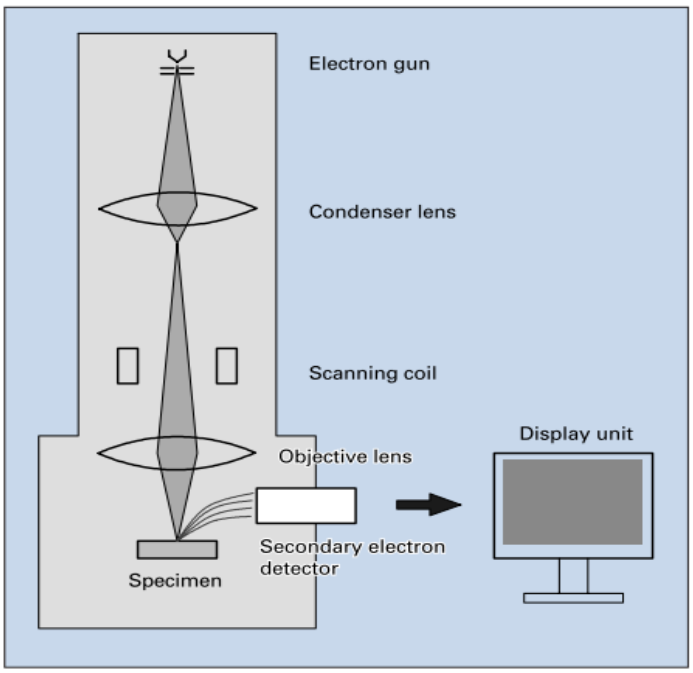

Figure 3.6. Schematic of the component of an SEM obtained from (128).

The components of SEM are an electron source, lenses, scanning coils, a specimen, a detector and a display unit (Figure 3.6). The electron source generates electron beams, which pass through magnetic lenses. These lenses include a condenser lens and an objective lens and are used to prevent the electron beam from straying and helping focus the beam onto the specimen surface**.** The scanning coils are utilized to move the electron beam from one area to another area on the specimen. The specimen chamber contains the specimen stage and the specimen holder; the sample is prepared on the copper grid and then placed on the specimen holder on the stage. The stage allows the sample to be moved to select the area of interest before imaging (129).

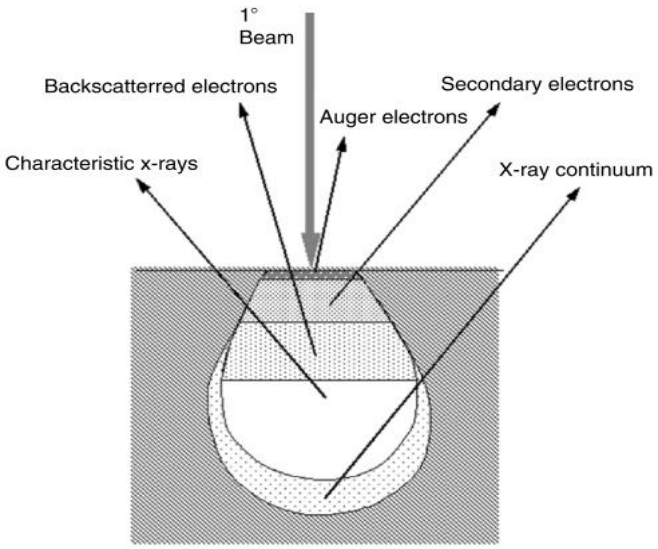

Figure 3.7. Representation of a variety of signals produced after the electron beam interacts with the sample (129).

The basic principle of SEM is that the electron beam interacts with the sample in the specimen. This interaction generates a variety of signals, such as secondary electrons, backscattering electrons (BSEs), X-ray or Auger electrons and cathodoluminescence (Figure 3.7). These signals depend on the accelerating voltage and atomic number. The high accelerating voltage leads to the electrons penetrate deep into the sample bring about missing the information of the samples' surface. At fixed accelerating voltage, the electrons penetrate deeper on the sample with low atomic number compare with the sample with the high atomic number because

a large number of atoms prevent electron penetration. The BSEs also depends on the atomic number. BSEs signal is high in samples with high atomic numbers because these samples have high amount of positive charges on the nucleus causing high electrons backscatter producing atomic contrast in SEM images (129).

Most SEM is operated under a higher vacuum system to prevent scattering of the electron beam and contamination of the electron guns due to the discharge of the gun. Bioorganic nanomaterials and colloidal AuNPs suspension must be completely dry, as the fluids will degas and contaminate the SEM. Biomolecules also need staining since they contain low atomic numbers elements, such as carbon, hydrogen and oxygen, which have low imaging contrast. A stain with higher atomic number atoms, such as uranyl acetate (UA) is employed for the imaging of protein aggregation. As shown in Figure 3.8, UA in solution comprises acetate ion and uranyl ion. The UA binds to the protein, providing a higher contrast due to the higher atomic number of uranium-238 (130).

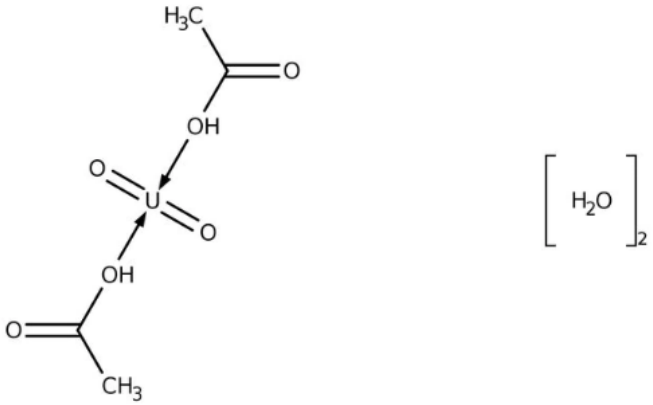

Figure 3.8. Chemical structure of uranyl acetate dihydrate $UO_2(CH_3COO)_2 \cdot 2H_2O$.

Chapter 4: Lyz-AuNCs for Studying HEWL Aggregation

4.1 Abstract

Protein aggregation leads to many diseases. The aggregation of protein can be induced by modifying the pH, protein concentration and temperature, or by adding chemicals such as urea. A well-known protein that is used for investigating protein aggregation is HEWL because of its ability to self-assemble. Despite the variety of methods used to study protein aggregation, the detection of the oligomer is a difficult task due to the fact ThT is not sensitive to detect protein unfolding or oligomers. Therefore, a new method of detection is needed. One new invention is Lyz-AuNCs, which have not been previously used in the study of protein aggregation. This chapter discusses the fluorescence properties of AuNCs at different pH and concentration of HEWL. Under these conditions, the optical properties of Lyz-AuNCs are monitored using UV-Vis absorbance spectroscopy and fluorescence techniques. The measurement showed an increase in fluorescence intensity and wavelength but a decline in the fluorescence lifetime when the pH increases. The decrease in the fluorescence lifetime indicated that an increase in the fluorescence emission is not due to a decrease in the quenching process. The redshift is due to an increase in the fluorescence intensity associated with a short lifetime emission. The above result does not apply at a pH range of 4 to 6 due to an aggregation of Lyz-AuNCs, which leads to a decrease in the fluorescence intensity. At pH 3, the fluorescence intensity of Lyz-AuNCs increased linearly with a redshift alongside a decrease in the contribution of long lifetime component, but no change was observed in the short lifetime component with an increasing concentration of HEWL. In the case of pH 12, the fluorescence intensity increased at 5 mg/ml of HEWL without further change in both the intensity and wavelength of Lyz-AuNCs. This result shows that Lyz-AuNCs are sensitive to the concentration of HEWL at pH 3

compared to pH 12. The exact interaction between Lyz-AuNCs and HEWL is still unknown and requires further examination.

4.2 Introduction

Protein aggregation causes numerous diseases, as discussed in Chapter 1 (see 1.1: Protein denaturation). Many studies show that the majority of proteins can misfold and aggregate depending on the conditions. Among these proteins, HEWL has been widely used for studying protein aggregation due to its ability to self-assemble, an excellent solubility in water and small size (129 residues) (see 2.2.6 Lysozyme background in Chapter 2) (131). It has been found that HEWL aggregates under different conditions, such as an increasing the concentration of HEWL (132), changing its pH (98), a high temperature (133,134) or when adding chemicals such as urea. In this chapter, the effect of changing the pH and increasing the concentration of HEWL will be discussed, and the effects of temperature and denatured chemicals will be discussed in Chapter 5.

It has been found that pH plays an important role in the aggregation of HEWL. The change in the pH leads to a change in the surface charge of the protein. Each protein has an isoelectric point (pI), where the total surface charge of the protein is zero. At a pH level higher than pI, the surface charge of the protein is negative. Likewise, the surface charge of the protein is positive at a pH lower than pI (135). These surface charges prevent protein from aggregation due to strong repulsive forces. For example, HEWL aggregates and precipitates at pH 11.35 because of low repulsive force. The effect of changing the pH on HEWL has been studied. At a fixed HEWL concentration (1 mM), the carboxylate group in Glu 35 in HEWL monomers becomes deprotonation at a pH range of 5 to 10 causing the formation of HEWL dimer. At a pH higher than 10, higher-order oligomers and amorphous precipitates form (71). At a pH of 12.2, the formation of amyloid fibrils rapidly occurs at room temperature due to weak repulsive forces (98,136–138). At pH 2, the surface charge of HEWL is positive; leading to the prevention of aggregation due to strong repulsive forces. Therefore, a higher temperature is needed to form amyloid fibrils

at pH 2 (139). The pH is important to the stability of the protein. The change in the pH to be close to the pI of proteins leads to the neutral surface charge and reduce the protein stability. As a result, a protein aggregates.

Many researchers have studied the effect of HEWL concertation on aggregation. Ravi et al. report that high concertation of HEWL induces HEWL aggregations (98). Burnett et al. found a range from 10 to 100 $mgml^{-1}$ concentrations of HEWL forms aggregate species at 55℃, without stirring (132). It is also possible amyloid fibrils forms at low concentration of HEWL. Sian-Yang Ow and Dave E. Dunstan found that at an acidic pH, concertation of 2.5 $mgml^{-1}$ yielded a higher number of amyloid fibrils at 65℃ at magnetically stirred (550 rpm) (134).

The amount of concentration can affect the type of aggregations either amorphous aggregate species or amyloid fibrils. Burnett et al. found at pH ~3, amyloid fibrils are formed at HEWL concentrations below 70 $mgml^{-1}$, while amorphous aggregates species occurs in a pH range from 4 to 12 within a range from 10 to 100 $mgml^{-1}$ of HEWL concentrations. They also found that the formation of the amyloid fibrils is a slower process in comparison to the amorphous aggregates species (132). They also reported that amorphous aggregates do not grow to form amyloid fibres after 3 months. Proteins monomers interact with each other forming amorphous aggregates. The change in the structure of the protein in amorphous aggregates may be more difficult and energy comparing with proteins monomers (132). However, Homchaudhuri et al. found that at a pH 12.2, HEWL molecules aggregate and forms amyloid fibrils at room temperature at a concentration of HEWL below 3 μM (98).

They also reported that the aggregation size of HEWL relies on the concentration of HEWL. Increasing the concentration of HEWL yields aggregates species with larger sizes (136). The structure of HEWL changes at pH 12.2, leading to expose the hydrophobic amino acid to solvent. The monomer of these unfolded HEWL interacts with each other via non-covalent interactions causing protein aggregations. The HEWL monomers interact with oligomers or other monomer and leading to an

decrease in the concentration of HEWL monomer with time. At low concertation, the interaction event reduces, leading to form the small size of aggregation. With increasing the concertation of HEWL monomers, interaction event increases leading to form large size of aggregation (98).

Thioflavin T (ThT) is a dye which is used to detect the presence of amyloids fibrils. The fluorescence of ThT enhances when ThT molecules bind to amyloids fibrils. Although traditional method such as ThT has been applied to study protein aggregation in particles amyloid formations, detection at an early stage aggregations such as oligomers is challenging because ThT cannot detect protein unfolding or oligomers (26). As a result, tracking protein aggregation is not an easy task.

The detection of the aggregation of protein in the early stages is necessary for several reasons. First, early diagnosis of amyloid diseases, such as AD, provides effective and lower-cost treatments (140). Second, oligomers are more toxic to cells in comparison to amyloids fibrils (141). One possible method that has not been fully explored is the application of AuNCs.

AuNCs have gained a great deal of attention due to their properties. In order to employ the photoluminescence properties of AuNCs to study protein aggregation, it is essential to comprehend the photoluminescence properties of AuNCs and their behaviours in certain conditions. In the previous study, the photoluminescence properties of AuNCs have been studied using different methods. These include time-resolved photoluminescence spectroscopy, and temperature dependence (142). Other methods used to characterize protein encapsulated AuNCs include (UV-Vis) absorbance measurement and TEM (143–145). These methods help to provide some insight into the photoluminescence properties of AuNCs.

The structure of the AuNCs is commonly noted as their exact formula. In other words, it is represented as $Au_n(SR)_{m,}$ where n and m are the numbers of the gold atom and thiolate ligands, respectively. For example, glutathione-capped [Au_{25} $(SG)_{18}$]. It is preferable to use a formula for AuNCs since the number of Au atoms

and ligands are an extremely crucial factor in the photoluminescence properties of AuNCs. There have been several attempts to propose theories to understand the photoluminescence mechanism for AuNCs. The free-electron theory explains a fundamental concept of the photoluminescence properties of AuNCs. At the size of nanoparticles, AuNPs exhibit plasmonic optics due to the free electrons in the surface of AuNPs. However, when the sizes of AuNPs are reduced to the Fermi wavelength, the energy band splits into an independent energy state. As shown in the following equation:

$$E_\delta = E_F / N^{1/3} \qquad (4\text{-}1)$$

Where E_δ is the numeric size of the energy level spacing (the value of AuNCs), N is the atom number of Au, and E_f is the Fermi energy.

According to the equation (4-1), the photoluminescence emission wavelength depends on the size of AuNCs (57). When the size of AuNCs increases their fluorescence emission wavelength also increases as seen in the PAMAM-AuNCs (57). Moreover, it has been found that the property of the fluorescence can be impacted by the ligand. In the case of thiolate - AuNCs, the outmost Au (Au+) binds to the thiolate ligands on the shell. It has been found that the shell of AuNCs emits light. The photoluminescence of the shell arises from the charge transfer from ligands to metal (LMCT or LMMCT). In particular, the charge transfer is from sulphite to gold (146).

The AuNCs become stable by forming strong covalent bonds between gold and sulphur. This bond significantly influences the electronic structure of AuNCs that cannot be interpreted using free-electron theory only. Therefore, it is proposed that the fluorescence of AuNCs arises from the core of AuNCs and the shell. The second mechanism is reasonable in explaining the QY of AuNCs. It has been found that the QY of AuNCs is dependent on ligands. Some ligands can transfer higher electrons from sulphur to gold compared with other ligands that result in higher fluorescence

intensity (79) as discussed in Chapter 1 (see 1.5: Factors influencing fluorescence properties).

The information contained within photoluminescence properties, such as red emission origination, a bandwidth of photoluminescence intensity and the photoluminescence lifetime of AuNCs, has stemmed from studying BSA-Au_{25}NCs and glutathione Au_{28}NCs. The origination of their red emission is still debated. Some suggest that red emission arises from the transition from the intraband's lowest unoccupied molecular orbital (LUMO) to the highest occupied molecular orbital (HOMO) (147). In contrast, others suggest that it arises from the electron transfer from the interband's 6sp conduction band to the filled 5d band (79,148). Both BSA-Au_{25}NCs and glutathione Au_{28}NCs show two photoluminescence bands. In BSA-Au_{25}NCs, the first band (band I) is at 1.76 eV arising from the electron transition in icosahedral core and the second band (band II) is at 1.94 eV arising from the electron transition in Au-residue shell (142). One of the bands of glutathione Au_{28}NCs is at 1.5 eV which is ascribed to fluorescence and the second band is at 1.15 eV which is ascribed to phosphorescence (147). The difference can be contributed to different ligands.

Wen et al. found that the BSA-Au_{25}NCs have two lifetimes. One is a prompt fluorescence in a nanosecond time scale with a primarily dominant wavelength range of 550 nm to 600 nm. The second is delayed fluorescence in a microsecond time scale with a primarily dominant wavelength range of 650 nm to 800 nm. Delayed fluorescence has two explanations. One explanation is attributed to the excited triplet state (E-type), where the electron transitions from a triplet state to a singlet state through thermal activation. Hence, the lifetime of the delayed fluorescence is equal to the phosphorescence since both the singlet and triplet states are in balanced temperatures. Another possible explanation for the delay in the fluorescence is due to triplet−triplet annihilation (P-type). The lifetime of delayed fluorescence is shorter than the phosphorescence due to the biphotonic process. Wen et al. found that the delayed fluorescence is thermal activation. In

other words, the delayed fluorescence can be ascribed to an excited triplet state (E-type) since the lifetime does not change with excitation fluence, as seen in triplet−triplet annihilation (P-type). In $Au_{25}(SR)_{18}$, the band l arises from an electron transition from LUMO + 1 to HOMO (6sp, delocalized in core) with three degenerated states since the bandwidth of band l is 253.5 meV, whereas band ll arises from LUMO + 2 to HOMO (Au(I)−thiolate complex with 5d electron structure) with one state (142). The increase in the bandwidth of band l is derived by the thermal population through reverse ISC (149).

The long lifetime can arise due to the presence of Au-S bonds. It was found that Au(I) can form complex and triplet states; therefore, BSA-Au_8NCs does not show long lifetimes since the formation of Au(I)-S semirings does not occur in BSA-Au_8NCs (150). Despite the fact that the transition in the triplet is forbidden, the strong metal-induced spin−orbit coupling helps to increase intersystem crossing efficiency by reducing the effect of the spin-forbidden transition occurring in the relaxation of the triplet (149).

Understanding the fluorescence properties of Lyz-AuNCs allows for the extension of their application. In this chapter, the fluorescence properties of AuNCs will be studied under two conditions. The first condition is the different pH. The second condition is the different concentrations of HEWL. This research aims to test the sensitivity of the Lyz-AuNCs to environmental changes and protein aggregations to understand the behaviours of AuNCs. The finding shall shine a light to their applications in future studies of protein aggregations.

4.3 Experimental

4.3.1 Sample Preparation

Lysozyme from chicken egg whites (L-6876) (>99.0%), gold (III) chloride trihydrate (>49.0%), phosphate buffered saline (PBS) and sodium hydroxide (NaOH) solution (1.0M) were purchased from Sigma-Aldrich. Hydrochloric acid (HCl) solution (0.5M) was purchased from Fluka.

Before the synthesis of Lyz-AuNCs, all glassware was soaked in decon 90 overnight. Methanol and deionized water were then added, and the glassware was cleaned with a brush. After that, the glassware was washed twice using methanol and deionized water. Next, they were rinsed with deionized water. Finally, the glassware was left to dry.

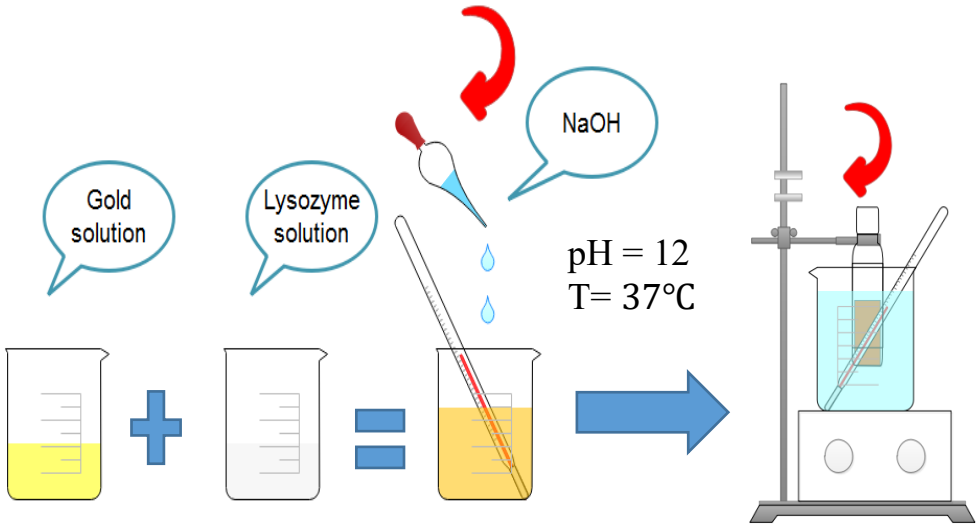

Figure 4.1: Illustration of the synthesis of Lyz-AuNCs.

The preparation of the Lyz-AuNCs was done according to studies by Hui Wei et al., with slight modifications (32,77). A 5ml HEWL solution (10 $mgml^{-1}$) was mixed with a 5ml $HAuCl_4$ solution (4mM) and stirred strenuously by a stirrer bar at 37°C. Five minutes later, 0.5ml NaOH (1M) was added to the mixture, causing an increase of the pH up to 12. The solution was kept at 37°C overnight. The final product is stock Lyz-AuNCs solution (0.33 mM, 10.5 ml) with pH 12. Figure 4.1 shows the steps in the synthesis of the Lyz-AuNCs. After mixing $HAuCl_4$ solution with HEWL, the colour of solution changed from yellow to light brown. The yellow solution does not show red fluorescence emission under UV light (33). However, the light brown solution shows red fluorescence emission under UV light after 12 h which is a characteristic of Au_{25}NC as shown in fig 4.2. The peak fluorescence intensity of Lyz-AuNCs at 700 nm at excitation 470 nm. In the previous study, the peak fluorescence intensity of Lyz-AuNCs at 657 nm at excitation wavelength 360 nm (32), 636 at 657 nm at excitation wavelength 400 nm (77). Possibly the different in our result is due

to using a different concentration of both HEWL and $HAuCl_4$ solution. In the literature, The peak fluorescence emission is the characteristic of AuNC can be in range from 640-700 nm (151). In particular, it was observed in the synthesis of BSA-Au_{25}NCs (96,150).

After 12 hours, the next step was to perform the dialysis of the Lyz-AuNCs in order to remove excess chemicals. A 3-12 ml cassette size with a membrane molecular-weight cut-off (MWCO) of 10,000, as obtained from Thermo Fisher Scientific, was selected to perform dialysis of 10 ml of Lyz-AuNCs. The dialysis procedure of Lyz-AuNCs was performed according to Thermo Fisher Scientific (152) recommendations as follows. The buffer for the solution was prepared by dissolving nine tablets of phosphate buffered saline (PBS) in 1.8 litres of distilled water in a 20 litres glass beaker. According to the procedure of dialysis, the volume of the buffer should be 200-500 times higher compared to the sample volume. The dialysis cassette was removed from a plastic bag and then attached to a buoy. Then the dialysis cassette was immersed into the buffer for two minutes. Next, the dialysis cassette was removed from the buffer and tapped gently on paper towels to remove any excess solution.

The next step in the dialysis process was to fill the dialysis cassette with Lyz-AuNCs. The needle was attached to the syringe and then filled the dialysis cassette with Lyz-AuNCs and a small amount of air. Next, the syringe was inserted on a top corner of the dialysis cassette to fill it with Lyz-AuNCs. After emptying the syringe from the Lyz-AuNCs, all the air was removed from the dialysis cassette. Then the dialysis cassette was slipped into the buoy and immersed the dialysis cassette in the buffer solution. A long magnetic bar stirrer was used to stir the dialysis cassette in the buffer. Every two hours, the buffer was changed, and upon the third immersion, the dialysis cassette was stored overnight. The final stage was to remove the Lyz-AuNCs from the dialysis cassette using a syringe. The syringe was filled with a small amount of air, then inserted the syringe in the top corner of the dialysis cassette and injected air slowly into the cassette. After that, the dialysis cassette was turned

until the syringe is in the bottom corner. In this position, the sample was collected in the corner of the dialysis cassette, and it was easy to pull all the Lyz-AuNCs and place them in the 30 ml bottle to be ready for use. The pH of Lyz-AuNCs was changed from pH 12 to 7.4 dialysis

Assuming that the concentration of Lyz-AuNCs did not change after the dialysis. For measurement purposes, the Lyz-AuNCs was diluted to final concentration 33 µM and filled to 3 ml in 1 cm X 1 cm in a quartz cuvette since a plastic or glass cuvette absorbed UV light. Its pH was varied by adding hydrochloric acid and sodium hydroxide. The pH was measured using a F-51 pH meter purchased from HORIBA. The concentration of Lyz-AuNCs did not change when hydrochloric acid (sodium hydroxide) was added because the volume of hydrochloric acid (sodium hydroxide) is small volume in µM compared to the volume of Lyz-AuNCs. For studying the effect of adding HEWL on fluorescence properties of Lyz-AuNCs, HEWL was dissolved in 3 mL of Lyz-AuNCs solution. The weight of HEWL was varying from 15 mg to 105 mg with increments were 15 mg. All the sample measured at room temperature. More detail is added in a appendix 1.

4.3.2 Spectroscopic Measurements

All the UV-Vis measurements were done using the PerkinElmer UV/VIS spectrometer Lambda 25. The UV/VIS range of the electromagnetic spectrum covered the range of 250 – 700 nm with a speed scan of 480 nm/minute. The data were analysed using the spectrograph version 1.2.7.

All fluorescence emissions of the Lyz-AuNCs were measured by using Fluorolog-3 spectrometer (Horiba, UK). The experimental design used excitation wavelength was 470 nm, and slit widths were 6 nm, and the emission wavelength was measured at a range of 500 to 850 nm with 6 nm increments. Data were analysed using Origin Pro software version 9.6.5169.

The Time-Resolved Fluorescence spectrometer with the time-correlated single-photon counting (TCSPC) technique in a Horiba Jobin Yvon IBH was used to measure

fluorescence lifetimes, emission spectra and the anisotropy decay of Lyz-AuNCs. The instrument contains a DeltaFlex hybrid (Horiba Scientific), motorised polarisers and a Horiba TBX-580c photon-detection module. The excitation source was a pulsed Delta Diode of 482 nm, with a temporal width of 50 ps (full width at half maximum) and a repetition rate of 100 MHz, operating with a delay of 10 ns and a coaxial delay of 95 ns. The excitation polariser was kept at angle 0^0 and the emission polariser at a magic angle 55^0 to avoid anisotropy effects during the lifetime measurement and time-resolved emission spectra (TRES). A decay curve was accumulated until 10,000 counts, and the tag range was 13 μs. TRES was obtained by using a single excitation wavelength at 482 nm and selecting the range of emission wavelength from 500-800 nm. Increments were 20 nm and the fixed time interval was 20 minutes. Data were analysed with Horiba Scientific DAS6 version 6.8.16.

The fluorescence intensity decays for the Lyz-AuNCs was analysed with the following formula:

$$I(t) = \sum_{i=1}^{n} \alpha_i e^{\left(\frac{-t}{\tau_i}\right)} \quad (4\text{-}2)$$

Where α_i denotes the amplitudes, and τ_i is the lifetime.

The amplitudes was calculated using Equation (4-3).

$$\sum_i \alpha_i = 1 \quad (4\text{-}3)$$

4.4 Results and Discussion

After 12 hours, the colour of the reaction changed from light yellow to a light brown, indicating synthesis of the AuNCs. Figure 4.2 shows the Lyz-AuNCs under light and UV-Vis light.

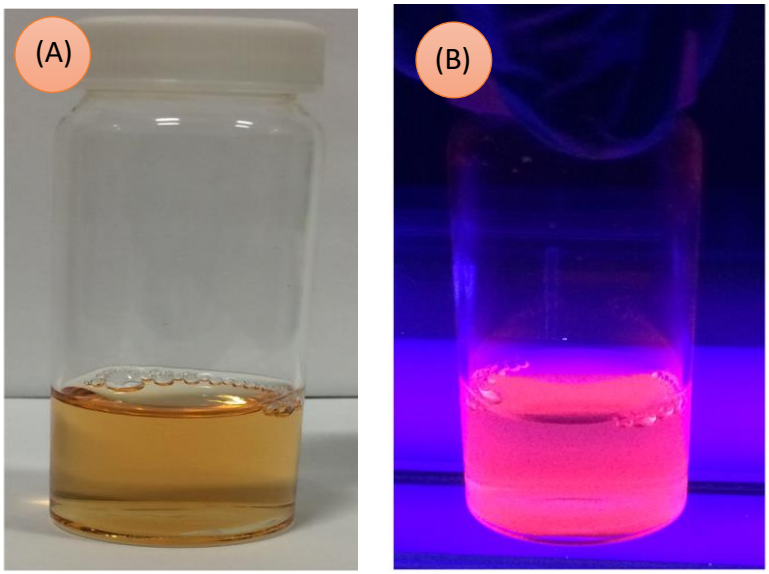

Figure 4.2:Photographs of Lyz-AuNCs (A) visible and (B) UV light.

4.4.1 Effect of pH on Lyz-AuNCs

The effect of pH on the optical properties of the Lyz-AuNCs is studied at various pH from 1.6 to 12. Figure 4.3 (A) shows the UV-Vis spectra of Lyz-AuNCs at different pH. There was no peak around 520 nm, indicating that there are no AuNPs formed during the synthesis of AuNCs. There was no change in the absorption of Lyz-AuNCs at pH from 1.6 to 3 and from 7 to 12. An increased absorbance was observed at pH 6, and decreased absorbance was found at pH 4 and 5.

These observed changes were due to the fact that the pH was near the isoelectric point (pI) of Lyz-AuNCs that was found to be 5.5 (67). The pI is the pH of the protein solution at which the total charges on the protein's surface are zero. As a pH below pH 5.5, a repulsive interaction occurs between proteins due to the positive charges on the protein's surface. In a similar manner, above pH 5.5, negative charge on the surface of protein increases as pH increase, leading to a repelling action in each protein (135). These repulsive forces decrease as pH approaching pI. At the pH closes to pI, near neutral net surface charge results in aggregation and precipitation that reduces the concentration of Lyz-AuNC in solution and its absorbance. The aggregation of protein in suspension also results in

an increase in scattering, thus increases the absorption as seen for Lyz-AuNC at pH 6.

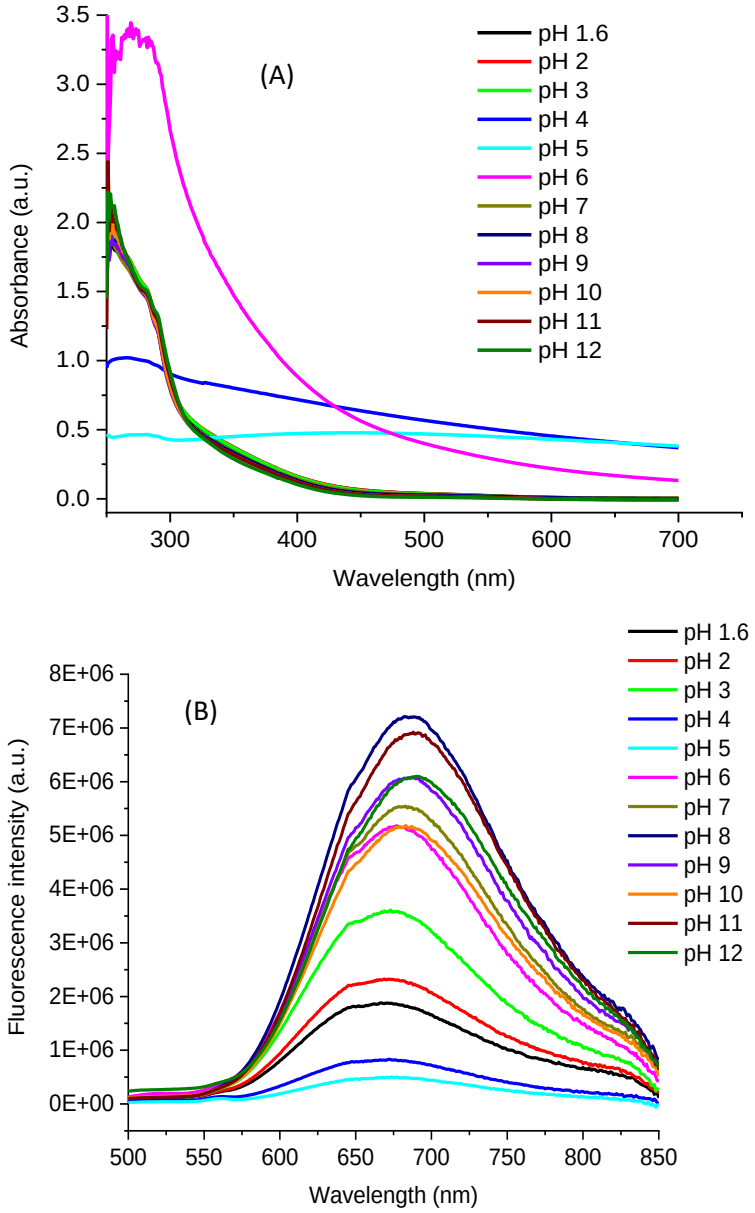

Figure 4.3: The change in (A) Absorption spectra and (B) Fluorescence emission spectra of Lyz-AuNCs with an increase in the pH at excitation wavelength is 470 nm**.**

Figure 4.3 (B) shows the fluorescence spectra of Lyz-AuNCs at an excitation wavelength of 470 nm at different pH. A single peak centred at 700 nm at pH 7 is due to the emission of AuNCs.

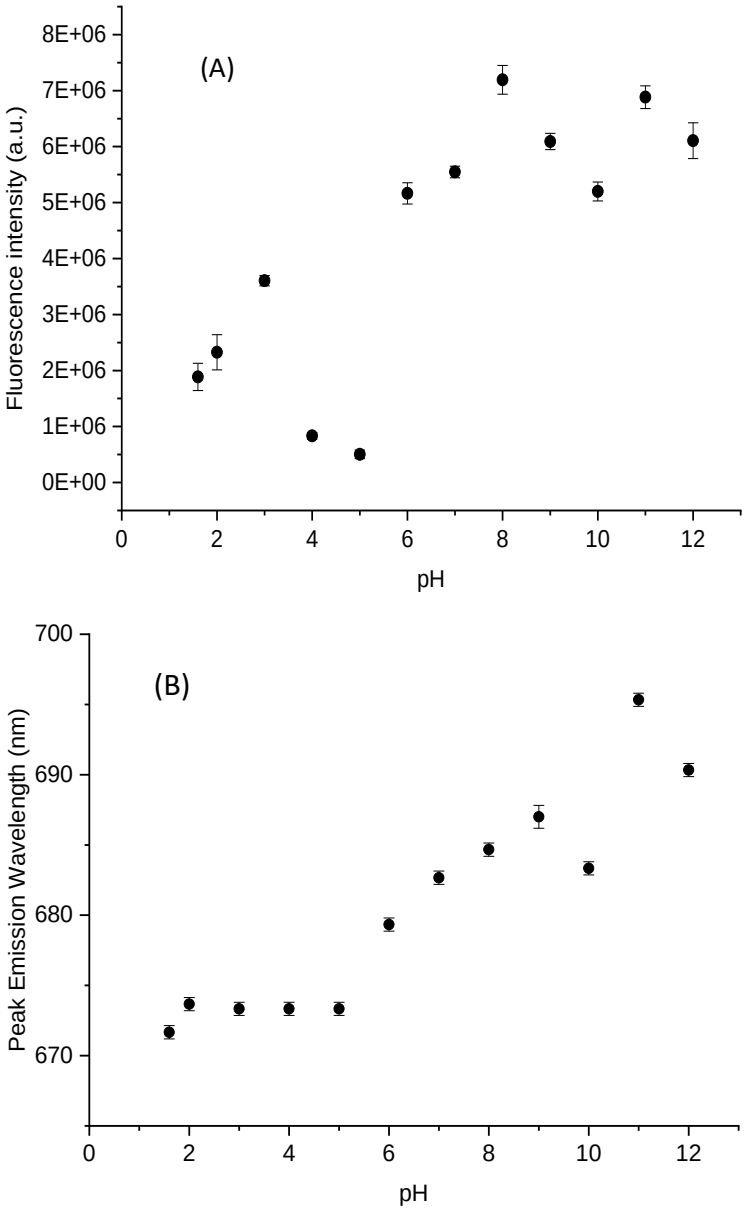

Figure 4.4: pH dependence of (A) peak fluorescence emission and (B) peak emission wavelength. Measured at an excitation wavelength is 470 nm.

Figure 4.4 (A) shows the peak fluorescence intensity of AuNCs at 700 nm as a function of pH. The peak fluorescence intensity of AuNCs increase with increasing the pH. As the pH increase from 1.6 to 3, the fluorescence intensity of the AuNCs increase by 66%. As the pH increase from 3 to 5, the fluorescence intensity of the AuNCs decrease by 85% of the fluorescence intensity at a pH of 7 consistent with the decreases of absorbance observed in Figure 4.3 (A). As the pH increase from 5 to 7, the fluorescence intensity of the AuNCs increase by 83 %. As the pH increases

from 7 to 12, the fluorescence intensity of the AuNCs fluctuates. In Figure 4.4 (B) there is no change in the peak emission wavelength of the AuNCs as the pH increases from 1.6 to 5. The peak emission wavelength then increases around 17 as the pH rises from 5 to 12.

The effect of pH on the fluorescence properties of the AuNCs has been studied in by Cao et al. (153). They found that at an excitation wavelength of 500 nm, the fluorescence intensity of the AuNCs increases when the pH rises from 2 to 11, while the peak emission wavelength slightly changes from 2 to 9. There are significant increases around 12 nm from a pH of 9 to 12 (153).

The large redshift in fluorescence emission due to pH has also previously been observed for BSA-Au_{25}NCs by Wen et al. (154). The redshift in the fluorescence emission wavelength can be due to a Quantum Confined Stark Effect (QCSE). QCSE is the shifting of electrons in a quantum well to lower discrete energy in the presence of an external electric field while increasing the discrete hole states of a system to higher energies (154).

Due to the polar nature of the Lyz-AuNCs molecules and the highly negative zeta potential of Lyz-AuNCs previously reported being greater than negative 60mV below pH 11 (155). It is possible the redshift is governed by the polar characteristics of QCSE which have been observed arising in similar fluorescence quantum dot systems (156–158). However, the fluorescence intensity would be expected to decreases if QCSE was the reason for the observed fluorescence redshift for Lyz-AuNC. It has been shown that the fluorescence intensity of the InGaN quantum dot decreases as the external lateral electric field increases (157).

Wen et al. have also observed a two-band fluorescence emission from BSA-Au_{25}NCs, describing the AuNC with a “core/shell” fluorescence model derived from thiolate-protected Au_{25} in which the core and shell are each responsible for a fluorescence band which makes up the red fluorescence peak (54,142,159). This core/shell structure originates from the metal core state and surface states of the SR – Au – SR – Au – SR staples, respectively. AuNC in BSA binds to sulphur (S) atoms

(via cysteine) but with a much-reduced number than that in thiolate-protected Au_{25} (96). Although the exact atomic structure is unknown, S-Au bonds (and possible bonds of gold to other neighbouring amino acids) form a motif that stabilizes the gold core. It is plausible that two emission bands have different structural characteristics and different sensitivity to local environmental changes.

In terms of exploring the effect of pH on the fluorescence properties of Lyz-AuNCs, the lifetime measurement of Lyz-AuNCs as a function of pH was performed at an excitation wavelength of 470 nm and an emission wavelength of 650 nm. The fluorescence decay of Lyz-AuNCs was fit to an exponential of three. The good fit was tested by chi-squared goodness of fit parameter and the values of amplitudes. The figure 4.5 shows the fluorescence decays curve of Lyz-AuNCs (red decays curve) and fit with three exponential (black line). A non-random weighted residuals for 3 exponential fitting to a fluorescence decay curve of Lyz-AuNCs is shown below the fluorescence decay curve. The results are shown in Table 4.1.

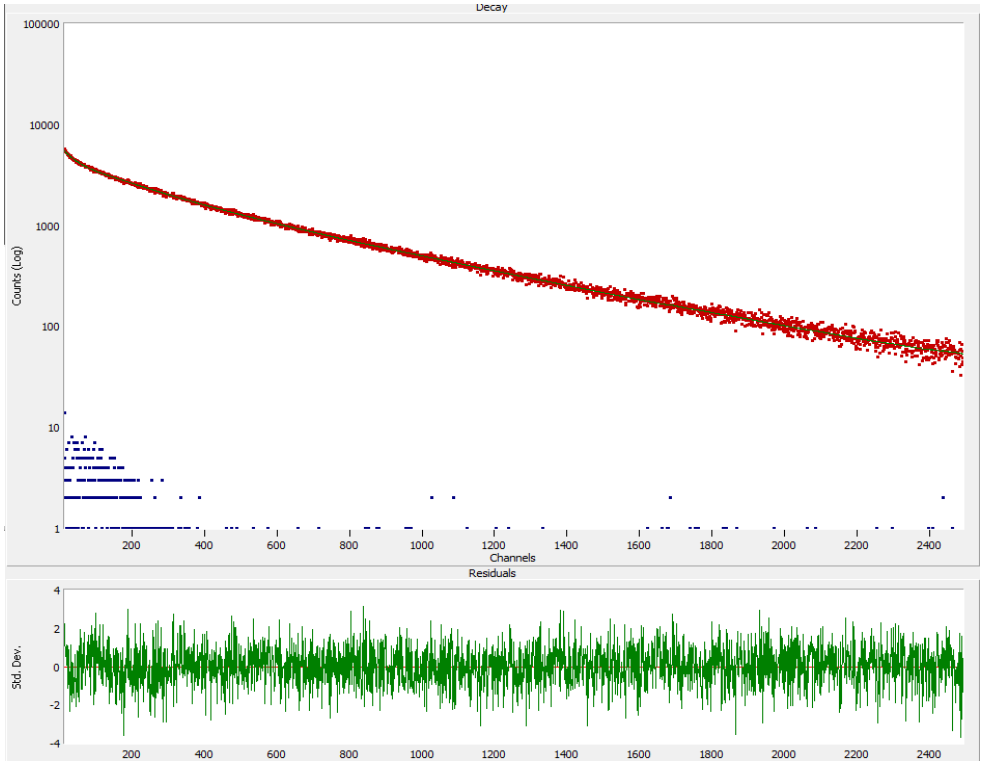

Figure 4.5: The fluorescence decay of Lyz-AuNCs at pH 7 was analysed using DAS6 and fit to an exponential of three. The prompt (blue), fluorescence decay (red) and the solid (black) line is a fitting function.

Table 4.1. Fluorescence lifetimes of AuNCs emission τ and amplitudes α as a function of pH. Measured at an excitation 482 nm.

pH	τ_1 (ns)	α_1	τ_2 (ns)	α_2	τ_3 (ns)	α_3	χ^2
1.6	2222 ± 12	0.76	647 ± 31	0.21	96 ± 5	0.03	1.10
2	2314 ± 14	0.72	746 ± 31	0.24	103 ± 4	0.04	1.07
3.5	2069 ± 7	0.75	681 ± 24	0.21	124 ± 4	0.04	1.05
7	2057 ± 7	0.72	723 ± 23	0.24	128 ± 4	0.04	1.06
8	2117 ± 8	0.73	804 ± 35	0.24	139 ± 5	0.03	1.07
9	2074 ± 8	0.74	721 ± 27	0.23	102 ± 5	0.03	1.07
10	2048 ± 8	0.73	763 ± 29	0.23	133 ± 5	0.04	1.05
11	2046 ± 8	0.71	808 ± 27	0.25	139 ± 4	0.04	1.09
12	2037 ± 9	0.70	851 ± 32	0.27	148 ± 5	0.03	1.03

The fluorescence lifetimes of protein encapsulated AuNCs are 2 exponential in nature (96,143,160,161), which compares well to the idea of a two band fluorescence emission model. Due to the structure of protein encapsulated AuNCs which consists of icosahedral core and Au-residue shell, the fluorescence emission is ascribed from both icosahedral core with a short lifetime and Au-residue shell with long lifetime. Therefore, the fluorescence decay of Lyz-AuNCs was fit with three exponential using equation (4-2). The third lifetime in our measurement can be attributed to the light scattering from the sample. The long lifetime of 2057±7 ns arises from band ll (the shell), while the short lifetime of 723±23 ns arises from band l (the core), similar to BSA-Au_{25}NCs at a pH of 7 (96).

It was found in figure 4.6 and table 4.1 that as the pH is increased from 1.6 to 12, the long lifetime τ_1 decreases from 2.4 to 2.0 μs, while the short lifetime τ_2 slightly increases but remains within the uncertainty associated with the measurement. This has been previously observed in BSA-Au_{25}NCs (96) where changing pH results in protein unfolding, thus changing the local environment of the AuNCs. HEWL is more

rigid than BSA, but AuNC is more exposed to the solvent in comparison to that in HSA and is, therefore, more sensitive to pH variation.

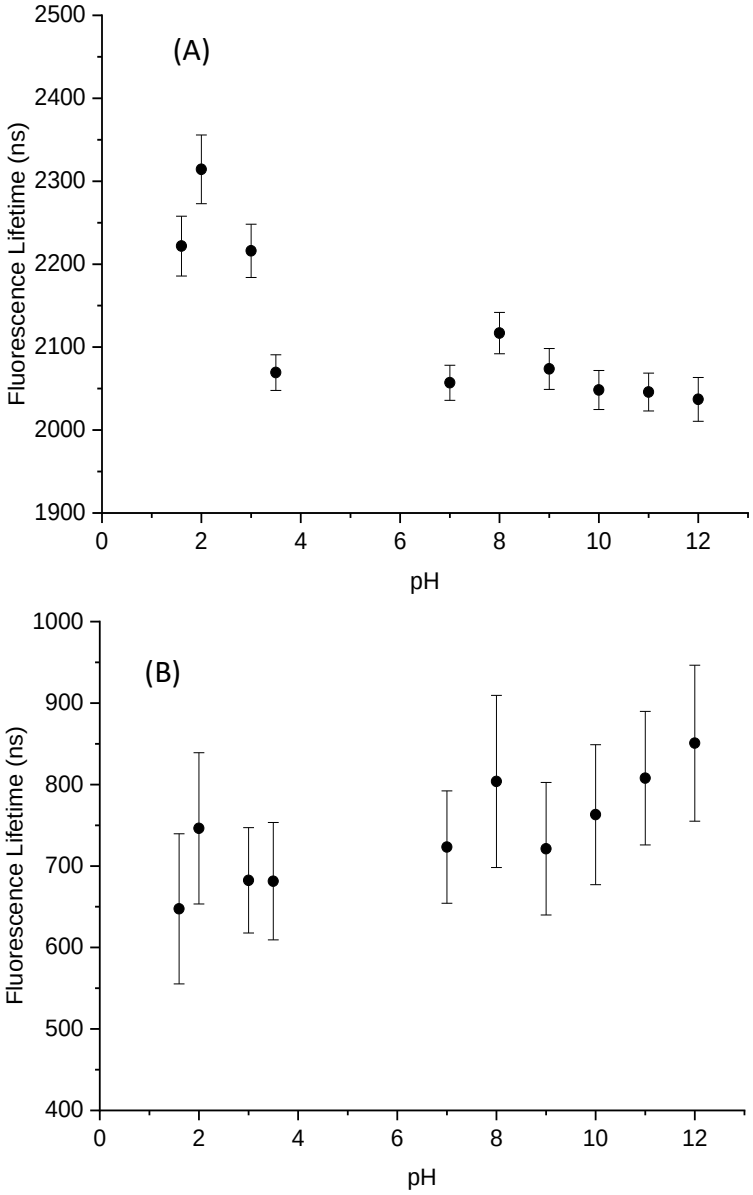

Figure 4.6: The fluorescence lifetime of AuNCs in the Lyz-AuNCs at an excitation wavelength 470 nm, emission wavelength of 670 nm. Long lifetime τ_1 originated from the shell (A) and short lifetime τ_2 originated from the core (B) as a function of pH. (The error bars are 3*S.dev).

Only one fluorescence lifetime component is observed to be significantly affected by changing pH. The increase in the fluorescence intensity correlated to the decrease of fluorescence lifetime suggests that this is not due to a reduced

collisional quenching effect but possibly a mechanism of enhanced radiative process arising in a basic environment.

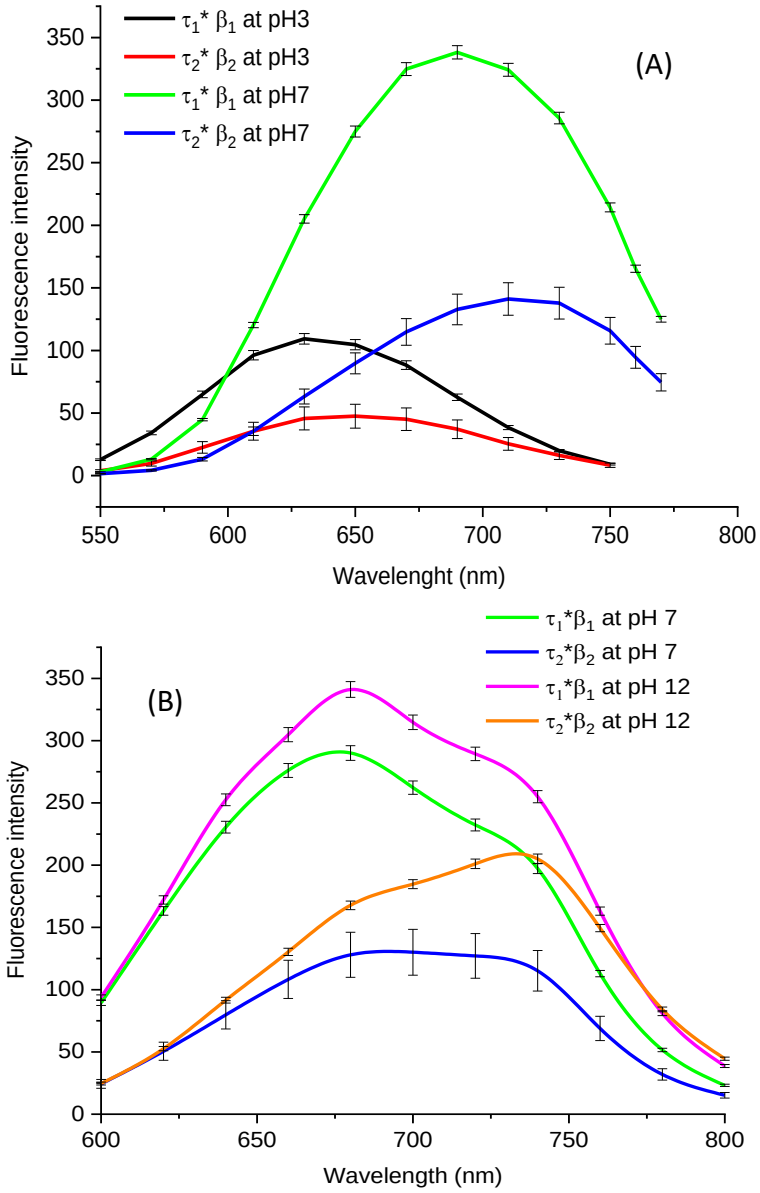

Figure 4.7: The TRES measurement of Lyz-AuNCs at pH 3 (A) and pH 12 (B) compared with pH 7.

To further understand the correlation between the two fluorescence components and the overall increase in intensity and redshift previously observed, TRES measurements were taken of Lyz-AuNCs emission at pH 7, 3 and 12, as shown in Figure 4.7. The structure of HEWL changes at both the pH of 3 and the pH of 12. The pH of 7 is chosen as a reference because HEWL maintains its natural structure.

Interestingly the TRES show both components increase in intensity and redshift as pH change from 3 to 7, despite the decrease in fluorescence lifetime for the longer-lived fluorescence component. Previously, changes in the relative intensity of the two bands at different pH were observed (96). TRES of BSA-Au_{25}NCs has shown two emission bands of 650 nm and 680 nm corresponding to $\tau_1 = 2.40\ \mu s$ and $\tau_2 = 1.17\ \mu s$ at pH 12, and emission bands at 620 nm and 640 nm with corresponding to lifetimes of $\tau_1 = 4.46\ \mu s$ and $\tau_2 = 1.94\ \mu s$ (96) at pH 3.

Figure 4. 7 (B) shows that two components increases in intensity and redshift as the pH goes up from 7 to 12. The fluorescence intensity at pH 3 is lower compared to that at pH 7 and pH 12. This finding coincides with lifetime measurements of the Lyz-AuNCs, where lifetime at pH 3 is longer than that at pH 7 and pH12. It is possible that a decrease in the lifetime leads to an increase in the radiative rate, hence increasing the fluorescence intensity.

4.4.2 Effect of HEWL Concentration on Lyz-AuNCs

To test the sensitivity of Lyz-AuNCs fluorescence to native protein interactions, 3 mg of HEWL was added to 3 ml of diluted 10% Lyz-AuNCs at different pH, as shown in Figure 4.8.

It was found that the samples at pH range between 11 and 4 were not stable as precipitation observed as shown in Figure 4.8. Moreover, the structure of HEWL does not change as the pH level increases from 4 to 11. It has two transition points. One point is at an acidic pH level below 4 (162,163) and the second point is at an alkaline pH level above 11 (164). Both transition points cause the protein to unfold. Therefore, we conducted the experiment at pH 12.5 and 3 not only because samples are stable but also because HEWL changes its structures and aggregation states at these pH conditions.

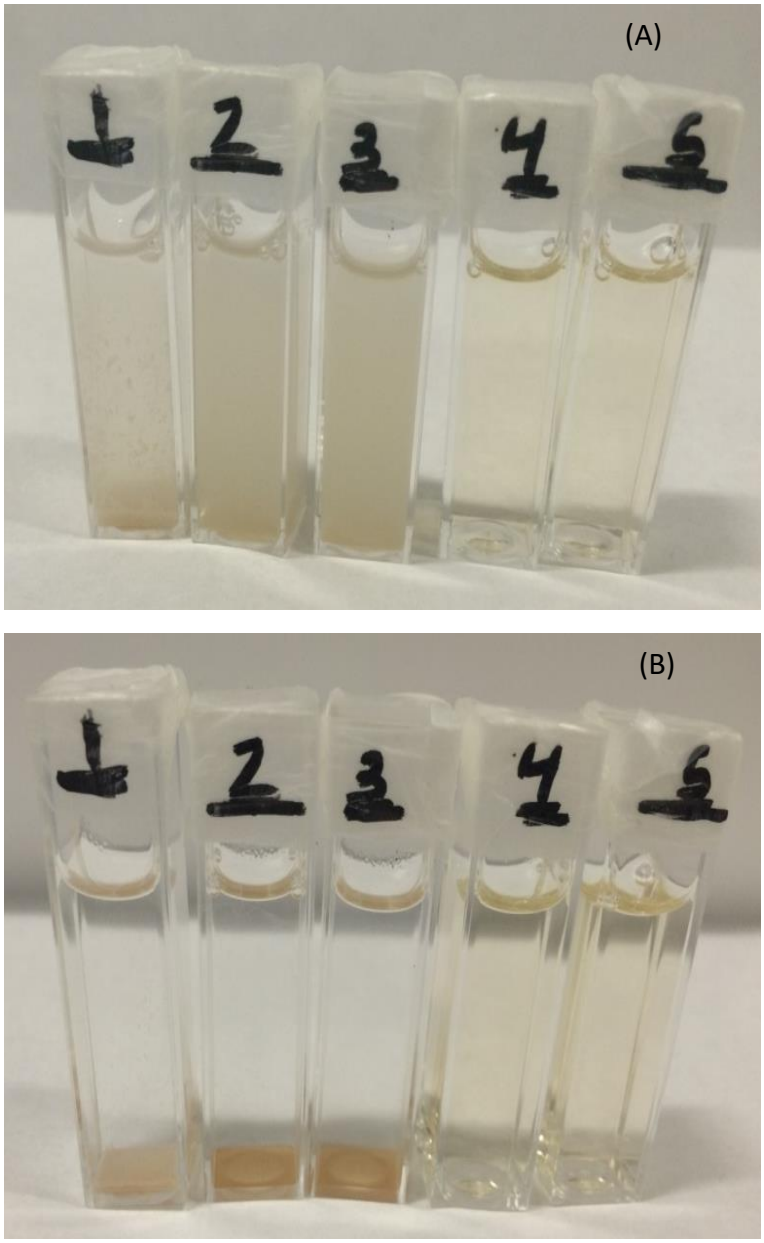

Figure 4.8: HEWL dissolved in Lyz-AuNCs with final concentrations of 1 mg/ml and 0.47 mg/ml, respectively. (A) and (B) illustrate the sample after one hour and 24 hours of adding HEWL. pH of samples from 1 to 5 are pH 10, pH 9, pH 7, pH 2.5 and pH 3.

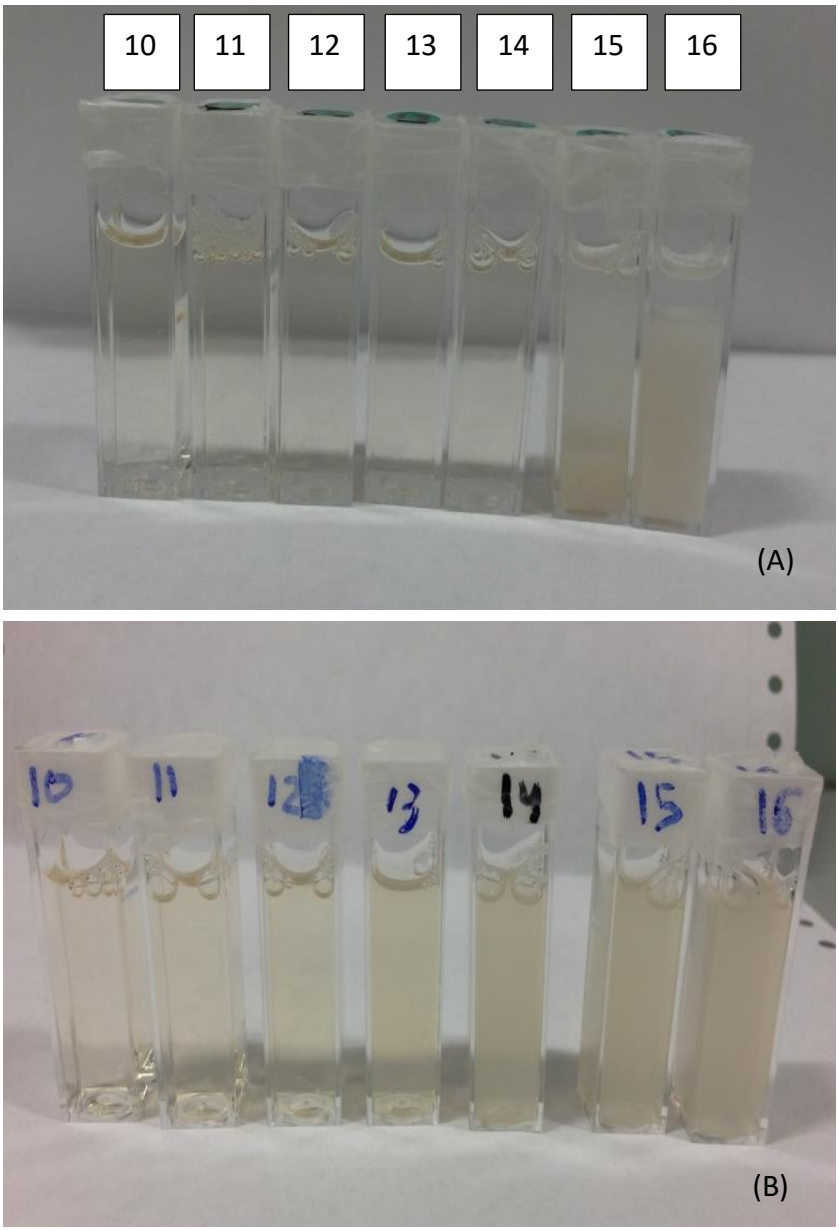

Figure 4.9: Lyz-AuNCs at different concentrations of HEWL from 0 to 35 mg/ml at pH 12.5 (A) and pH 3 (B).

Figure 4.9 (A) shows that the sample of Lyz-AuNCs after dissolve HEWL at pH 12.5 did not change until the concentration of HEWL reaches 30 mg/ml (sample number 15). Figure 4.9 (B) shows that sample of Lyz-AuNCs after dissolving HEWL at pH 3 changes at the concentration of HEWL reach 10 mg/ml (sample number 12). As the concertation of HEWL increases the aggregation increases.

The surface charge on the Lyz-AuNCs and HEWL plays a significant role in stabilizing the sample and preventing aggregation. Sample with a high net negative (positive) charge on the surface presents large negative (positive) zeta potential and repulsive forces. These repulsive forces prevent the formation of aggregation (135). The sample is soluble when the zeta potential is higher (lower) than +30 mV (-30 mV) (165).

The zeta potential of both HEWL and Lyz-AuNCs was studied by Russel et al. (166). It was found that the zeta potential of HEWL and Lyz-AuNCs are around 30 mV and 20 mV at pH 3. The isoelectric point of HEWL is 11.35 (98), and the isoelectric point of Lyz-AuNCs is 5.5 (67,155). When increasing the pH up to 11, the surface charge of HEWL becomes close to zero, and the surface charge of Lyz-AuNCs becomes approximately -60 mV (155). Therefore, the interactions between HEWL and Lyz-AuNCs are different at pH 3 and pH 12.5. At pH 12.5, no aggregation occurs at a concentration below 30 mg/ml due to the large repulsive force between HEWL and Lyz-AuNCs. At a pH 3, aggregation occurs at HEWL increases from 10 mg/ml, since the repulsive forces between HEWL and Lyz-AuNCs are weak.

The fluorescence emission characteristics were monitored upon introducing increasing concentrations of HEWL to the solution. The Lyz-AuNCs were excited at 470 nm, and small increments of HEWL were added; the results are shown in Figure 4.10.

A small and gradual increase in fluorescence emission was observed at pH 3. A red-shift in fluorescence emission wavelength was observed upon first adding 5 mg/ml HEWL to solution from 673 nm to 678 nm. Further increases in HEWL concentration in solution yielded no clear further changes in fluorescence wavelength. No clear trend was evident for changes observed with the sample at pH 12.5. Clearly, fluorescence emission intensity characteristics were not as sensitive or as unambiguous a method of probing protein/protein interactions where precipitation due to the formation of large aggregates results in changes in particle concentration. Therefore, fluorescence emission lifetimes were studied

upon adding HEWL to Lyz-AuNCs to determine any sensitivity of Lyz-AuNCs to protein/protein interactions at both pH 3 and pH 12.5.

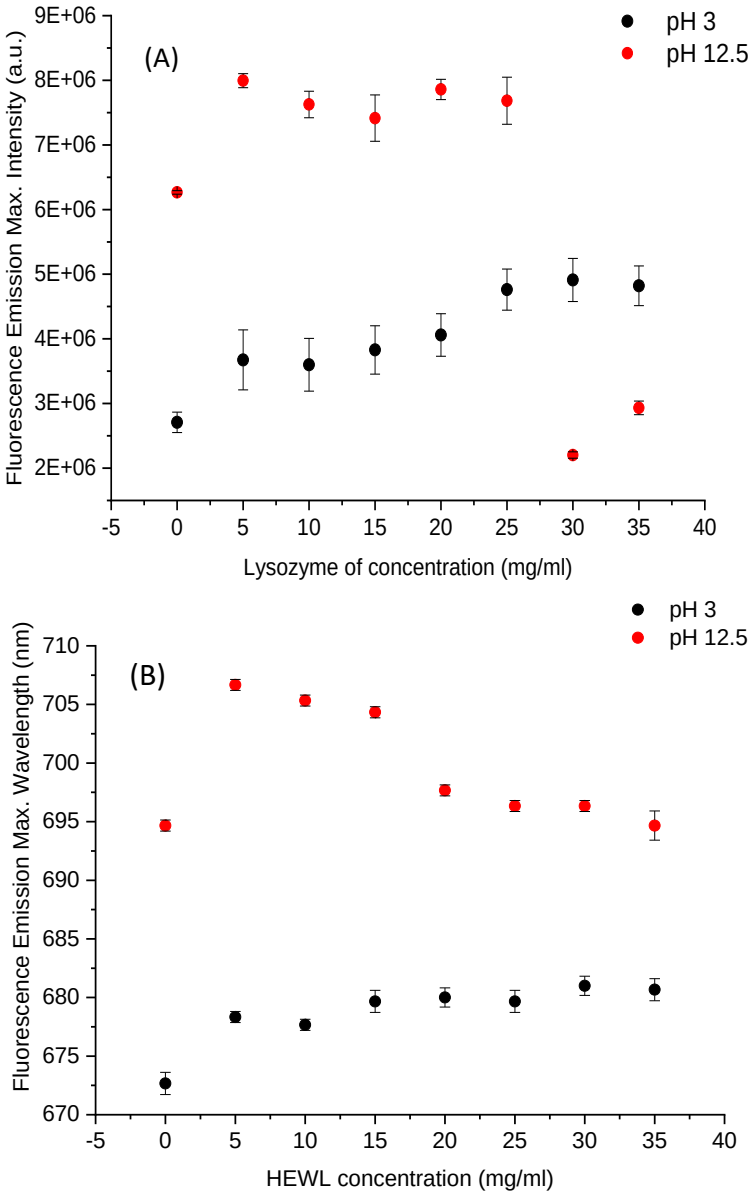

Figure 4.10: Fluorescence emission maximum intensity of Lyz-AuNCs (A) and fluorescence emission maximum wavelength (B) at different pH (pH 3 indicated in black, pH 12.5 indicated in red) as a function of HEWL addition in solution. Measured at an excitation wavelength is 470 nm.

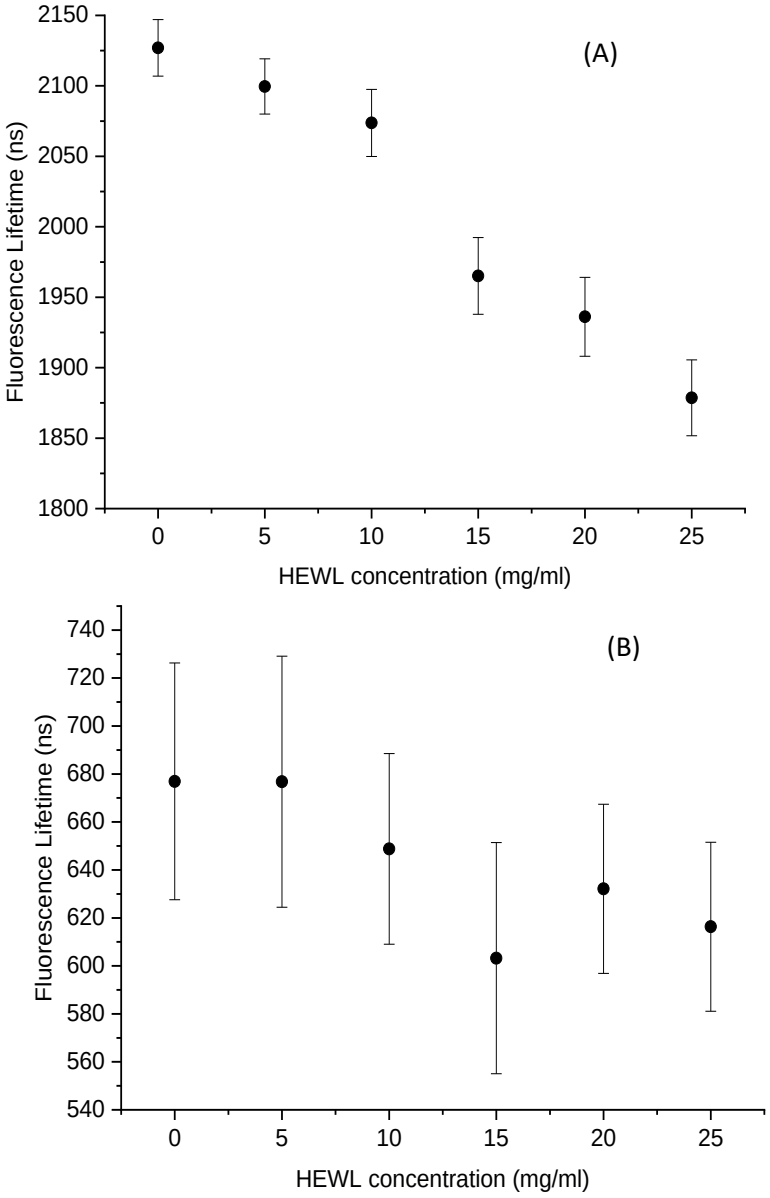

Figure 4.11: Fluorescence lifetime of Lyz-AuNCs as a function of HEWL concentration at an excitation wavelength of 470 nm. (A) and (B) represent long and short lifetimes at pH 3. (The error bars are 3*S.dev).

Table 4.2. Fluorescence lifetimes of AuNCs emission τ and amplitudes α as a function of HEWL concentration at pH 3. Measured at an excitation wavelength of 482 nm.

[HEWL] (mg/ml)	τ_1 (ns)	α_1	τ_2 (ns)	α_2	τ_3 (ns)	α_3	χ^2
0	2127 ± 7	0.71	677 ± 16	0.25	100 ± 3	0.04	1.04
5	2099 ± 6	0.74	677 ± 17	0.23	101 ± 3	0.03	1.00
10	2073 ± 8	0.62	649 ± 13	0.33	110 ± 3	0.05	1.07
15	1965 ± 9	0.59	603 ± 16	0.35	110 ± 4	0.06	1.01
20	1936 ± 9	0.52	632 ± 12	0.41	113 ± 3	0.07	1.12
25	1878 ± 9	0.47	616 ± 12	0.45	114 ± 3	0.08	1.14

The lifetimes of Lyz-AuNCs as a function of HEWL concentration was measured at both pH levels of 12.5 and 3. At a pH level of 3, HEWL concentrations higher than 25 mg/ml were avoided since large aggregations cause precipitation, leading to complications in lifetime measurement. Fluorescence lifetimes were estimated using three exponential models, as shown in Table 4.2 and Table 4.3. Figure 4.11 and Figure 4.12 depict the two lifetime components of AuNCs emission as a function of HEWL concentration at pH 3 and pH 12.5.

It was found that at pH 3 the longer fluorescence lifetime,τ_1, linearly decreased from 2.13 μs to 1.88 μs between 0 and 25 mg/ml added. No changes in τ_2 at pH 3 as lysozyme is added to the Lyz-AuNCs solution were detected within the measurement error, as shown in Figure 4.11, and table 4.2. At pH 12.5, both fluorescence lifetimes were observed to be unaffected by the addition of HEWL to the Lyz-AuNCs solution, as shown in Figure 4.12, and table 4.3. Again, it is the long lifetime component which is sensitive to environmental changes at pH 3. The lack of sensitivity at pH 12.5 suggests that the interaction between Lyz-AuNCs and HEWL does not affect the micro-environment in which the AuNCs is located within the Lyz-AuNCs complex.

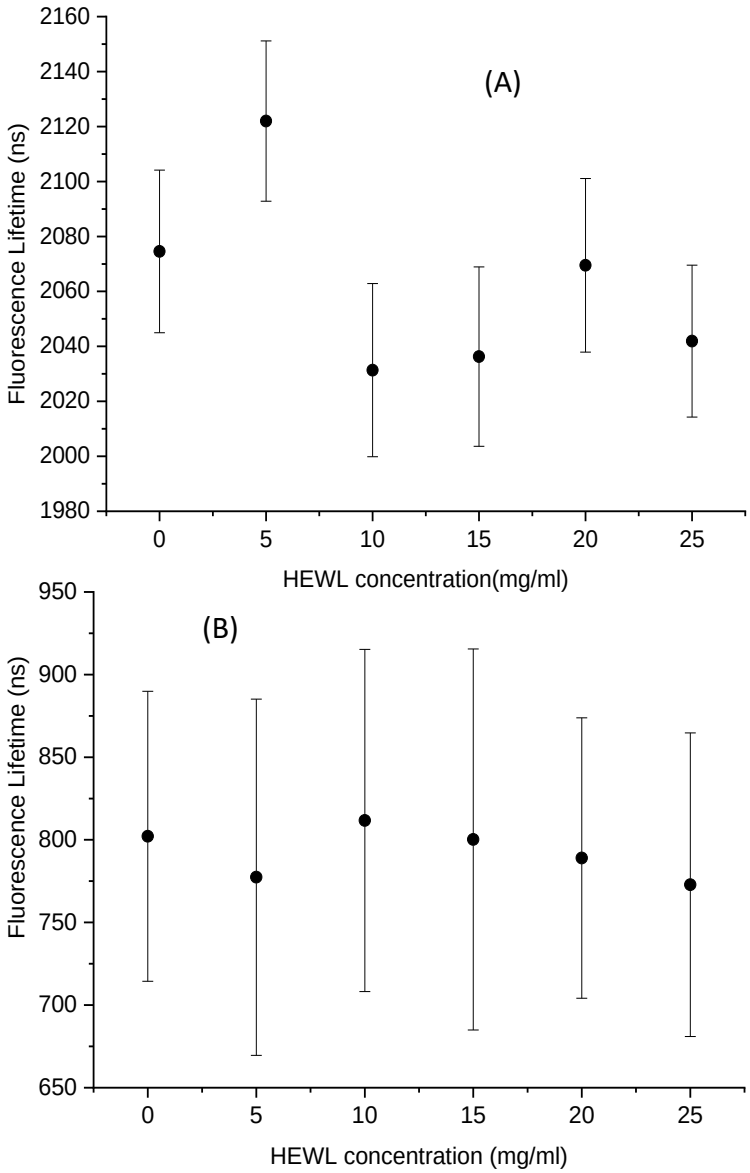

Figure 4.12: Fluorescence lifetime of Lyz-AuNCs as a function of HEWL concentration at an excitation wavelength of 470 nm. (A) and (B) represents long and short lifetimes at pH 12.5. (The error bars are 3*S.dev).

Table 4.3. Fluorescence lifetimes of AuNCs emission τ and amplitudes α as a function of HEWL concentration at pH 12.5. Measured at an excitation wavelength of 482 nm.

[HEWL] (mg/ml)	τ_1 (ns)	α_1	τ_2 (ns)	α_2	τ_3 (ns)	α_3	χ^2
0	2074 ± 10	0.68	802 ± 29	0.28	138 ± 5	0.04	1.08
5	2122 ± 10	0.77	777 ± 36	0.20	118 ± 6	0.03	1.08
10	2031 ± 10	0.69	812 ± 35	0.27	145 ± 6	0.04	1.03
15	2036 ± 11	0.70	800 ± 38	0.26	136 ± 6	0.04	1.02
20	2069 ± 11	0.70	789 ± 28	0.27	119 ± 5	0.03	1.03
25	2041 ± 9	0.73	773 ± 31	0.24.	116 ± 5	0.03	1.02

Time-resolved fluorescence anisotropy of the Lyz-AuNCs at pH 3 and pH 12.5 in the presence and absence of HEWL was carried out to observe whether aggregation took place. Previous studies reported a loss of alpha helicity after the synthesis of encapsulated AuNCs in HEWL (161) and the formation of the dimmer (67). The hydrodynamic radii of the Lyz-AuNCs were found to be 3.73 ± 0.8 nm at pH 3 and 3.84 ± 0.52 nm at pH 12.5; comparing well with previously reported values (155). An increase in the hydrodynamic radii to 6.49 ± 1.28 nm was observed upon adding 25 mg/ml of HEWL to Lyz-AuNCs at pH 3. Interestingly, an increase in hydrodynamic radius to 5.86 ± 1.37 nm at pH 12.5 was also observed. The difference in hydrodynamic radii indicates that the Lyz-AuNCs and HEWL begin to form small initial aggregates of 2–4 protein molecules in size at pH 3 and pH 12.5 in different conformations. This perhaps is not too surprising since Lyz-AuNCs and HEW have a similar positive zeta potential at pH 3 whereas in highly basic conditions HEWL has a weak negative zeta potential and Lyz-AuNCs have a very strong negative zeta potential (155). It has been previously shown by Burnett et al. that environmental conditions affect the aggregate morphologies of HEWL and as such supports the theory that the differences observed in fluorescence lifetimes for Lyz-AuNCs under different pH conditions may arise from different aggregation forms (132). It is possible that the reason for a decrease in τ_1 at pH 3 is due to the binding of HEWL to Lyz-AuNCs near the AuNC nucleation sites and shielding of AuNC from the acidic environment, thus resulting in enhancement of the radiative rate.

To better understand the fluorescence mechanism when adding lysozyme to Lyz-AuNCs at pH 3 and 12.5, the TRES of AuNCs was measured in the presence and absence of HEWL in solution, as shown in Figure 4.13.

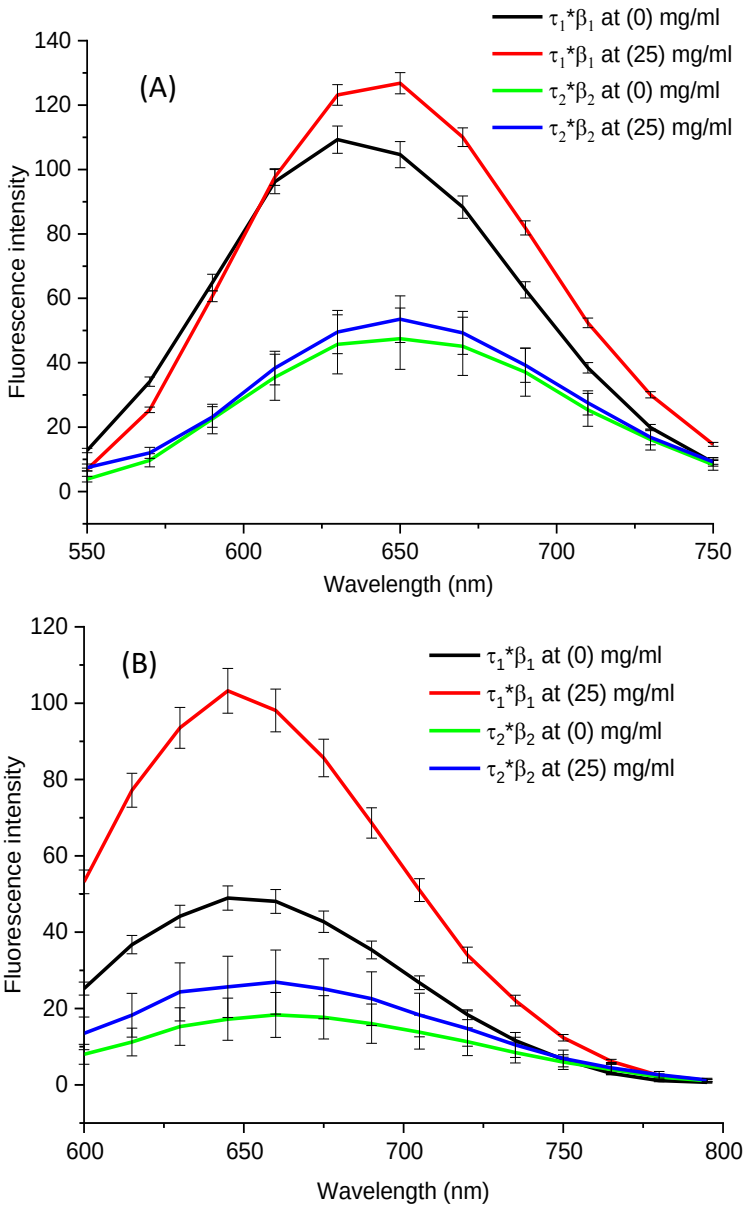

Figure 4.13: Time-resolved emission spectra of Lyz-AuNCs at an excitation wavelength of 482 nm in the presence and absence of HEWL in solution at pH 3 (A) and pH 12.5 (B).

From Figure 4.13 (A) at pH 3, we can see that the longer lifetime τ_1 emission increases and redshifts, while the emission from τ_2 remains unchanged; confirming that the smaller fluorescence increase and redshift seen previously in Figure 4.10. Figure 4.13 (B) shows that there is no obvious change in emission wavelength for both lifetime contributions while the longer lifetime τ_1 emission increases consistent with Figure 4.10.

It can be directly attributed to the changes in the fluorescence emission of τ_1. Comparing this to the previous TRES measurements of Figure 4.7 (A), we can see that while the changes in the fluorescence emission spectra and fluorescence emission lifetimes are similar for increasing pH and adding HEWL to solution, the underlying mechanism for these observations is different. In the case of increasing pH, we observe a large intensity increase and redshift for both fluorescence components whereas upon adding HEWL to solution only τ_1 undergoes a slight increase in intensity and redshift. Previously we have observed that the diameter of Lyz-AuNCs remains quite consistent at 8.0 nm across a pH range of 2–11 (with the exception of aggregates forming around the isoelectric point of Lyz-AuNCs at pH 4 and 5)(155). Therefore, we can rule out the formation of aggregates as the reason for the observed fluorescence changes. It is more likely that the observed changes to both τ_1 and τ_2 are caused electrostatically since the Lyz-AuNCs complex has been observed to become more negatively charged at higher pH. However, in the case of adding HEWL to the Lyz-AuNCs solution, it is more plausible that the observed changes in fluorescence characteristics are due to the formation of small initial protoaggregates of 2–4 proteins in size. Previously Siddiqui et al. have shown the increase and redshift of intrinsic hemagloblin fluorescence upon macromolecular crowding and aggregation caused by bovine serum albumin (BSA) interaction (167). Initial aggregate formation alone, however, did not result in changes to the fluorescence characteristics of AuNCs at pH 12.5 when adding HEWL, only at pH 3, therefore the aggregation morphology must play an important role since the morphology at pH 3 and pH 12.5 can be expected to be different due to changes in protein surface charge and interaction of HEWL (167). Therefore, it seems likely that

the changes to τ_1 only arise from a physical interaction of the AuNCs with the surrounding microenvironment due to initial aggregate induced conformational changes.

4.5 Conclusions

Here we have presented the environmental induced effects of Lyz-AuNCs fluorescence characteristics including fluorescence emission intensity, peak emission wavelength, fluorescence lifetime and time resolved emission. It was found that the fluorescence emission intensity and peak fluorescence wavelength of Lyz-AuNCs increases and red-shifts upon changing pH from acidic to basic conditions when exciting the AuNCs directly at 470 nm. The longer fluorescence lifetime component τ_1 was also seen to decrease in highly basic conditions. We have also reported the interaction between Lyz-AuNCs and varying concentrations of HEWL at different pH. Clear changes to the fluorescence characteristics of Lyz-AuNCs were observed at pH 3, as the concentration of HEWL increases the fluorescence emission intensity increase with a small redshift in peak wavelength and a decrease in the long lifetime τ_1. Conversely, no clear trend was observed at pH 12.5 for Lyz-AuNCs fluorescence. This is thought to be due to differences in the small aggregate morphology at pH 3 and pH 12.5 as Lyz-AuNC-native lysozyme proto-aggregates begin to form. Further studies are needed to determine the exact nature of Lyz-AuNCs-native lysozyme proto-aggregate formations; however, these initial results show the sensitivity of Lyz-AuNCs to environmental changes and early aggregation, which may be utilized in the future as a means of studying and modelling lysozyme aggregation.

Chapter 5: Lyz-AuNCs for Studying Lysozyme Unfolding

5.1 Abstract

The unfolding of proteins leads to a variety of diseases due to aggregation or loss of protein function. Monitoring the fluorescence properties of Lyz-AuNCs in such cases is highly valuable because the quantity of published research on this topic is low. The most common method for unfolding proteins is to use urea, sodium dodecyl sulphate (SDS), and a denaturation temperature of 65 °C for hen egg-white lysozyme (HEWL). The fluorescence properties of Lyz-AuNCs were studied in the presence of urea, SDS, and at 65 °C using steady-state and time-resolved fluorescence spectroscopies. The absorption and structure of Lyz-AuNCs were studied using UV-Vis and CD measurements. It was found that as the concentration of urea and SDS increased, the fluorescence intensity of Lyz-AuNCs decreases at an excitation wavelength of 470 nm. At an excitation wavelength of 295 nm, the fluorescence intensity fluctuated in the presence of urea and significantly decreased as the concentration of SDS increased up to 1 mM. The CD measurements showed that the ellipticity reduced without changing the wavelength in the presence of urea, while in the presence of SDS, the signal increased, indicating a variation in Lyz-AuNCs structure. This change affects the FRET mechanism at an excitation wavelength of 295 nm, leading to a decrease in the fluorescence intensity of AuNCs. Long-time incubation of Lyz-AuNCs at 65 °C leads to a continued decrease in the fluorescence intensity of AuNCs, possible due to the formation of amyloid. In addition, fluorescence lifetime measurements confirmed quenching to be collisional via oxygen dissolved in a solution which increases as the AuNC was exposed to the solvent during unfolding. Moreover, the longer decay component τ_1 was observed to decrease as the protein unfolded, due to the increased collisional quenching. It is suggested that AuNC sensitivity to solvent exposure might be utilised in the future

as a new approach to studying and possibly even detecting amyloidosis type diseases.

5.2 Introduction

The function of a protein is dependent on its three-dimensional structure. Any change in the protein structure can lead to many diseases due to changes in the function of cells (see 1.2 Protein Denaturation in Chapter 1). The structure of lysozyme can be changed by altering the surrounding environment, including the pH, higher protein concentration (see 4.2 Introduction in Chapter 4), altering the concentration of urea, SDS or expose to elevated temperature as will be discussed below.

Urea consists of two amide groups bound to a carbonyl functional group, as shown in Figure 5.1 (A) (168). Urea is used to induce protein unfolding (121,169). It has been found that urea interacts with proteins through two methods. One method is known as direct interaction where urea binds to a protein via non-polar interactions or attractive (repulsive) interactions. The second method is known as indirect interactions, where urea interacts with water near the protein, reducing the hydrophobic structure of the protein and allowing the water to penetrate to the protein centre (170).

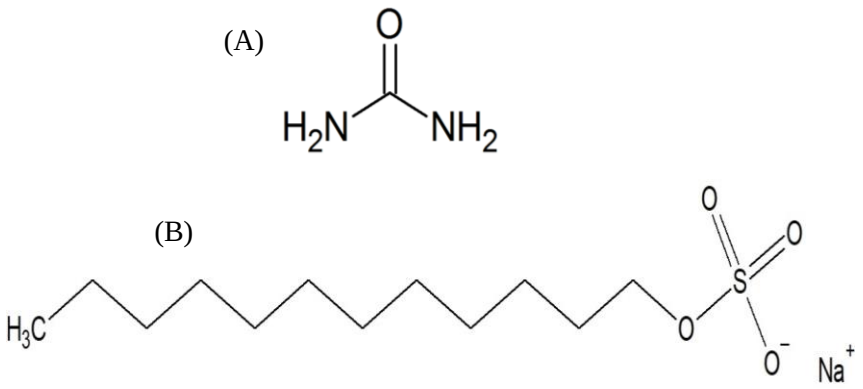

Figure 5.1. (A) urea structure, (B) sodium dodecyl sulphate (SDS) structure

The effect of urea on HEWL has been studied using several methods. In particular, Raman spectroscopy can be used to study the amide I band region and

monitor changes in the α-helix, β-sheets, and random structures (i.e. change in the secondary structure). It has been found that in the presence of urea, there is no major change in the secondary structure. Low-frequency Raman spectroscopy can also be used to show changes in hydrogen bonding in the sample. When urea bind to the water near the protein leads to reduce the intensity of low-frequency Raman spectroscopy. This result shows that urea is indirect interact with protein and cause this protein unfolding. Studying the change in HEWL activity provides an indication of the change in the structure of HEWL. It has been found that HEWL activity decreases by about 15% in the presence of 8 M of urea (171). Most previous studies have focused on the unfolding of HEWL at 8 M urea concentration because urea is not as strong a denaturing agent as guanidine hydrochloride GuHCl (171). Urea at a concentration of 7.4 M is sufficient to denature 50% of HEWL (172). The minimum required urea concentration to change the conformation of HEWL is 8 M (173).

The second condition is sodium dodecyl sulphate (SDS). SDS is a negatively charged surfactant molecule containing 12 carbon atoms as a non-polar hydrophobic tail bound to a sulphate group as a polar head (Figure 5.1 (B)). SDS has been used for studying HEWL aggregation (21), unfolding (22), and the formation of amyloid (174). The SDS interacts with proteins through attraction interactions and hydrophobic interactions. Proteins have a positive charge when the pH is below their isoelectric point (pI). In order to induce aggregation, it is important to increase the attraction force and hydrophobic attraction by using SDS and protein at a pH two units below their pI. It has been shown that SDS induces aggregation and formation of amyloid for 25 proteins in different classes at a pH two units below the pI. In contrast, at a pH two units above the pI, no aggregation was observed due to the negative charge on the surface of protein increasing the repulsion force and preventing aggregation (120,174). The formation of the amyloid occurs when the secondary structure shows a higher content of β-sheet and a lower content of the α-helices. In the presence of SDS, there is an increase in β-sheet content that indicates the formation of amyloid fibrils (174).

The third condition is temperature. The temperature can change the structure of a protein by affecting the hydrophobic interactions and the formation of hydrogen bonds. The structure of a native protein is stable by a variety of interactions. Among these interactions, hydrophobic interaction is significantly important for stabilizing the protein folds. The strength of these interactions is highly dependent on temperature and can be weak at low temperatures (cold denaturation) or high temperatures such as 65℃ (175). Hydrogen bonds are also affected by temperature; it has been found that the length of the hydrogen bond increases with increasing temperature (176). Changing the hydrophobic interactions and hydrogen bond leads to changes in the secondary structure of a protein. For example, the effect of temperature on the secondary structure of HEWL has been the focus of many studies. At higher concentrations of HEWL (200 mg/ml), using a Fourier-transform infrared (FTIR) measurement shows a decrease in the α-helix and β-sheet intensity at higher temperatures, indicating the unfolding of HEWL (177). At pH 1.6 and at low concentrations of HEWL, the change in the secondary structure of HEWL as the temperature increases from 35 to 55 °C is a decrease in the α-helix structure and an increase in β-sheet structure. Furthermore, increasing the temperature from 55 to 90 °C produces a slight change in the secondary structure, indicating that unfolding is completed at 55 °C (134). As the temperature is increased towards the denaturation temperature (i.e., 65 °C) HEWL aggregates due to a decrease in the intermolecular repulsive forces accompanied by a change in the secondary structure, in particular, a decrease in α-helix structure and increase in β-sheet structure (134). It has been found that the higher temperature induces the formation of amyloid at acid pH (133,139).

The Thioflavin T (ThT) is a cationic benzothiazole dye which has been used to detect amyloid fibrils. The fluorescence intensity of ThT in aqueous solution is low due to an increase in the non-radiative rate while the fluorescence intensity of ThT enhances in the presence of amyloid fibrils (178,179). Several models have been proposed to explain the increase in ThT fluorescence intensity in the presence of amyloid fibrils such as ThT forms micelles (180) or dimers (181). The long axis of

ThT monomer bind into the long axis of amyloid fibrils (182). The binding of ThT to amyloid fibrils proposal has been proven by experimental and theoretical works (183,184).

Several researchers have studied the effect of the temperature of the fluorescence properties of AuNCs. This research showed a decrease in the intensity and a redshift in the peak emission wavelength of the BSA-Au_{25}NCs with increasing temperature from 77 to 300 K (142). The decrease in fluorescence intensity is due to thermally activated defect/surface trapping. Redshift in the peak emission wavelength due to an increase in electron−phonon and electron−defect/surface scattering interaction (142). The fluorescence lifetime of BSA-Au_{25}NCs decreases from 4.85 to 1.55 μs, with increasing temperature from 77 to 300 K (150). Other research found that increasing the temperature from 20 to 80 °C, the fluorescence intensity and the lifetime of AuNCs decreases (185). Increasing the temperature from 22 to 55 °C resulted in a decrease in the fluorescence intensity of AuNCs, but for three types of proteins (BSA, HEWL, and trypsin) the fluorescence intensity of the AuNCs was recovered by decreasing the temperature from 55 to 22 °C. In addition, a redshift is observed in the peak emission of Lyz-AuNCs around 20 nm (67). A redshift was observed in previous research (67,185) that is believed due to electron-phonon interaction and surface scattering (142).

Nevertheless, exploring the fluorescence properties of Lyz-AuNCs in the presence of urea and SDS, and the effect of long time incubation at 65 °C has not been reported. This motivates us to explore the fluorescence properties of Lyz-AuNCs under these conditions. It is vital to understand the effect of unfolding protein on the fluorescence properties of AuNCs. Since the unfolding of the protein leads to many diseases due to changes to the function and aggregation, it is important to determine the change in Lyz-AuNCs structure before using them in biological applications, such as an antibiotic, since HEWL can act as an antibiotics agents against bacteria (111) and AuNCs also have Antibiotics properties (145). It is also an important industrial product since HEWL has other applications in preserving food

(110). In this chapter, the effect of chemical denaturants (urea), chemical surfactant (SDS), and an elevated temperature at 65 °C on the fluorescence properties of Lyz-AuNCs are studied. This study shows that fluorescence properties of AuNC can be used as an indicator for protein unfolding.

5.3 Experimental

5.3.1 Sample Preparation

The Lysozyme from chicken egg-white (L-6876; > 99.0%), gold (III) Chloride trihydrate (> 49.0%), phosphate buffered saline and sodium hydroxide (NaOH) solution (1.0 M), urea (> 99.0%), sodium dodecyl sulphate (SDS) (> 99.0%), Thioflavin T (ThT) were purchased from Sigma-Aldrich.

To study the effect of urea and SDS on the Lyz-AuNCs, Lyz-AuNCs was synthesized using a similar method to that described in Chapter 4 (see 4.3.1: Sample Preparation). A stock solution of urea was freshly prepared by dissolving 7.3 grams of urea crystals in 13.50 mL of water at room temperature yielding Urea (8.5 M, 13.50 mL) and then diluting and mixing with Lyz-AuNCs to yield a final concentration of Lyz-AuNCs of 33 µM. The urea concentration was changed from 0 to 8 M. To prepare stock SDS solution, 92.63 mg of SDS powder was dissolved in 1.07 ml of water; the final concentration was 0.3 M. This was then mixed with Lyz-AuNCs to yield a final concentration of Lyz-AuNCs 33 µM, and the concentration of SDS was changed from 0 to 9 mM. More detail is added in the appendix see (3. Preparing Mixture of The urea and Lyz-AuNCs and 4. Preparing Mixture of the SDS and Lyz-AuNCs)

To study the effect of persistent heating at 65 °C, the Lyz-AuNCs was diluted to a concentration of 33 µM and measured at room temperature and 65 °C for 16 h. The measurement was done automatically by setting the software of the fluorolog 3 spectrofluorometer to measure every 30 mins for 16 h. A stock solution of ThT was mixed with Lyz-AuNCs to yield a final concentration of ThT of 66 µM and 33 µM of

Lyz-AuNCs. The fluorescence of ThT was studied in the HEWL and Lyz-AuNCs measured for 10 h.

5.3.2 Spectroscopic Measurements.

All UV-Vis measurements were performed using PerkinElmer UV/VIS spectrometer Lambda 25. The UV/VIS range of the electromagnetic spectrum covers the range 250–800 nm with a scan speed of 480 nm/minute. The data were analysed using the spectrograph version 1.2.7.

All fluorescence emission of Lyz-AuNCs was measured using Fluorolog-3 spectrometer (Horiba, UK). The experimental setup is as follows: using an excitation wavelength of 295 nm with a slit width of 6 nm, emission wavelengths were measured from 300 to 850 nm with 6 nm increments; using excitation wavelengths of 440 and 470 nm with a slit width of 6 nm, emission wavelengths were measured from 450 to 850 nm with slit widths at 6 nm. Data were analysed with Origin Pro software version 9.6.5169. For studying the effect of temperature on the Lyz-AuNCs, the Fluorolog-3 spectrometer was equipped with a temperature controller model lfi 3751.

Time-resolved fluorescence spectrometry with the time-correlated single-photon counting (TCSPC) technique in a Horiba Jobin Yvon IBH was used to measure the fluorescence lifetimes, emission spectra, and anisotropy decay of Lyz-AuNCs. The instrument contains the delta flex hybrid (Horiba Scientific), motorised polarisers, and a Horiba TBX-580c photon-detection module. The excitation source was a pulsed Delta Diodes of 482 nm having a temporal width of 50 ps (full width at half maximum) and a repetition rate of 100 MHz and operating with a delay of 10 ns and a coaxial delay of 95 ns. The excitation polariser was kept at angle 0° emission polariser at a magic angle of 55° to avoid anisotropy effects during the lifetime measurement. The decay curve was accumulated for 10,000 counts, and the tag range was 13 μs. Data were analysed with Horiba Scientific DAS6 version 6.8.16 software.

5.4 Results and Discussion

5.4.1 Effect of Urea on Lyz-AuNCs

The effect of urea on Lyz-AuNCs structure was studied by varying the concertation of urea from 0 M to 8 M and measuring the optical properties of Lyz-AuNCs. The first optical property is the absorbance of Lyz-AuNCs, as shown in Figure 5.2.

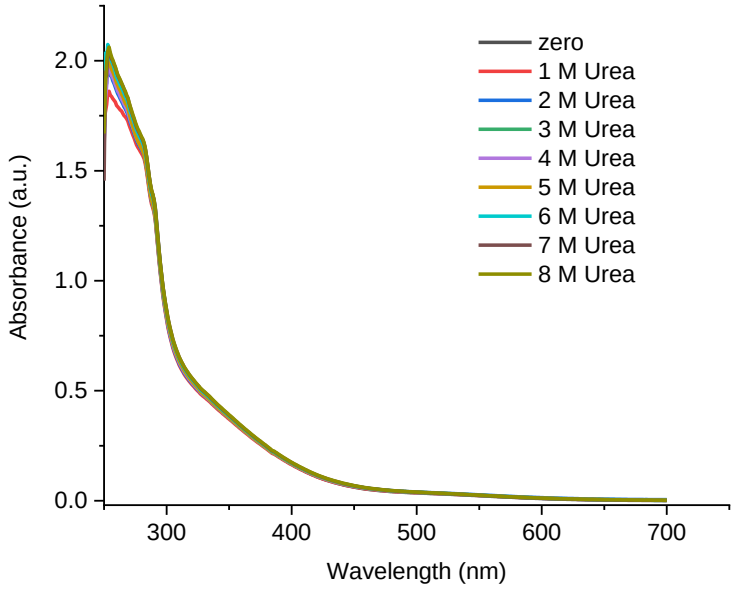

Figure 5.2. Absorption spectra of Lyz-AuNCs as a function of urea concentration at pH 7.4.

The peak at 280 nm is due to the presence of amino acids (i.e. Tyrosine (Tyr), Tryptophan (Trp), and Phenylalanine (Phe)). There is no change in absorbance with increasing urea concentration. In addition, there is no change in the colour of the sample and no increase in the absorbance at wavelength 350 nm, which indicates that there is no aggregation.

To understand the photophysics of lysozyme unfolding via AuNC fluorescence, we increased the concentration of urea in a solution of Lyz-AuNCs in steps of 1 M and measured the changes in the Lyz-AuNCs emission spectrum when exciting at 295 nm and 470 nm, as shown in Figures 5.3 (A) and 5.3 (B), respectively.

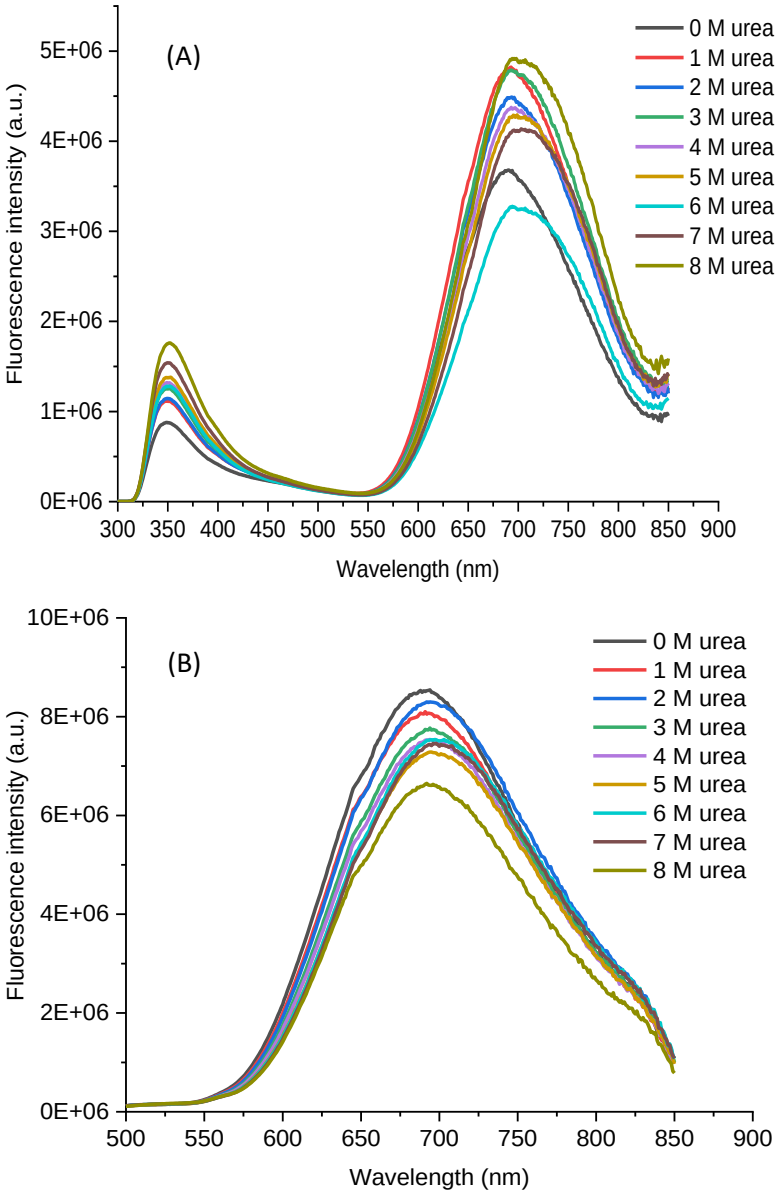

Figure 5.3. Fluorescence emission spectra of Lyz-AuNCs with increasing concentration of urea added to the solution at pH 7.4, (A) an excitation 295 nm and (B) an excitation 470 nm.

From Figures 5.3 (A) we can see two peaks; the first peak centred at ~ 350 nm corresponds to the emission from Trp, and a second larger fluorescence peak centred at ~ 700 nm originates from the AuNCs. To better understand the protein tertiary structure with increasing concentration of urea, we observed the Trp peak fluorescence emission intensity and wavelength as a function of urea concentration, as shown in Figures 5.4.

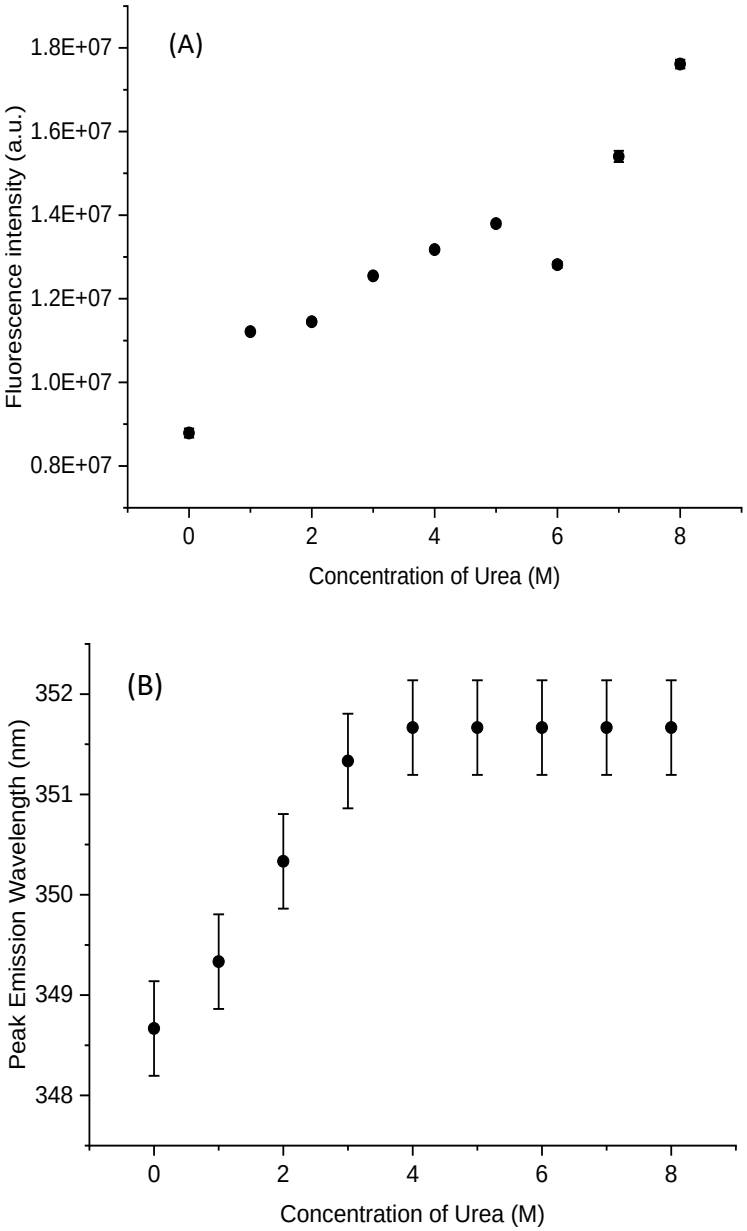

Figure 5.4. (A) Peak emission intensity and (B) peak emission wavelength of Trp in Lyz-AuNCs as a function of urea concentration.

To better understand the change in the fluorescence intensity and wavelength of Trp, it is important to locate the Trp in HEWL to understand the unfolding dynamics and hence the fluorescence properties of AuNCs. HEWL has four Trps (Trp 62, Trp 63, Trp 108, and Trp 111) that are surrounded by solvent and located in the helix-loop-helix domain. Trp 28 is located in helixes 25 to 28, and Trp 123 is located in 120 to 125 residues, which are both buried in the hydrophobic side (22). The emission maximum can be seen to increase consistently (apart from a small dip at 6 M) as a

function of urea concentration as well as a redshift of 4 nm in the peak emission wavelength from 0–4 M of urea and no further changes in the concentration range of 4–8 M of urea, suggesting that Trp is already water exposed during the partial unfolding at concentrations between 0 and 4 M. This agrees with Kurtin et al., suggesting reduced quenching from neighbouring residues for the increase in fluorescence intensity and Trp becoming exposed to the polar water environment of the solution for the redshift in the peak emission wavelength (186).

To illustrate the changes in fluorescence emission of AuNCs during lysozyme unfolding, the peak emission intensity and wavelengths of AuNCs fluorescence as a function of urea concentration in solution when excited at 295 and 470 nm were noted as shown in Figures 5.5 and 5.6, respectively. From Figures 5.5, it can be seen that the fluorescence emission intensity of AuNCs fluctuates when excited at 290 nm but decreases linearly when excited at 470 nm as a function of urea concentration in solution.

The decrease in emission intensity observed as the protein unfolds when excited at 470 nm is most likely due to increased collisional quenching of the AuNCs as it becomes more exposed to the surrounding solvent (96). The minimal change in emission intensity, when excited at 295 nm, implies that while increasing collisional quenching and decreasing the FRET efficiency as a result of a possible increase in the separation between Trp and the AuNCs as the lysozyme unfold results in a decrease in emission, another effect modifies the emission of AuNCs.

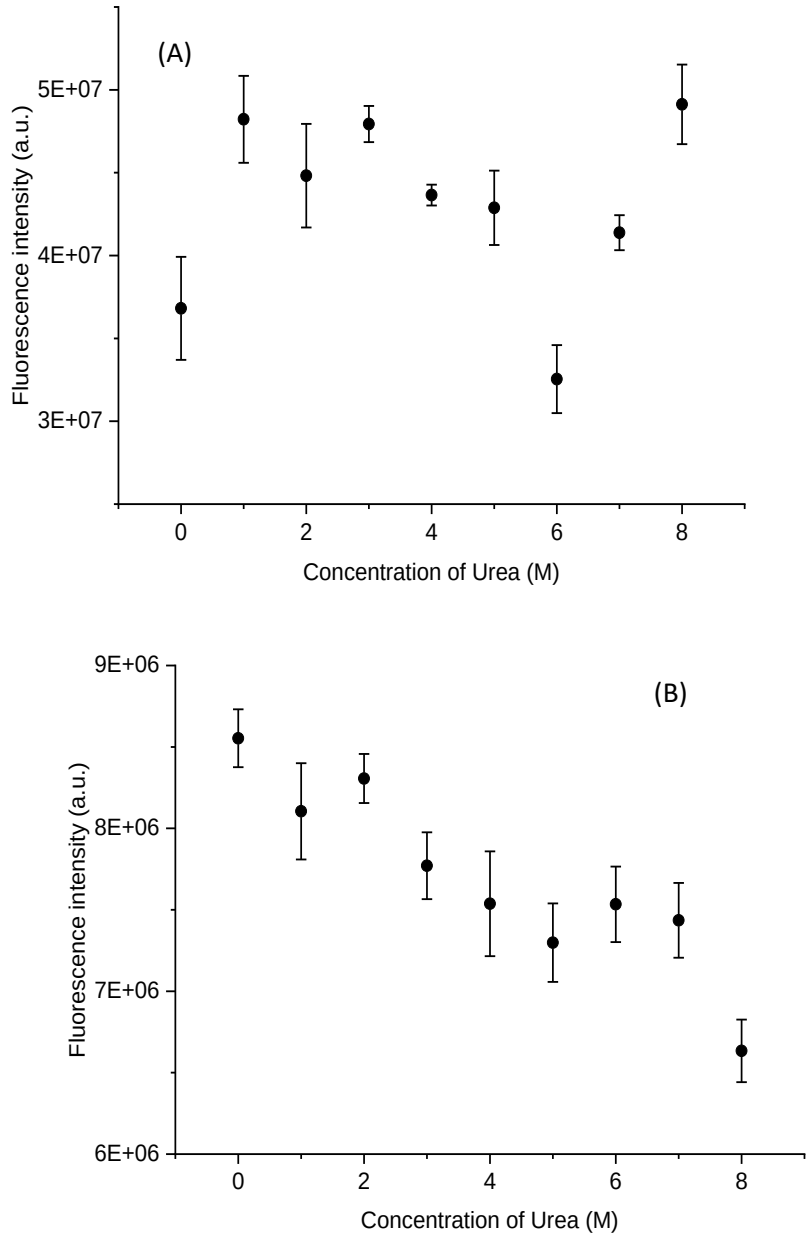

Figure 5.5. Fluorescence emission maximum intensity of AuNCs emission from Lyz-AuNCs, as a function of increasing urea concentration in solution; (A) an excitation wavelength 295 nm and (B) an excitation wavelength 470 nm.

Figure 5.6 shows that the AuNCs maximum emission wavelength redshifts as the urea concentration increases. The redshift of AuNCs emission and decrease in intensity were also reported in solvent-exposed AuNCs encapsulated in different proteins than lysozyme (185). However, an apparent difference in the redshift across the urea concentration range was observed when excited at 295 nm and 470 nm, 16 nm vs. 4 nm, suggesting that different excitation routes lead to different

inter-system crossing pathways. In addition to conformational effects, the changes in AuNCs characteristics may also arise due to the interactions between urea and cysteine residues. Previously, it has been shown that urea preferentially binds to cysteine residues (30, 80 and 94) leading to changes in the structure at the disulphide bonds present in lysozyme (170,172).

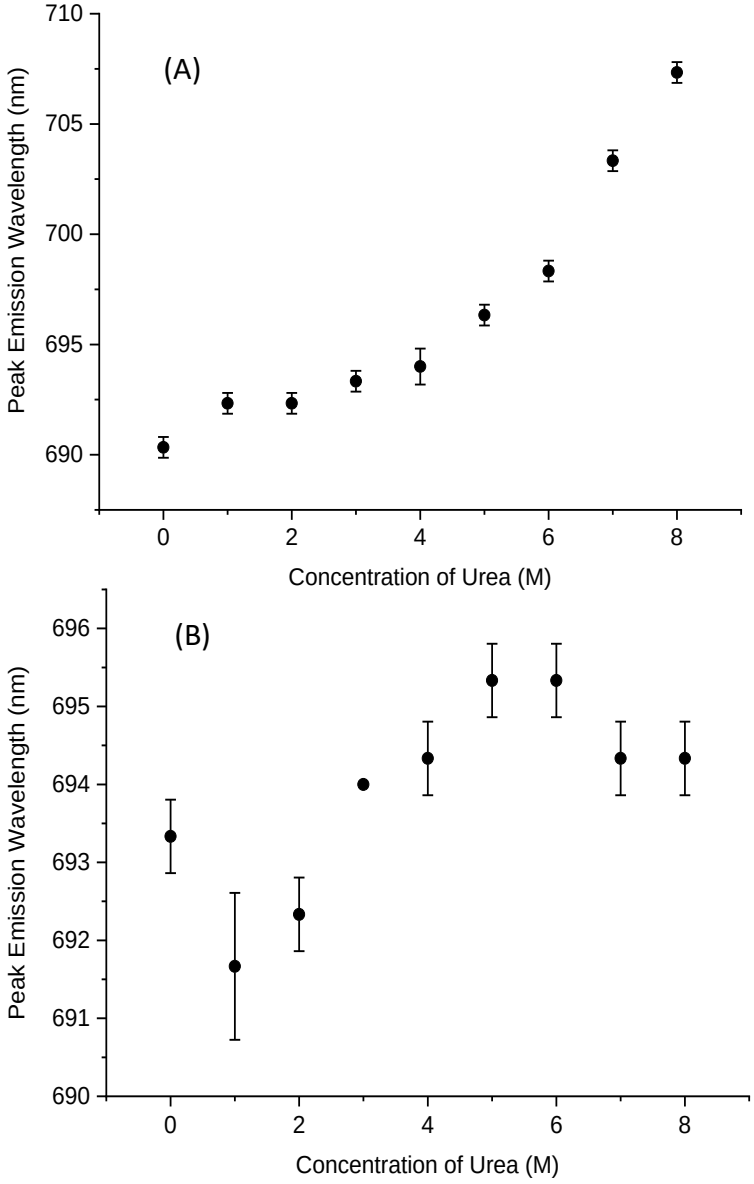

Figure 5.6. Fluorescence emission maximum wavelength of AuNCs emission from Lyz-AuNCs, as a function of increasing urea concentration in solution; (A) excitation wavelength 295 nm and (B) excitation wavelength 470 nm.

It is well known that sulphur–gold bonds are present within all protein encapsulated AuNCs, measured via X-ray photoelectron spectroscopy (XPS), acting as a critical stabilizing agent which is needed to form clusters within the protein (67,142,187). Therefore, it is reasonable to assume that urea may modify the binding of the AuNCs to the protein, altering the fluorescence characteristics in the process. Further study is needed to disclose the mechanism.

To further explore the characteristics of AuNCs emission during protein unfolding, the fluorescence lifetimes of AuNCs as a function of urea concentration were measured. Fluorescence lifetimes were measured using a 482 nm pulsed light source over a measurable time of 13 μs. The resulting fluorescence decay curves were analysed using a 3-exponential model. The results of the analysis are shown in Table 5.1. The three exponential models is shown to be a good fit to the fluorescence decay curve using the least-squares method of goodness of fit analysis with a χ^2 value between 1.00 and 1.13 for all the data.

Table 5.1 Fluorescence lifetimes of AuNCs emission τ with amplitudes α with different concentrations of urea added. Measured at an excitation wavelength of 482 nm.

[urea] (M)	τ_1 (ns)	α_1	τ_2 (ns)	α_2	τ_3 (ns)	α_3	χ^2
0	2264 ± 6	0.71	795 ± 17	0.25	121 ± 3	0.04	1.09
1	2136 ± 5	0.73	728 ± 15	0.24	109 ± 3	0.03	1.05
2	2091 ± 5	0.73	706 ± 17	0.23	102 ± 3	0.04	1.12
3	2168 ± 6	0.71	760 ± 17	0.25	119 ± 3	0.04	1.08
4	2045 ± 6	0.73	717 ± 19	0.23	110 ± 3	0.04	1.09
5	2016 ± 5	0.73	697 ± 16	0.24	97 ± 3	0.03	1.11
6	2014 ± 6	0.72	720 ± 17	0.25	106 ± 3	0.03	1.10
7	1975 ± 5	0.73	679 ± 15	0.24	92 ± 3	0.03	1.13
8	1922 ± 8	0.75	617 ± 26	0.22	89 ± 5	0.03	1.08

The two major lifetime components of ~ 2000 ns and ~ 700 ns compare well with the previously reported lifetime values for protein encapsulated AuNCs (96,188,189). The shorter lifetime component is probably the result of scattered light from the sample.

From Table 1, we can see a clear decrease in the longer lifetime value τ_1 of 2264 ± 6 ns at 0 M of urea to 1922 ± 8 ns at 8 M of urea, whereas the decrease in the second shorter lifetime τ_2 is much smaller. This decrease in lifetime for τ_1 suggests that as the protein unfolds, the AuNCs undergoes increased collisional quenching due to increased solvent exposure. To show the effect of added urea in solution with Lyz-AuNCs on the encapsulating protein's structure, CD spectroscopy was carried out on Lyz-AuNCs with increasing urea concentration, as shown in Figure 5.7.

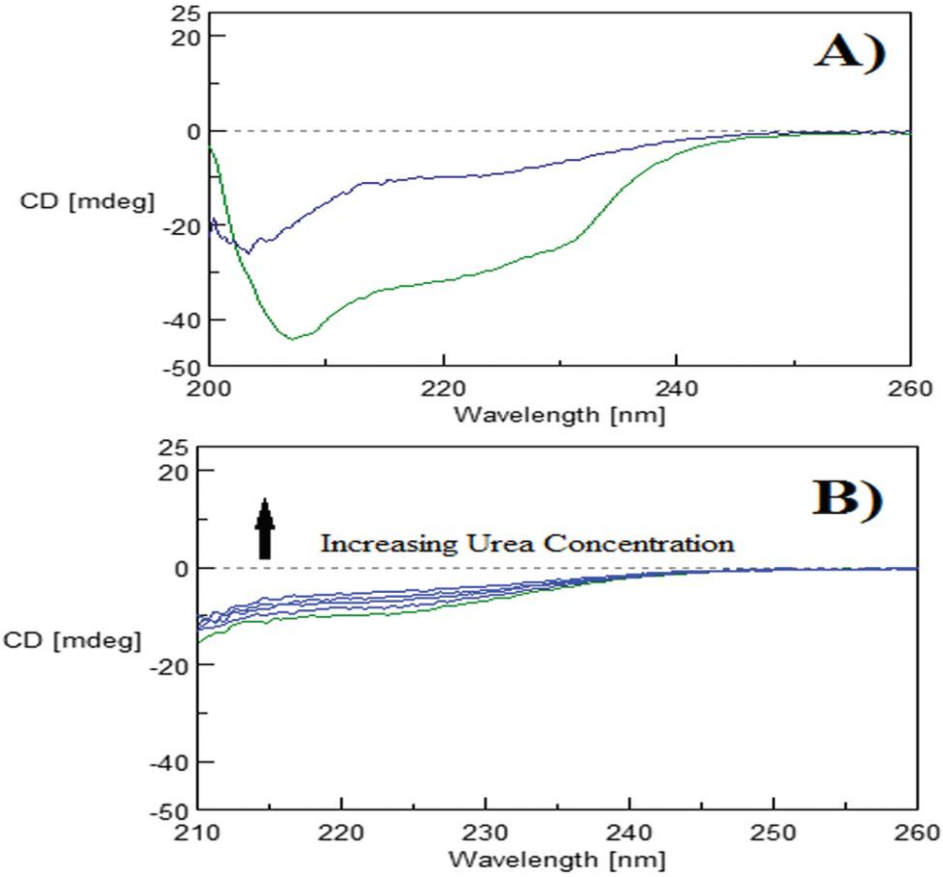

Figure 5.7. CD spectra of: (A) lysozyme (green) and Lyz-AuNCs (blue). (B) Lyz-AuNCs with increasing urea concentration obtained from (161). All CD spectra were recorded in PBS buffer solution at pH 7.4. (Courtesy of Dr. Barbara Jachimska of Jerzy Haber Institute of Catalysis and Surface Chemistry, Polish Academy of Sciences).

The CD spectroscopy has been used to study the secondary structure of many proteins. The far-UV CD spectra provides information on the secondary structure of many proteins because the electron transition $n - \pi^*$ results in a signal between

215–230 nm, the α-helix structure shows the negative bands at 222 nm, and the β-sheet shows negative bands at 216–218 nm (190). HEWL contains two domains: α domain in the range of residues 1–36 and residues 87–129 and β sheet in the range of residues 37–86. The far-UV CD spectra show two negative peaks at 222 nm and 208 nm in water at pH 7 (164).

Figure 5.7 (A) shows the CD spectra of HEWL and Lyz-AuNCs. The signal at wavelength 208 nm decreased and shifted to a shorter wavelength at 204 nm after the synthesis of AuNCs, indicating a reduction of the α-helix content. The effect of the synthesis of AuNCs on the structure has been studied in a variety of proteins. For example, it has been found that native lactoferrin (NLf) has two negative bands at 208 and 222 nm due to the α-helix content. After the synthesis of AuNCs the band at 208 nm shifts to 202 nm, indicating a decrease in the α-helix that was accompanied by an increase in the β-sheet and random coil structures (94). Russel et al. found a decrease in HEWL at the band at 208 nm after the synthesis of AuNCs due to a decrease in the α-helix content (166). The change in the structure of HEWL was due to the breaking of the disulphide bonds between Cys and the binding of Cys to Au. As a result of this binding, the α-helix content decreases (80).

Upon increasing the urea concentration in solution with Lyz-AuNCs, we observe that the spectral trough position does not change but decreases slightly in magnitude, as seen in Figure 5.7 (B). This small decrease in magnitude is attributed to urea having a small effect on the Lyz-AuNCs conformation, resulting in further loss of the native structure. From this study, we can ascertain that the AuNCs fluorescence of Lyz-AuNCs is sensitive to the partial conformational changes induced using urea despite the impact of urea on the structure of Lyz-AuNCs being small. The urea binding may be partially responsible for changes in the AuNCs emission, especially in the case of 295 nm excitation wavelength due to conformational changes increasing the separation between Trp and AuNCs resulting in a decrease in the FRET efficiency between the two fluorophores.

5.4.2 Effect of SDS on Lyz-AuNCs

The influence of SDS induced lysozyme unfolding on the fluorescence characteristics of AuNCs was also studied in a similar fashion to urea. SDS was added to a solution of Lyz-AuNCs at concentrations between 0 and 9 mM and the optical properties of Lyz-AuNCs. The first optical property is the absorbance of Lyz-AuNCs (Figure 5.8).

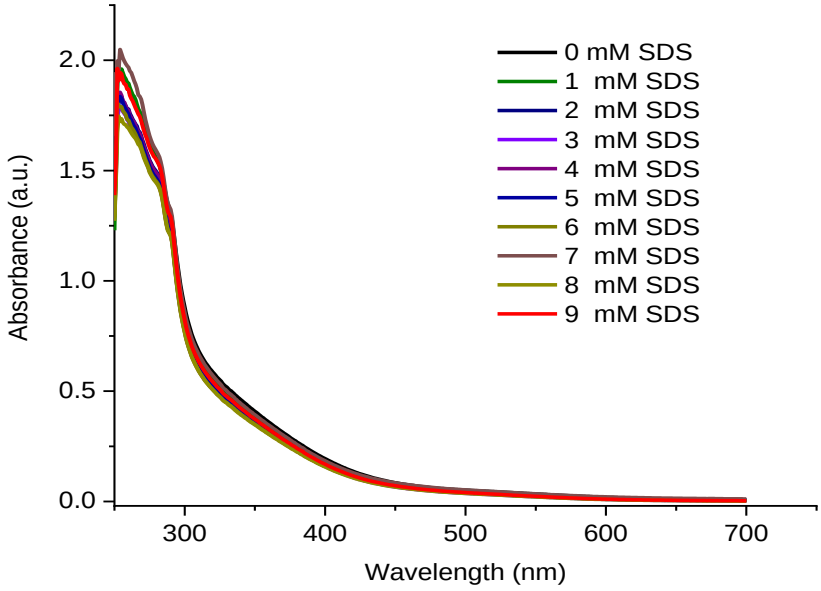

Figure 5.8. Absorption spectra of Lyz-AuNCs as a function of SDS concentration at pH 7.4.

The peak at 280 nm is due to the presence of amino acid Tyr, Trp, and Phe. There is no major change in absorbance with increasing the concentration of SDS. Moreover, there is no change in the colour of the sample and no increase in the absorbance at wavelength 350 nm, which indicates that there is no aggregation.

The fluorescence spectra of Lyz-AuNCs with different concentrations of SDS added were measured at both 295 nm and 470 nm excitation wavelength, as shown in (Fig. 5.9A, B).

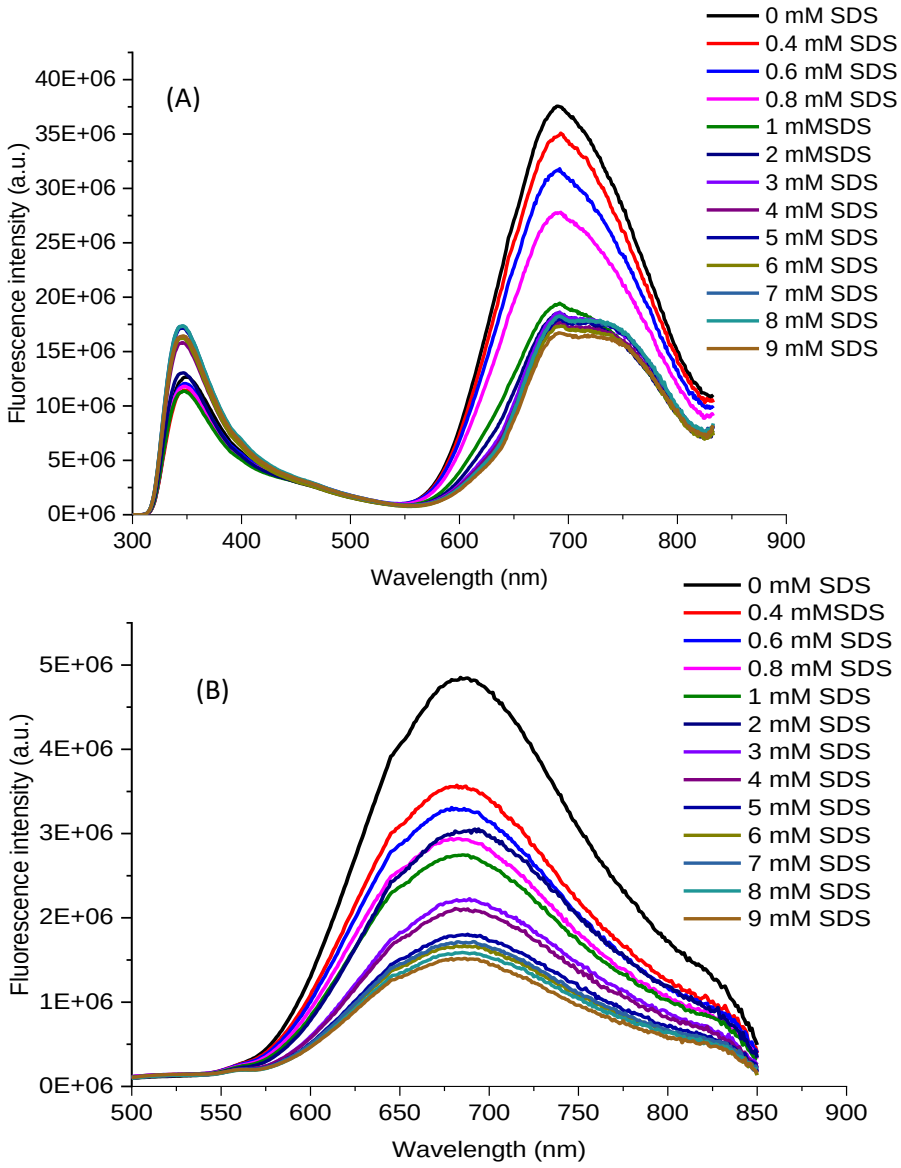

Figure 5.9. Fluorescence emission spectra of Lyz-AuNCs with increasing concentration of SDS added to the solution, (A) an excitation wavelength 295 nm and (B) an excitation wavelength 470 nm.

From Figures 5.9 (A) we again see the characteristic 2 peak fluorescence emission spectra of Lyz-AuNCs when excited at 295 nm, with the first peak originating from Trp and the second from AuNCs. Figures 5.9 (B) shows the fluorescence emission spectra of Lyz-AuNCs when the AuNCs are directly excited at 470 nm. Interestingly, in both spectra, the peak maximum wavelength of AuNCs does not shift upon adding SDS; however, a small blue shift of 2 nm was observed for the peak emission wavelength of Trp. This 2 nm blue shift agrees well with Sun et al. who also observed a 2 nm blue shift for Trp emission when lysozyme and SDS

were in solution with the same ratio of SDS to lysozyme (22). At this SDS/lysozyme ratio, the same group reported a decrease in the α-helix content of the protein. This suggests that SDS does cause a change in the protein conformation at these concentrations but does not alter the binding of AuNCs to protein as urea does and that surface Trp becomes buried within the hydrophobic structure.

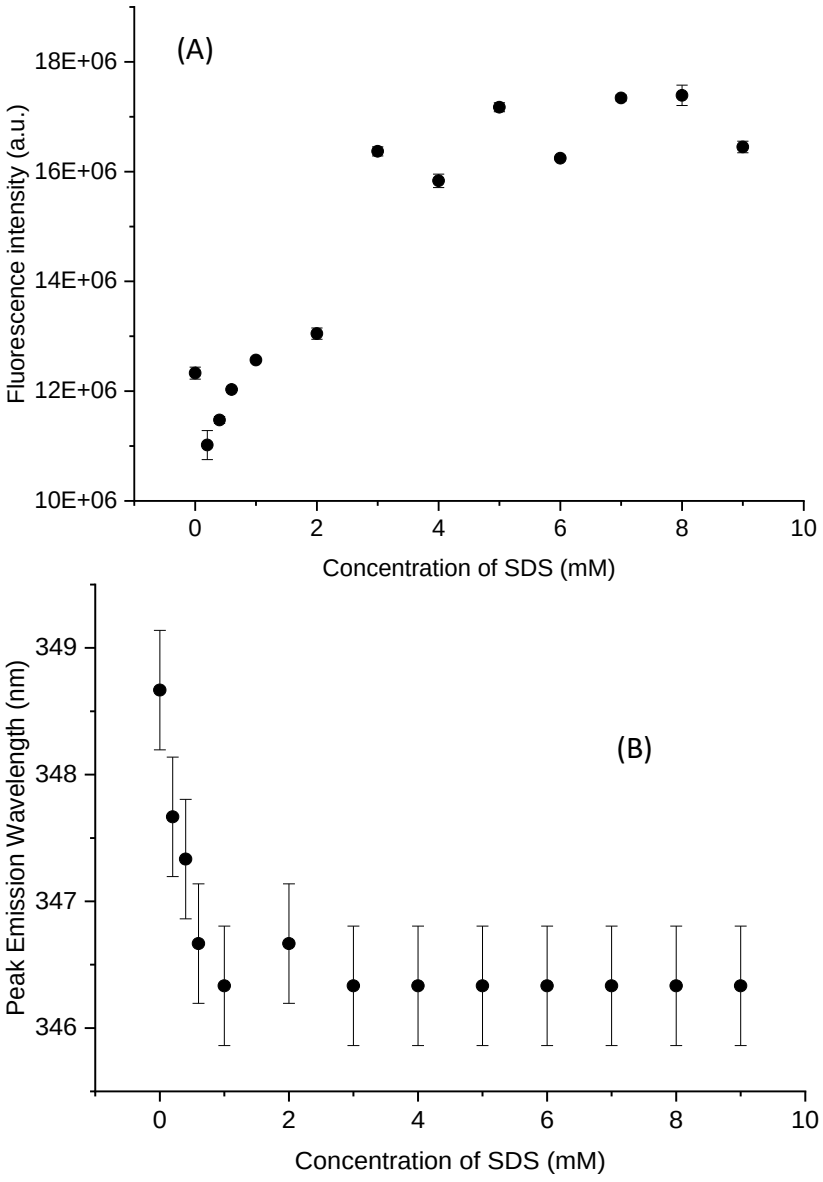

Figure 5.10. (A) The peak emission intensity and (B) The peak emission wavelength of Trp in Lyz-AuNCs as a function of the concentration of SDS.

To better display the effect of SDS on the fluorescence intensity of Trp and AuNCs, the maximum fluorescence intensities of both were plotted as a function of

SDS concentration, as shown in Figure 5.10 and Figure 5.11. From Figure 5.10., we can see that the maximum fluorescence intensity of native Trp initially increases before levelling off as a function of SDS concentration. Between 0 and 3 mM of SDS concentration in solution, the fluorescence maximum of native Trp fluorescence rises linearly with SDS concentration.

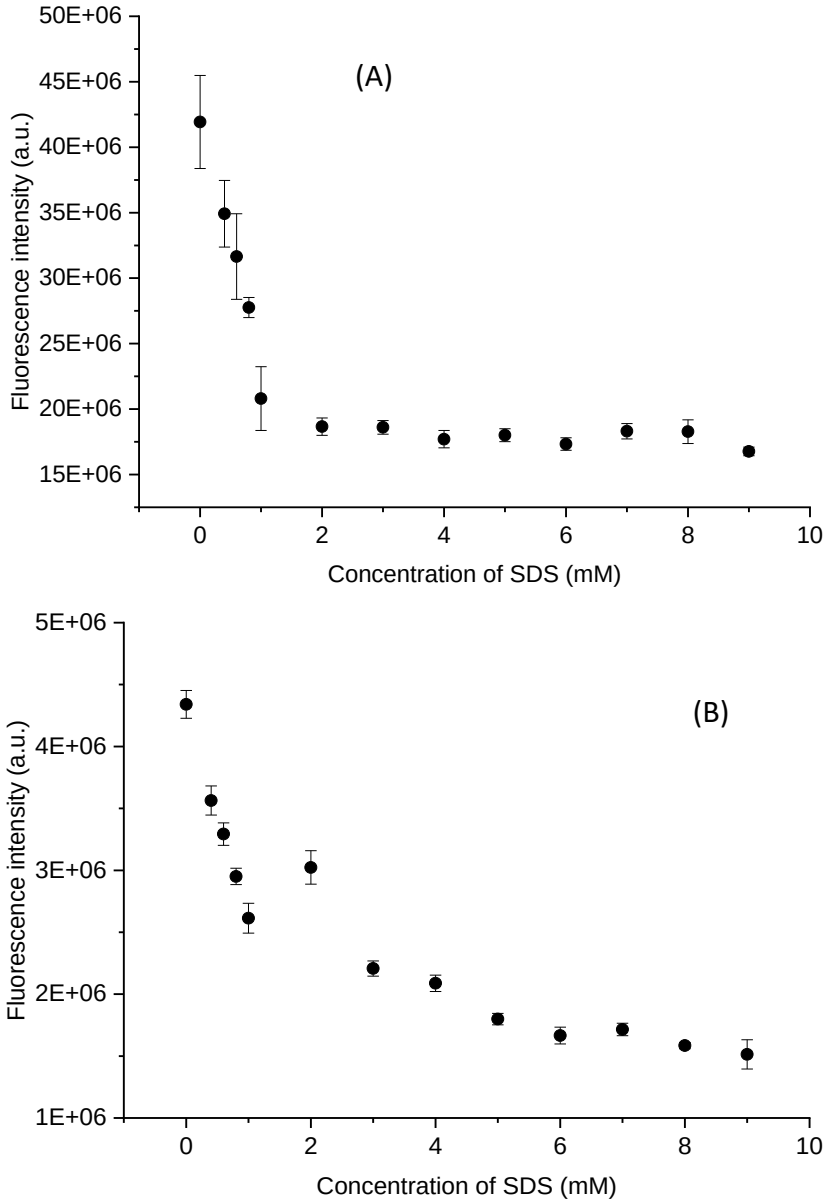

Figure 5.11. Fluorescence emission maximum intensity of AuNCs emission from Lyz-AuNCs, as a function of increasing SDS concentration in solution; (A) an excitation wavelength 295 nm and (B) an excitation wavelength 470 nm.

This rise could be due to the fact that Trp is less exposed to water resulting from the protein conformational change introduced by SDS binding to lysozyme (191). It is also possible that this increase arises from a reduced energy transfer due to an increase in Trp/AuNCs separation. From Figure 5.11, we can see that the AuNCs fluorescence emission maximum has a rapid linear decrease between 0 and 1 mM of SDS in solution and then a slower linear decrease between 1 and 9 mM of SDS in solution when exciting at both 295 nm and 470 nm.

The same initially fast decrease for both excitations wavelength indicate that the decrease is not governed by a decrease in FRET efficiency due to increased Trp/AuNCs separation. However, the magnitude of the fluorescence maximum intensity decrease is slightly larger when excited at 295 nm compared with 470 nm indicating the contribution from a reduced FRET. Due to the rapid decrease, it is most likely that the protein undergoes major unfolding at the location of the AuNCs between concentrations of 0–1 mM SDS, resulting in increased collisional quenching of the AuNCs in solution. Further increase in SDS does not cause a significant decrease in the AuNCs emission intensity maximum, suggesting no major alteration in the local environment around the AuNCs.

In order to determine that the change in AuNCs emission is due to collisional quenching as lysozyme unfolds rather than the interaction with SDS, we studied the fluorescence lifetimes of Lyz-AuNCs, focussing on directly exciting the AuNCs at different concentrations of SDS in solution. The results of this experiment are shown in Table 5. 2. As in previous studies with urea, we use a 3 exponential function to fit the measured fluorescence decay curves, with a χ^2 value between 1.05 and 1.15, indicating that the data description is of good quality. Again, we find that only the longer decay time,τ_1, is sensitive to the increasing SDS concentration in solution, with τ_2 fluctuating but remaining within error and τ_3, the scattering proportion of the fitted decay curve.

Table 5. 2. Fluorescence lifetimes of AuNCs τ with amplitudes α with different concentrations of SDS added. Measured at an excitation wavelength of 482 nm.

[SDS] (mM)	τ_1 (ns)	α_1	τ_2 (ns)	α_2	τ_3 (ns)	α_3	χ^2
0	2159 ± 8	0.70	825 ± 28	0.26	160 ± 5	0.04	1.05
1	2049 ± 8	0.70	755 ± 22	0.27	125 ± 5	0.03	1.10
2	2057 ± 10	0.68	824 ± 31	0.28	146 ± 5	0.04	1.14
3	2037 ± 9	0.68	802 ± 34	0.28	148 ± 5	0.04	1.11
4	2015 ± 9	0.68	758 ± 26	0.28	127 ± 5	0.04	1.15
5	1979 ± 9	0.68	757 ± 31	0.28	140 ± 5	0.04	1.14
6	1962 ± 8	0.70	723 ± 23	0.27	108 ± 4	0.03	1.14
7	1973 ± 7	0.72	714 ± 23	0.25	114 ± 5	0.03	1.09
8	2078 ± 10	0.66	821 ± 32	0.30	147 ± 5	0.04	1.13
9	1909 ± 8	0.68	742 ± 18	0.28	143 ± 10	0.04	1.14

The long fluorescence lifetime was seen to decrease by ~ 100 ns between concentrations of 0 and 1 mM SDS in solution and then only a further decrease by 150 ns between concentrations of 1 and 9 mM, indicating that collisional quenching takes place and that the biggest local environmental change due to unfolding happens within the 0–1 mM SDS concentration range, agreeing well with the fluorescence emission spectra data as shown in Figure 5.10. Due to the lack of redshift in the fluorescence peak emission wavelength for AuNCs excited at both 295 nm and 470 nm, the changes in the fluorescence emission maximum and fluorescence decay time can be attributed to the effect of solvent exposure and increased collisional quenching as a result.

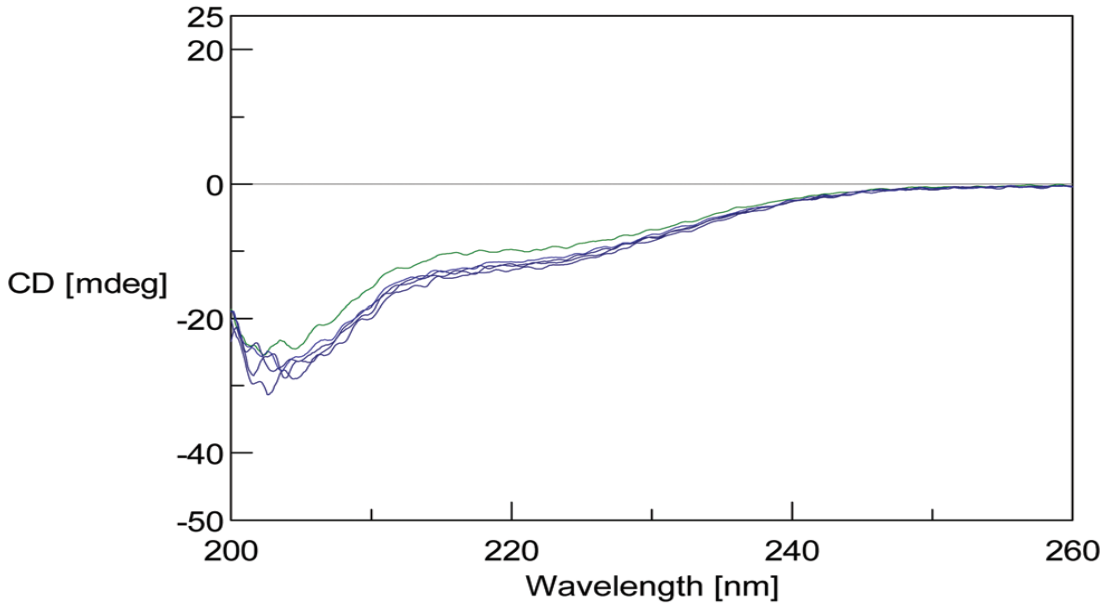

Figure 5.12. CD spectra of Lyz-AuNCs with increasing SDS in solution obtained from (161). The Lyz-AuNCs spectrum is shown in green, while Lyz-AuNCs with SDS added spectra are shown in blue. All measurements were taken in PBS buffer at pH 7.4. (Courtesy of Dr. Barbara Jachimska of Jerzy Haber Institute of Catalysis and Surface Chemistry, Polish Academy of Sciences).

To show the effect of added SDS in solution with Lyz-AuNCs on the encapsulating protein's structure, CD spectroscopy was carried out on Lyz-AuNCs with increasing SDS concentration, as shown in Figure 5.12. From Figure 5.12, we can see that initially upon adding 2 mM of SDS to Lyz-AuNCs in solution, an increase in the α-helix content is observed, and upon further increasing the SDS concentration, no clear further changes are observed in the Lyz-AuNCs structure. The initial increase in the disordered structure feature seen as a trough at 203 nm further lends weight to the idea that the dramatic initial decrease in AuNCs fluorescence observed results from a major unfolding of the encapsulating protein.

5.4.3 Effect of Elevated Temperature on Lyz-AuNCs

In order to remove any effects caused by interactions between the protein and denaturants, temperature-based experiments were carried out to better understand the response of AuNCs fluorescence to the unfolding and exposure of AuNCs to the solvent. To this end, samples of Lyz-AuNCs were heated and stabilised at 65 °C and the fluorescence emissions of Trp and AuNCs were monitored over a

period of 16 hours, exciting at 295 nm and 470 nm. This temperature was selected as Venkataramani et al. previously showed that lysozyme begins to lose its tertiary structure at this temperature (177). The fluorescence emission maximum of Trp as a function of time spent at 65 °C is shown in Figure 5.13. Interestingly, Trp emission decreases in two steps, similar to the AuNCs emission decreases, as seen in Figure 5.11. The fast decrease in Trp emission in the first hour of heating indicates that the protein undergoes a major unfolding event resulting in Trp becoming solvent exposed and undergoes increased collisional quenching. The peak emission wavelength was also red shifted during this time by 4 nm and then remained unchanged for the duration of the experiment. From 1–16 hours, the fluorescence maximum emission intensity continues to decrease linearly but at a slow rate, indicating that the protein undergoes further unfolding, exposing the Trp to higher rates of collisional quenching.

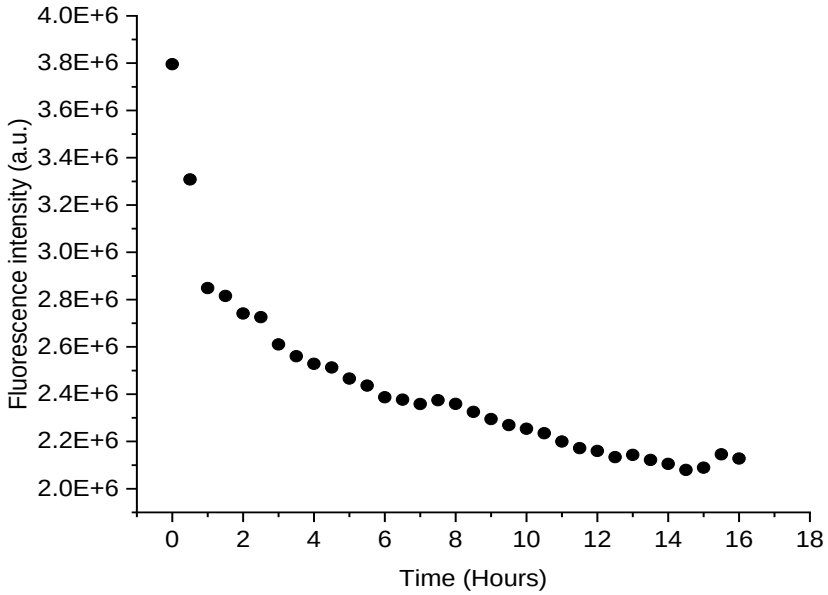

Figure 5.13. The peak emission intensity and of Trp in Lyz-AuNCs as a function of time length at 65 °C at an excitation wavelength of 295 nm.

The fluorescence emission maximum of AuNCs was also recorded during heating, exciting at 295 nm and 470 nm. The results are displayed in Figure 5.14

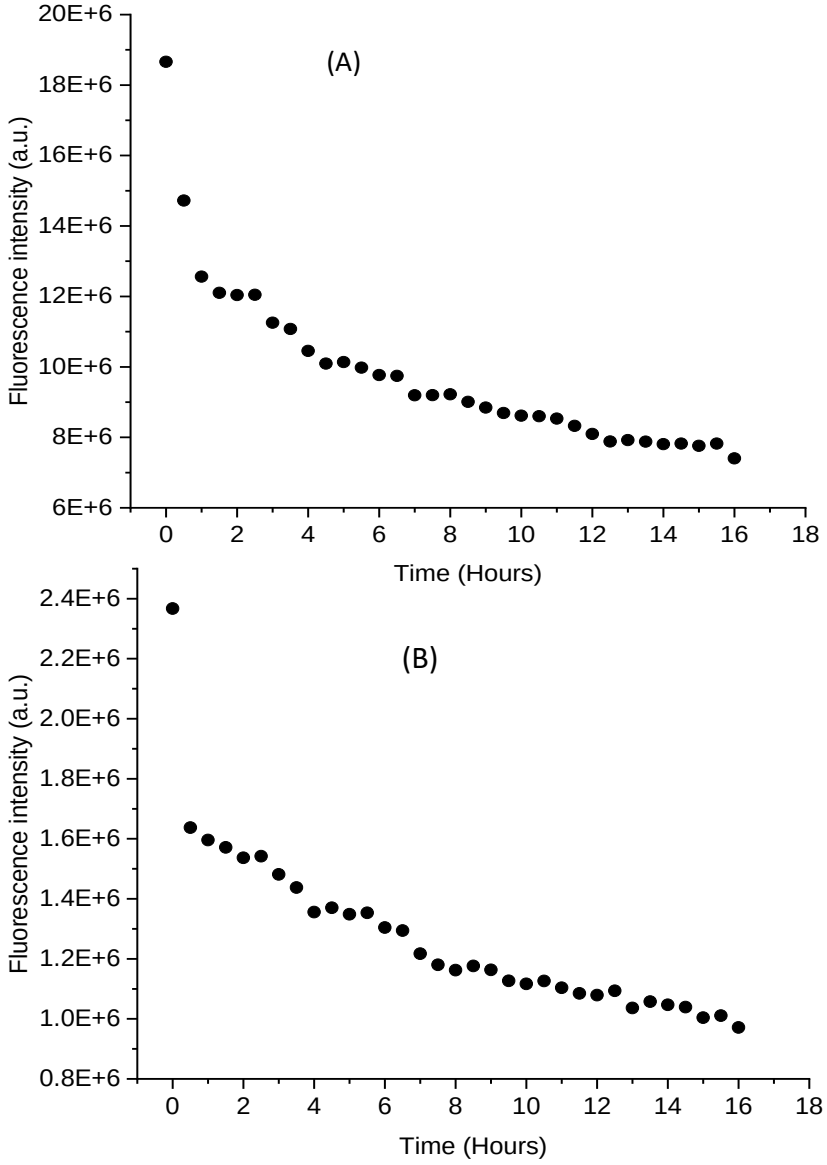

Figure 5.14. The peak emission intensity of AuNCs in Lyz-AuNCs as a function of time length at 65 °C (A) at an excitation wavelength of 295 nm and (B) at an excitation wavelength of 470 nm.

Figures 5.14 show the effect of temperature on the fluorescence intensity of Lyz-AuNCs is measured at 65 °C for 16 h at both excitation wavelengths 295 and 470 nm. The fluorescence intensity of AuNCs decreases about 60% and 58% at excitation wavelengths 295 and 470 nm, respectively.

The previous study showed that HEWL is stable at low temperatures. As the denaturation temperature increases, HEWL aggregates due to a decrease in the intermolecular repulsive forces that accompany changes in the secondary structure, in particular the decrease in α-helix structure and increase in β-sheets structure. As

the temperature increases from 35°C to 55 °C, there is a decrease in the α-helix structure and an increase in β-sheets. There is a slight change in the secondary structure with a further increase in the temperature from 55 to 90 °C, indicating that the unfolding is complete at 55 °C. At pH 1.6, the decrease in the α-helix structure and increase in β-sheets structure occurred first 40 °C, while at pH 5.9, this change occurs at 60 °C (134). From previous research, HEWL does not show any change in secondary structure at pH 7 until reaching 65 °C (177).

Exposure of protein to elevated temperature can lead to disordered or ordered aggregation depending on the temperature. For example, at pH 1.6, no fibrils are formed below 55 °C, whereas the fibrils are longer and present in higher quantities between 65 and 70 °C. Higher amounts of short fibrils are formed above 80 °C (134). Therefore, Thioflavin-T (ThT) is used to detect amyloid formation (more discussion in Chapter 6).

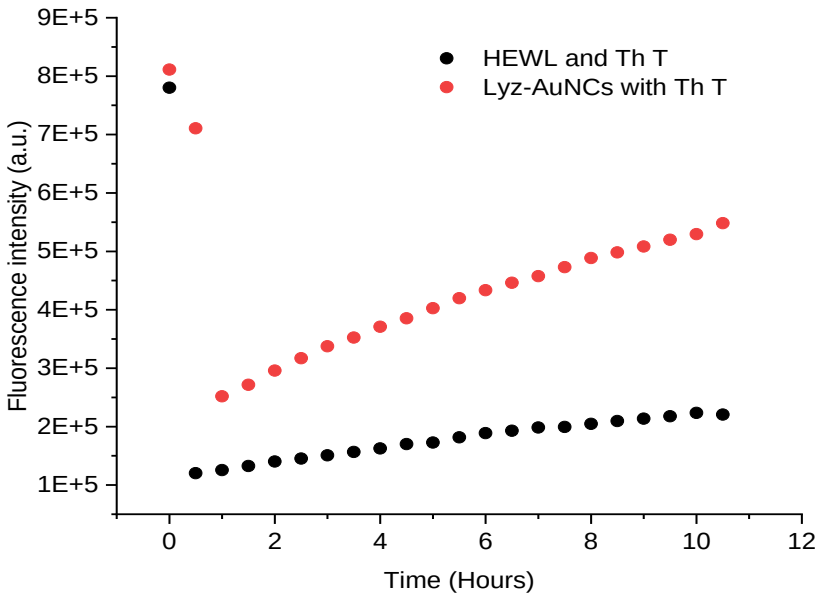

Figure 5.15. The fluorescence intensity of ThT in HEWL (black circles) and in Lyz-AuNCs (red circles) as a function of time length at 65 °C at an excitation wavelength of 440 nm.

Figure 5.15 compares the fluorescence intensity of ThT in HEWL and in Lys-AuNC as a function of time under 65 °C. It was found that the fluorescence intensity of ThT decreases by about 69% and 83% in HEWL and Lyz-AuNCs, respectively after 1 h. The low ThT fluorescence intensity due to charge transition from locally excited (LE) state to twisted internal charge transfer (TICT) state at elevated temperature

leads to non-fluorescence emission (192). There is no change in the peak emission wavelength of ThT. After 10 h, the fluorescence intensity of ThT increases about 1.8 fold and 2 fold in HEWL and Lyz-AuNCs, respectively. The higher intensity in Lyz-AuNCs is possible due to the presence of the AuNCs, which leads to changes in the structure of lysozyme. This may result in an increase in the simplicity of lysozyme to form β-sheets content at a higher temperature. Ow and Dunstan found that the fluorescence intensity of ThT is high at 65 °C, which indicates the formation of amyloid at this temperature (134). This change in the structure may cause a change in the fluorescence intensity of AuNCs.

5.4.4 Effect of Oxygen on Lyz-AuNCs

In solution, oxygen is well known to act as a collisional quencher of numerous fluorescent molecules and dyes (193–195) due to its triplet ground state inducing intersystem crossing.

To confirm the effect of collisional quenching on the fluorescence characteristics of Lyz-AuNCs, oxygen was removed by bubbling nitrogen into the Lyz-AuNCs solution, a commonly used technique for the removal of dissolved oxygen in water (196). Nitrogen gas was bubbled through the solution of Lyz-AuNCs for 20 minutes, and fluorescence spectra and fluorescence lifetime measurements were immediately carried out, as shown in Figure 5.16 and Table 5.3.

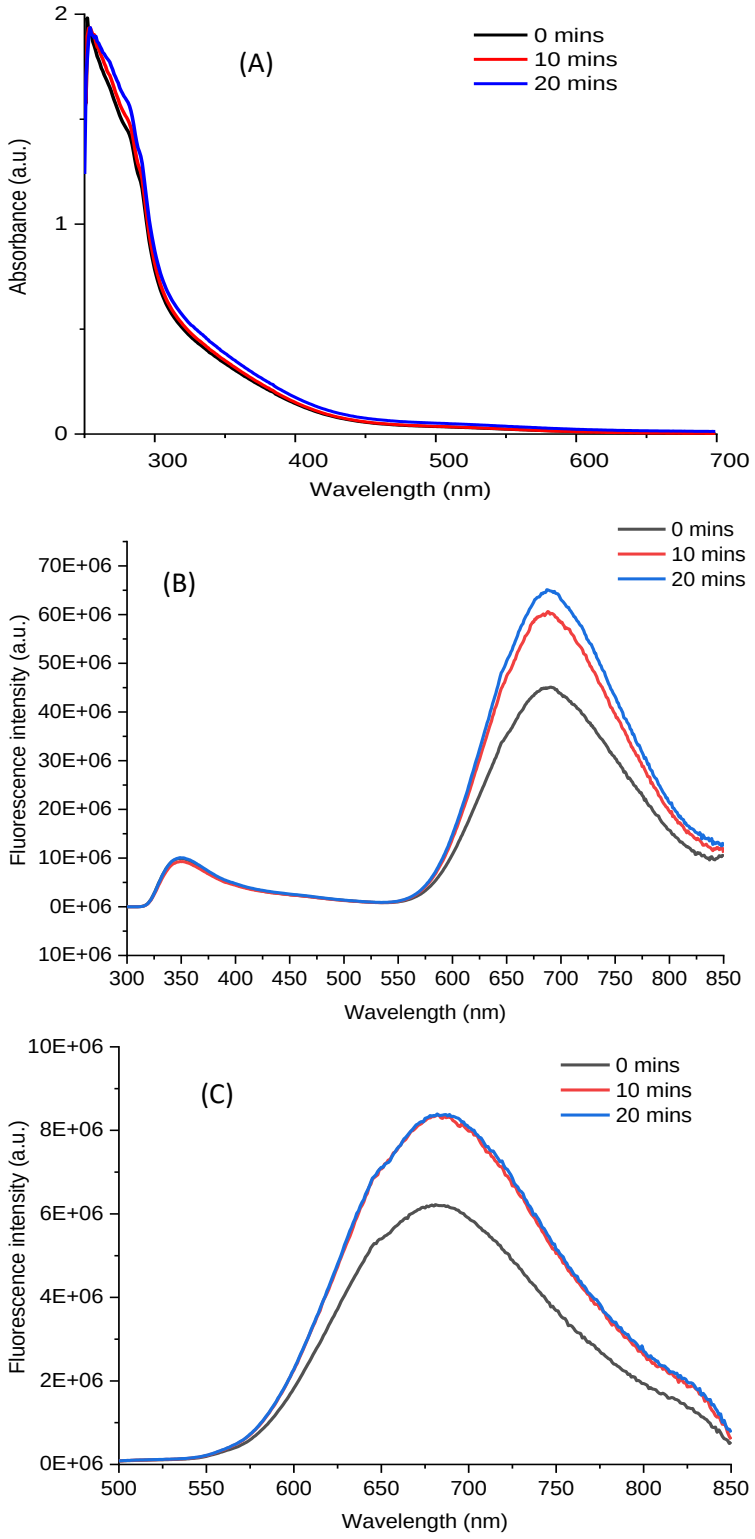

Figure 5.16. UV-Vis spectra and fluorescence emission spectra of Lyz-AuNCs was exposed to nitrogen gas for (0, 10, and 20) min. (A) UV-Vis spectra of Lyz-AuNCs, (B) Fluorescence emission of Lyz-AuNCs at an excitation wavelength 295 nm, (C) Fluorescence emission of Lyz-AuNCs at an excitation wavelength 470 nm. Lyz-AuNCs before exposure to nitrogen gas (black), Lyz-AuNCs after exposure to nitrogen gas for 10 mins (red), and for 20 mins (blue).

From Figure 5.16, it is clear that while Trp emission is not affected by the removal of oxygen possibly due to FRET with AuNCs and its faster decay time, the AuNCs themselves have a large increase in the fluorescence emission intensity due to a reduced non-radiative relaxation resulting from oxygen collisional quenching. Upon excitation wavelength at 470 nm, the same effect can be seen. As previously, a 3 exponential fitting was used to fit the fluorescence decay curve and results are shown in Table 5.3. No change in τ_3 was found as might be expected for scattered light. An increase in fluorescence decay time indicates that collisional quenching has been reduced upon the removal of dissolved oxygen, resulting in the AuNCs remaining in the excited state for a longer period of time on average.

Table 5.3. Fluorescence lifetime τ and amplitudes α of Lyz-AuNCs before (zero) and after bubbled for nitrogen gas (20 mins).

Time (mins)	τ_1 (ns)	α_1	τ_2 (ns)	α_2	τ_3 (ns)	α_3	χ^2
Zero	2357 ± 20	0.33	1021 ± 45	0.33	199 ± 7	0.40	1.07
20	2647 ± 25	0.32	1100 ± 43	0.32	184 ± 7	0.40	1.10

The effect of oxygen on the fluorescence of BSA-Au_{25}NCs has been studied by Tarasankar Das et al. (197). They reported the fluorescence intensity of BSA-Au_{25}NCs decreases by 41% in the presence of oxygen due to the diffusion-controlled processes, with a decrease in the lifetime of Au_{25}NCs in the presence of oxygen (197). The increase of lifetime of AuNCs in the removal of oxygen observed here indicates the quenching due to oxygen is dynamic in nature.

5.5 Conclusion

The sensitivity of AuNCs to lysozyme unfolding induced via urea, SDS, and elevated temperature has been elucidated via steady-state, time-resolved fluorescence and CD spectroscopy. It was found that in all three cases the major factor of reduced fluorescence emission was due to the exposure of the AuNC to the surrounding solvent and subsequent collisional quenching by dissolved oxygen.

In the case of urea and SDS induced quenching, tryptophan emission was initially recorded to increase, however, the mechanism is believed to be different; for urea, the observed increase was attributed to reduced quenching and FRET from neighbouring residues, while for SDS the Trp becomes less solvent exposed and thus collisional quenching decreases. In the case of SDS and elevated temperature, an initial fast linear decrease of AuNCs maximum fluorescence intensity was observed followed by a long, slow linear decrease. For SDS, it was seen that the CD spectra rapidly change upon initial addition of SDS, with subsequent increases in SDS concentration having less of an effect on the protein structure. We believe that the initial fast decrease is due to a rapid change in the protein structure at the location of the AuNCs, resulting in solvent exposure, followed by further unfolding of the protein which did not significantly affect the AuNCs location in terms of further solvent exposure. The fluorescence decay components of AuNCs, when excited at 482 nm, were found to be partly sensitive to protein unfolding. The longer decay component τ_1 was observed to decrease as the protein unfolded, due to the increased collisional quenching. The shorter decay component τ_2 was found to be less if at all sensitive to the protein unfolding. Oxygen removal studies found that AuNC fluorescence emission is highly sensitive to dissolved oxygen in solution. Therefore, oxygen is the most likely reason for quenching upon protein unfolding. This study highlights the possibility of using AuNCs as a useful probe for protein unfolding studies. It is envisaged that further studies on the location of AuNCs within each protein would shed light on employing AuNCs to study protein unfolding dynamics.

Chapter 6: Interaction between Human Beta Amyloid ($A\beta_{40}$) and Lyz-AuNCs

6.1 Abstract

Accumulations of abnormal proteins called amyloid fibrils (e.g. beta-amyloid ($A\beta_{40}$) fibrils) can cause a variety of diseases such as Alzheimer's disease (AD). Thus, to develop a therapy, it is important to identify candidates to inhibit the aggregation of $A\beta_{40}$. This chapter reported the study on the effect of HEWL on $A\beta_{40}$ aggregations. Furthermore, it investigated the interaction between Lyz-AuNCs and $A\beta_{40}$ as well as the effects of the former on amyloid fibril formation. These interactions were studied using UV–Vis spectroscopy, steady-state and time-resolved fluorescence spectroscopy and SEM. It was found that the fluorescence intensity of Thioflavin T (ThT) in $A\beta_{40}$ remains low in the presence of HEWL, indicating that HEWL can inhibit amyloid fibril formation. Moreover, blue shift and decrease in the absorbance at the 280 nm suggested the formation of large aggregation after adding HEWL to $A\beta_{40}$, possibly due to electrostatic interaction between HEWL and $A\beta_{40}$. A decrease in the fluorescence intensity of tryptophan (Trp) in HEWL with a blue shift further confirmed the interaction between $A\beta_{40}$ and HEWL.

In the case of the Lyz-AuNCs, the absorbance at 350 nm increased slightly after adding them to $A\beta_{40}$, possibly due to binding between the AuNCs and $A\beta_{40}$. The fluorescence intensity of ThT did not change after two weeks, indicating the absence of fibrils, as confirmed by SEM. The decrease in the fluorescence intensity of Trp in the Lyz-AuNCs was accompanied by a redshift of 2 nm, suggesting that a change in the local environment occurred due to the binding of the Lyz-AuNCs to $A\beta_{40}$. Moreover, the increase in the concentration of $A\beta_{40}$ from 6–16 μM decreased the fluorescence intensity of the AuNCs. Both the lifetime measurement and Stern–Volmer plots showed that the decrease in the fluorescence intensity was due to static quenching. This study demonstrated that Lyz-AuNCs efficiently inhibited the

aggregation of $A\beta_{40}$ in vitro as native lysozyme; furthermore, they did not form large lysozyme-peptide particles as native lysozyme did. Thus Lyz-AuNCs could be a promising candidate for AD treatment as well as an ideal probe to study $A\beta_{40}$ accumulation and neuroinflammation in AD pathology.

6.2 Introduction

Misfolding in amyloid fibrils and the aggregation of these insoluble proteins into assemblies can lead to many diseases depending on the protein types (10). For example, hereditary systemic amyloidosis results from human lysozyme gene mutations (5). Another well-known disease associated with high levels of beta-amyloid (Aβ) in the brain is Alzheimer's disease (AD) (140). Aβ is formed as a cleavage product by two proteases, ß-secretase and γ-secretase. These products are known as beta-amyloid precursor proteins (198). Their number of amino acid residues varies up to 43 (199). $A\beta_{40}$ and $A\beta_{42}$ are the predominant peptides in neuritic plaque (141,200).

AD leads to a reduction in brain function. It is mostly diagnosed in the elderly population worldwide (140,201) An estimated 5.7 million people have been diagnosed with AD in the US (140), while the corresponding numbers are 50,000 in the Kingdom of Saudi Arabia (202) and more than 1,000,000 in the UK (203). The mortality of AD increased, whereas those of heart disease, stroke and prostate cancer decreased from 2000–2015 (140). Therefore, it is crucial to identify inhibitors to prevent the aggregation of amyloid-β species.

Several methods have been used to inhibit $A\beta_{40}$ aggregations. Examples include using chaperones, namely molecules that help to restore misfolded protein structures (15,204). When proteins are misfolded in the body, chaperones such as Hsp70 interact with them to regulate their folding (15).

Various non-chaperones can also help to regulate the folding of proteins in vitro, such as clusterin, a2-Macroglobulin (a2M), pyruvate kinase, lactoglobulin β-lactalbumin and human lysozyme (119,205). However, efficient inhibition of $A\beta_{40}$ amyloid formation occurs at only suitable non-chaperone: $A\beta_{40}$ ratios. For example, low concentrations of clusterin, a2M or human lysozyme can induce the formation of $A\beta_{40}$ amyloids (15).

However, the above mentioned biomolecules suffer from limitations and can cause side effects. It was found that clusterin cannot refold non-native enzymes that have lost its structure due to heat. The ability of clusterin to bind to $A\beta_{40}$ and prevent amyloid formation is highly specific in the early stages of aggregation. This ability decreases with the ageing of $A\beta_{40}$ amyloid aggregations, following which clusterin cannot restore the structure of $A\beta_{40}$ peptides. a2M can prevent proteinase K from destroying prion proteins, leading to prion disease pathology (15). Therefore, developing a new $A\beta_{40}$ inhibitor using nanotechnology, including AuNPs or AuNCs, has attracted great interest in recent years.

The effects of the size, shape and surface chemistries of AuNPs on polypeptide aggregations have been studied (86,206). These studies found that AuNPs can inhibit the formation of amyloid fibrils depending on their size and surface charge. Liao et al. found that bare AuNPs and carboxyl-conjugated AuNPs inhibited $A\beta_{40}$ amyloid fibril aggregations (87). Gao and co-workers found that the size of the AuNPs determines whether they accelerate or inhibit amyloid fibril aggregations. They observed that while AuNCs can inhibit $A\beta_{40}$ amyloid fibril aggregations, large-sized AuNPs hasten $A\beta_{40}$ amyloid fibril aggregations (85), as discussed in Chapter 1 (see 1.6: The Effect of AuNCs and AuNPs on Peptide and Protein Structure).

AuNCs are beneficial in brain imaging and therapy due to their fluorescence, non-toxic and biocompatible properties (31,59,207). In addition, AuNCs can cross the blood-brain barrier in contrast to Thioflavin T (ThT) (88,208). This feature is most desirable in medical applications since most drugs are unable to pass through

the blood-brain barrier without disruption. Previous works show that AuNCs can be used as a drug or imaging tool for AD (209,210).

AuNCs can be synthesised using different proteins, including the hen egg white lysozyme (HEWL). Lysozymes are of varied types (e.g. human lysozyme and HEWL). HEWL is typically chosen in this study because it is non-toxic, easily available for commercial use and inexpensive. More importantly, it is similar to human lysozyme, which serves as an antimicrobial agent (see 2.2.6: Lysozyme Background in Chapter 2). A considerable amount of human lysozyme is found in human saliva, spleen, tears, and the liver, and crucially, it is also present in cerebrospinal fluid (CSF). Increased levels of human lysozyme have been reported in the CSF of patients with AD, suggesting that it acts as a defence against amyloid-β species aggregation (119). Previous studies have found that human lysozyme inhibits the aggregation of $A\beta_{40}$ and $A\beta_{42}$ (70,205,211).

This chapter presents the study on the interactions of Lyz-AuNCs with $A\beta_{40}$ in comparison with the interaction of HEWL with $A\beta_{40}$. Three questions were investigated: first, can HEWL inhibit the aggregation of amyloid fibrils, similar to the human lysozyme? Second, can Lyz-AuNCs inhibit the aggregation of $A\beta_{40}$? Third, how do $A\beta_{40}$ monomers affect the fluorescence properties of Lyz-AuNCs? Studying the interaction between Lyz-AuNCs and $A\beta_{40}$ could lead to an alternative AD treatment method and serve as a potential tool to detect amyloid-β species simultaneously, using the fluorescence properties of AuNCs. Moreover, the results of this work could lead to potential drug discoveries, with the inexpensiveness of the protein and its great abundance.

6.3 Thioflavin T

Thioflavin T (ThT) is a positively charged aromatic heterocyclic compound and is used as a sheet-sensing dye. ThT has been applied in the detection of amyloids since the interactions between it and amyloid fibrils are highly specific; in other words, the fluorescence properties of ThT do not change when a protein folds,

unfolds or folds partially. Moreover, the fluorescence intensity of ThT does not increase in amorphous aggregates (another type of aggregation which does not have the amyloid fibril (β sheet) structure). Therefore, ThT is considered to be a convenient diagnostic tool (212).

In order to appreciate the mechanism behind the detection of amyloids by ThT, it is important to understand the chemical structure of ThT and its relevant physical properties. Figure 6.1 shows that the ThT structure is made up of three parts: a benzothiazole ring, a benzene ring and the dimethylamino group. The benzothiazole ring is polar because it has two polar atoms, N and S. These atoms have high electronegativity, while the benzene ring is hydrophobic (non-polar) because the C and H atoms of the ring have low electronegativity and bind to the dimethylamino group which is characterised by low electronegativity and contains two methyl groups at the end (180,192).

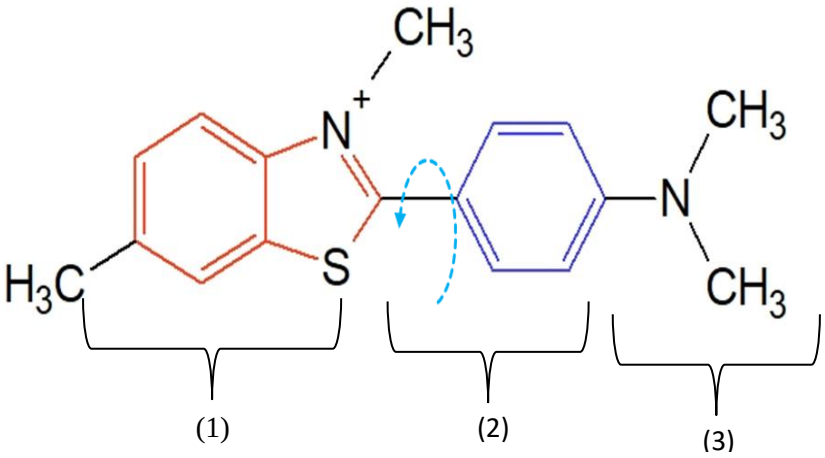

Figure 6.1. Structure of Thioflavin T (ThT), comprising the benzothiazole ring (red), benzene ring (blue) and dimethylamino group (black).

The fluorescence intensity of ThT is still not well understood; nevertheless, several researchers have attempted to explain its fluorescence mechanism. Khurana et al. suggested that ThT molecules can exist as micelles in water, and the positively charged N in molecules interact with water, while the hydrophobic region in the interior avoids interactions with water. The formation of micelles leads to an increase in the fluorescence intensity of ThT at concentrations higher than critical

micellar concentrations (approximately 4 $\pm$ 0.5 μM). Compared with monomer ThT binding to amyloid fibrils, the micelles of ThT provide higher fluorescence intensity in the presence of amyloid fibrils. This is possibly due to the hydrophobic interactions between the ThT micelles and amyloids (180).

Stsiapura et al. argued that the micelles model suffers from a drawback; ThT has a positive charge that acts as a repulsive force and prevents the formation of micelles, specifically in the hydrophobic region surrounding the fibrils. Therefore, another model was proposed, wherein the fluorescence intensity of ThT increases when the microenvironment becomes highly viscous or rigid as a result of binding to amyloid fibrils. ThT is a molecular rotor; the bonds between the benzothiazole and aminobenzene rings undergo rotation. The fluorescence intensity varies depending on the angle between the benzothiazole and aminobenzene rings. When ThT is excited, two decay processes are possible. The first is a radiative transition, wherein the electron transfers from the locally excited (LE) state to ground state; the angle shifts from 37°–21°, as an example. The second decay process involves a non-radiative transition, wherein the electrons transfer from the LE state (known as planar conformation) to the twisted internal charge transfer (TICT) state (known as non-planar conformation), before transferring to the ground state. This transition occurs when the angle is shifted from 37°–90°. When ThT binds to amyloids forming a rigid planar conformation, its fluorescence intensity increases due to the reduction in the TICT state. The surrounding environment (e.g. higher viscosity and temperature) can also affect the fluorescence intensity of ThT (192,213).

6.4 Experiment

6.4.1 Sample Preparation

HEWL, ThT, hydrochloric acid (HCl; 1 N), sodium hydroxide (NaOH; 1 N) and gold (III) chloride trihydrate ($HAuCl_4{\cdot}H_2O$; $\geq$ 99.9%) were purchased from Sigma-Aldrich Chemicals. Amyloid β-Peptide (1–40) (human) was purchased from Tocris, Bio-Techne. 1,1,1,3,3,3-Hexafluoro-2-propanol (HFIP $\geq$ 99.5%) was purchased from

Acros Organics. (Hydroxymethyl) aminomethane (Tris base ≥ 99.8%) and uranyl acetate (UA ≥ 98%) were purchased from Thermo Fisher Scientific and Agar Scientific, respectively.

To prepare $A\beta_{40}$ for an experiment, 1 mg of $A\beta_{40}$ was dissolved in 2.310 mL of HFIP solution. The solution was sonicated for 10 min to dissociated the aggregations form of $A\beta_{40}$ (214,215), as shown in Figure 6.2. Then, the solution was divided into several Eppendorf® LoBind microcentrifuge tubes and dried (the HFIP was evaporated at 25 ℃). In order to remove the HFIP completely, the samples were dried under the hood and then stored at −20°C (216).

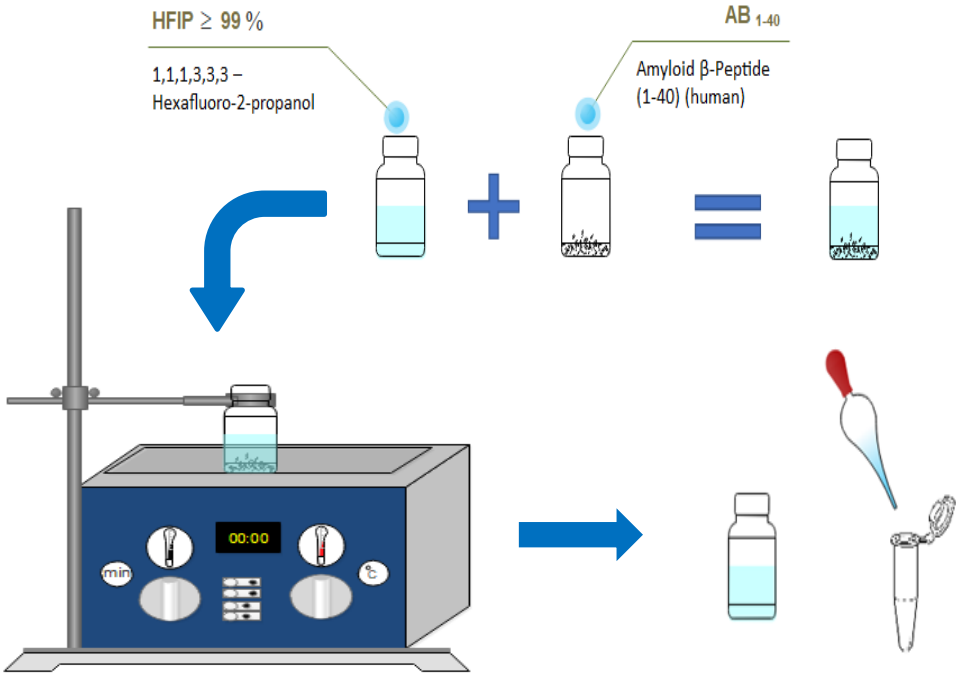

Figure 6.2. Preparation of $A\beta_{40}$ for the experiments

For the ThT fluorescence assay, 3 mM ThT stock solution was diluted in 50 mM Tris-HCl buffer (pH 7.4) to final concentration 10 µM. HEWL 1 mg was dissolved in Tris-HCl buffer (50 mM, 1 mL) to final concentration 70 µM at (pH 7.4). Then HEWL was mixed with Th T diluted in 50 mM Tris-HCl buffer (pH 7.4) to final concentration 25 µM of HEWL and 10 µM of ThT. Then, 100 µL of this solution was added to 5

nmol Aβ$_{40}$ in an Eppendorf® tube to yield a mixture containing 10 µM ThT, 50 µM Aβ$_{40}$ and 25 µM HEWL.

Lyz-AuNCs were synthesised, as explained in Chapter 4 (see Section 4.3.1. titled Sample Preparation) and dialyses against 50 mM Tris-HCl buffer (pH 7.4). The Lyz-AuNCs was mixed with Th T diluted in 50 mM Tris-HCl buffer (pH 7.4) to final concentration 25 µM of Lyz-AuNCs and 10 µM of ThT. Then, 100 µL of this solution was added to 5 nmol Aβ$_{40}$ in an Eppendorf® tube to yield a mixture containing 10 µM ThT, 50 µM Aβ$_{40}$ and 25 µM Lyz-AuNCs. It has been reported that 10 µM ThT is the effective concentration for amyloid formation studies (217). The mixture in the Eppendorf® tube was sonicated for a few minutes. The sample was placed in a micro cuvette for measurement. All the samples were measured at 37°C.

To study the effect of Aβ$_{40}$ on the fluorescence of Lyz-AuNCs, the Lyz-AuNCs were diluted in 50 mM Tris-HCl buffer (pH 7.4) and then mixed with different concentrations of Aβ$_{40}$ to yield mixtures containing 0–16 µM Aβ$_{40}$ and 25 µM Lyz-AuNCs. The mixture in the Eppendorf® tube was sonicated for a few minutes. The sample was placed in a micro cuvette for measurement. The quenching parameters ware calculated using the Stern–Volmer equation to interpret the type of quenching (91).

$$\frac{F_0}{F} = 1 + k_q \tau_0 [Q] = 1 + K_S [Q] \qquad (6\text{-}1)$$

Where F_0 and F are the fluorescence intensity without and with the quencher, respectively; k_q and K_s are the bimolecular quenching constant and the Stern–Volmer constant, respectively; [Q] is the concentration of Aβ$_{40}$ during the experiment and τ_0 is the average lifetime of the AuNCs in the absence of Aβ$_{40}$.

6.4.2 Spectroscopy Measurements

Each sample was placed in a 100 µL micro quart cuvette and measured using UV–Vis spectroscopy. The absorption spectra were recorded on a PerkinElmer Lambda 25 UV/Vis spectrometer. The fluorescence spectra were performed on a Fluorolog-3 spectrometer (Horiba, UK). ThT emissions were obtained by exciting the sample at a

wavelength of 440 nm and detecting emissions between 450 and 850 nm. The emissions from Trp in both HEWL and the Lyz-AuNCs were obtained by exciting the sample at a wavelength of 295 nm and detecting the emissions in the wavelength range of 300–850 nm. The emissions of the AuNCs were obtained by exciting the sample at 470 nm and detecting the emissions from 500–850 nm.

The lifetime measurements were performed using the time-correlated single-photon counting technique in a Horiba Jobin Yvon IBH equipped with a delta diode excitation wavelength source of 482 nm and a light emitting diode of 435 nm. All the decays were collected at a magic angle polarisation and analysed using IBH DAS6 software version 6.8.16 provided with the instrument.

The fluorescence intensity decays for the Lyz-AuNCs and ThT were analysed with the following formula:

$$I(t) = \sum_{i=1}^{n} \alpha_i e^{\left(\frac{-t}{\tau_i}\right)} \quad (6\text{-}2)$$

Where α_i denotes the amplitudes, and τ_i is the lifetime.

The average lifetime was calculated using Equation (6-3).

$$\bar{\tau} = \frac{\alpha_1\tau_1^2+\alpha_2\tau_2^2}{\alpha_1\tau_1+\alpha_2\tau_2} \quad (6\text{-}3)$$

Scanning electron microscopy (SEM) was used to study the morphology of the aggregations. Amyloid fibril formations were assessed by applying 10 µL of the sample to holey carbon films on 300 mesh copper grids. A filter paper was used to remove excess fluid after 2 min. After that, the grids were negatively stained with 2% (w/v) uranyl acetate. All the samples were incubated overnight before recording the images. The samples were observed by an FEI Quanta 250 FEG-SEM.

6.5 Results and Discussion

6.5.1 Effect of HEWL on $A\beta_{40}$

The UV–Vis measurements were used to assess the absorption of the sample for 96 hrs in order to study the interaction of $A\beta_{40}$ with HEWL. Figure 6.3 shows the absorption spectra of HEWL–ThT in the absence and presence of $A\beta_{40}$. Three peaks were observed. The peak at 415 nm was the peak of ThT absorption, while that at 273 nm was the peak of the aromatic amino acids (Trp and Try).

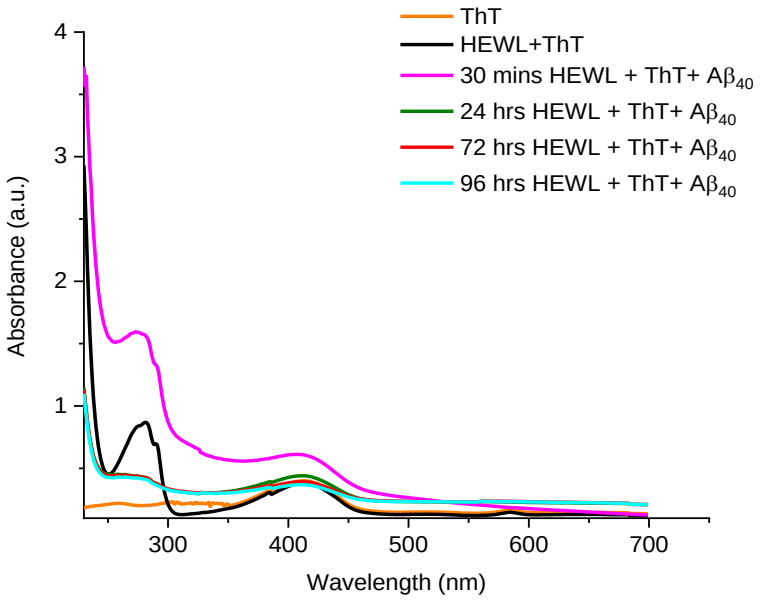

Figure 6.3. Absorption spectra of 25 µM HEWL and 10 µM ThT in the absence and presence of 50 µM $A\beta_{40}$ at pH 7.4 over 96 h.

Figure 6.3 shows an increase in the absorption of the amino acids by approximately 68% with a blue shift of about 7 nm in the presence in $A\beta_{40}$ at 30 min. After 24 h, the absorption of the amino acids decreased by approximately 39% at 273 nm, following which no changes in the absorption of the amino acids were observed after 24 h. In addition, an increase in the absorption of ThT by approximately 28% was noted in the presence of $A\beta_{40}$ at 30 min, followed by a reduction to its initial value after 24 h. No change in the absorption of ThT was observed after 24 h.

The increasing absorption of ThT and the amino acids after 30 min could be due to the binding of HEWL to $A\beta_{40}$, leading to the formation of a large HEWL–$A\beta_{40}$ complex. These large particles scatter light, resulting in higher attenuation. The blue shift in the absorption of the amino acids was due to the increases in the hydrophobicity around them. A blue shift in the absorption of the peak at 275 nm was also observed in previous studies (e.g. a blue shift was noted in the absorption peak of haemoglobin at 270 nm after binding to paraquat (218)). After 24 h, a decrease in the absorption of the amino acids occurred in the presence of $A\beta_{40}$ possibly due to HEWL binding to $A\beta_{40}$ and the resulting large aggregations followed by precipitation. The precipitation of large aggregations was observed at 24 h after the commencement of the experiment. Luo et al. noticed a decrease in the signal of circular dichroism measurements after 24 h. They ascribed the reduction in the signal to the formation of the complex (211), and their results coincide with our finding. The formation of the complex is shown in Figure 6.12 (B and E).

The ThT fluorescence in the $A\beta_{40}$–HEWL complex was studied to detect the formation of amyloids. Figure 6.4 shows the fluorescence intensity of ThT in three samples ($A\beta_{40}$, HEWL, and the combination of $A\beta_{40}$ and HEWL), measured over 12 h and 96 h each. The fluorescence kinetic assays of the amyloid formation of $A\beta_{40}$ over 96 h showed no major change in the fluorescence intensity of ThT before 24 h. The fluorescence intensity of ThT increased to approximately four-fold after 48 h. A slight drop was observed in the fluorescence intensity of ThT after 96 h. The fluorescence of ThT did not change in the HEWL sample. For the sample containing both HEWL and $A\beta_{40}$, the fluorescence intensity of ThT decreased to approximately 85% of the initial value after 4 h. Then, from 4 to 6.5 h, the fluorescence intensity of ThT increased to about twice the value at 4 h. From 6.5 to 72 h, no change was noted in the ThT fluorescence intensity. From 72 to 96 h, the fluorescence intensity of ThT decreased further.

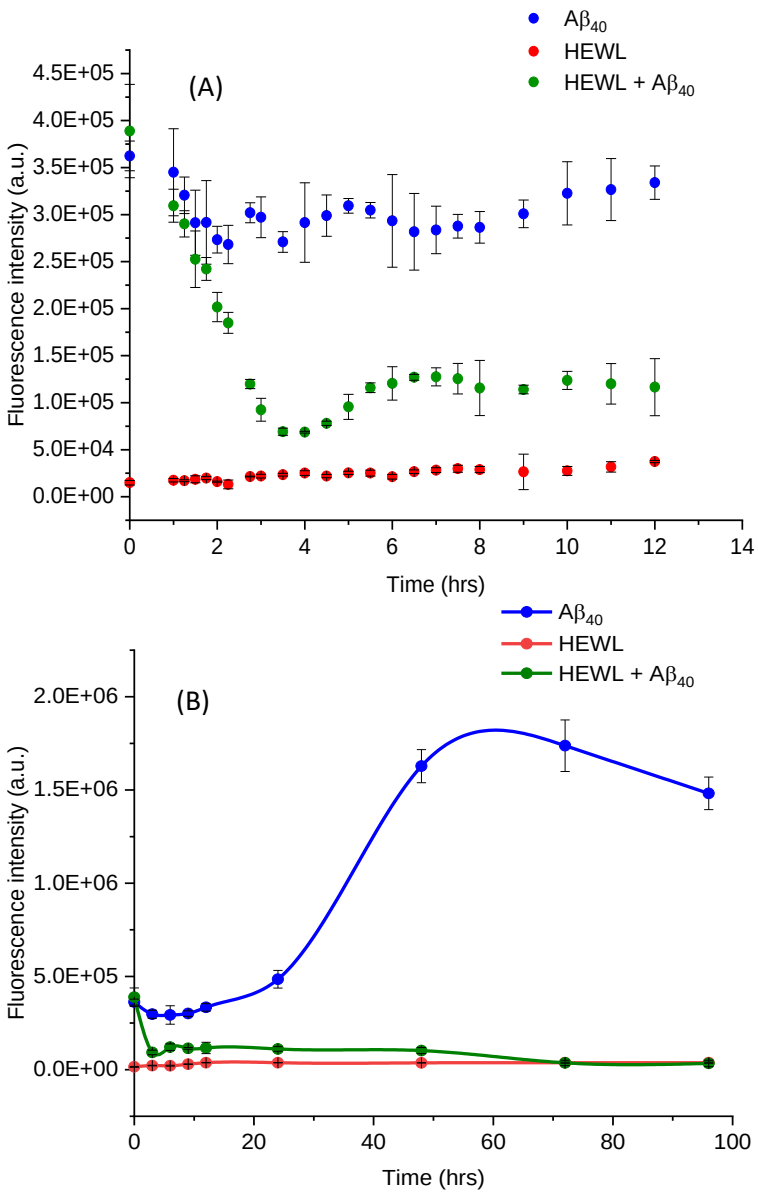

Figure 6.4. Effect of the HEWL on $A\beta_{40}$ amyloid fibril formation and the associated enhance in fluorescence intensity of ThT. ThT fluorescence assays of solutions of fresh native $A\beta_{40}$ (50 µM) incubated at 37 ℃ at pH 7.4 in the absence (blue) and presence (green) of HEWL (25 µM). HEWL (25 µM) without $A\beta_{40}$ was also monitored as control (red) (A) over 12 h and (B) over 96 h. Measured at an excitation wavelength of 440 nm.

The assays were conducted over 12 and 96 h to monitor the changes in the fluorescence intensity of ThT in detail. Luo et at. analysed the changes in the fluorescence intensity of ThT over 12 h only, since they only studied the rapid growth rate of the amyloid fibrils. Higher aggregation rates have been attributed to stirring the sample for 12 h (86,211).

As per Figure 6.4 (B), in the presence of $A\beta_{40}$, the kinetic fluorescence assays of $A\beta_{40}$ amyloid formation over 96 h indicated three stages of amyloid formation. The first stage was the lag phase, defined as the time needed to form nuclei from monomers in the solution. During this stage, the fluorescence intensity of ThT did not change. The second stage involved growth or elongation (known as the transition zone), wherein the monomers bind together to form small aggregates (e.g. dimers, trimers and oligomers) depending on their numbers. This stage occurred after 24 h and was marked by a linear increase in the fluorescence intensity over time until the intensity reached approximately four times the initial value (after 48 h). The final stage was the plateau phase, wherein the concentration of the monomers was at equilibrium with their numbers. This stage was marked by the formation of amyloid fibrils (14). The fluorescence intensity of ThT dropped slightly after 96 h.

Figure 6.4 (B) shows the lag phase at approximately 24 h, and no change in the fluorescence intensity of ThT was observed. It is expected that at the start of the experiment, $A\beta_{40}$ exists in the monomer form, and aggregation of the amyloids is absent. The use of HFIP (100%) during the preparation of $A\beta_{40}$ helped disrupt the hydrophobic interaction in the aggregated species, leading to the removal of pre-existing aggregations (214,215). After that, a growth phase from 24–72 h was noted, wherein the fluorescence intensity of ThT increased until it equalled four times the initial value. This increase in the fluorescence intensity was due to the formation of amyloids. Finally, no change in the fluorescence intensity of ThT was observed after 72 h. Our results show that the complete formation of $A\beta_{40}$ took 3 days, which coincides well with a previous report (122).

A different method can be applied to shorten the time period for $A\beta_{40}$ amyloid fibril formation. For instance, the solution can be shaken or stirred, as shown by Luo et al. in ref (211); in this case, the amyloid formation starts after 2 h. $A\beta_{40}$ aggregates rapidly at pH 5 compared to pH 7.4 (219).

The drop in the fluorescence intensity of ThT after 96 h was due to precipitation of mature amyloid fibrils. This drop was also observed in Figure 6.3 and in a previous study (205). The decrease in the fluorescence intensity was attributed to the aggregation of large particles and their subsequent precipitation, leading to a reduction in the number of excitable ThT molecules.

The fluorescence of ThT did not change in the sample containing only HEWL. Homchaudhuri et al. found that HEWL does not aggregate at pH 7 and a concentration of 40 μM at room temperature (136). Luo et al. noted that human lysozyme did not form amyloids in the absence of $A\beta_{40}$; therefore, the fluorescence intensity of ThT did not increase (211).

Figure 6.4 (A) shows that the initial fluorescence intensity of ThT was higher in the presence of both HEWL and $A\beta_{40}$ than that with HEWL alone. This was due to the presence of $A\beta_{40.}$ A previous study showed that the fluorescence intensity of ThT increased with the rise in the concentration of $A\beta_{40}$ (217).

In the presence of both HEWL and $A\beta_{40}$, the fluorescence intensity of ThT was the same as that of ThT in the presence of $A\beta_{40}$. The decrease in the fluorescence intensity of ThT from 30 min to 3 h was possibly due to the formation of large aggregates between HEWL and $A\beta_{40}$ followed by precipitation. After 3 h, the molecules reached the equilibrium state and were distributed uniformly in the solution. Thus, the fluorescence intensity of ThT did not decrease further.

Luo et al. found that human lysozyme inhibits $A\beta_{40}$ aggregation when the ratio of lysozyme to $A\beta_{40}$ is 2:1 or higher (211). No increase in the fluorescence intensity of ThT was observed in the presence of both HEWL and $A\beta_{40}$ after 96 h, suggesting delayed or inhibited the formation of amyloid fibrils. This indicates that lysozyme from hen egg white interacts with $A\beta_{40}$ in a manner similar to human lysozyme (119,205,211).

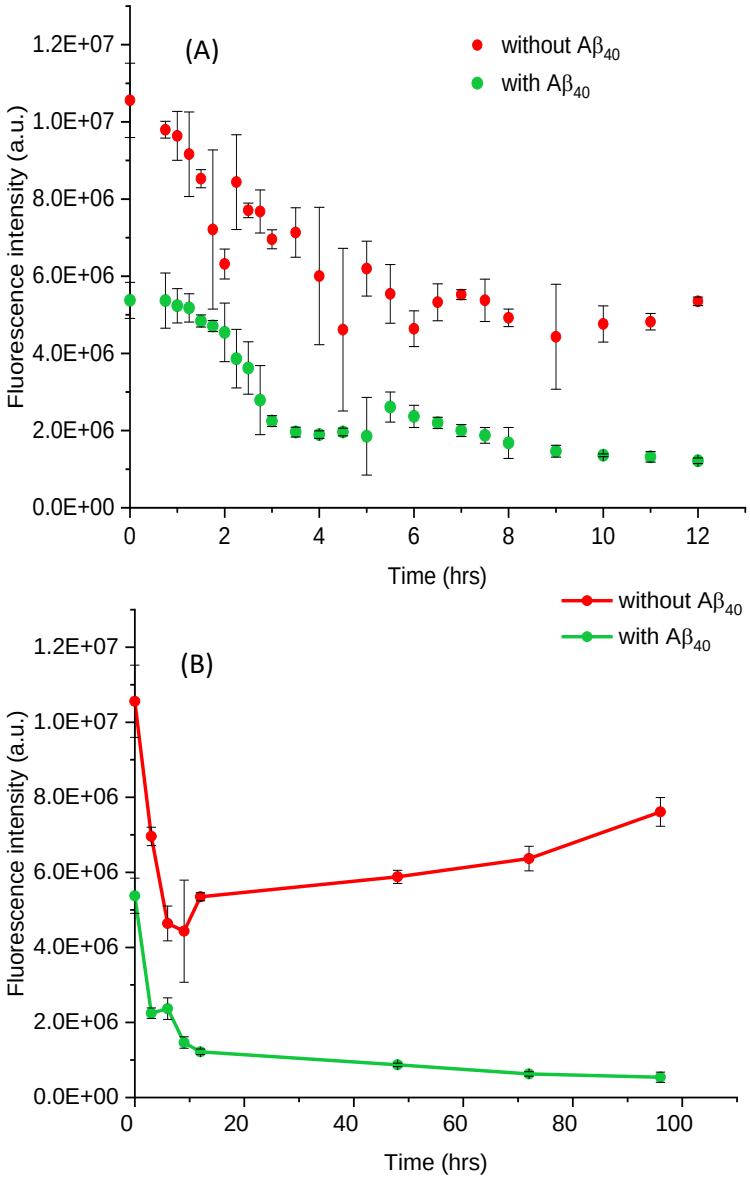

Figure 6.5. Kinetic assays of Trp fluorescence intensities in 25 µM HEWL in the absence (red line) and presence (green line) of 50 µM $A\beta_{40}$ over 12 h (A) and 96 h (B). Measured at an excitation wavelength of 295 nm.

The fluorescence properties of Trp in HEWL in the presence and absence of $A\beta_{40}$ were studied to monitor the change in the surrounding environment of Trp due to the modified structure of HEWL or binding to $A\beta_{40}$.

Figures 6.5 (A) and (B) show the fluorescence intensities of Trp in HEWL in the absence and presence of $A\beta_{40}$ measured over 12 and 96 h, respectively. In the absence of $A\beta_{40}$, the fluorescence intensity of Trp decreased by approximately 50%

at 12 h, and it does not change after that. In the presence of Aβ$_{40}$, the fluorescence intensity of Trp decreased to approximately 77% of the initial value after 12 h, and then gradually decreased until 96 h.

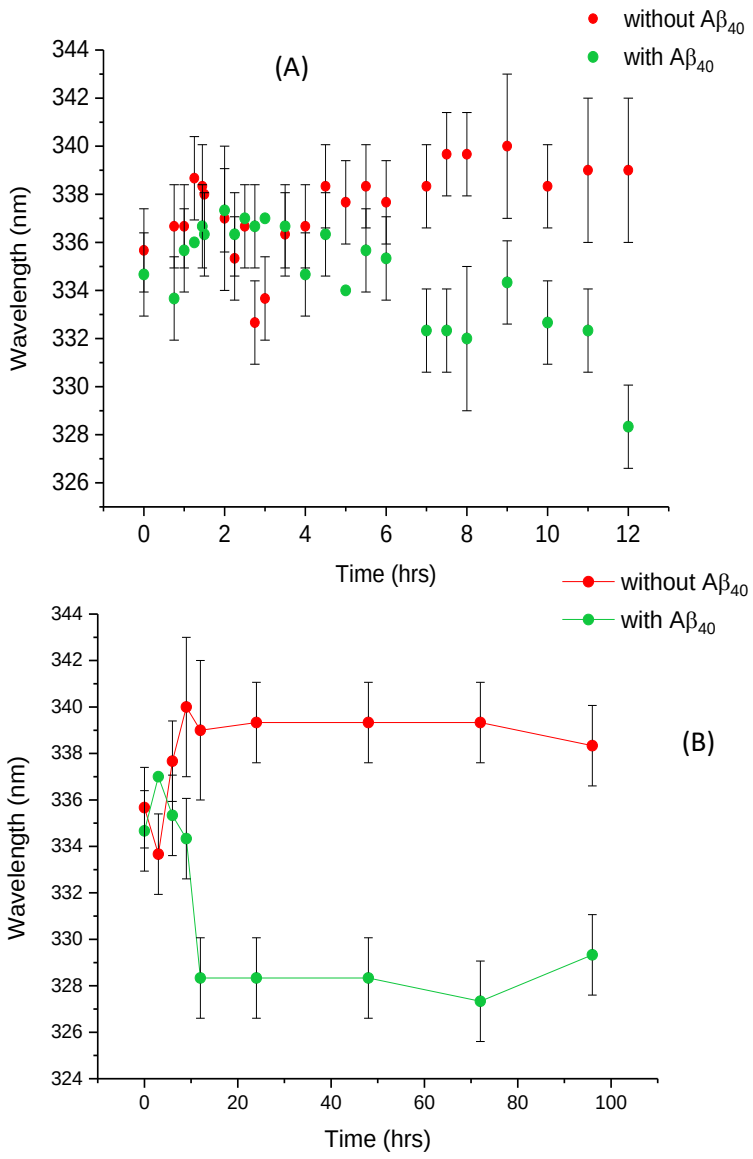

Figure 6.6. Kinetic assays of Trp fluorescence emission wavelengths in 25 µM HEWL in the absence (red line) and presence (green line) of 50 µM Aβ$_{40}$ over 12 h (A) and over 96 h (B). Measured at an excitation wavelength of 295 nm.

Figures 6.6 (A) and (B) show the fluorescence emission wavelengths of Trp in HEWL in the absence and presence of Aβ$_{40}$. The wavelength of Trp changed from 335 to 340 nm in the absence of Aβ$_{40}$. In the presence of Aβ$_{40}$, a shift from 335 to 328 nm was observed after 96 h.

The change in the fluorescence intensity and emission wavelength of Trp in the absence of $A\beta_{40}$ was probably due to the modification in the structure of HEWL over time. It is possible that Trp was surrounded by polar amino acids, as discussed in Chapters 5.

In the presence of $A\beta_{40}$, the decrease in the fluorescence intensity of Trp was possibly due to electrostatic interaction between HEWL and $A\beta_{40}$. At pH 7.4, the surface charge of HEWL is positive, and that of $A\beta_{40}$ is negative since the isoelectric points of both HEWL and $A\beta_{40}$ are approximately 11.35 and 5.3, respectively (71,220). As a result of this interaction, a higher reduction was observed in the fluorescence intensity of Trp in the presence of $A\beta_{40}$ compared to its absence. It is more likely that the decrease in the fluorescence intensity of Trp resulted from the formation of large aggregates and their subsequent precipitation, as confirmed by the UV–Vis measurement (see Figure 6.3).

The fluorescence emission wavelength of Trp was sensitive to surrounding environments, as shown in Figure 6.6. A redshift was noted when Trp was exposed to the polar molecules, whereas a blue shift was observed when Trp was near the non-polar (hydrophobic) molecules (221). According to Luo et al., the hydrophobic interaction between $A\beta_{40}$ and human lysozyme prevents $A\beta_{40}$ from forming beta-amyloids at a human lysozyme: $A\beta_{40}$ ratio of 1:1 (205,211).

The binding of $A\beta_{40}$ with human lysozyme was studied via computer simulation by Luo et al. (211). Three sites, A, B and C, play a role in this phenomenon. At site A, the phenylalanine (Phe 4), arginine (Arg 5) and histidine (His 6) amino acids of $A\beta_{40}$ bind to form the arginine (Arg 62), tyrosine (Tyr 63) and tryptophan (Trp 64) amino acids of human lysozyme. At site B, the glutamine (Gln 15) to valine (Val 24) and isoleucine (Ile 31) to valine (Val 40) ranges of $A\beta_{40}$ peptides interact with the α-helix range from aspartic acid (Asp 102) to arginine (Arg 107) and the loop range from the glutamine (Gln 117) to arginine (Arg 122) amino acids of human lysozyme. At site C, the isoleucine (Ile 31) to valine (Val 40) amino acids of $A\beta_{40}$ interact with the arginine (Arg 119) and serine (Ser 24) amino acids of human lysozyme (211). Luo et

al. also show that phenylalanine, tyrosine and tryptophan are affected by changes in the interactions between $A\beta_{40}$ and human lysozyme. Since the structures of human lysozyme and HEWL are similar, the results suggest that HEWL binds to $A\beta_{40}$, leading to the blue shift in the peak emission wavelength of Trp due to hydrophobic interactions.

6.5.2 Effect of Lyz-AuNCs on $A\beta_{40}$

Figure 6.7 shows the absorption spectra of Lyz-AuNCs without and with $A\beta_{40}$. An increase of approximately 23% in the absorption of Lyz-AuNCs was observed after adding $A\beta_{40}$. After 12 h, no change was noted. Furthermore, an increase of approximately 23% in the absorption was noted at 350 nm. The increase in the absorption of Lyz-AuNCs in the presence of $A\beta_{40}$ can be ascribed to the binding of $A\beta_{40}$ to Lyz-AuNCs. The change in the absorbance peak at 350 nm was used to measure turbidity. A rise in turbidity indicates an increase in the size of the proteins as a result of protein-protein aggregation (21,120,174).

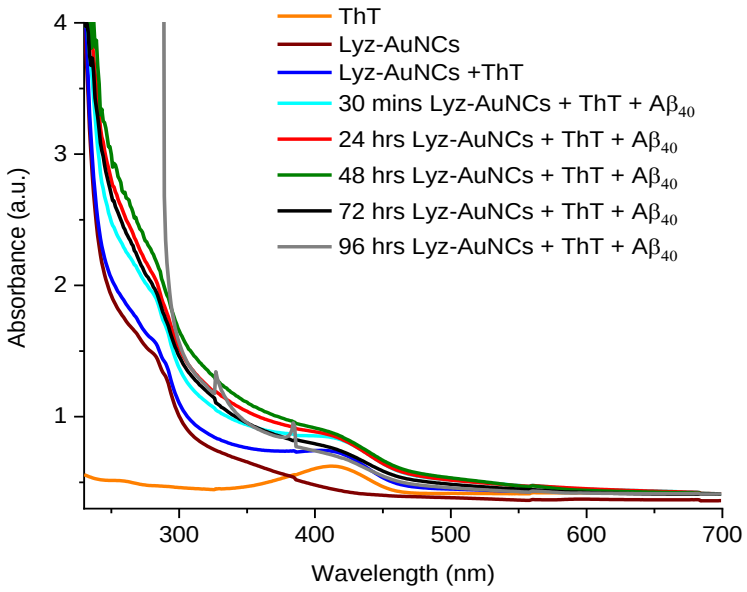

Figure 6.7. Absorption spectra of 25 µM Lyz-AuNCs in the absence and presence of 50 µM $A\beta_{40}$ at pH 7.4 over 96 h.

Similarly, the fluorescence intensity of ThT was monitored to detect the formation of amyloids in the three samples ($A\beta_{40}$, Lyz-AuNCs, and the combination of $A\beta_{40}$ and Lyz-AuNCs).

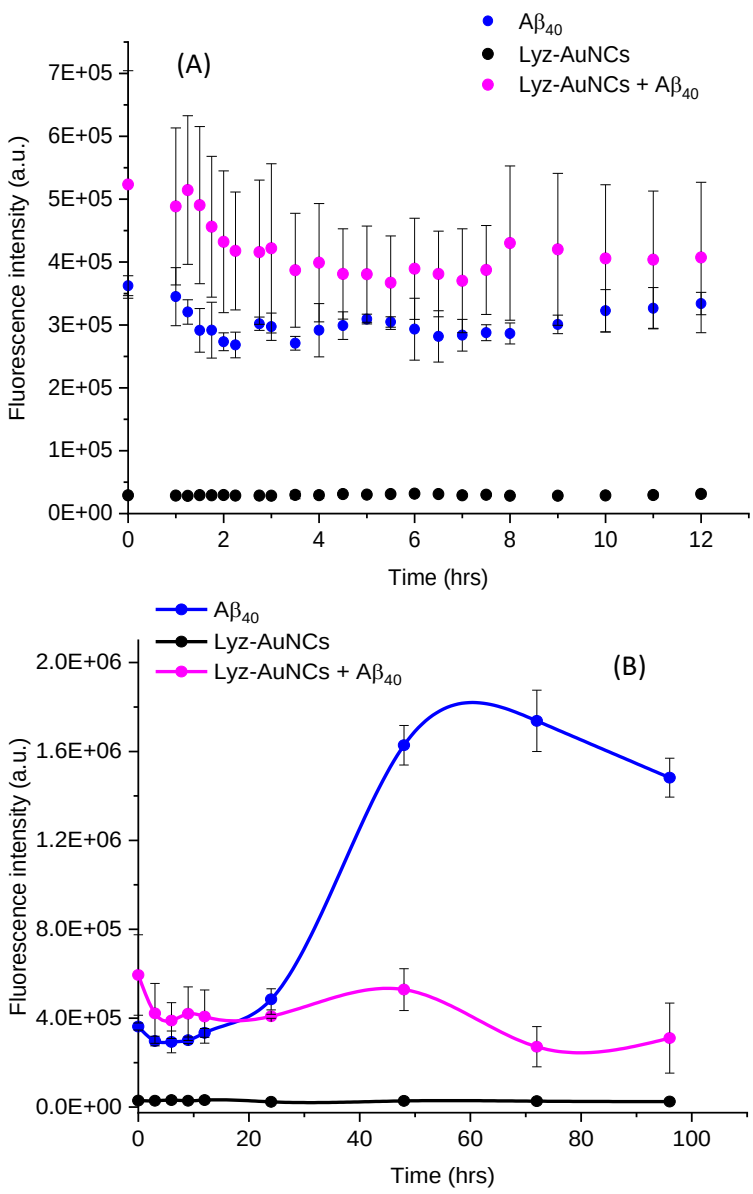

Figure 6.8. Effect of the Lyz-AuNCs on $A\beta_{40}$ amyloid fibril formation and the associated enhance in fluorescence intensity of ThT. ThT fluorescence assays of solutions of fresh native $A\beta_{40}$ (50 µM) incubated at 37 ℃ at pH 7.4 in the absence (blue) and presence (pink) of Lyz-AuNCs (25 µM). Lyz-AuNCs (25 µM) without $A\beta_{40}$ was also monitored as control (black) (A) over 12 h and (B) over 96 h. Measured at an excitation wavelength of 440 nm.

Figures 6.8 (A) and (B) show the ThT fluorescence kinetic assays of amyloid formation in $A\beta_{40}$, with and without Lyz-AuNCs together with Lyz-AuNCs control over 12 h and 96 h. The fluorescence intensity of ThT in Lyz-AuNCs remained stable over 96 h. In the case of $A\beta_{40}$ with the presence of Lyz-AuNCs, the intensity of ThT did not change significantly over 48 h, followed by a slight decrease after 96 h. This is in significant contrast to what observed in $A\beta_{40}$ without Lyz-AuNCs where the

fluorescence intensity of ThT in $A\beta_{40}$ increased to four times of the initial value after 72 h. This indicates that Lyz-AuNCs inhibited the formation of amyloid $A\beta_{40}$.

It is noted that the initial fluorescence intensities of ThT in the presence of both $A\beta_{40}$ and Lyz-AuNCs were higher than that in other samples. One of the hypotheses suggests that the increase in ThT fluorescence intensity is due to the prevention of the bond rotation between the benzene and benzothiazole rings, causing a reduction in the non-radiative pathway and thereby increasing the radiative emission (213). Therefore, the higher intensity is attributable to the fact that ThT becomes more rigid in the presence of the complex formed between $A\beta_{40}$ and Lyz-AuNCs. It is less likely that this intensity increase is due to amyloid formation since the amyloids would need to be highly ordered aggregated, which requires a considerable amount of time.

The initial value of the fluorescence intensity of ThT was found lower in Lyz-AuNCs compared with that in $A\beta_{40}$ or $A\beta_{40}$ with Lyz-AuNCs. It is possible that the fluorescence intensity of ThT increased due to the presence of a higher concentration of $A\beta_{40}$ (similar to Figure 6.4, where the fluorescence intensity of ThT in the presence of HEWL was very low).

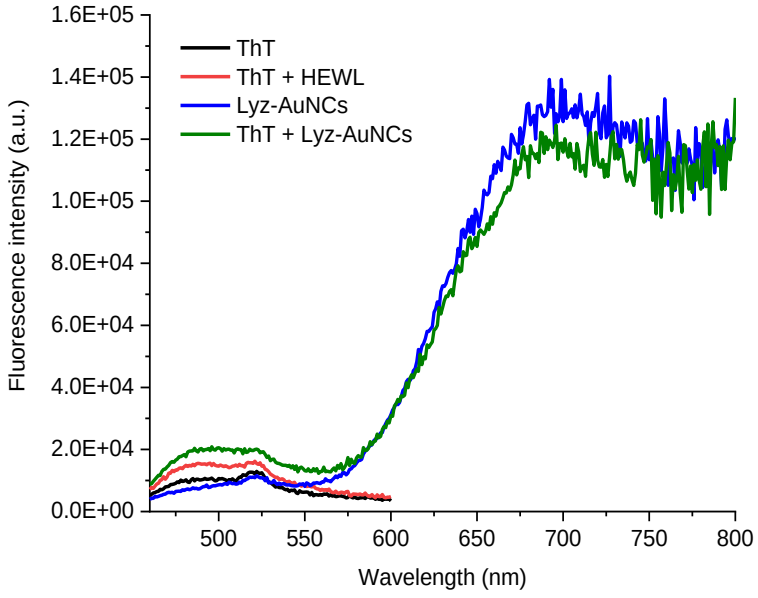

Figure 6.9. The fluorescence intensity of 10 µM ThT in the absence (black) and presence (red) of 25 µM HEWL. The fluorescence intensity of ThT and 25 µM Lyz-AuNCs in the absence (green) and presence (blue) of ThT. Measured at an excitation wavelength of 440 nm.

Table 6.1. Average lifetimes $\langle\tau\rangle$ of ThT in the presence of HEWL and Lyz-AuNCs calculated from triple-exponential fits of ThT emission decay curves. χ^2 is the Chi-Square goodness-of-fit test. All samples were in 50 µM Tris-HCl buffer at pH 7.4 and 37°C measured at the excitation wavelength of 435 nm

Sample	$\langle\tau\rangle$	χ^2
HEWL + ThT	0.7432507	1.20
Lyz-AuNCs + ThT	0.8102064	1.19

It is possible that the fluorescence intensity of ThT may be affected by the presence of AuNCs, therefore, the emission spectra of ThT in HEWL and Lyz-AuNCs, as well as the emission of AuNCs with and without ThT, were compared in Figure 6.9. The fluorescence intensity of ThT was found higher in the presence of Lyz-AuNCs compared with their absence. In addition, the intensity of AuNCs emission at 690 nm doesn't increase in the presence of ThT. This suggests that there was no FRET between ThT and AuNCs. In fact, the average lifetime of ThT increased in the presence of AuNCs, as shown in Table 6.1, confirmed the absence of FRET, consistent with the intensity analysis.

In a similar manner, the fluorescence properties of Trp in the Lyz-AuNCs were monitored in the absence and presence of $A\beta_{40}$ to study the effect of $A\beta_{40}$ binding on the structure of Lyz-AuNCs.

Figures 6.10 (A) and (B) show the Trp fluorescence intensities in the Lyz-AuNCs with and without $A\beta_{40}$ over 12 h and 96 h, respectively. In the absence of $A\beta_{40}$, the fluorescence intensity of Trp in the Lyz-AuNCs did not change after 96 h. Once the Lyz-AuNCs and $A\beta_{40}$ were mixed, the fluorescence intensity of Trp decreased by approximately 49% and 82% of the initial value after 12 h and 96 h, respectively.

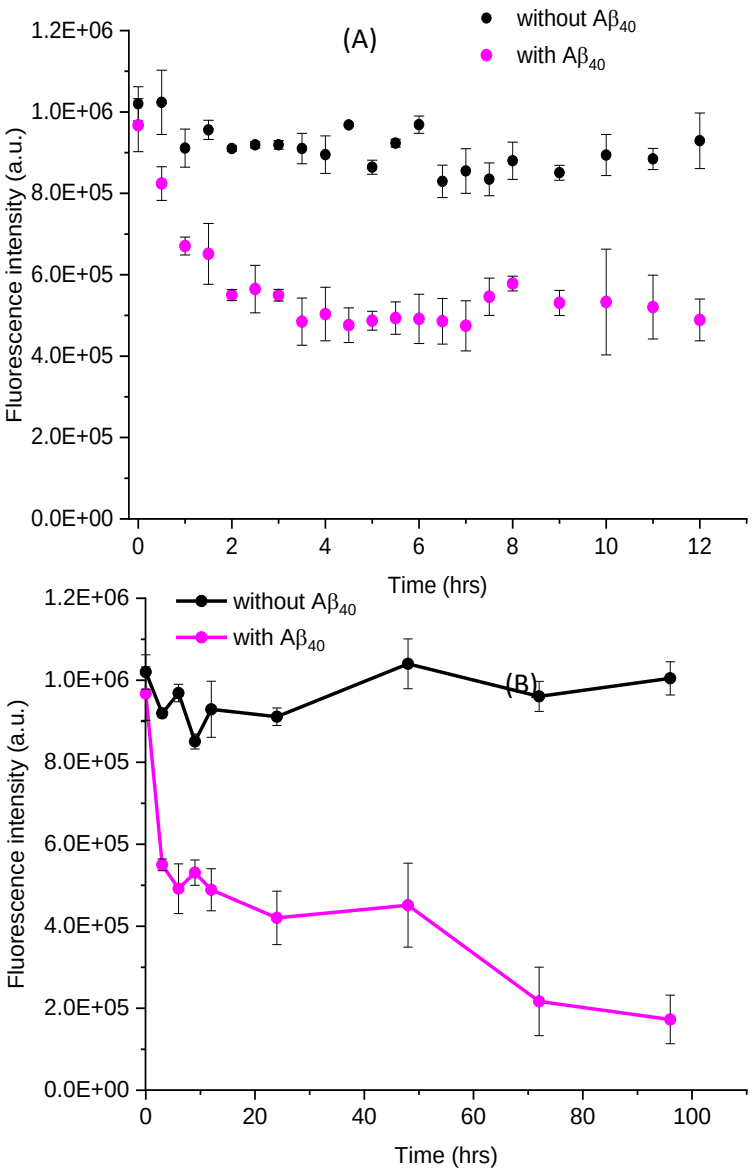

Figure 6.10. Kinetic assays of Trp fluorescence intensities in 25 µM Lyz-AuNCs in the absence (black) and presence (pink) of 50 µM $A\beta_{40}$ over 12 h (A) and 96 h (B). Measured at an excitation wavelength of 295 nm.

Figure 6.11 (A) and (B) show the kinetic assays of the Trp fluorescence emission wavelengths in the Lyz-AuNCs with and without $A\beta_{40}$ over 12 h and 96 h, respectively. The fluorescence emission wavelengths of Trp in the Lyz-AuNCs in the absence of $A\beta_{40}$ showed a redshift of approximately 2 nm. A similar wavelength shift was observed in Lyz-AuNCs in the presence of $A\beta_{40}$ suggests no influence of $A\beta_{40}$ on the emission wavelength of Trp.

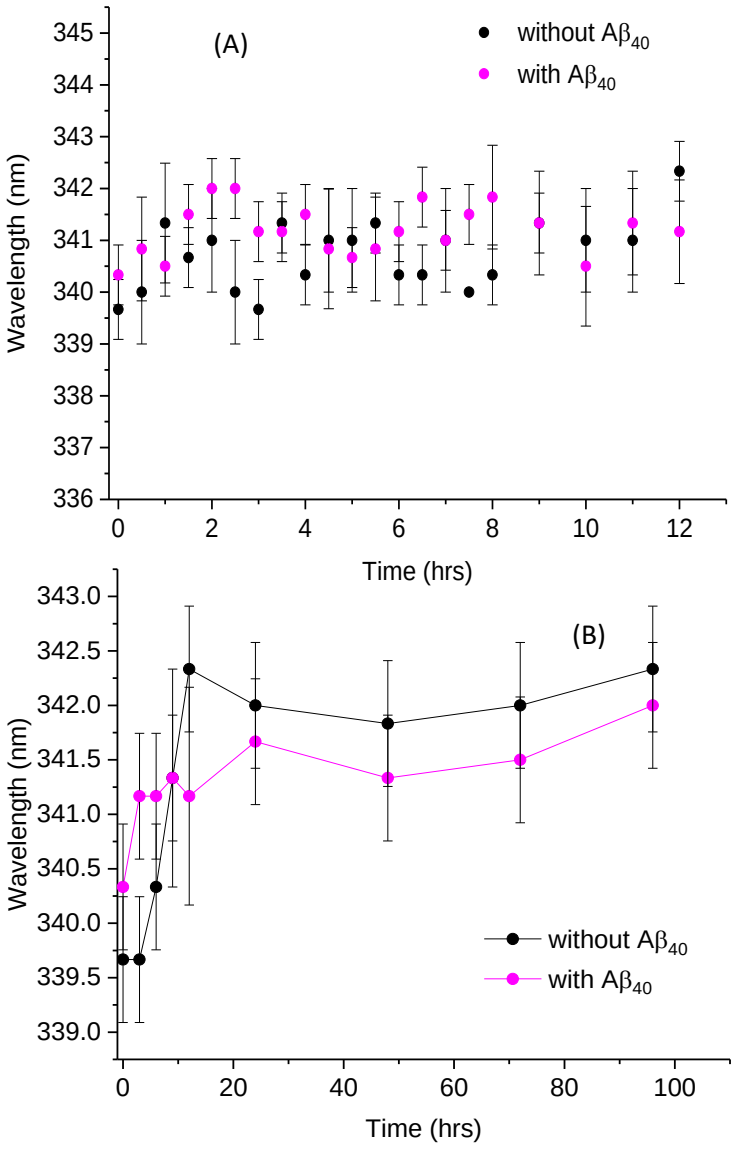

Figure 6.11. Kinetic assays of Trp fluorescence emission wavelengths in Lyz-AuNCs in the absence (black) and presence (pink) of $A\beta_{40}$ over 12 h (A) and 96 h (B). Measured at an excitation wavelength of 295 nm.

The decrease in the fluorescence intensity of Trp in the presence of $A\beta_{40}$ was possibly due to the binding of the Lyz-AuNCs to $A\beta_{40}$. It has been reported that the fluorescence intensity of Trp decreases when the negative charge is closer to the indole ring or the positive charge is closer to the electron acceptor due to stabilisation of the charge transfer state (191). Evidence of $A\beta_{40}$ binding to Lyz-AuNCs was provided by the UV–Vis spectra shown in Figure 6.7. The decreases of Trp emission in Lyz-AuNCs with $A\beta_{40}$ are comparable to HEWL with $A\beta_{40}$. However,

the wavelength changes are different. The wavelength of Trp in HEWL changed from 335 to 340 nm over 96 h, while 2 nm redshift from 340nm was observed in Lyz-AuNCs over the same time period. Moreover, a blue shift from 335 to 328 nm was observed after 96 h in HEWL with $A\beta_{40}$, in contrast to 2nm redshift in Lyz-AuNCs with $A\beta_{40}$. The fluorescence emission wavelength of Trp is sensitive to the polarity of the surrounding environment. This suggests that interaction of Lyz-AuNCs with $A\beta_{40}$ can prevent amyloid formation as HEWL does but generates complexes different from that of HEWL with $A\beta_{40}$.

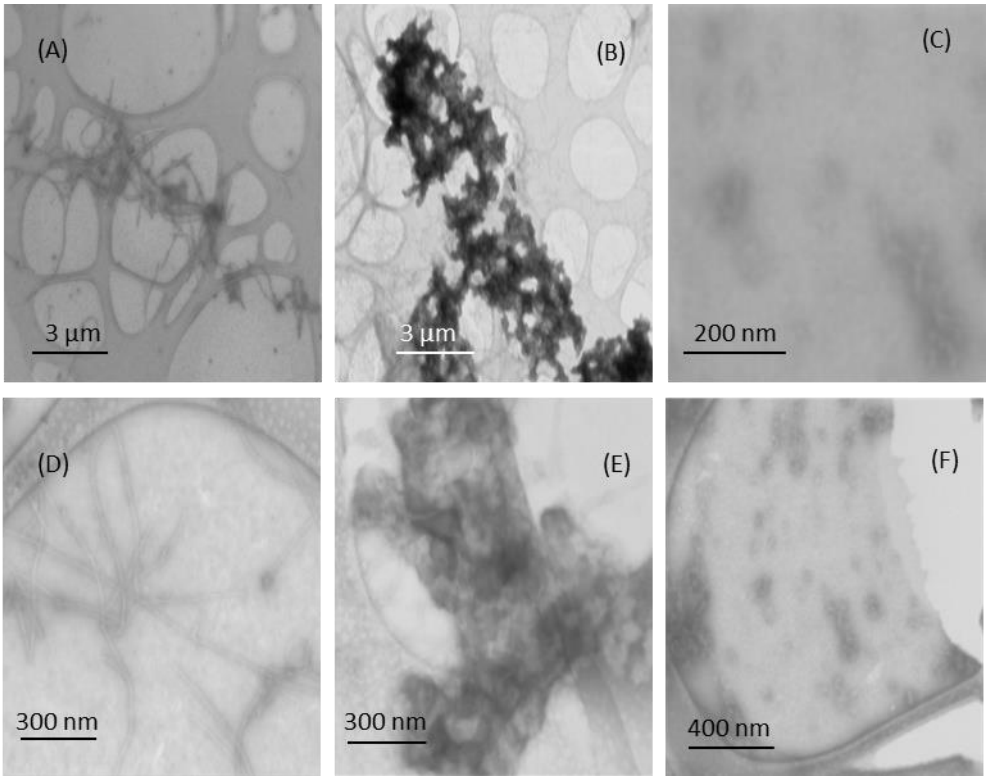

Figure 6.12. Scanning electron microscope (SEM) images of (A) and (D) $A\beta_{40}$ Amyloids. (B) and (E) $A\beta_{40}$ + HEWL (C) and (F) $A\beta_{40}$ + Lyz-AuNCs. All images are in negative stain (2% (w/v) uranyl acetate). Images were taken after two weeks of incubation.

To confirm that HEWL and Lyz-AuNCs inhibited the formation of amyloid fibrils from $A\beta_{40}$, SEM was performed on $A\beta_{40}$, $A\beta_{40}$ with HEWL and $A\beta_{40}$ with Lyz-AuNCs after ageing for 2 weeks. Formation of amyloid fibrils from $A\beta_{40}$ was evident in Figure 6.12 (A) and (D). A large aggregation of $A\beta_{40}$ and HEWL was observed in images (B) and (E). The aggregation was much smaller and less in $A\beta_{40}$ with Lyz-AuNCs as per images (C) and (F). These results coincide with the absorbance

measurements shown in Figure 6.4 and 6.7 where a decrease of absorbance indicated precipitation due to the formation of large aggregator from $A\beta_{40}$ with HEWL while a small decrease was found in $A\beta_{40}$ with Lyz-AuNCs. It was reported that growth of AuNCs within HEWL changed its isoelectric point from 11 to 5.5 (67). Therefore Lyz-AuNCs has a negative surface charge at pH 7.4 similar to $A\beta_{40}$, and this negatively charged surface could have prevented the formation of large aggregations due to repulsion.

6.5.3 Effect of $A\beta_{40}$ on Fluorescence of Lyz-AuNCs

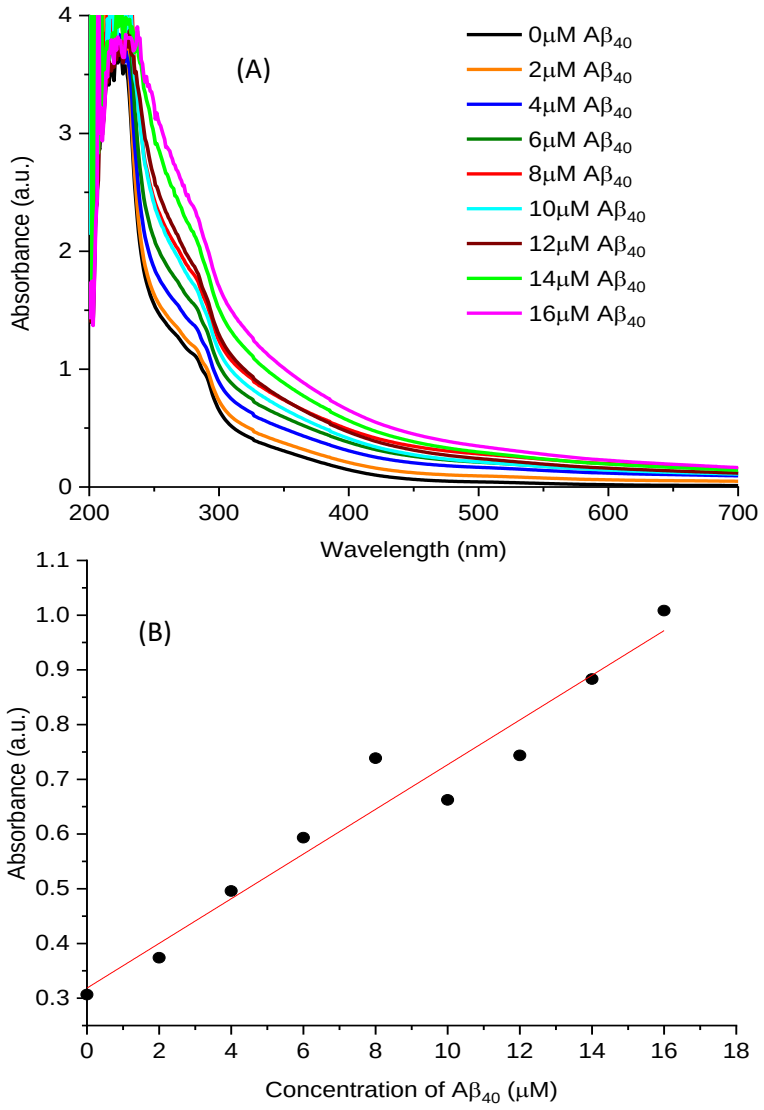

Figure 6.13. (A) Absorption spectra of 25 μM Lyz-AuNCs at different concentrations of $A\beta_{40}$. (B) Absorption at 350 nm as a function of the concentration of $A\beta_{40}$. (Measured in 50 μM Tris-HCl buffer at pH 7.4 and 37°C.)

To explore the possibility of employing AuNCs as a potential tool for $A\beta_{40}$ detection, the effect of $A\beta_{40}$ on the fluorescence properties of the AuNCs was studied by varying the concentrations of $A\beta_{40}$ from 0 to 16 µM. Figures 6.13 (A) and (B) show the effect of the $A\beta_{40}$ concentration on the absorption of the Lyz-AuNCs. A rise in the absorption at 350 nm as a function of $A\beta_{40}$ concentration indicates an increase in the size of the Lyz-AuNCs due to the formation of $A\beta_{40}$–Lyz-AuNCs complexes.

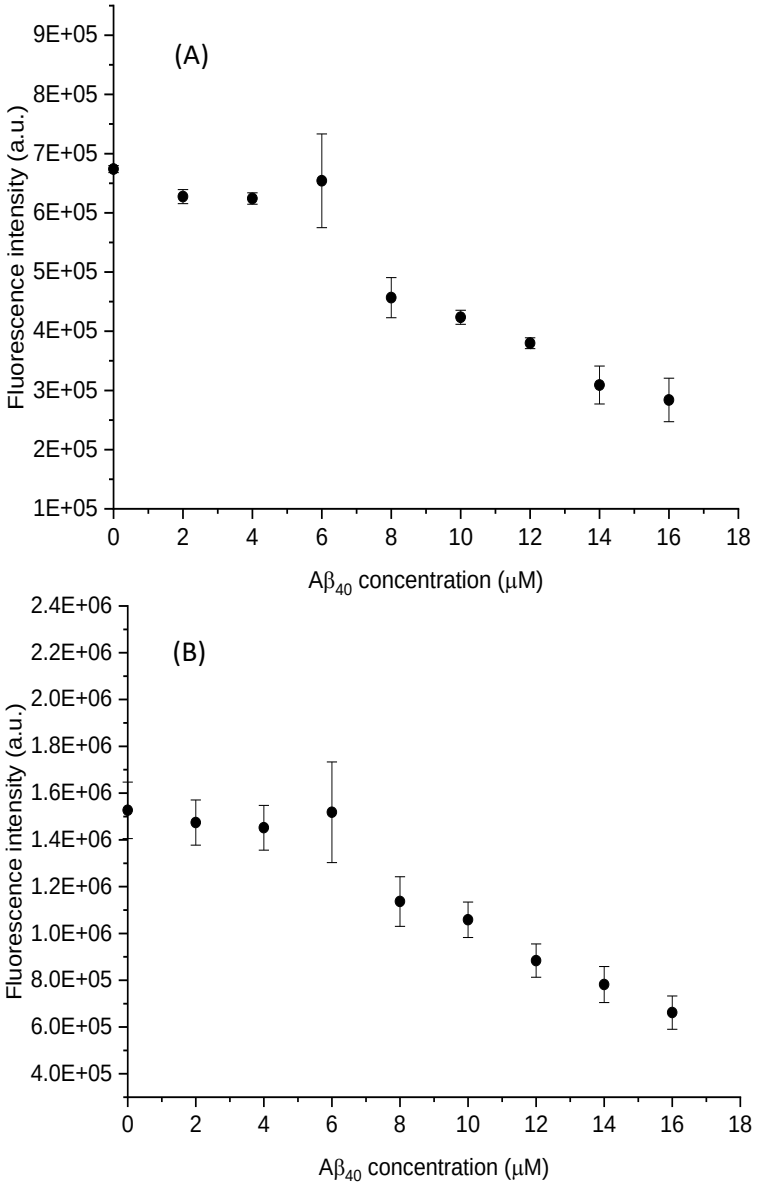

Figure 6.14. Peak fluorescence intensities of (A) Trp and (B) AuNCs in Lyz-AuNCs at different concentrations of $A\beta_{40}$ in 50 µM Tris-HCl buffer at pH 7.4 and 37°C. (Measured at the excitation wavelength of 295 nm.)

Figure 6.14 shows the fluorescence intensities of Trp and AuNCs at the excitation wavelength of 295 nm as a function of $A\beta_{40}$ concentration. Both did not change when the concentration of $A\beta_{40}$ increased from 0 to 6 µM. At $A\beta_{40}$ concentrations exceeding 6 µM, the fluorescence intensities of Trp and AuNCs decreased linearly and dropped by approximately 58% and 57% at 16 µM, respectively. The decrease in fluorescence intensities of Trp and AuNCs was due to the interaction between $A\beta_{40}$ and Lyz-AuNCs, as discussed above.

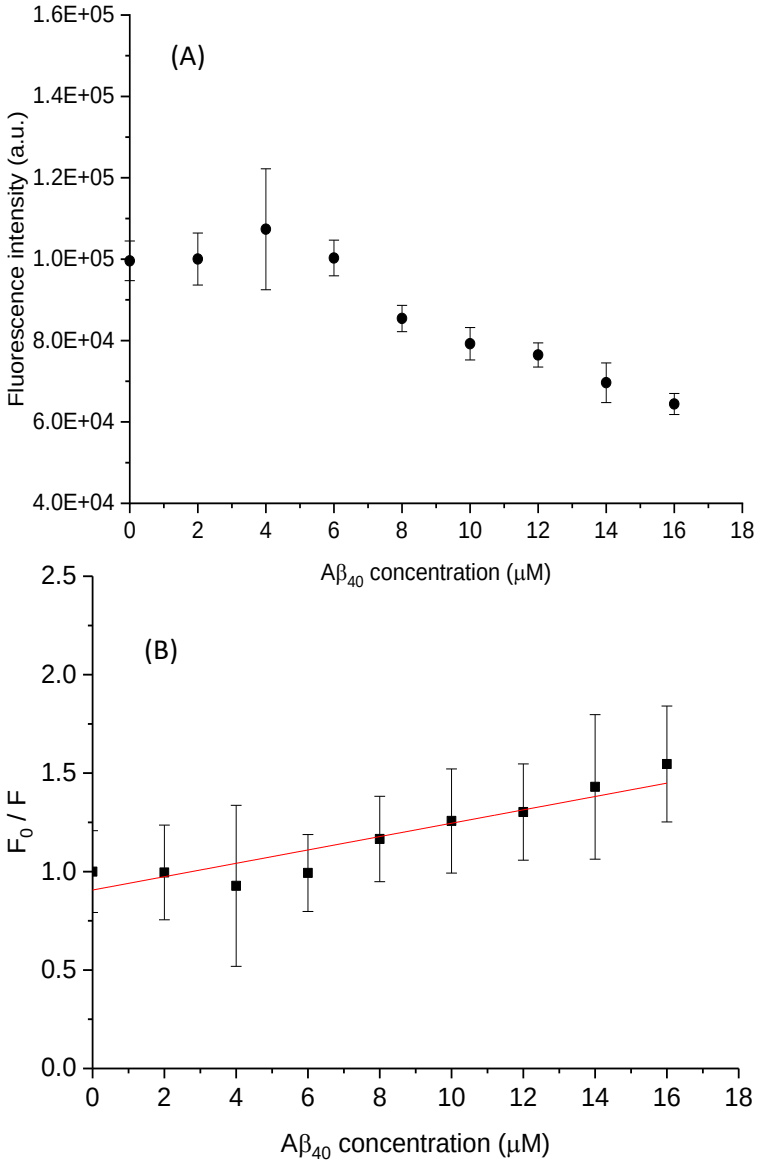

Figure 6.15. Effect of the $A\beta_{40}$ concentration on the fluorescence intensity of Lyz-AuNCs at pH 7.4 and 37°C (A) emission intensity of Lyz-AuNCs as a function of $A\beta_{40}$ concentration. (B) Stern–Volmer plot for Lys-AuNCs in the presence of different concentrations of $A\beta_{40}$. The error bars indicated the relative standard deviation of three repeated experiments. Measured at the excitation wavelength of 470 nm.

Figure 6.15 (A) shows that the fluorescence intensity of the AuNCs at the excitation wavelength of 470 nm. The fluorescence intensity of the Lyz-AuNCs was not sensitive to $A\beta_{40}$ concentrations below 6 μM. At higher $A\beta_{40}$ concentrations, the fluorescence intensity decreased and was approximately 35% of initial intensity at 16 μM.

To understand the type of quenching, we showed the Stern-Volmer plot (F_0/F versus $A\beta_{40}$ concentration) of the interaction between the Lyz-AuNCs and $A\beta_{40}$ (0–16 μM) at the excitation wavelength of 470 nm in Figure 6.15 (B). The values of k_q, the bimolecular quenching constant, and K_s, the Stern–Volmer constant can be calculated from Equation (6-1).

$$\frac{F_0}{F} = 1 + k_q \tau_0 [Q] = 1 + K_S [Q] \qquad (6\text{-}1)$$

The estimated values of k_q and K_s are shown in Table 6.2.

Table 6.2. Estimated values of k_q and K_s of AuNCs

$K_s\ 10^6 \mathrm{M}^{-1}$	$K_q\ 10^{12} \mathrm{M}^{-1}\mathrm{S}^{-1}$
0.03394	$= 0.034 \times 2.03102 = 6.91 \times 10^{-2}$

Table 6.3. Fluorescence lifetimes of AuNCs emission τ and amplitudes α at different concentrations of $A\beta_{40}$. Lyz-AuNCs was in 50 μM Tris-HCl buffer at pH 7.4 and 37°C measured at the excitation wavelength of 482 nm.

$[A\beta_{40}]$ (μM)	τ_1 (ns)	α_1	τ_2 (ns)	α_2 (%)	τ_3 (ns)	α_3 (%)	χ^2	$\bar{\tau}$ (ns)
0	2267 ± 12	0.67	826 ± 30	0.28	147 ± 4	0.05	1.00	2077
2	2365 ± 15	0.65	888 ± 37	0.28	159 ± 4	0.06	1.05	2018
4	2303 ± 13	0.68	801 ± 42	0.27	143 ± 5	0.05	1.07	2035
6	2268 ± 13	0.69	780 ± 32	0.26	138 ± 5	0.05	1.09	2048
8	2337 ± 15	0.67	832 ± 40	0.28	139 ± 5	0.05	1.06	2027
10	2365 ± 18	0.67	847 ± 44	0.28	150 ± 6	0.05	1.11	1988
12	2359 ± 21	0.66	872 ± 45	0.28	165 ± 6	0.06	1.10	2012
14	2264 ± 17	0.70	743 ± 37	0.26	122 ± 7	0.04	1.12	2045
16	2341 ± 21	0.67	811 ± 52	0.28	142 ± 7	0.05	1.08	2029

Table 6.2 shows that the quenching constant of the biomolecules was $6.91 \times 10^{10} \times \mathrm{M}^{-1} \times \mathrm{S}^{-1}$. This value is higher than the diffusion constant of biomolecules in the environment in the presence of dynamical quenching (namely, $2 \times 10^{10}\mathrm{M}^{-1}\mathrm{S}^{-1}$) (222,223), implying a nature of static quenching.

Further lifetime measurement was conducted at an excitation wavelength of 482 nm to confirm the type of quenching. The fluorescence lifetimes of the AuNCs were analysed using the three-exponential model seen below.

$$\mathrm{I(t)} = \sum_{\mathrm{i=1}}^{\mathrm{n}} \alpha_{\mathrm{i}} \mathrm{e}^{\left(\frac{-\mathrm{t}}{\tau_{\mathrm{i}}}\right)} \qquad (6\text{-}2)$$

Where α_i is the amplitude, and τ_i is the lifetime.

In order to ensure a good fit for the fluorescence decay curve, we conducted the goodness of fit analysis with the least-squares method using weighted residuals between 1.00 and 1.12 for all the decay curves (Table 6-3).

The average lifetime was calculated using Equation 6-3.

$$\bar{\tau} = \frac{\alpha_1\tau_1^2+\alpha_2\tau_2^2}{\alpha_1\tau_1+\alpha_2\tau_2} \qquad (6\text{-}3)$$

It is clear that the lifetimes of AuNCs did not change as the concentration of $A\beta_{40}$ increased. This indicated that the quenching was static rather than dynamic. In the former, the quencher binds to the fluorophore, forming a non-fluorescent complex. This contrasts to collisional quenching, wherein the quencher interacts with a fluorophore in the excited state without forming a complex, leading to a reduction in a lifetime (91).

The fluorescence intensity of the AuNCs in the Lyz-AuNCs was monitored both in the absence and presence of 50 µM $A\beta_{40}$ and 10 µM of ThT in a similar manner (as shown in Figure 6.5) in order to study the effect of $A\beta_{40}$ on the kinetic fluorescence intensity of the AuNCs. Studying this effect can provide additional information on the binding between $A\beta_{40}$ and Lyz-AuNCs. This information can aid the use of the fluorescence properties of the AuNCs in imaging applications.

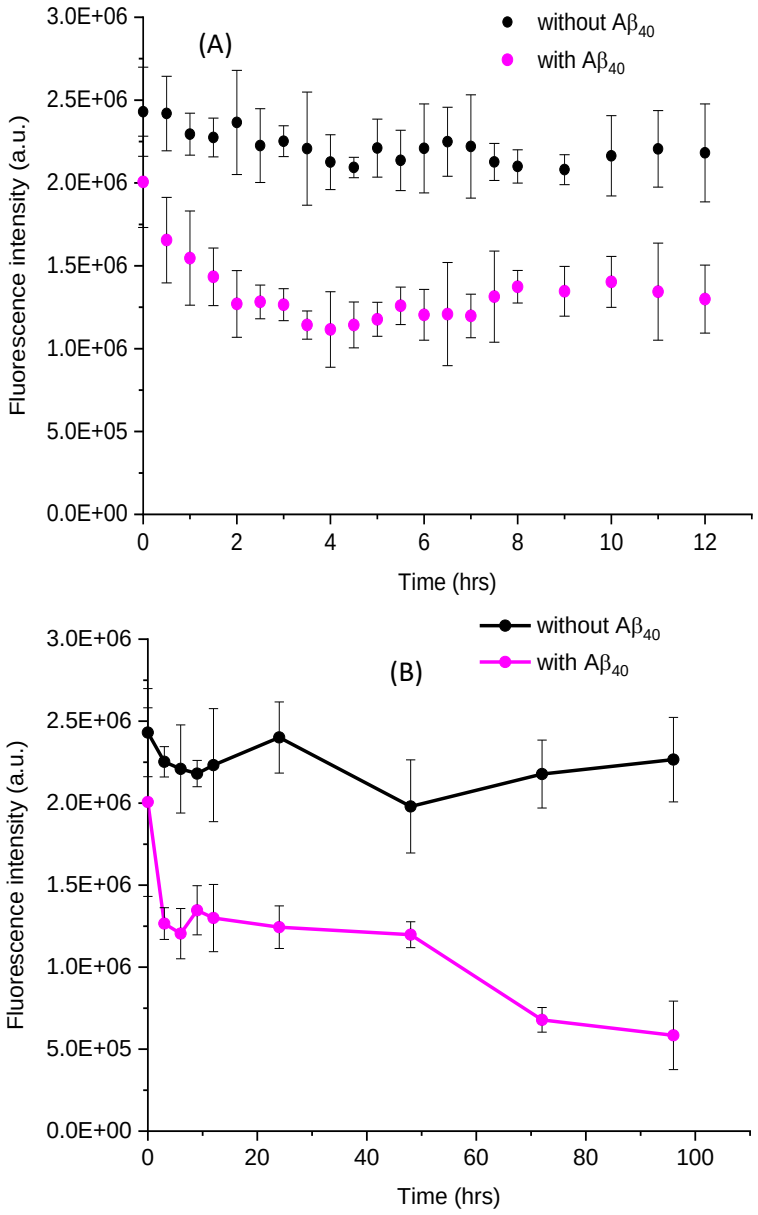

Figure 6.16. Kinetic assays of the fluorescence intensities of AuNCs in Lyz-AuNCs and 10 µM ThT in the absence (black) and presence (pink) of $A\beta_{40}$ in 50 µM Tris-HCl buffer at pH 7.4 and 37°C over 12 h (A) and 96 h (B). The sample was measured at the excitation wavelength of 295 nm.

Figures 6.16 (A) and (B) show the kinetic fluorescence assays of Lyz-AuNCs in the presence and absence of $A\beta_{40}$ over 12 h and 96 h at an excitation wavelength of 295 nm, respectively. In the absence of $A\beta_{40}$, no change was noted in the fluorescence intensity of the AuNCs over 96 h. Once the Lyz-AuNCs and $A\beta_{40}$ were mixed, the fluorescence intensity of AuNCs decreased and was approximately 44% of the initial value after 4 h. The fluorescence intensity of the AuNCs remained stable from 4 h to

48 h. After 48 h, the fluorescence intensity decreased and reached to approximately 71% of its initial value.

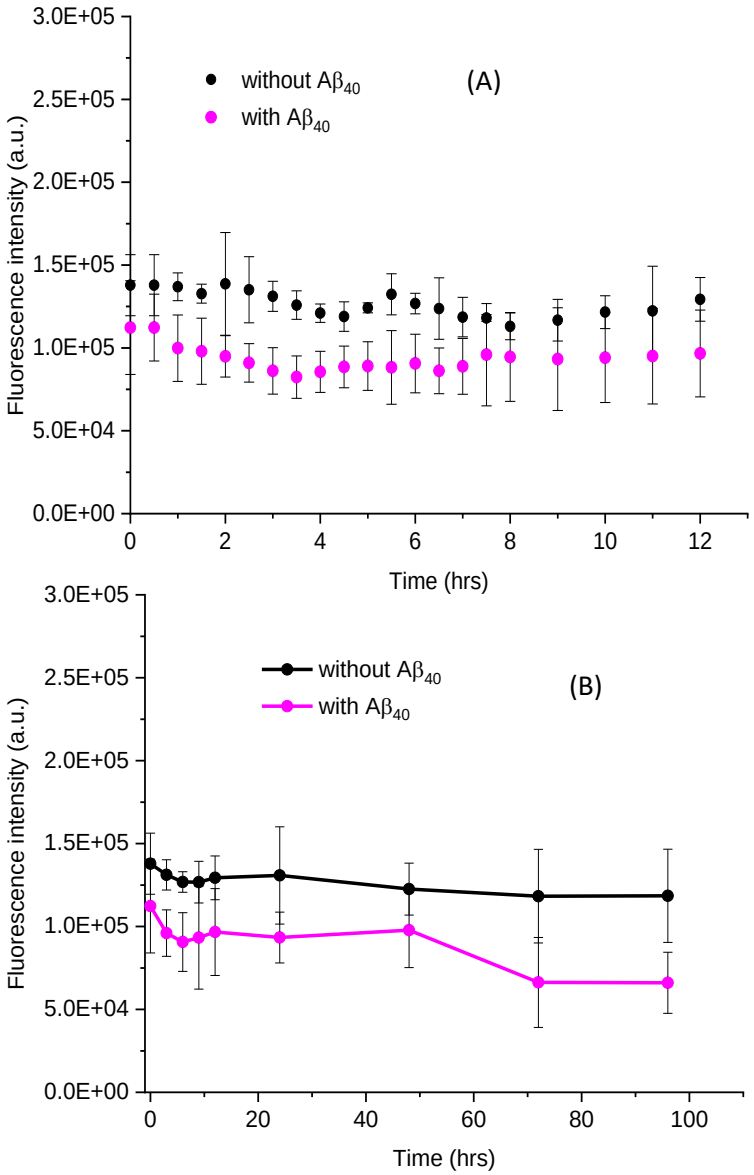

Figure 6.17. Kinetic assays of the fluorescence intensities of AuNCs in Lyz-AuNCs and 10 µM ThT in the absence (black) and presence (pink) of $A\beta_{40}$ over 12 h (A) and 96 h (B) The sample was measured at the excitation wavelength of 470 nm.

Figures 6.17 (A) and (B) show the kinetic fluorescence assays of Lyz-AuNCs in the presence and absence of $A\beta_{40}$ over 12 h and 96 h at an excitation wavelength of 470 nm, respectively. In the absence of $A\beta_{40}$, no change was noted in the fluorescence intensity of the AuNCs after 96 h. In the presence of $A\beta_{40}$, the fluorescence intensity decreased slightly in the first 4 h. After a stable period between 4 and 48 h, the fluorescence intensity decreased to approximately 41% of the initial value at 72 h.

It is possible that $A\beta_{40}$ binds to Lyz-AuNCs, resulting in decreased fluorescence intensity. However, the reduction in the fluorescence intensity of the AuNCs at the excitation wavelength of 295 nm was more than that at the excitation wavelength of 470 nm. This can be attributed to the FRET from Trp to the AuNCs at the excitation wavelength of 295 nm. The fluorescence intensity of Trp decreased in the presence of $A\beta_{40}$, as shown in Figure 6.10 (A) and (B). This suggested that fluorescence of AuNCs in $A\beta_{40}$-LyzAuNCs complex excited at 470 nm was stable for about two days and was sensitive to concentration of $A\beta_{40}$ between 4-16 μM.

6.6 Conclusion

$A\beta_{40}$ aggregation was studied in the presence of either HEWL or Lyz-AuNCs. It was found that both HEWL and Lyz-AuNCs can inhibit the formation of amyloid fibrils, as confirmed by fluorescence spectra of ThT and SEM images. The UV-Vis spectra suggested that HEWL could bind to $A\beta_{40}$ and form large HEWL–$A\beta_{40}$ complexes. The changes in Trp fluorescence intensities and wavelengths provided further evidence of HEWL binding to $A\beta_{40}$. Furthermore, the steady increase in the absorbance at 350 nm with time and $A\beta_{40}$ concentration indicated that $A\beta_{40}$ was bound to Lyz-AuNCs.

Moreover, the decreases in the fluorescence intensity of Trp in the presence of $A\beta_{40}$ provided additional evidence for the binding of $A\beta_{40}$ to Lyz-AuNCs. Significantly, the fluorescence wavelength of Trp in HEWL and Lyz-AuNCs in the presence of $A\beta_{40}$ showed different shift, indicating the structural difference between $A\beta_{40}$-HEWL and $A\beta_{40}$-Lyz-AuNC. Indeed, SEM imaging disclosed that HEWL formed large aggregators with $A\beta_{40}$ while small complexes were formed between Lyz-AuNCs and $A\beta_{40.}$ This is believed due to different isoelectric points between HEWL and Lyz-AuNCs.

In addition, the interaction of $A\beta_{40}$ with the Lyz-AuNCs in the absence of ThT showed a decrease in the fluorescence intensity of AuNCs when the $A\beta_{40}$ concentration varied from 6 to 16 μM. At $A\beta_{40}$ concentrations below 6 μM, the

fluorescence intensity of the AuNCs did not change. The results of the lifetime measurement showed that the decrease in the fluorescence intensity was due to static quenching. This chapter presented our findings on the effect of Lyz-AuNCs and HEWL on $A\beta_{40}$ Ageing and suggested that Lyz-AuNCs could be a potential candidate to prevent/reduce amyloid fibre formation.

Chapter 7: Conclusions and Future Work

7.1 Conclusions

This thesis represents a study on the fluorescent properties of Lyz-AuNCs when lysozymes are denatured by changing the pH, increasing the concentration of HEWL, elevated temperature and adding chemicals such as urea and SDS. The study was conducted to understand the fluorescent properties of Lyz-AuNCs in these conditions and, hence, to enhance our knowledge of applying the fluorescent properties of Lyz-AuNCs as a tool for studying protein structures. In addition, it represents the effect of HEWL and Lyz-AuNCs on inhibiting the formation of the amyloid fibril $A\beta_{40}$. The purpose of this study was to develop a new inhibitor to prevent $A\beta_{40}$ aggregation and to use the fluorescent properties of Lyz-AuNCs as a detector of $A\beta_{40}$.

The study demonstrates that the fluorescent properties of Lyz-AuNCs are sensitive to changes in pH, as discussed in Chapter 4. It was found that the fluorescent intensity of Lyz-AuNCs at an alkaline pH is higher than that at an acidic pH. A time-resolved fluorescence spectrum revealed two-lifetime components and fluorescence contribution arising from long lifetime component decreases in alkaline pH. A redshift in the peak emission wavelength was also observed when increasing the pH, possibly due to the increased contribution of the fluorescence from the short lifetime component at pH 12. The change in the fluorescent properties of Lyz-AuNCs due to changes in pH may imply the possibility of employing the fluorescent properties of Lyz-AuNCs in the study of protein structures. As discussed in Chapter 4, Protein's structure changes due to changes in the pH, for example, HEWL has 2 transition stages. One point is at an acidic pH level below four (162,163) and the second point is at an alkaline pH level (164).

Moreover, the influence of the HEWL concentration on the fluorescence of Lyz-AuNCs at pH >11 and <pH 4 was studied. In cases of an acidic pH, we found that the fluorescence intensity increases linearly, and a redshift occurs with the increase of

HEWL. In addition, the long lifetime component decreases as the concentration of HEWL increases. The TRES measurement disclosed a redshift in the emission associated with the long lifetime component after adding HEWL at pH < 4. This finding shows that the fluorescent properties of Lyz-AuNCs sensitive to protein's concentration, therefore it can be used to study and model lysozyme aggregation.

We have investigated the unfolding lysozyme introduced via urea, SDS and temperature and its influence on the fluorescent properties of AuNCs. It has been shown that fluorescence intensity is sensitive to the unfolding of the protein (as seen in Chapter 5). Adding urea and SDS to Lyz-AuNCs leads to a decrease in the fluorescent intensity of AuNCs at an excitation wavelength of 470 nm. This decrease is due to the quenching resulting from the unfolding of the protein and subsequent exposure of AuNCs to the oxygen in the solvent. There is a redshift in the peak emission wavelength of AuNCs in the presence of urea, possibly due to the interaction between urea and cysteine, while the SDS does not change the peak emission wavelength of AuNCs. At 295 nm excitation wavelength, the fluorescent intensity of AuNCs fluctuated in the presence of urea but decreased dramatically in the presence of SDS. This indicates a FRET process between Trp and AuNCs in the presence of urea and SDS that affects the fluorescent intensity of AuNCs, in addition to quenching intruded by oxygen. The interaction of SDS on HEWL is different from urea, as shown in CD measurements, the SDS leads to increase the α-helix while the urea leads to reduce the α-helix. Therefore, Different changes in the Lyz-AuNCs structure leads to an effect on the FRET process and hence on the fluorescent intensity of AuNCs.

Prolonged exposure of Lyz-AuNCs to a temperature of 65℃ leads to a continuing decrease in fluorescence intensity. This change in intensity is due to a change in the structure of Lyz-AuNCs and forms amyloid. ThT is used to confirm the formation of amyloid in both Lyz-AuNCs and HEWL. These studies highlight the possibility of using the fluorescent properties of AuNCs as an indicator for protein unfolding.

This thesis documents the effect of HEWL and Lyz-AuNCs on inhibiting the formation of the amyloid fibril $A\beta_{40}$. The purpose of this study was to develop a new $A\beta_{40}$ inhibitor and to use the fluorescent properties of Lyz-AuNCs as a detector of $A\beta_{40}$. The $A\beta_{40}$ aggregation in the presence of either HEWL or Lyz-AuNCs was studied in Chapter 6. The ThT assay and SEM confirm that both HEWL and Lyz-AuNCs prevent the formation of amyloid fibrils. Moreover, the fluorescent properties of Lyz-AuNCs are sensitive to the presence of $A\beta_{40}$. This study shows that both HEWL and Lyz-AuNCs can be used as an inhibitor of $A\beta_{40}$.

7.2 Future Work

It has been shown that HEWL can control the growth of gram-positive bacteria, but does not affect the gram-negative bacteria. Another study has been done by Rubén Vilcacundo et al. found that, when the native HEWL is denatured, it cannot affect the growth of gram-positive bacteria, but it can control gram-negative bacteria (224). The impact of denaturing Lyz-AuNCs on both gram-negative and gram-positive bacteria remains an open question. In previous research, Kaiyuan Zheng et al. found that AuNCs can kill both gram-negative and gram-positive bacteria. Once the AuNCs is uptaking by bacteria, AuNCs cause a metabolic imbalance. As a result, a greater amount of reactive oxygen species produce bacteria, leading to bacteria death (145). Studying these functional properties of AuNCs would probably broaden the application of Lyz-AuNCs in the food preservation and pharmaceutical industries.

As we report that Lyz-AuNCs inhibit the amyloid formation of $A\beta_{40}$ in Chapter 6, further studies should investigate the ability of Lyz-AuNCs to cross BBB. Studying the ability of Lyz-AuNCs to cross BBB is essential for imaging and treatment. In previous studies, an adult mouse and brain endothelial cells (bEnd.3) can be used to evaluate the impact of AuNCs on BBB model in vivo and vitro, respectively. bEnd.3 acts similar to BBB in mammals where only selective and specific biomolecules can cross BBB. This method has been used by Nair et al. to test the glutathione (GSH-AuNC) with L-Dopa enter the cell. They found that the GSH-AuNCs with L-Dopa can

enter and clean from the cell faster compared with GSH-AuNCs in vitro. Their study shows that GSH-AuNCs has a long time in the cell around 3 h. In vivo, they also found that GSH-AuNCs with L-Dopa can be used for brain imaging (210). Lai et al. also studied the possibility of using AuNCs for imaging of Alzheimer's disease in vivo. They found that $HAuCl_4$ cross the BBB of the AD mice and form AuNCs in the hippocampus. These AuNCs provide fluorescence emission that can be used for imaging in contrast to the health mice (209). These previous researches suggested AuNCs can be used as brain imaging. Hence, provide a new method for diagnosing and treatment of Alzheimer disease.

References

1. Hawe A, Sutter M, Jiskoot W. Extrinsic fluorescent dyes as tools for protein characterization. Pharmaceutical research. 2008 Jul 1;25(7):1487-99.

2. Yerbury JJ, Stewart EM, Wyatt AR, Wilson MR. Quality control of protein folding in extracellular space. EMBO Rep. 2005 Dec;6(12):1131-6.

3. Vladimir N. Uversky, Anthony Fink. The pathogenesis of Alzheimer's disease: general overview In: Editor Liana G. Apostolova and Jeffrey L. Cummings, editors. Protein misfolding, aggregation and conformational diseases: Part B: molecular mechanisms of conformational diseases. Springer Science & Business Media; 2007 May 26.p 9-10

4. Thomas PJ, Qu BH, Pedersen PL. Defective protein folding as a basis of human disease. Trends in biochemical sciences. 1995 Nov 1;20(11):456-9.

5. Pepys MB, Hawkins PN, Booth DR, Vigushin DM, Tennent GA, Soutar AK, Totty N, Nguyen O, Blake CC, Terry CJ, Feest TG. Human lysozyme gene mutations cause hereditary systemic amyloidosis. Nature. 1993 Apr 8;362(6420):553-7.

6. Lasagna-Reeves CA, Clos AL, Castillo-Carranza D, Sengupta U, Guerrero-Muñoz M, Kelly B, et al. Dual role of p53 amyloid formation in cancer; loss of function and gain of toxicity. Biochemical and biophysical research communications. 2013 Jan 18;430(3):963-8.

7. Hardy JA, Higgins GA. Alzheimer's disease: the amyloid cascade hypothesis. Science. 1992 Apr 10;256(5054):184-6.

8. Polymeropoulos MH, Lavedan C, Leroy E, Ide SE, Dehejia A, Dutra A, et al. Mutation in the α-synuclein gene identified in families with Parkinson's disease. science. 1997 Jun 27;276(5321):2045-7.

9. Scherzinger E, Sittler A, Schweiger K, Heiser V, Lurz R, Hasenbank R, et al. Self-assembly of polyglutamine-containing huntingtin fragments into amyloid-like fibrils: implications for Huntington's disease pathology. Proc. Natl. Acad. of Sci. 1999 Apr 13;96(8):4604-9.

10. Rambaran RN, Serpell LC. Amyloid fibrils: abnormal protein assembly. Prion. 2008 Jul 1;2(3):112-7.

11. Vetri V, Canale C, Relini A, Librizzi F, Militello V, Gliozzi A, et al. Amyloid fibrils formation and amorphous aggregation in concanavalin A. Biophysical chemistry. 2007 Jan 1;125(1):184-90.

12. Waugh DF, Wilhelmson DF, Commerford SL, Sackler ML. Studies of the nucleation and growth reactions of selected types of insulin fibrils. J. Am. Chem. Soc. 1953 Jun;75(11):2592-600.

13. Dobson CM. Protein folding and misfolding. Nature. 2003 Dec;426(6968):884-90.

14. Arosio P, Knowles TP, Linse S. On the lag phase in amyloid fibril formation. Phys. Chem. Chem. Phys. 2015;17(12):7606-18.

15. Wilson MR, Yerbury JJ, Poon S. Potential roles of abundant extracellular chaperones in the control of amyloid formation and toxicity. Mol. BioSyst. 2008;4(1):42-52.

16. Manno M, Craparo EF, Podestà A, Bulone D, Carrotta R, Martorana V, Tiana G, San Biagio PL. Kinetics of different processes in human insulin amyloid formation. J. Mol. Biol. 2007 Feb 9;366(1):258-74.

17. Goldsbury C, Kistler J, Aebi U, Arvinte T, Cooper GJ. Watching amyloid fibrils grow by time-lapse atomic force microscopy. J. Mol. Biol. 1999 Jan 8;285(1):33-9.

18. Jimenez JL, Guijarro JI, Orlova E, Zurdo J, Dobson CM, Sunde M, et al. Cryo-electron microscopy structure of an SH3 amyloid fibril and model of the molecular packing. The EMBO journal. 1999 Feb 15;18(4):815-21.

19. Sachse C, Xu C, Wieligmann K, Diekmann S, Grigorieff N, Fändrich M. Quaternary structure of a mature amyloid fibril from Alzheimer's Aβ (1-40) peptide. J. Mol. Biol. 2006 Sep 15;362(2):347-54.

20. Eisenberg D, Jucker M. The amyloid state of proteins in human diseases. Cell. 2012 Mar 16;148(6):1188-203.

21. Chaturvedi SK, Khan JM, Siddiqi MK, Alam P, Khan RH. Comparative insight into surfactants mediated amyloidogenesis of lysozyme. International journal of biological macromolecules. 2016 Feb 1;83:315-25.

22. Sun Y, Pedro Filho LO, Bozelli JC, Carvalho J, Schreier S, Oliveira CL. Unfolding and folding pathway of lysozyme induced by sodium dodecyl sulfate. Soft Matter. 2015;11(39):7769-77.

23. Imoto T, Forster LS, Rupley JA, Tanaka F. Fluorescence of lysozyme: emissions from tryptophan residues 62 and 108 and energy migration. Proc. Nat. Acad. Sci. 1972 May 1;69(5):1151-5.

24. Frid P, Anisimov SV, Popovic N. Congo red and protein aggregation in neurodegenerative diseases. Brain Research Reviews. 2007 Jan 1;53(1):135-60.

25. Levine III H. Thioflavine T interaction with synthetic Alzheimer's disease β-amyloid peptides: Detection of amyloid aggregation in solution. Protein Science. 1993 Mar;2(3):404-10.

26. Persichilli C, Hill SE, Mast J, Muschol M. Does thioflavin-T detect oligomers formed during amyloid fibril assembly. Biophys. J. 2011 Feb 2;100(3): 3781-90.

27. Maezawa I, Hong HS, Liu R, Wu CY, Cheng RH, Kung MP, et al. Congo red and thioflavin-T analogs detect Aβ oligomers. Journal of neurochemistry. 2008 Jan;104(2):457-68.

28. Ghosh SK, Pal T. Interparticle coupling effect on the surface plasmon resonance of gold nanoparticles: from theory to applications. Chem. Rev. 2007 Nov 14;107(11):4797-862.

29. Díaz SA, Hastman DA, Medintz IL, Oh E. Understanding energy transfer with luminescent gold nanoclusters: a promising new transduction modality for biorelated applications. J.of Mater. Chem. B. 2017;5(39):7907-26.

30. Shang L, Dong S, Nienhaus GU. Ultra-small fluorescent metal nanoclusters: synthesis and biological applications. Nano today. 2011 Aug 1;6(4):401-18.

31. Zheng Y, Lai L, Liu W, Jiang H, Wang X. Recent advances in biomedical applications of fluorescent gold nanoclusters. Advances in Colloid and Interface Science. 2017 Apr 1;242:1-6.

32. Wei H, Wang Z, Yang L, Tian S, Hou C, Lu Y. Lysozyme-stabilized gold fluorescent cluster: synthesis and application as Hg^{2+} sensor. Analyst. 2010;135(6):1406-10.

33. Kawasaki H, Yoshimura K, Hamaguchi K, Arakawa R. Trypsin-stabilized fluorescent gold nanocluster for sensitive and selective Hg^{2+} detection. Analytical Sciences. 2011 Jun 10;27(6):591-6.

34. Chen LY, Wang CW, Yuan Z, Chang HT. Fluorescent gold nanoclusters: recent advances in sensing and imaging. Anal. Chem. 2015 Jan 6;87(1):216-29.

35. Selvaprakash K, Chen YC. Using protein-encapsulated gold nanoclusters as photoluminescent sensing probes for biomolecules. Biosensors and bioelectronics. 2014 Nov 15;61:88-94.

36. Deng HH, Wu GW, Zou ZQ, Peng HP, Liu AL, Lin XH, Xia XH, Chen W. pH-Sensitive gold nanoclusters: preparation and analytical applications for urea, urease, and urease inhibitor detection. Chem. Commun. 2015;51(37):7847-50.

37. Nair LV, Philips DS, Jayasree RS, Ajayaghosh A. A Near-Infrared Fluorescent Nanosensor (AuC@ Urease) for the Selective Detection of Blood Urea. Small. 2013 Aug 26;9(16):2673-7.

38. Lin CA, Yang TY, Lee CH, Huang SH, Sperling RA, Zanella M, et al. Synthesis, characterization, and bioconjugation of fluorescent gold nanoclusters toward biological labeling applications. ACS nano. 2009 Feb 24;3(2):395-401.

39. Su X, Jiang H, Wang X. Thiols-induced rapid photoluminescent enhancement of glutathione-capped gold nanoparticles for intracellular thiols imaging applications. Anal. Chem. 2015 Oct 20;87(20):10230-6.

40. Chen TH, Tseng WL. (Lysozyme Type VI)-Stabilized Au_8 Clusters: Synthesis mechanism and application for sensing of glutathione in a single drop of blood. Small. 2012 Jun 25;8(12):1912-9.

41. Thomas A.C. Kennedy, James L. MacLean, Juewen Liu. Blue emitting gold nanoclusters templated by poly-cytosine DNA at low pH and poly-adenine DNA at neutral pH. Chemical Communications. 2012;48(54):6845-7.

42. Liu G, Shao Y, Wu F, Xu S, Peng J, Liu L. DNA-hosted fluorescent gold nanoclusters: sequence-dependent formation. Nanotechnology. 2012 Dec 5;24(1):015503.

43. Jiang H, Zhang Y, Wang X. Single cytidine units-templated syntheses of multi-colored water-soluble Au nanoclusters. Nanoscale. 2014;6(17):10355-62.

44. Negishi Y, Nobusada K, Tsukuda T. Glutathione-protected gold clusters revisited: bridging the gap between gold (I)− thiolate complexes and thiolate-protected gold nanocrystals. Journal of the American Chemical Society. 2005 Apr 13;127(14):5261-70.

45. Chaki NK, Singh P, Dharmadhikari CV, Vijayamohanan KP. Single-electron charging features of larger, dodecanethiol-protected gold nanoclusters: electrochemical and scanning tunneling microscopy studies. Langmuir. 2004 Nov 9;20(23):10208-17.

46. Nair LV, Nazeer SS, Jayasree RS, Ajayaghosh A. Fluorescence imaging assisted photodynamic therapy using photosensitizer-linked gold quantum clusters. Acs Nano. 2015 Jun 23;9(6):5825-32.

47. Kumar S, Jin R. Water-soluble Au 25 (Capt) 18 nanoclusters: synthesis, thermal stability, and optical properties. Nanoscale. 2012;4(14):4222-7.

48. Shang L, Dörlich RM, Brandholt S, Schneider R, Trouillet V, Bruns M, Gerthsen D, Nienhaus GU. Facile preparation of water-soluble fluorescent gold nanoclusters for cellular imaging applications. Nanoscale. 2011;3(5):2009-14.

49. Paau MC, Lo CK, Yang X, Choi MM. Synthesis of 1.4 nm α-cyclodextrin-protected gold nanoparticles for luminescence sensing of mercury (II) with picomolar detection limit. The Journal of Physical Chemistry C. 2010 Sep 30;114(38):15995-6003.

50. Lee D, Donkers RL, Wang G, Harper AS, Murray RW. Electrochemistry and optical absorbance and luminescence of molecule-like Au38 nanoparticles. Journal of the American Chemical Society. 2004 May 19;126(19):6193-9.

51. Shang L, Yang L, Stockmar F, Popescu R, Trouillet V, Bruns M, Gerthsen D, Nienhaus GU. Microwave-assisted rapid synthesis of luminescent gold nanoclusters

for sensing Hg 2+ in living cells using fluorescence imaging. Nanoscale. 2012;4(14):4155-60.

52. Shiraishi Y, Arakawa D, Toshima N. pH-dependent color change of colloidal dispersions of gold nanoclusters: Effect of stabilizer. The European Physical Journal E. 2002 Jul;8(4):377-83.

53. Jin R. Quantum sized, thiolate-protected gold nanoclusters. Nanoscale. 2010;2(3):343-62.

54. Luo Z, Yuan X, Yu Y, Zhang Q, Leong DT, Lee JY, Xie J. From aggregation-induced emission of Au (I)–thiolate complexes to ultrabright Au (0)@ Au (I)–thiolate core–shell nanoclusters. Journal of the American Chemical Society. 2012 Oct 10;134(40):16662-70.

55. Liu J, Duchesne PN, Yu M, Jiang X, Ning X, Vinluan III RD, Zhang P, Zheng J. Luminescent gold nanoparticles with size-independent emission. Angewandte Chemie International Edition. 2016 Jul 25;55(31):8894-8.

56. Zheng J, Petty JT, Dickson RM. High quantum yield blue emission from water-soluble Au8 nanodots. Journal of the American Chemical Society. 2003 Jul 2;125(26):7780-1.

57. Zheng J, Nicovich PR, Dickson RM. Highly fluorescent noble-metal quantum dots. Annu. Rev. Phys. Chem.. 2007 May 5;58:409-31.

58. Chen Y, Zheng X, Wang X, Wang C, Ding Y, Jiang X. Near-infrared emitting gold cluster–poly (acrylic acid) hybrid nanogels. ACS Macro Letters. 2014 Jan 21;3(1):74-6.

59. Huang X, Luo Y, Li Z, Li B, Zhang H, Li L, Majeed I, Zou P, Tan B. Biolabeling hematopoietic system cells using near-infrared fluorescent gold nanoclusters. The Journal of Physical Chemistry C. 2011 Sep 1;115(34):16753-63.

60. Schaeffer N, Tan B, Dickinson C, Rosseinsky MJ, Laromaine A, McComb DW, Stevens MM, Wang Y, Petit L, Barentin C, Spiller DG. Fluorescent or not? Size-dependent fluorescence switching for polymer-stabilized gold clusters in the 1.1–1.7 nm size range. Chemical communications. 2008(34):3986-8.

61. Xie J, Zheng Y, Ying JY. Protein-directed synthesis of highly fluorescent gold nanoclusters. Journal of the American Chemical Society. 2009 Jan 28;131(3):888-9.

62. Kawasaki H, Hamaguchi K, Osaka I, Arakawa R. ph-Dependent synthesis of pepsin-mediated gold nanoclusters with blue green and red fluorescent emission. Advanced Functional Materials. 2011 Sep 23;21(18):3508-15.

63. West AL, Griep MH, Cole DP, Karna SP. DNase 1 retains endodeoxyribonuclease activity following gold nanocluster synthesis. Analytical chemistry. 2014 Aug 5;86(15):7377-82.

64. Wen F, Dong Y, Feng L, Wang S, Zhang S, Zhang X. Horseradish peroxidase functionalized fluorescent gold nanoclusters for hydrogen peroxide sensing. Analytical chemistry. 2011 Feb 15;83(4):1193-6.

65. Joseph D, Geckeler KE. Synthesis of highly fluorescent gold nanoclusters using egg white proteins. Colloids and Surfaces B: Biointerfaces. 2014 Mar 1;115:46-50.

66. Liu CL, Wu HT, Hsiao YH, Lai CW, Shih CW, Peng YK, Tang KC, Chang HW, Chien YC, Hsiao JK, Cheng JT. Insulin-directed synthesis of fluorescent gold nanoclusters: Preservation of insulin bioactivity and versatility in cell imaging. Angewandte Chemie International Edition. 2011 Jul 25;50(31):7056-60.

67. Xu Y, Sherwood J, Qin Y, Crowley D, Bonizzoni M, Bao Y. The role of protein characteristics in the formation and fluorescence of Au nanoclusters. Nanoscale. 2014;6(3):1515-24.

68. Masse F, Ouellette M, Lamoureux G, Boisselier E. Gold nanoparticles in ophthalmology. Med. Res. Rev. 2019 Jan;39(1):302-27.

69. Vasilescu A, Wang Q, Li M, Boukherroub R, Szunerits S. Aptamer-based electrochemical sensing of lysozyme. Chemosensors. 2016 Jun;4(2):10.

70. Luo J, Wärmländer SK, Gräslund A, Abrahams JP. Cross-interactions between the Alzheimer disease amyloid-β peptide and other amyloid proteins: a further aspect of the amyloid cascade hypothesis. Journal of Biological Chemistry. 2016 Aug 5;291(32):16485-93.

71. Swaminathan R, Ravi VK, Kumar S, Kumar MV, Chandra N. Lysozyme: a model protein for amyloid research. In advances in protein chemistry and structural biology 2011 Jan 1; 84,p.63-111.

72. Santiago Gonzalez B, Rodríguez MJ, Blanco C, Rivas J, López-Quintela MA, Martinho JM. One step synthesis of the smallest photoluminescent and paramagnetic PVP-protected gold atomic clusters. Nano letters. 2010 Oct 13;10(10):4217-21.

73. Zhang H, Huang X, Li L, Zhang G, Hussain I, Li Z, Tan B. Photoreductive synthesis of water-soluble fluorescent metal nanoclusters. Chemical Communications. 2012;48(4):567-9.

74. Li L, Li Z, Zhang H, Zhang S, Majeed I, Tan B. Effect of polymer ligand structures on fluorescence of gold clusters prepared by photoreduction. Nanoscale. 2013;5(5):1986-92.

75. Wang J, Zhang G, Li Q, Jiang H, Liu C, Amatore C, Wang X. In vivo self-bio-imaging of tumors through in situ biosynthesized fluorescent gold nanoclusters. Scientific reports. 2013 Jan 29;3:1157.

76. Li W, Gao Z, Su R, Qi W, Wang L, He Z. Scissor-based fluorescent detection of pepsin using lysozyme-stabilized Au nanoclusters. Anal. Methods. 2014;6(17):6789-95.

77. Lin YH, Tseng WL. Ultrasensitive sensing of Hg^{2+} and CH_3Hg^+ based on the fluorescence quenching of lysozyme type VI-stabilized gold nanoclusters. Anal. Chem. 2010 Nov 15;82(22):9194-200.

78. Söptei B, Nagy LN, Baranyai P, Szabó I, Mező G, Hudecz F, Bóta A. On the selection and design of proteins and peptide derivatives for the production of photoluminescent, red-emitting gold quantum clusters. Gold Bull. 2013 Sep 1;46(3):195-203.

79. Wu Z, Jin R. On the ligand's role in the fluorescence of gold nanoclusters. Nano lett. 2010 Jul 14;10(7):2568-73.

80. Ghosh D, Baksi A, Mudedla SK, Nag A, Ganayee MA, Subramanian V, et al. Gold-induced unfolding of lysozyme: toward the formation of luminescent clusters. J. of Phys. Chem. C. 2017 Jun 22;121(24):13335-44.

81. Baksi A, Xavier PL, Chaudhari K, Goswami N, Pal SK, Pradeep T. Protein-encapsulated gold cluster aggregates: the case of lysozyme. Nanoscale. 2013;5(5):2009-16.

82. Mudedla SK, Singam EA, Vijay Sundar J, Pedersen MN, Murugan NA, Kongsted J, et al. Enhancement of internal motions of lysozyme through interaction with gold nanoclusters and its optical imaging. J. of Phys. Chem. C. 2015 Jan 8;119(1):653-64.

83. Barros HR, Kokkinopoulou M, Riegel-Vidotti IC, Landfester K, Thérien-Aubin H. Gold nanocolloid–protein interactions and their impact on β-sheet amyloid fibril formation. RSC adv. 2018;8(2):980-6.

84. Gladytz A, Wagner M, Häupl T, Elsner C, Abel B. Structure-making effects of metal nanoparticles in amyloid peptide fibrillation. Part. Part. Syst. Charact. 2015 May;32(5):573-82.

85. Gao G, Zhang M, Gong D, Chen R, Hu X, Sun T. The size-effect of gold nanoparticles and nanoclusters in the inhibition of amyloid-β fibrillation. Nanoscale. 2017;9(12):4107-13.

86. Moore KA, Pate KM, Soto-Ortega DD, Lohse S, van der Munnik N, Lim M, et al. Influence of gold nanoparticle surface chemistry and diameter upon Alzheimer's disease amyloid-β protein aggregation. J. Biol. Eng. 2017 Dec;11(1):5.

87. Liao YH, Chang YJ, Yoshiike Y, Chang YC, Chen YR. Negatively charged gold nanoparticles inhibit Alzheimer's amyloid-β fibrillization, induce fibril dissociation, and mitigate neurotoxicity. Small. 2012 Dec 7;8(23):3631-9.

88. Gao G, Chen R, He M, Li J, Wang L, Sun T. Gold nanoclusters for Parkinson's disease treatment. Biomaterials. 2019 Feb 1;194:36-46.

89. Han X, Man Z, Xu S, Cong L, Wang Y, Wang X, et al. A gold nanocluster chemical tongue sensor array for Alzheimer's disease diagnosis. Colloids and Surfaces B: Biointerfaces. 2019 Jan 1;173:478-85.

90. Shinde KN, Dhoble SJ, Swart HC, Park K. Basic mechanisms of photoluminescence. Phosphate phosphors for solid-state lighting. Berlin, Heidelberg: Springer; 2012. p. 41-59.

91. Lakowicz JR. 3rd edn. Principles of fluorescence spectroscopy. New York, USA: Springer; 2013.

92. Royer CA. Fluorescence spectroscopy. Protein stability and folding 1995. p. 65-89.

93. Birch DJ, Chen Y, Rolinski OJ. Fluorescence. In: David L. Andrews. Photonics: Biomedical Photonics, Spectroscopy, and Microscopy. 2015 Feb 23:1-58.

94. Xavier PL, Chaudhari K, Verma PK, Pal SK, Pradeep T. Luminescent quantum clusters of gold in transferrin family protein, lactoferrin exhibiting FRET. Nanoscale. 2010;2(12):2769-76.

95. Raut S, Chib R, Butler S, Borejdo J, Gryczynski Z, Gryczynski I. Evidence of energy transfer from tryptophan to BSA/HSA protected gold nanoclusters. Methods Appl. Fluoresc. 2014 Aug 22;2(3):035004.

96. Russell BA, Kubiak-Ossowska K, Mulheran PA, Birch DJ, Chen Y. Locating the nucleation sites for protein encapsulated gold nanoclusters: a molecular dynamics and fluorescence study. Phys. Chem. Chem. Phys. 2015;17(34):21935-41.

97. Hussain SA. An introduction to fluorescence resonance energy transfer (FRET). arXiv preprint arXiv:0908.1815. 2009 Aug 13.

98. Ravi VK, Swain T, Chandra N, Swaminathan R. On the characterization of intermediates in the isodesmic aggregation pathway of hen lysozyme at alkaline pH. PloS one. 2014 Jan 28;9(1):e87256.

99. Li C, Sutter JU, Birch DJ, Chen Y. Fluorescence anisotropy of protein-Gold nanoclusters. In: 2012 12th IEEE International Conference on Nanotechnology (IEEE-NANO). 2012 Aug 20. p. 1-4.

100. Soleilhac A, Bertorelle F, Antoine R. Sizing protein-templated gold nanoclusters by time resolved fluorescence anisotropy decay measurements. Spectrochimica Acta Part A: Molecular and Biomolecular Spectroscopy. 2018 Mar 15;193:283-8.

101. Loefroth JE. Time-resolved emission spectra, decay-associated spectra, and species-associated spectra. J. Phys Chem. 1986 Mar;90(6):1160-8.

102. Robert C. Neuman J. Peptides , Proteins , and α -Amino Acids from Organic Chemistry. In: Organic Chemistry. 2013. p. 1–6.

103. Wade LG. Amino acids, peptides, and proteins. Organic Chemistry. 2010. p. 1188 – 1191.

104. Masterton WL, Hurley CN. Organic Polymers, Natural and Synthetic. In: Chemistry: principles and reactions. Cengage Learning; 2015 Jan 2. p. 702–711

105. Tropp BE. Principles of molecular biology. Jones & Bartlett Publishers; 2012 Dec 14. P 27-33.

106. Ouellette RJ, Rawn JD. Principles of organic chemistry. 2015 Feb 13. p. 371-3.

107. Tan SY, Tatsumura Y. Alexander Fleming (1881–1955): discoverer of penicillin. Singapore medical journal. 2015 Jul;56(7).p.366-7.

108. Fleming A. On a remarkable bacteriolytic element found in tissues and secretions. Proceedings of the Royal Society of London. Series B, Containing Papers of a Biological Character. 1922 May 1;93(653):306-17.

109. Benkerroum N. Antimicrobial activity of lysozyme with special relevance to milk. Afr. J. Biotechnol. 2008 Dec 29;7(25): 4856-67

110. Hughey VL, Wilger PA, Johnson EA. Antibacterial activity of hen egg white lysozyme against Listeria monocytogenes Scott A in foods. App. Environ. Microbiol. 1989 Mar 1;55(3):631-8.

111. Ibrahim HR, Higashiguchi S, Koketsu M, Juneja LR, Kim M, Yamamoto T, et al. Partially unfolded lysozyme at neutral pH agglutinates and kills Gram-negative and Gram-positive bacteria through membrane damage mechanism. J. Agric. Food Chem. 1996 Dec 18;44(12):3799-806.

112. Lesnierowski G, Kijowski J, Cegielska-Radziejewska R. Ultrafiltration-modified chicken egg white lysozyme and its antibacterial action. International journal of food science & technology. 2009 Feb;44(2):305-11.

113. Zhou P, Sun X, Zhang Z. Kidney–targeted drug delivery systems. Acta Pharmaceutica Sinica B. 2014 Feb 1;4(1):37-42.

114. Canfield RE. The amino acid sequence of egg white lysozyme. J. Biol. Chem. 1963 Aug 1;238(8):2698-707.

115. Blake CC, Koenig DF, Mair GA, North AC, Phillips DC, Sarma VR. Structure of hen egg-white lysozyme: a three-dimensional Fourier synthesis at 2 Å resolution. Nature. 1965 May 22;206(4986):757-61.

116. Chevrier DM, Chatt A, Zhang P. Properties and applications of protein-stabilized fluorescent gold nanoclusters: short review. J.of Nanophotonics. 2012 Jul;6(1):064504.

117. Wei H, Wang Z, Zhang J, House S, Gao YG, Yang L, et al. Time-dependent, protein-directed growth of gold nanoparticles within a single crystal of lysozyme. Nature nanotechnology. 2011 Feb;6(2):93-7.

118. Upstone SL. Ultraviolet/visible light absorption spectrophotometry in clinical chemistry. Encyclopedia of Analytical Chemistry: Applications, Theory and Instrumentation. 2006 Sep 15. p. 1699–1714

119. Helmfors L, Boman A, Civitelli L, Nath S, Sandin L, Janefjord C, et al. Protective properties of lysozyme on β-amyloid pathology: implications for Alzheimer disease. Neurobiology of disease. 2015 Nov 1;83:122-33.

120. Khan JM, Qadeer A, Chaturvedi SK, Ahmad E, Rehman SA, Gourinath S, et al. SDS can be utilized as an amyloid inducer: a case study on diverse proteins. PloS one. 2012 Jan 12;7(1):e29694.

121. Kumaran R, Ramamurthy P. Denaturation mechanism of BSA by urea derivatives: evidence for hydrogen-bonding mode from fluorescence tools. J. fluoresc. 2011 Jul 1;21(4):1499-508.

122. Lindberg DJ, Wranne MS, Gatty MG, Westerlund F, Esbjörner EK. Steady-state and time-resolved Thioflavin-T fluorescence can report on morphological differences in amyloid fibrils formed by Aβ (1-40) and Aβ (1-42). Biochem. Biophys. Res. commun. 2015 Mar 6;458(2):418-23.

123. Baig MM, Chen YC. Gold nanocluster-based fluorescence sensing probes for detection of dipicolinic acid. Analyst. 2019;144(10):3289-96.

124. Instruments Edinburgh Ltd. What is TCSPC? Time-Correlated Single-Photon Counting. Technical Note. 2012.

125. Birch DJ, Imhof RE. Topics in Fluorescence Spectroscopy, vol. 1: Techniques.2002.p 1-11

126. Wahl M (PicoQuant G. Time-correlated single photon counting. Tech Note. :1–14

127. Ameloot M, Acuña AU, Valeur B. Fluorescence anisotropy measurements in solution: Methods and reference materials (IUPAC Technical Report). Pure Appl Chem. 2013 Jan 11;85(3):589-608.

128. JEOL. Scanning Electron Microscope A To Z:3.

129. Zhou W, Apkarian R, Wang ZL, Joy D. Fundamentals of scanning electron microscopy (SEM). In scanning microscopy for nanotechnology. New York, USA: Springer; 2006 .p. 1-40.

130. Caffrey M, Morris SJ, Feigenson GW. Uranyl acetate induces gel phase formation in model lipid and biological membranes. Biophys. J. 1987 Sep 1;52(3):501-5.

131. Kumar S, Ravi VK, Swaminathan R. How do surfactants and DTT affect the size, dynamics, activity and growth of soluble lysozyme aggregates?. Biochem. J. 2008 Oct 15;415(2):275-88.

132. Burnett LC, Burnett BJ, Li B, Durrance ST, Xu S. A lysozyme concentration, pH, and time-dependent isothermal transformation diagram reveals fibrous amyloid and non-fibrous, amorphous aggregate species. Open Journal of Biophysics. 2014 Mar 21;2014.39-50.

133. Krebs MR, Wilkins DK, Chung EW, Pitkeathly MC, Chamberlain AK, Zurdo J, Robinson CV, Dobson CM. Formation and seeding of amyloid fibrils from wild-type hen lysozyme and a peptide fragment from the β-domain. J. Mol Biol. 2000 Jul 14;300(3):541-9.

134. Ow SY, Dunstan DE. The effect of concentration, temperature and stirring on hen egg white lysozyme amyloid formation. Soft Matter. 2013;9(40):9692-701.

135. Novák P, Havlíček V. Protein extraction and precipitation. In Proteomic profiling and analytical chemistry 2016 Jan 1. p. 51-62.

136. Homchaudhuri L, Kumar S, Swaminathan R. Slow aggregation of lysozyme in alkaline pH monitored in real time employing the fluorescence anisotropy of covalently labelled dansyl probe. FEBS letters. 2006 Apr 3;580(8):2097-101.

137. Sophianopoulos AJ, Van Holde KE. Evidence for dimerization of lysozyme in alkaline solution. J. Biol. Chem. 1961 Dec 1;236(12):PC82-3.

138. Sophianopoulos AJ, Van Holde KE. Physical studies of muramidase (lysozyme) II. pH-dependent dimerization. J. Biol. Chem. 1964 Aug 1;239(8):2516-24.

139. Arnaudov LN, de Vries R. Thermally induced fibrillar aggregation of hen egg white lysozyme. Biophys. J. 2005 Jan 1;88(1):515-26.

140. Alzheimer's Association. 2018 Alzheimer's disease facts and figures. Alzheimer's & Dementia. 2018 Mar 1;14(3):367-429.

141. Sengupta U, Nilson AN, Kayed R. The role of amyloid-β oligomers in toxicity, propagation, and immunotherapy. EBioMedicine. 2016 Apr 1;6:42-9.

142. Wen X, Yu P, Toh YR, Tang J. Structure-correlated dual fluorescent bands in BSA-protected Au25 nanoclusters. J. Phys. Chem. C. 2012 May 31;116(21):11830-6.

143. Liu J, Lu L, Xu S, Wang L. One-pot synthesis of gold nanoclusters with bright red fluorescence and good biorecognition abilities for visualization fluorescence enhancement detection of E. coli. Talanta. 2015 Mar 1;134:54-9.

144. Ding W, Liu Y, Li Y, Shi Q, Li H, Xia H, Wang D, Tao X. Water-soluble gold nanoclusters with pH-dependent fluorescence and high colloidal stability over a wide pH range via co-reduction of glutathione and citrate. RSC advances. 2014;4(43):22651-9.

145. Zheng K, Setyawati MI, Leong DT, Xie J. Antimicrobial gold nanoclusters. ACS nano. 2017 Jul 25;11(7):6904-10.

146. Nasaruddin RR, Chen T, Yan N, Xie J. Roles of thiolate ligands in the synthesis, properties and catalytic application of gold nanoclusters. Coordination Chemistry Reviews. 2018 Aug 1;368:60-79.

147. Link S, Beeby A, FitzGerald S, El-Sayed MA, Schaaff TG, Whetten RL. Visible to infrared luminescence from a 28-atom gold cluster. J. Phys. Chem. B. 2002 Apr 4;106(13):3410-5.

148. Devadas MS, Kim J, Sinn E, Lee D, Goodson III T, Ramakrishna G. Unique ultrafast visible luminescence in monolayer-protected Au25 clusters. J. Phys. Chem. C. 2010 Dec 30;114(51):22417-23.

149. Zhao Q, Li F, Huang C. Phosphorescent chemosensors based on heavy-metal complexes. Chem. Soc. Rev. 2010;39(8):3007-30.

150. Wen X, Yu P, Toh YR, Hsu AC, Lee YC, Tang J. Fluorescence dynamics in BSA-protected Au25 nanoclusters. The J. Phys. Chem. C. 2012 Sep 6;116(35):19032-8.

151. Xavier PL, Chaudhari K, Baksi A, Pradeep T. Protein-protected luminescent noble metal quantum clusters: an emerging trend in atomic cluster nanoscience. Nano reviews. 2012 Jan 1;3(1):14767.

152. Scienti T. c, Innovative devices for secure sample dialysis.

153. Cao XL, Li HW, Yue Y, Wu Y. pH-Induced conformational changes of BSA in fluorescent AuNCs@ BSA and its effects on NCs emission. Vibrational Spectroscopy. 2013 Mar 1;65:186-92.

154. Wen X, Yu P, Toh YR, Tang J. Quantum confined stark effect in Au8 and Au25 nanoclusters. J. Phys. Chem. C. 2013 Feb 21;117(7):3621-6.

155. Russell BA, Jachimska B, Komorek P, Mulheran PA, Chen Y. Lysozyme encapsulated gold nanoclusters: effects of cluster synthesis on natural protein characteristics. Phys. Chem. Chem. Phys. 2017;19(10):7228-35.

156. Wen GW, Lin JY, Jiang HX, Chen Z. Quantum-confined Stark effects in semiconductor quantum dots. Phys. Rev. B. 1995 Aug 15;52(8):5913.

157. Robinson JW, Rice JH, Lee KH, Na JH, Taylor RA, Hasko DG, et al. Quantum-confined Stark effect in a single InGaN quantum dot under a lateral electric field. Appl. Phys. Lett. 2005 May 23;86(21):213103.

158. Empedocles SA, Bawendi MG. Quantum-confined stark effect in single CdSe nanocrystallite quantum dots. Science. 1997 Dec 19;278(5346):2114-7.

159. Akola J, Walter M, Whetten RL, Häkkinen H, Grönbeck H. On the structure of thiolate-protected Au25. J. Am. Chem. Soc. 2008 Mar 26;130(12):3756-7.

160. Raut S, Chib R, Rich R, Shumilov D, Gryczynski Z, Gryczynski I. Polarization properties of fluorescent BSA protected Au 25 nanoclusters. Nanoscale. 2013;5(8):3441-6.

161. Alkudaisi N, Russell BA, Jachimska B, Birch DJ, Chen Y. Detecting lysozyme unfolding via the fluorescence of lysozyme encapsulated gold nanoclusters. J. Mater. Chem. B. 2019;7(7):1167-75.

162. McAllister C, Karymov MA, Kawano Y, Lushnikov AY, Mikheikin A, Uversky VN, Lyubchenko YL. Protein interactions and misfolding analyzed by AFM force spectroscopy. J. Mol. Biol. 2005 Dec 16;354(5):1028-42.

163. Babu KR, Bhakuni V. Ionic-strength-dependent transition of hen egg-white lysozyme at low pH to a compact state and its aggregation on thermal denaturation. Eur. J. Biochem. 1997 May;245(3):781-9.

164. Hameed M, Ahmad B, Fazili KM, Andrabi K, Khan RH. Different molten globule-like folding intermediates of hen egg white lysozyme induced by high pH and tertiary butanol. J. Biochem. 2007 Apr 1;141(4):573-83.

165. Malvern. Zeta potential theory. In: Zetasizer Nano Series User Manual. 2009. p. 16–1 to 16–12.

166. Russell BA, Jachimska B, Komorek P, Mulheran PA, Chen Y. Lysozyme encapsulated gold nanoclusters: effects of cluster synthesis on natural protein characteristics. Phys. Chem. Chem. Phys. 2017;19(10):7228-35.

167. Siddiqui GA, Naeem A. Aggregation of globular protein as a consequences of macromolecular crowding: A time and concentration dependent study. Int. J. Biol. Macromol. 2018 Mar 1;108:360-6.

168. Higgins C. Urea and the clinical value of measuring blood urea concentration. Acutecaretesting. Org. 2016 Aug:1-6.

169. Shimaki N, IKEDA K, HAMAGUCHI K. Interaction of urea and guanidine hydrochloride with lysozyme. J. Biochem. 1971 Sep 1;70(3):497-508.

170. Gao M, She ZS, Zhou R. Key residues that play a critical role in urea-induced lysozyme unfolding. J. Phys. Chem. B. 2010 Dec 2;114(47):15687-93.

171. Hedoux A, Krenzlin S, Paccou L, Guinet Y, Flament MP, Siepmann J. Influence of urea and guanidine hydrochloride on lysozyme stability and thermal denaturation; a correlation between activity, protein dynamics and conformational changes. Phys. Chem. Chem. Phys. 2010;12(40):13189-96.

172. Chang JY, Li L. The unfolding mechanism and the disulfide structures of denatured lysozyme. FEBS letters. 2002 Jan 30;511(1-3):73-8.

173. Pike AC, Acharya KR. A structural basis for the interaction of urea with lysozyme. Protein Science. 1994 Apr;3(4):706-10.

174. Khan JM, Chaturvedi SK, Rahman SK, Ishtikhar M, Qadeer A, Ahmad E, Khan RH. Protonation favors aggregation of lysozyme with SDS. Soft matter. 2014;10(15):2591-9.

175. Van Dijk E, Hoogeveen A, Abeln S. The hydrophobic temperature dependence of amino acids directly calculated from protein structures. PLoS Comput Biol. 2015 May 22;11(5):e1004277.

176. Cordier F, Grzesiek S. Temperature-dependence of protein hydrogen bond properties as studied by high-resolution NMR. J. Mol. Biol. 2002 Apr 12;317(5):739-52.

177. Venkataramani S, Truntzer J, Coleman DR. Thermal stability of high concentration lysozyme across varying pH: A Fourier Transform Infrared study. J. pharm. Bioallied sci. 2013 Apr;5(2):148.

178. Langkilde AE, Vestergaard B. Methods for structural characterization of prefibrillar intermediates and amyloid fibrils. FEBS letters. 2009 Aug 20;583(16):2600-9.

179. LeVine III H. [18] Quantification of β-sheet amyloid fibril structures with thioflavin T. InMethods in enzymology 1999 Jan 1 (Vol. 309, pp. 274-284). Academic Press.

180. Khurana R, Coleman C, Ionescu-Zanetti C, Carter SA, Krishna V, Grover RK, Roy R, Singh S. Mechanism of thioflavin T binding to amyloid fibrils. Journal of structural biology. 2005 Sep 1;151(3):229-38.

181. Groenning M, Olsen L, van de Weert M, Flink JM, Frokjaer S, Jørgensen FS. Study on the binding of Thioflavin T to β-sheet-rich and non-β-sheet cavities. Journal of structural biology. 2007 Jun 1;158(3):358-69.

182. Krebs MR, Bromley EH, Donald AM. The binding of thioflavin-T to amyloid fibrils: localisation and implications. Journal of structural biology. 2005 Jan 1;149(1):30-7.

183. Wu C, Wang Z, Lei H, Duan Y, Bowers MT, Shea JE. The binding of thioflavin T and its neutral analog BTA-1 to protofibrils of the Alzheimer's disease Aβ16–22 peptide probed by molecular dynamics simulations. Journal of molecular biology. 2008 Dec 19;384(3):718-29.

184. Kitts CC, Bout DA. Near-field scanning optical microscopy measurements of fluorescent molecular probes binding to insulin amyloid fibrils. The Journal of Physical Chemistry B. 2009 Sep 3;113(35):12090-5.

185. Chib R, Butler S, Raut S, Shah S, Borejdo J, Gryczynski Z, Gryczynski I. Effect of quencher, denaturants, temperature and pH on the fluorescent properties of BSA protected gold nanoclusters. J. Lumin. 2015 Dec 1;168:62-8.

186. Kurtin WE, Lee JM. The free energy of denaturation of lysozyme: An undergraduate experiment in biophysical chemistry. Biochemistry and Molecular Biology Education. 2002 Jul;30(4):244-7.

187. Garcia AR, Rahn I, Johnson S, Patel R, Guo J, Orbulescu J, et al. Human insulin fibril-assisted synthesis of fluorescent gold nanoclusters in alkaline media under physiological temperature. Colloids and Surfaces B: Biointerfaces. 2013 May 1;105:167-72.

188. Alkudaisi N, Russell BA, Birch DJ, Chen Y. Lysozyme encapsulated gold nanoclusters for probing the early stage of lysozyme aggregation under acidic conditions. J. Photochem. Photobiol. B: Biology. 2019 Aug 1;197:111540.

189. Raut S, Chib R, Rich R, Shumilov D, Gryczynski Z, Gryczynski I. Polarization properties of fluorescent BSA protected Au 25 nanoclusters. Nanoscale. 2013;5(8):3441-6.

190. Corrêa DH, Ramos CH. The use of circular dichroism spectroscopy to study protein folding, form and function. Afr. J. Biochem. Res.. 2009 May;3(5):164-73.

191. Callis PR, Liu T. Quantitative prediction of fluorescence quantum yields for tryptophan in proteins. J. Biol. Chem. B. 2004 108, 4248–59.

192. Stsiapura VI, Maskevich AA, Kuzmitsky VA, Uversky VN, Kuznetsova IM, Turoverov KK. Thioflavin T as a molecular rotor: fluorescent properties of thioflavin T in solvents with different viscosity. J. Phys. Chem. B. 2008 Dec 11;112(49):15893-902.

193. Vaughn WM, Weber G. Oxygen quenching of pyrenebutyric acid fluorescence in water. Dynamic probe of the microenvironment. Biochemistry. 1970 Feb 1;9(3):464-73.

194. Lakowicz JR, Weber G. Quenching of fluorescence by oxygen. Probe for structural fluctuations in macromolecules. Biochemistry. 1973 Oct 1;12(21):4161-70.

195. Magde D, Wong R, Seybold PG. Fluorescence quantum yields and their relation to lifetimes of rhodamine 6G and fluorescein in nine solvents: Improved absolute standards for quantum yields. Photochem. Photobiol. 2002 Apr;75(4):327-34.

196. Butler IB, Schoonen MA, Rickard DT. Removal of dissolved oxygen from water: a comparison of four common techniques. Talanta. 1994 Feb 1;41(2):211-5.

197. Das T, Ghosh P, Shanavas MS, Maity A, Mondal S, Purkayastha P. Protein-templated gold nanoclusters: size dependent inversion of fluorescence emission in the presence of molecular oxygen. Nanoscale. 2012;4(19):6018-24.

198. Chow VW, Mattson MP, Wong PC, Gleichmann M. An overview of APP processing enzymes and products. Neuromolecular Med. 2010 Mar 1;12(1):1-2.

199. Lin YS, Bowman GR, Beauchamp KA, Pande VS. Investigating how peptide length and a pathogenic mutation modify the structural ensemble of amyloid beta monomer. Biophys. J. 2012 Jan 18;102(2):315-24.

200. Jarrett JT, Berger EP, Lansbury Jr PT. The carboxy terminus of the beta amyloid protein is critical for the seeding of amyloid formation: Implications for the pathogenesis of Alzheimer's disease. Biochemistry. 1993 May 1;32(18):4693-7.

201. Yang HD, Kim DH, Lee SB, Young LD. History of Alzheimer's Disease. Dementia and neurocognitive disorders. 2016 Dec 1;15(4):115-21.

202. Omicsonline.org. (2020). Saudi Alzheimers disease Association. [online] Available at: https://www.omicsonline.org/societies/saudi-alzheimers/ [Accessed 14 Oct. 2018].

203. Association A. Alzheimer's & Dementia Help | UK | Alzheimer's Association [Internet]. Alzheimer's Association. 2020 [cited 14 October 2018]. Available from: https://www.alz.org/uk/dementia-alzheimers-uk.asp

204. Sörgjerd K, Zako T, Sakono M, Stirling P, Leroux M, Saito T, Nilsson P, Sekiguchi M, Saido T, Maeda M. P4-355: Human prefoldin can inhibit BETA-AMYLOID fibrillation and contribute to formation of non-toxic BETA-AMYLOID aggregates. Alzheimer's & Dementia. 2012 Jul;8:782.

205. Luo J, Wärmländer SK, Gräslund A, Abrahams JP. Non-chaperone proteins can inhibit aggregation and cytotoxicity of Alzheimer amyloid β peptide. J. Biol. Chem. 2014 Oct 3;289(40):27766-75.

206. Kim Y, Park JH, Lee H, Nam JM. How do the size, charge and shape of nanoparticles affect amyloid β aggregation on brain lipid bilayer?. Scientific reports. 2016 Jan 19;6:19548.

207. Luo Z, Zheng K, Xie J. Engineering ultrasmall water-soluble gold and silver nanoclusters for biomedical applications. ChemComm. 2014;50(40):5143-55.

208. Zhang E, Fu A. A new strategy for specific imaging of neural cells based on peptide-conjugated gold nanoclusters. Int. J. Nanomedicine. 2015;10:2115.

209. Lai L, Zhao C, Li X, Liu X, Jiang H, Selke M, Wang X. Fluorescent gold nanoclusters for in vivo target imaging of Alzheimer's disease. RSC advances. 2016;6(36):30081-8.

210. Nair LV, Nair RV, Shenoy SJ, Thekkuveettil A, Jayasree RS. Blood brain barrier permeable gold nanocluster for targeted brain imaging and therapy: an in vitro and in vivo study. J Mater. Chem. B. 2017;5(42):8314-21.

211. Luo J, Wärmländer SK, Gräslund A, Abrahams JP. Human lysozyme inhibits the in vitro aggregation of Aβ peptides, which in vivo are associated with Alzheimer's disease. ChemComm. 2013;49(58):6507-9.

212. Sulatskaya AI, Maskevich AA, Kuznetsova IM, Uversky VN, Turoverov KK. Fluorescence quantum yield of thioflavin T in rigid isotropic solution and incorporated into the amyloid fibrils. PloS one. 2010 Oct 29;5(10):e15385.

213. Stsiapura VI, Maskevich AA, Kuzmitsky VA, Turoverov KK, Kuznetsova IM. Computational study of thioflavin T torsional relaxation in the excited state. J. Phys. Chem. A. 2007 Jun 7;111(22):4829-35.

214. Stine WB, Dahlgren KN, Krafft GA, LaDu MJ. In vitro characterization of conditions for amyloid-β peptide oligomerization and fibrillogenesis. J. Biol. Chem. 2003 Mar 28;278(13):11612-22.

215. Lesné S, Koh MT, Kotilinek L, Kayed R, Glabe CG, Yang A, Gallagher M, Ashe KH. A specific amyloid-β protein assembly in the brain impairs memory. Nature. 2006 Mar;440(7082):352-7.

216. Amaro M, Wellbrock T, Birch DJ, Rolinski OJ. Inhibition of beta-amyloid aggregation by fluorescent dye labels. Appl. Phys. Lett. 2014 Feb 10;104(6):063704.

217. Xue C, Lin TY, Chang D, Guo Z. Thioflavin T as an amyloid dye: fibril quantification, optimal concentration and effect on aggregation. R. Soc. open sci. 2017 Jan 4;4(1):160696.

218. Wang YQ, Zhang HM, Zhang GC, Liu SX, Zhou QH, Fei ZH, Liu ZT. Studies of the interaction between paraquat and bovine hemoglobin. Int. J. Biol. Macromol. 2007 Aug 1;41(3):243-50.

219. Klug GM, Losic D, Supundi, Subasinghe S, Aguilar MI, Martin LL, Small DH. β-Amyloid protein oligomers induced by metal ions and acid pH are distinct from those generated by slow spontaneous ageing at neutral pH. Eur. J. Biochem. 2003 Nov;270(21):4282-93.

220. Hortschansky P, Schroeckh V, Christopeit T, Zandomeneghi G, Fändrich M. The aggregation kinetics of Alzheimer's β-amyloid peptide is controlled by stochastic nucleation. Protein science. 2005 Jul;14(7):1753-9.

221. Vivian JT, Callis PR. Mechanisms of tryptophan fluorescence shifts in proteins. Biophys. J. 2001 May 1;80(5):2093-109.

222. Shanmugaraj K, Ilanchelian M. A “turn-off” fluorescent sensor for the selective and sensitive detection of copper (ii) ions using lysozyme stabilized gold nanoclusters. RSC advances. 2016;6(59):54518-24.

223. Roy AS, Ghosh P. Characterization of the binding of flavanone hesperetin with chicken egg lysozyme using spectroscopic techniques: effect of pH on the binding. J. Incl. Phenom. Macrocycl. Chem. 2016 Feb 1;84(1-2):21-34.

224. Vilcacundo R, Méndez P, Reyes W, Romero H, Pinto A, Carrillo W. Antibacterial activity of hen egg white lysozyme denatured by thermal and chemical treatments. Scientia pharmaceutica. 2018 Dec;86(4):48.

Appendix

1. Preparing Mixtures of The HEWL and Lyz-AuNCs

The preparation of Lyz-AuNCs as shown in chapter 4 is the following :

A 50 mg of HEWL was dissolved in 5 ml of water. HEWL (5 ml, 10mg/ml) was mixed with $HAuCl_4$ solution (5 ml, 4 mM). After 5 mins 0.5ml NaOH (1M) was added to the mixture. The final concentration of Lyz-AuNCs is 50 mg/(10.5 ml X 14.3 kDa) = 0.33 mM. where the molecular weight of HEWL is 14.3 kDa

The Lyz-AuNCs (10.5 ml, 0.33 mM) assume that the concentration of the final product after dialyses did not change. Assuming that all HEWL molecules are attached with AuNCs and the remain Au ion are removed through dialyses.

Explain the concentration of HEWL

Then 0.3 ml of Lyz-AuNCs was dissolved in 2.7 ml of water yield the final volume is 3 ml The final concentration of Lyz-AuNCs is obtained using the following equation

$$C_2 = \frac{C_1 \times V_1}{V_2} \qquad (1)$$

$$C_2 = \frac{C_1 \times V_1}{V_2} = \frac{0.33\ mM \times 0.3\ mL}{3\ ml} = 0.033\ mM = 33\ \mu M$$

[Lyz-AuNCs] C_1 (mM)	The volume of Lyz-AuNCs V_1 (mL)	The weight of HEWL (mg)	The volume of Lyz-AuNCs + HEWL V_2 (mL)	[HEWL] (mg/ml)	[Lyz-AuNCs] C_2 (µM)
0.33	0.3	15	3	5	33
0.33	0.3	30	3	10	33
0.33	0.3	45	3	15	33
0.33	0.3	60	3	20	33
0.33	0.3	75	3	25	33
0.33	0.3	90	3	30	33
0.33	0.3	105	3	35	33

2. The absorbance of HEWL concentration

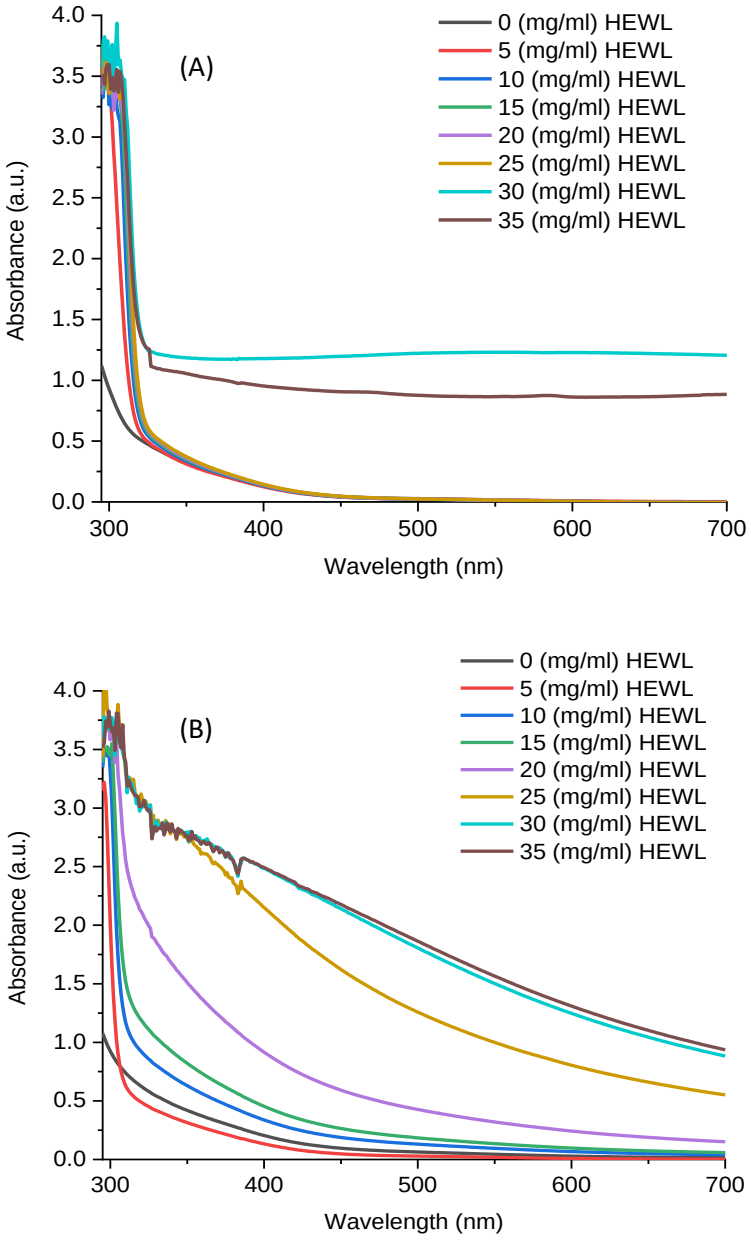

Figure A.1 Absorbance spectra of Lyz-AuNCs as a function of HEWL concentration (A) at pH 12.5 and (B) at pH 3.

Figure A.1 shows the UV-Vis spectra of Lyz-AuNCs with various concentration of HEWL at pH 12.5 and pH 3. At pH 12.5, the absorption at 350 nm does not change with the increases of HEWL until it reaches 30 mg/ml. On the other hand, absorption at 350 nm increases as a HEWL increases as shown in Figure A.1 (B).

3. Preparing Mixtures of The Urea and Lyz-AuNCs

The Lyz-AuNCs is prepared as shown in chapter 4 and explained above. The Lyz-AuNCs (0.33 mM, 10.5 mL). A stock solution of urea was freshly prepared by dissolving 7.3 grams of urea crystals in 13.50 mL of water at room temperature yielding Urea (8.5 M, 13.50 mL) and then diluting and mixing with Lyz-AuNCs to yield a final concentration of Lyz-AuNCs of 33 µM. The urea concentration was changed from 0 to 8 M. The volume of water and urea solution are changed in order to maintain the concentration of Lyz-AuNCs. The table below shows the amount of water and urea solution are needed to obtain the desire concentration of both Lyz-AuNCs and SDS

The volume of Lyz-AuNCs V_1 (mL)	The volume of urea V_1 (mL)	The volume of water (mL)	The volume of mixture is V_2 (mL)	[urea] C_2 (M)	[Lyz-AuNCs] C_2 (µM)
0.3	0	2.7	3	0	33
0.3	0.33	2.37	3	1	33
0.3	0.66	2.04	3	2	33
0.3	1	1.70	3	3	33
0.3	1.33	1.37	3	4	33
0.3	1.66	1.04	3	5	33
0.3	2	0.70	3	6	33
0.3	2.33	0.37	3	7	33
0.3	2.66	0.04	3	8	33

4. Preparing Mixtures of The SDS and Lyz-AuNCs

To prepare stock SDS solution, 92.63 mg of SDS powder was dissolved in 1.07 ml of water; the final concentration was 0.3 M. This was then mixed with Lyz-AuNCs to yield a final concentration of Lyz-AuNCs 33 µM, and the concentration of SDS was changed from 0 to 9 mM. The volume of water and SDS solution are changed in order to maintain the concentration of Lyz-AuNCs. The table below shows the amount of water and SDS solution are needed to obtain the desire concentration of both Lyz-AuNCs and SDS

The volume of Lyz-AuNCs V_1 (µL)	The volume of SDS V_1 (µL)	The volume of water (µL)	The volume of mixture is V_2 (ml)	[SDS] C_2 (M)	[Lyz-AuNCs] C_2 (µM)
300	0	2700	3	0	33
300	2	2698	3	0.2	33
300	4	2696	3	0.4	33
300	6	2694	3	0.6	33
300	8	2692	3	0.8	33
300	10	2690	3	1	33
300	20	2680	3	2	33
300	30	2670	3	3	33
300	40	2660	3	4	33
300	50	2650	3	5	33
300	60	2640	3	6	33
300	70	2630	3	7	33
300	80	2620	3	8	33
300	90	2610	3	9	33